

UNCLASSIFIED

AD NUMBER
AD809980
NEW LIMITATION CHANGE
TO Approved for public release, distribution unlimited
FROM Distribution authorized to U.S. Gov't. agencies and their contractors; Administrative/Operational Use; OCT 1966. Other requests shall be referred to Air Force Flight Dynamics Lab., Wright-Patterson AFB, OH 45433.
AUTHORITY
AFFDL ltr, 27 Feb 1975

THIS PAGE IS UNCLASSIFIED

REPRODUCTION QUALITY NOTICE

This document is the best quality available. The copy furnished to DTIC contained pages that may have the following quality problems:

- **Pages smaller or larger than normal.**
- **Pages with background color or light colored printing.**
- **Pages with small type or poor printing; and or**
- **Pages with continuous tone material or color photographs.**

Due to various output media available these conditions may or may not cause poor legibility in the microfiche or hardcopy output you receive.



If this block is checked, the copy furnished to DTIC contained pages with color printing, that when reproduced in Black and White, may change detail of the original copy.

AFFDL-TR-65-195

809980

**ADVANCED RE-ENTRY SYSTEMS
HEAT-TRANSFER MANUAL
FOR
HYPERSONIC FLIGHT**

*ALFRED C. THOMAS,
ANDREW PERLBACHS,
and
A. L. NAGEL*

THE BOEING COMPANY

TECHNICAL REPORT AFFDL-TR-65-195

OCTOBER 1966

This document is subject to special export controls and each transmittal to foreign governments or foreign nationals may be made only with prior approval of the Air Force Flight Dynamics Laboratory (FDMG), Wright-Patterson Air Force Base, Ohio 45433.

AIR FORCE FLIGHT DYNAMICS LABORATORY
RESEARCH AND TECHNOLOGY DIVISION
AIR FORCE SYSTEMS COMMAND
WRIGHT-PATTERSON AIR FORCE BASE, OHIO

NOTICES

When Government drawings, specifications, or other data are used for any purpose other than in connection with a definitely related Government procurement operation, the United States Government thereby incurs no responsibility nor any obligation whatsoever; and the fact that the Government may have formulated, furnished, or in any way supplied the said drawings, specifications, or other data, is not to be regarded by implication or otherwise as in any manner licensing the holder or any other person or corporation, or conveying any rights or permission to manufacture, use, or sell any patented invention that may in any way be related thereto.

Copies of this report should not be returned to the Research and Technology Division unless return is required by security considerations, contractual obligations, or notice on a specific document.

**ADVANCED RE-ENTRY SYSTEMS
HEAT-TRANSFER MANUAL
FOR
HYPERSONIC FLIGHT**

*ALFRED C. THOMAS,
ANDREW PERLBACHS,
and
A. L. NAGEL*

This document is subject to special export controls and each transmittal to foreign governments or foreign nationals may be made only with prior approval of the Air Force Flight Dynamics Laboratory (FDMC), Wright-Patterson Air Force Base, Ohio 45433.

FOREWORD

This report, identified as Reinstated Documentation Sub-Item No. 8-44, is submitted pursuant to ASD Message ASKIT-2-9-2-E dated 2 September 1964 and ASD Message ASKB-00006 dated 17 October 1964, issued under Contract AF33(657)-7132. The work was administered under the direction of the Flight Dynamics Laboratory, Aeronautical Systems Division, Wright Air Development Division, Wright-Patterson Air Force Base, Ohio, Mr. Richard D. Neumann, Project Engineer. The report was prepared by the Performance and Aerothermodynamics organization of the Aerospace Division, The Boeing Company, Seattle, Washington, under the direction of A. L. Nagel. The report was written by Messrs. Nagel, Alfred C. Thomas, lead engineer, and Andrew Perlbachs.

The report covers work conducted from October 1964 to August 1965. It was submitted in August 1965, revised and resubmitted in June 1966.

The authors are indebted to Barbara J. Barrett for her devotion in assembling and her endless scrutiny in checking the charts and curves contained in this report, and to several former members of the X-20 Aerothermodynamics Group, without whose assistance this document could not have been written.

The technical report has been reviewed and is approved.

Donald G. Harvey Lt. Col.
for Philip P. Antonatos
Chief, Flight Mechanics Division
Air Force Flight Dynamics Laboratory

ABSTRACT

An advanced re-entry systems heat-transfer handbook for hypersonic flight has been developed using aerothermodynamic prediction methods developed during the X-20A (Dyna Soar) Program. It contains 1) design procedures for computing aerodynamic heating rates to re-entry vehicle configurational elements, 2) discussion of differences between aerodynamic heat transfer and pressure distributions observed in present day wind tunnels and those which would occur in actual free flight, 3) wind tunnel to flight extrapolation factors, 4) simplified expressions for estimating stagnation point and swept cylinder turbulent stagnation line heating rates, and 5) graphs for rapid calculation of heating rates and extrapolation to flight factors. The information presented is applicable to complex maneuverable vehicles as well as ballistic bodies.

CONTENTS

Section	Page
I. INTRODUCTION	1
II. METHODS FOR BASIC SHAPES	3
A. Flat Plate	4
B. Hemisphere	5
C. Infinite Cylinder	9
D. Sharp Unyawed Cone	10
E. Sharp Delta Wing	10
III. COMBINATIONS OF BASIC SHAPES	21
A. Hemisphere - Cone	21
B. Blunt Delta Wing	24
C. Deflected Flap	29
IV. SURFACE CONDITION EFFECTS	35
A. Shallow Surface Waves	35
B. Leakage	37
V. APPLICATION TO COMPLEX CONFIGURATIONS	40
A. Control Surface Gap	41
B. Fin Leading Edge and Canopy Interference Effects	42
VI. DESIGN CHARTS	46
A. Method of Presentation	46
B. Reference Conditions	47
C. Reference Condition Charts	49
D. Geometric Elements	50
1. Hemisphere	50
2. Infinite Cylinders	51
3. Sharp Flat Plates	52
4. Unyawed Cones	52
5. Delta Wings	53
6. Deflected Flaps	55
7. Surface Conditions	56
8. Control Surface Gaps	56
9. Canopy and Fin Leading Edges	57

TABLE OF CONTENTS (concluded)

Section	Page
VII. USE OF GROUND-FACILITY DATA IN DESIGN	106
A. Real-Gas Effects on Shock-Layer Properties	106
1. Pressures	106
2. Streamlines	107
3. Boundary Layer Properties	107
4. Heating Rates	108
E. Extrapolation of Ground-Facility Heat-Transfer Test Data to Flight Conditions	108
1. Compressibility Parameter (Δ)	109
2. Extrapolation Factor (ζ/Δ)	109
3. Correction Factors for Deflected Flaps	110
APPENDIX A SIMPLIFIED EQUATIONS	143
APPENDIX B LAMINAR AND TURBULENT $\rho_r \mu_r$ HEAT TRANSFER METHOD	151
APPENDIX C NONSIMILAR BOUNDARY LAYER PROGRAM	190
APPENDIX D FORMULATION OF PARAMETER $h\delta^*$	197
APPENDIX E SAMPLE SOLUTIONS	199
REFERENCES	210

ILLUSTRATIONS

<u>Figure</u>	<u>Title</u>	<u>Page</u>
2-1	PRESSURE DISTRIBUTION ON HEMISPHERE AND UNSWEPT INFINITE CYLINDER	17
2-2	STAGNATION POINT VORTICITY INTERACTION EFFECT	18
2-3	WEDGE, CONE, AND STAGNATION POINT PROPORTIONALITY CONSTANT	19
2-4	BOEING MODIFIED NEWTONIAN HYPERSONIC PRESSURE COEFFICIENTS	20
3-1	UNYAWED BLUNT CONE SURFACE PRESSURE	33
3-2	BLUNT DELTA WING LOWER SURFACE CENTERLINE PRESSURE	34
4-1	EFFECT OF LEAKAGE ON LAMINAR HEAT TRANSFER	39
5-1	RE-ENTRY VEHICLE	44
5-2	HYPERSONIC CRUISE VEHICLE	44
5-3	CONTROL SURFACE GAP GEOMETRY	45
6-1	EQUIVALENT RECOVERY TEMPERATURE	58
6-2	LAMINAR REFERENCE HEAT TRANSFER COEFFICIENT	59
6-3	WALL TEMPERATURE CORRECTION FACTOR FOR LAMINAR REFERENCE HEAT TRANSFER COEFFICIENT	60
6-4	TURBULENT REFERENCE HEAT TRANSFER COEFFICIENT	61
6-5	WALL TEMPERATURE CORRECTION FACTOR FOR TURBULENT REFERENCE HEAT TRANSFER COEFFICIENT	62
6-6	RADIUS CORRECTION FACTOR FOR TURBULENT REFERENCE HEAT TRANSFER COEFFICIENT	63
6-7	REFERENCE REYNOLDS NUMBER	64
6-8	REFERENCE REYNOLDS NUMBER	65
6-9	HEMISPHERE LAMINAR HEATING DISTRIBUTION	66
6-10	HEMISPHERE REFERENCE REYNOLDS NUMBER AT LOCATION OF MAXIMUM TURBULENT HEATING	67
6-11	LOCATION OF MAXIMUM TURBULENT HEATING ON HEMISPHERE	68

ILLUSTRATIONS (continued)

<u>Figure</u>	<u>Title</u>	<u>Page</u>
6-12	HEMISPHERE TURBULENT HEATING DISTRIBUTION	69
6-13	HEMISPHERE AND UNSWEPT INFINITE CYLINDER MAXIMUM TURBULENT HEATING	70
6-14	VORTICITY INTERACTION FUNCTIONS	71
6-15	STAGNATION POINT VORTICITY INTERACTION EFFECT	72
6-16	SWEPT INFINITE CYLINDER STAGNATION LINE LAMINAR HEATING	73
6-17	SWEPT INFINITE CYLINDER LAMINAR HEATING DISTRIBUTION	74
6-18	SWEPT INFINITE CYLINDER STAGNATION LINE TURBULENT HEATING	75
6-19	SWEPT INFINITE CYLINDER TURBULENT HEATING DISTRIBUTION	76
6-20	UNSWEPT INFINITE CYLINDER REFERENCE REYNOLDS NUMBER AT LOCATION OF MAXIMUM TURBULENT HEATING	77
6-21	LOCATION OF MAXIMUM TURBULENT HEATING ON UNSWEPT INFINITE CYLINDER	78
6-22	UNSWEPT INFINITE CYLINDER TURBULENT HEATING DISTRIBUTION	79
6-23	SHARP FLAT PLATE HEATING	80
6-24	WALL TEMPERATURE CORRECTION FACTORS FOR SHARP FLAT PLATES, UNYAWED SHARP CONES, AND SHARP DELTA WINGS	81
6-25	DISTANCE CORRECTION FACTORS FOR SHARP FLAT PLATES, UNYAWED SHARP CONES, AND SHARP DELTA WINGS	82
6-26	UNYAWED SHARP CONE HEATING	83
6-27	UNYAWED BLUNT CONE LAMINAR HEATING	84
6-28	UNYAWED BLUNT CONE REFERENCE REYNOLDS NUMBER	85
6-29	UNYAWED BLUNT CONE AND BLUNT DELTA WING LAMINAR TO TURBULENT HEAT TRANSFER CORRELATION	86
6-30	SHARP DELTA WING LOWER SURFACE CENTERLINE HEATING	87
6-31	EFFECT OF SWEEP ON SHARP DELTA WING LOWER SURFACE CENTERLINE HEATING	88

ILLUSTRATIONS (continued)

<u>Figure</u>	<u>Title</u>	<u>Page</u>
6-32	SHARP DELTA WING SPANWISE LAMINAR HEATING PARAMETER	89
6-33	SHARP DELTA WING SPANWISE TURBULENT HEATING PARAMETER	90
6-34	BLUNT DELTA WING LOWER SURFACE CENTERLINE LAMINAR HEATING	91
6-35	EFFECT OF SWEEP ON BLUNT DELTA WING LOWER SURFACE CENTERLINE HEATING	92
6-36	BLUNT DELTA WING LOWER SURFACE SPANWISE LAMINAR HEATING	93
6-37	BLUNT DELTA WING LOWER SURFACE SPANWISE LAMINAR HEATING	94
6-38	UNYAWED BLUNT DELTA WING LEADING EDGE STAGNA- TION LINE SHIFT	95
6-39	UNYAWED BLUNT DELTA WING LEADING EDGE EFFECTIVE SWEEP ANGLE	96
6-40	BLUNT DELTA WING LOWER SURFACE CENTERLINE REFERENCE REYNOLDS NUMBER	97
6-41	FLAP SURFACE MAXIMUM LAMINAR HEATING	98
6-42	FLAP SURFACE MAXIMUM TURBULENT HEATING - RATIO OF TURBULENT TO LAMINAR REFERENCE VALUES	99
6-43	SURFACE WAVE LAMINAR HEATING	100
6-44	SURFACE WAVE LAMINAR HEATING	101
6-45	SHARP FLAT PLATE LAMINAR DISPLACEMENT THICKNESS HEATING PARAMETER	102
6-46	EFFECT OF LEAKAGE ON LAMINAR HEAT TRANSFER	103
6-47	CONTROL SURFACE GAP HEATING (TIP FIN - ELEVON)	104
6-48	CANOPY INTERFERENCE - LAMINAR AND TURBULENT HEATING	105
7-1	REAL GAS EFFECT ON SHARP FLAT PLATE SURFACE PRESSURE	111
7-2	REAL GAS EFFECT ON FLAP SURFACE PRESSURE	112

ILLUSTRATIONS (continued)

<u>Figure</u>	<u>Title</u>	<u>Page</u>
7-3	FLAP SURFACE PRESSURE COMPARISON	113
7-4	REAL GAS EFFECT ON STAGNATION POINT PRESSURE	114
7-5	REAL GAS EFFECT ON STREAMLINE ANGLE FOR INFINITE SWEEP CYLINDER	115
7-6	REAL GAS EFFECT ON SHARP FLAT PLATE BOUNDARY LAYER TEMPERATURE PROFILE	116
7-7	REAL GAS EFFECT ON SHARP FLAT PLATE BOUNDARY LAYER DISPLACEMENT THICKNESS	117
7-8	SHARP FLAT PLATE HEATING COMPARISON	118
7-9	FLAP SURFACE HEATING COMPARISON	119
7-10	SWEPT INFINITE CYLINDER HEATING COMPARISON	120
7-11	SHARP FLAT PLATE LAMINAR COMPRESSIBILITY PARAMETER	121
7-12	SHARP FLAT PLATE TURBULENT COMPRESSIBILITY PARAMETER	122
7-13	UNYAWED SHARP CONE LAMINAR COMPRESSIBILITY PARAMETER	123
7-14	UNYAWED SHARP CONE TURBULENT COMPRESSIBILITY PARAMETER	124
7-15	SHARP DELTA WING COMPRESSIBILITY PARAMETERS	125
7-16	SWEPT INFINITE CYLINDER LAMINAR COMPRESSIBILITY PARAMETER	126
7-17	SWEPT INFINITE CYLINDER TURBULENT COMPRESSIBILITY PARAMETER	127
7-18	CONTROL SURFACE GAP COMPRESSIBILITY PARAMETERS	128
7-19	SHARP FLAT PLATE LAMINAR HEATING EXTRAPOLATION FACTOR	129
7-20	SHARP FLAT PLATE TURBULENT HEATING EXTRAPOLATION FACTOR	130
7-21	UNYAWED SHARP CONE LAMINAR HEATING EXTRAPOLATION FACTOR	131

ILLUSTRATIONS (concluded)

<u>Figure</u>	<u>Title</u>	<u>Page</u>
7-22	UNYAWED SHARP CONE TURBULENT HEATING EXTRA- POLATION	132
7-23	SHARP DELTA WING LAMINAR HEATING EXTRAPOLATION FACTOR	133
7-24	SHARP DELTA WING TURBULENT HEATING EXTRAPOLA- TION FACTOR	134
7-25	HEMISPHERE LAMINAR HEATING EXTRAPOLATION FACTOR	135
7-26	SWEPT INFINITE CYLINDER LAMINAR HEATING EXTRA- POLATION FACTOR	136
7-27	SWEPT INFINITE CYLINDER TURBULENT HEATING EXTRAPOLATION FACTOR	137
7-28	CONTROL SURFACE GAP LAMINAR HEATING EXTRAPOLA- TION FACTOR	138
7-29	CONTROL SURFACE GAP TURBULENT HEATING EXTRAPO- LATION FACTOR	139
7-30	FLAP SURFACE HEATING EXTRAPOLATION FACTOR	140
7-31	FLAP SURFACE HEATING EXTRAPOLATION FACTOR	141
A1	FREE STREAM PRESSURE IN HIGH ENTHALPY WIND TUNNELS	150
B1	EFFECT OF PRANDTL NUMBER ON REYNOLDS ANALOGY FACTOR	184
B2	CORRELATION OF REFERENCE DENSITY-VISCOSITY PRODUCT ($M = 0$)	185
B3	DENSITY-VISCOSITY PRODUCT CORRELATIONS	186
B4	PRESSURE GRADIENT EFFECT CORRELATION PARAMETERS	187
B5	PRESSURE GRADIENT EFFECT CORRELATION COMPARED WITH EXACT SOLUTIONS	188
B6	COMPARISON OF INCOMPRESSIBLE TURBULENT SKIN- FRICTION FORMULAS	189

SYMBOLS

a	local speed of sound
A	vorticity parameter, coefficient in eq. (2.12); parameter defined by eq. (4.5a); boundary layer thickness parameter, $2 + (\delta^*/\theta)$
ALT	altitude
a_n^*	speed of sound at leading edge of delta wing
B	parameter defined by eq. (4.5b)
c	specific heat of model skin
C	parameter defined by eq. (4.5c); constant; coefficient; correction factor
C_f	skin-friction coefficient, $\tau/[(\rho u^2)/2]$
c_p	specific heat at constant pressure
C_p	pressure coefficient
c_v	specific heat at constant volume
C_x, C_m	constants in boundary layer shear law, eq. (B13)
D	parameter defined by eq. (4.5d)
E	crossflow momentum thickness, eq. (B7)
\bar{E}	momentum-thickness ratio, E/θ
f	streamline-divergence parameter due to transverse pressure gradients, eq. (B9)
F	function of x, eq. (B10)
F_{Pr}	Prandtl-number function, eq. (B22)
F_x	equivalent distance function, eq. (B55)
F_1, F_2	parameters defined in figure 6-14
g	scale factor on y, eq. (B1)
G	boundary layer parameter, eq. (B16)

SYMBOLS (continued)

h	heat-transfer coefficient based on temperature, $\dot{q}/(T_{AW} - T_W)$; height
H	heat-transfer coefficient based on enthalpy, $\dot{q}/(i_{AW} - i_W)$; enthalpy
H_L	parameter defined by eq. (4.7a)
i	enthalpy
i_D	enthalpy absorbed in dissociation
J	streamwise pressure-gradient parameter, eqs. (B35) and (B49)
k	thermal conductivity
K	constant
K_1, K_2	parameters defined by eq. (4.4)
L	leakage parameter, eq. (4.7)
Le	Lewis number
\mathcal{L}	Lewis-number function, eqs. (B22) and (B28)
m	exponent on boundary-layer shear law, eq. (B13); viscous- flow exponent, eq. (3.17)
\dot{m}	mass flow rate
M	Mach number
n	defined by eq. (2.28); exponent
N	surface distance normal to and measured from swept delta- wing leading edge
$[0]$	on the order of magnitude of
P	pressure
$P(X)$	arbitrary function of X , eq. (B13a)
Pr	Prandtl number
P_{T_1}	stagnation-chamber pressure
P_{T_2}	pressure on reference body
\dot{q}	heating rate

SYMBOLS (continued)

\bar{q}_w	transformed heating rate, eq. (B11a)
$Q(X)$	arbitrary function of X, eq. (B13a)
r	radius; flow divergence parameter related to body geometry, eq. (B9a)
R	roughness element height; radius; gas constant
\mathcal{R}	gas constant for any gas
Re_o	Reynolds number at stagnation conditions, eq. (6.12)
Re_∞	free stream Reynolds number
Re_e	Reynolds number based on boundary layer edge conditions, eq. (B20)
R_r	reference Reynolds number, eq. (B54)
R_R	reference Reynolds number on stagnation line of a 60° swept infinite cylinder, 1 foot in radius
$R_{R\text{MAX}}$	Reynolds number at location of maximum turbulent heating
s	distance along streamline
S	Reynolds analogy parameter, eq. (B22); centerline surface distance measured from stagnation point
S_{eq}	skin friction equivalent distance, eq. (B18)
St	Stanton number, $h/(\rho u c_p)$
\mathcal{J}	Reynolds analogy factor, eq. (B21)
T	temperature
u	component of velocity in x-direction
\bar{u}	u/u_e
U	transformed velocity component, eq. (B10)
v	component of velocity in y-direction
V	transformed velocity, eq. (B10)
V_m	leakage velocity

SYMBOLS (continued)

VEL	free stream velocity
w	component of velocity in z-direction
W	roughness element width
x	coordinate along local body surface
x,y,z	Cartesian coordinates; curvilinear coordinates (see Appendix B)
x_{eq}	heat-transfer equivalent distance
X	surface distance; transformed x coordinate, eq. (B10)
y	coordinate normal to body surface
y_{max}	value of y at leading edge of delta wing
Y	transformed y coordinate, eq. (B10)
z	coordinate normal to x and y
Z	compressibility factor, $P/\rho RT$; transformed z coordinate, eq. (B10)
α	angle of attack; Prandtl number exponent, eq. (B42)
β	velocity or pressure-gradient parameter, eqs. (3.6) and (B41)
γ	ratio of specific heats, c_p/c_v
Γ	vorticity-interaction parameter, eq. (B31); pressure gradient function, eqs. (B35) and (B36)
δ	flow deflection angle; cone semi-vertex angle; flap deflection angle; boundary-layer thickness
δ_T	effective wedge angle
δ^*	boundary-layer displacement thickness
Δ	total streamline-divergence parameter; compressibility parameter, eq. (7.1); finite increment operator
Δ_s	shock standoff distance
ΔS	fictitious length (see Appendix C)
ϵ	emissivity; density ratio across normal shock; surface ray angle measured from sharp delta-wing apex; streamline angle

SYMBOLS (continued)

ξ	extrapolation factor
η	similarity parameter, eq. (B11a)
θ	boundary layer momentum thickness, eq. (B7); angular coordinate
θ^*	leading edge streamline angle
θ_s	shock wave angle
Θ	transformed momentum thickness, eq. (B11a)
λ	canopy angle
Λ	sweep angle
μ	absolute viscosity
ν	Prandtl-Meyer function
ρ	density
$\rho_r \mu_r$	reference density-viscosity product (see Appendix B)
σ	partial Prandtl number for translation, rotation, and vibration only (see Appendix B); Stefan-Boltzmann constant
σ_r	Prandtl number evaluated at enthalpy and pressure corresponding to $\rho_r \mu_r$
Σ	boundary layer parameter, eqs. (B37) and (B38)
τ	shear stress; model skin thickness
$\bar{\tau}$	transformed shear stress, eq. (B11)
ϕ	$\theta^{(m+1)/m}$, eq. (B13b)
ψ	yaw angle
ω	coefficient defined in eqs. (2.12) and (2.13)

Subscripts:

ATM	}	evaluated at sea level condition
atm,SL		
aw,AW		adiabatic wall
BC		blunt cone
BD		blunt delta wing

SYMBOLS (continued)

C	cone
c	crossflow
CYL	cylinder
DW	delta wing
e	at boundary-layer edge
eff, EFF	effective
eq	equivalent
EXP	on expansion surface
F	flap
f	on sphere in laminar flow; on 60° swept cylinder in turbulent flow
FLT	at flight conditions
FP	flat plate
G	control surface gap
HL	at hinge line
i	initial; perfect gas; index variable
I-I	at line of intersection
L	laminar, leakage
LE	leading edge
\bar{m}	at X_m ; mean
max, MAX	maximum
min, MIN	minimum
N	normal
n	in normal direction
NL	no leakage
o	tangential; at stagnation conditions; at laminar reference conditions

SYMBOLS (continued)

r	evaluated at enthalpy and pressure corresponding to conditions used to evaluate $\rho_r \mu_r$
REF	reference
ref	pertaining to reference streamline
RAD	radiated
RT	at turbulent reference conditions
s	streamwise
S	at stagnation point
S'	evaluated at stagnation enthalpy and local pressure
SC	sharp cone
SD	sharp delta wing
SH	at shoulder
SL	on stagnation line
sm, SM	smooth
SP	stagnation point
T	turbulent; total
vort	vorticity effects included
w, W	at wall
WT	at wind tunnel conditions
x	at distance x
θ	based on angular location
Λ	based on geometric sweep angle
0	at Mach number zero
2	behind shock wave
∞	free stream or undisturbed
+	just ahead of sudden compression

SYMBOLS (concluded)

- just behind sudden compression

Superscripts:

* at reference temperature defined by eq. (3.10a)

I. INTRODUCTION

Successful design of a maneuverable re-entry vehicle requires detailed knowledge of aerodynamic heating rates over all surfaces of the vehicle. Performance of the vehicle is limited by the temperature capability of structural materials which tend to establish lower limits on the radii of the nose and leading edges and upper limits on the angle of attack at which the vehicle can operate. Unfortunately, design features that are favorable from the performance standpoint often have undesirable heating characteristics. Aerodynamic heating studies, therefore, are required to determine the proper design compromises.

Aerodynamic heating rates are influenced by all of the properties of the flow field in addition to the influence of body surface conditions. In the external flow, the density, velocity, pressure (both level and gradient), streamline pattern, and chemical composition must all be determined before heating calculations can be made. At the body surface the important conditions are the wall temperature, smoothness, and permeability. The boundary layer state, which may be laminar, transitional or turbulent, may also depend upon all flow properties.

The ability to accurately predict inflight aerodynamic heating rates varies with geometry and flight condition. Analytic methods are available for simple shapes in laminar flow; for all other conditions a combination of theoretical and empirical methods must be used. A completely empirical approach is precluded by the limitations of testing facilities, none of which can provide completely satisfactory simulation of the re-entry environment.

This report presents a compilation of design methods for computing aerodynamic heating rates that were developed during the X-20 (Dyna-Soar) Program. The results of more than five years of aerodynamic heat transfer testing and analysis are reflected in these methods. Methods developed specifically for that program are presented in this report in a generalized manner intended to supply information useful for preliminary design of advanced re-entry vehicles. The methods presented were, however, developed to treat the critical design conditions for the X-20, and are not intended to be applied at velocities greater than 26,000 fps nor to surfaces cooled by mass injection. The flow is assumed to behave as a continuum, and to be in chemical equilibrium. With the exception of vorticity interaction in the region of the forward stagnation point, low Reynolds number effects are neglected. No mass addition effects are considered, but some information is given regarding leakage which may occur at panel joints or control surface hingelines. The effects of surface roughness were found to be large and are discussed. Flow field interference effects on X-20 fin leading edge and canopy heating were found to be severe and an approximate method that defines the upper limit is presented. While these assumptions, limits and approximations were appropriate and sufficient for X-20 design studies, they should be reviewed when considering other lifting re-entry vehicles.

The material that is presented in this report is divided into seven major sections. The following section (Section II) describes the methods for several basic two-dimensional and axisymmetric shapes. Combinations of these shapes are discussed in Section III, and surface condition effects on the level of basic smooth body heating rates are described in Section IV.

Suggestions pertaining to the application of the design methods to complex configurations are given in Section V. This section also contains two examples from the X-20 program that illustrate the requirement for detailed analysis tailored to the re-entry vehicle being studied.

Section VI contains charts that give numerical results for several basic geometric shapes, including the hemisphere, flat plate, swept cylinder, unyawed blunt and sharp cones, and blunt and sharp delta wings at angle of attack. Heating rates for all configurations are given by distribution curves which are to be multiplied by reference heating rates to give absolute values. This form of presentation is concise and simplifies the estimation of heating rates for geometries not specifically presented. Hemisphere stagnation point heating rates are used as laminar reference values for all shapes. Turbulent heating for sharp tip configurations are referenced to the turbulent heating rate for a 60-degree swept infinite cylinder. For blunt bodies it was found that better accuracy was obtained by referencing turbulent heating rates to laminar hemisphere stagnation point values.

Section VII discusses interpretation and use of data from wind tunnels and other ground-based test facilities. In some cases, wind tunnel data can be applied in flight by merely adjusting the level by use of the reference heating rates described in the previous paragraph. However, for complex geometries, further correction is often necessary because of real-gas and interacting flow field effects.

Appendices are included that:

1. Give simplified expressions that approximate some of the more complex heating formulas.
2. Show derivations of basic methods.
3. Provide a method for calculating laminar boundary layer displacement thickness.
4. Give examples of the application of the charts presented in Sections VI and VII.

II. METHODS FOR BASIC SHAPES

This section describes the methods that were used to predict heating rates for several basic shapes, including flat plate, sharp cone, sphere, infinite cylinder, and sharp delta wing. These geometries were selected because relatively detailed and accurate calculations can be made for each without relying heavily on experimental results, and because such calculations provide information that can be used in analyzing more practical configurations.

For the purposes of this section, heating calculations can usually be broken into two separate steps: 1) the calculation of the flow properties neglecting the effect of viscosity, and 2) calculation of the boundary layer using the inviscid flow results. The inviscid flow calculations must provide a complete description of conditions at the boundary layer outer edge, including the local pressure, velocity (both magnitude and direction), temperature, and chemical composition. No practical completely general method has been developed for calculating the inviscid flow for all of the basic shapes. It was therefore necessary to use several different methods to calculate the flow about the basic shapes, including normal and oblique shock theory, modified Newtonian theory, Prandtl-Meyer expansion theory, the method of characteristics, and the blunt body inverse method. In addition to these well known methods, an empirical pressure distribution was used for infinite cylinders, and a crossflow method was used for predicting delta wing streamlines. Except where otherwise noted real gas effects are included in the flow field calculations, using gas properties of reference 1. Chemical and thermal equilibrium has been assumed in all calculations.

In contrast to the variety of inviscid flow methods used, all of the boundary layer calculations for the basic shapes were made with a single method, the " $\rho_r \mu_r$ Method". This method, which was developed by R. A. Hanks in the course of the X-20 program, is applicable in either laminar or turbulent flow. The laminar flow version of the $\rho_r \mu_r$ method is based on exact similar solutions of the boundary layer equations. The exact solutions were used to construct curves of boundary layer parameters, including form factors, (δ^*/θ) , crossflow momentum thickness, Reynolds analogy factors, and effective values of the density-viscosity product. The boundary layer parameter curves are then applied in nonsimilar flows through the use of a momentum integral equation.

The turbulent flow form of the $\rho_r \mu_r$ method uses the same momentum integral equation, retaining terms that are often neglected, such as those related to the effect of pressure gradients on the turbulent boundary layer profiles. Although such profile changes are small, and cannot be exactly calculated, their effect may be to increase heating rates, and it is therefore unconservative to neglect them entirely. The evaluation of the turbulent boundary layer parameters was guided by the known laminar trends, and in some cases are taken directly from the aforementioned laminar curves. The actual values used were selected also on the basis of agreement with experimental results.

Since the $\rho_r \mu_r$ method embodies essentially all laminar similarity solutions as well as turbulent flow parameters, it is necessarily somewhat complex, and a complete description is given in Appendix B. For the following discussion of methods, it is sufficient to note that in addition to boundary layer edge pressure, density, etc., which are required by all boundary layer methods, the $\rho_r \mu_r$ method also requires knowledge of three flow divergence parameters, r , f , and Δ . The parameter r accounts for the effects of streamline divergence on heating due to body geometry, which is most simply exemplified by the increase in heating due to streamline divergence on an unyawed cone. The parameter f accounts for the effect of streamline divergence due to transverse pressure gradients, and so is affected by body shape only indirectly. The total streamline divergence is denoted by Δ , which is related to r and f by

$$\Delta = \text{constant} \cdot r \cdot f \quad (2.1)$$

where the constant is arbitrary. Referring to Appendix B it will be seen that r , f , and Δ can always be normalized so that absolute values are never required. Hence it is sufficient to determine the ratios r/r_1 , f/f_1 , and Δ/Δ_1 where the subscript 1 denotes some initial or reference value. In actual practice equation (2.1) is usually applied in the form:

$$\frac{\Delta}{\Delta_1} = \frac{r \cdot f}{r_1 \cdot f_1} \quad (2.1a)$$

The distinction between r , f , and Δ is necessary, since the ultimate effect of streamline divergence on heat transfer depends on the presence or absence of transverse pressure gradients.

The $\rho_r \mu_r$ method has been used for all heat transfer calculations presented in this report except where otherwise noted. In particular, laminar boundary layer calculations involving interactions with the external flow were calculated with the Boeing Nonsimilar Boundary Layer Program, which is described in Appendix C. This program numerically integrates the boundary layer equations in partial differential form, and so is free of similarity restrictions. This program was required for only three calculations: the expansion side of the deflected flap, the vorticity interactions at the stagnation point, and surface wave calculations described in Section IV. The particular methods used for each of the basic shapes are described below.

A. Flat Plate

Exact calculations of inviscid flow properties for the sharp-leading-edge flat plate were made using oblique-shock theory and real-gas properties. A description of real-gas oblique-shock theory is given in reference 2. The actual values used in this report were recalculated using gas properties

presented in reference 1. The three-dimensional flow parameters r , f , and Δ are constants for this case, so that r/r_1 , f/f_1 and Δ/Δ_1 are all unity.

B. Hemisphere

The pressure in the subsonic portion of the hemisphere flow field was calculated by Modified Newtonian theory. In the Newtonian theory, the free stream is regarded as an aggregation of particles that impinges on the surface of the body, and in so doing changes its momentum normal to the surface into pressure acting on the body. This idealization of the flow field leads to the following expression for the pressure coefficient

$$C_p = 2 \sin^2 \delta \quad (2.2)$$

where δ is the true flow deflection angle. The same equation is obtained if one considers the impact of a supersonic fluid stream on an inclined surface, provided the shock wave is close to the surface. This latter condition is approximately satisfied in hypersonic flight, for which the density ratio ρ_2/ρ_∞ is large, since the shock standoff distance, Δ_s , is related to the density ratio by

$$\Delta_s = [0] R (\rho_2/\rho_\infty) \quad (2.3)$$

$R = \text{Hemisphere radius}$

as shown in many references. See, for example, references 3 and 4.

Equation (2.2) is exact only if $\Delta_s = 0$. For a finite density ratio and hence finite Δ_s , improved accuracy can be obtained with Modified Newtonian theory

$$C_p = K \sin^2 \delta \quad (2.4)$$

where K is a constant which is expected to be near 2.0. Its actual value for the hemisphere can be calculated by normal shock theory and isentropic compression to zero velocity. The result is very well approximated by

$$K = 2 - \rho_\infty/\rho_2 \quad (2.5)$$

Equation (2.5), which is obtained by assuming that the density is constant on the stagnating streamline downstream of the bow shock, is derived in Chapter 7 of Truitt (reference 5), among other places.

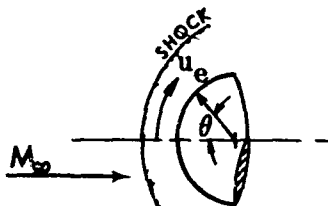
The pressure distribution in the supersonic flow portion of the hemisphere was calculated by Prandtl-Meyer expansion theory matched to values given by equation (2.4) in the vicinity of the sonic point. The actual matching point

was selected to make both the pressure distribution and its derivative continuous. The resulting pressure distribution is shown in figure 2-1.

Velocity distribution can be calculated from the pressure distribution either by isentropic expansion or by integrating the Bernoulli equation

$$\frac{du_e}{d\theta} = - \frac{1}{\rho_e u_e} \frac{dP}{d\theta} \quad (2.6)$$

where u_e and θ are defined in the sketch below



ρ_e is the boundary layer edge density and P is the local pressure. Because the pressure gradient and velocity are zero at the stagnation point the Bernoulli equation must be applied in the special form

$$\frac{\partial u}{\partial x} = \frac{\beta u_\infty}{R} = \sqrt{-\frac{1}{\rho_e} \frac{\partial^2 P}{\partial x^2}} \quad (2.7)$$

where x is measured from the stagnation point and β is the velocity gradient parameter. Using the Newtonian theory pressure distribution and the equation of state, equation (2.7) leads to

$$\beta = \frac{1}{u_\infty} \sqrt{2 \mathcal{R} (T Z)_0} \quad (2.8)$$

where \mathcal{R} is the gas constant, T is the real-gas temperature, and Z is the compressibility factor.

As pointed out in reference 3 the use of modified Newtonian theory for the hemisphere pressure distribution has been substantiated empirically. The Prandtl-Meyer matching method has also been verified in this manner. However, it is not necessary to only rely upon experimental data for their substantiation. Comparisons have been made with inverse-method calculations (reference 6) and with the integral method calculations of Belotserkovskii (reference 7) that show that the method described here is accurate to within a few percent.

Streamline divergence on a hemisphere is due entirely to body geometry, and is given by

$$\Delta/\Delta_{SH} = \cos \delta \quad (2.9)$$

where Δ is the local streamline divergence parameter, Δ_{Sn} is the streamline divergence parameter at $\delta = 0^\circ$, and δ is the true flow deflection angle.

The basic hemisphere heating rates for both laminar and turbulent flow were calculated by the $\rho_r \mu_r$ method. At very low Reynolds numbers and high Mach numbers a correction to the laminar heating rates must be made to account for the effects of vorticity in the external flow, which may become important when the boundary layer is not thin in comparison to the shock layer thickness. Analysis and experimental data have been published (e.g. references 8 - 10) that show increases in heating rate resulting from vorticity interaction.

There is considerable disagreement between the various published theoretical predictions of the vorticity effect. Many of the predictions contain rather drastic simplifications and/or patching of separate approximate solutions for various regions within the shock layer. The Nonsimilar Boundary Layer Program was used to obtain more complete numerical solutions to the boundary layer equations which included the effects of external vorticity.

A comparison between results obtained using the Nonsimilar Boundary Layer Program and those shown in reference 8 is shown in figure 2-2 in terms of the stagnation point vorticity interaction parameter Γ , defined in reference 8 as:

$$\Gamma = \frac{\omega}{\sqrt{Re_0} \sqrt{2\Delta}} \quad (2.10)$$

where Re_0 is a stagnation region Reynolds number defined as

$$Re_0 = \frac{\rho_0 \sqrt{i_0} R}{\mu_0} \quad (2.11)$$

and ρ_0 , μ_0 , and i_0 are respectively the density, viscosity, and enthalpy evaluated at stagnation conditions. The quantities A and ω are coefficients in an equation for the inviscid tangential velocity:

$$u(x, y) = A \sqrt{\frac{i_0 x}{R}} [1 + \omega(y/R) + \dots] \quad (2.12)$$

$$\text{with } A = \frac{R}{\sqrt{i_0}} \frac{\partial u}{\partial x}$$

$$\text{and } \omega = \left[\frac{\partial \bar{u}}{\partial (y/R)} \right]_e$$

where x and y are curvilinear coordinates tangential and normal to the body, R is the body radius, and \bar{u} is the velocity normalized with respect to the boundary layer edge velocity.

Physically the vorticity parameter Γ represents the ratio of the shear stress in the shock layer to the shear stress at the body surface, i.e.,

$$\Gamma \sim \frac{u_e \left(\frac{\partial u}{\partial y} \right)_e}{\rho_e u_0^2 C_{f\omega} \Gamma = 0}$$

where u_0 is the potential-flow velocity, the subscript e denotes evaluation at the edge of the boundary layer, and $C_{f\omega} \Gamma = 0$ is the vorticity-free skin-friction coefficient. Numerical values of Γ can be obtained if u_e and ω are known. The potential-flow velocity u_0 can be obtained from the Newtonian pressure distribution and the Bernoulli equation as defined by equation (2.8).* The vorticity parameter Γ was computed using the following equation for ω which is given in reference 8:

$$\omega = \left[\frac{\partial \bar{u}}{\partial (y/R)} \right]_e = \frac{\left[\left(\frac{\gamma}{\gamma-1} \right)^{1/2} - 1 \right] (1-\epsilon)}{\epsilon \left(1 - \sqrt{\frac{8}{3}} \epsilon + 3\epsilon \right)} = \frac{1-\epsilon}{\left(\frac{\Delta_s}{R} - \epsilon^2 \right)} \left[\left(\frac{\gamma}{\gamma-1} \right)^{1/2} - 1 \right] \quad (2.13)$$

where ϵ is the density ratio across the normal shock and Δ_s/R is the dimensionless shock standoff distance.

As shown in figure 2-2, Nonsimilar Boundary Layer Program calculations are somewhat lower than those by Ferri, et al. in reference 8. At the time calculations were made by The Boeing Company, there was considerable controversy over the magnitude of the vorticity interaction effects, with the majority of the published methods also falling well below the reference 8 prediction.** The controversy could not be resolved by experimental results, due to the extreme difficulty in obtaining reliable data. The Nonsimilar Boundary Layer Program calculations involved fewer simplifying assumptions than those in reference 8, which could be the source of the difference shown. However, an extensive review of the assumptions involved in the reference 8 analysis was made, using the detailed information provided by the Nonsimilar Boundary Layer Program, without discovering any serious discrepancy.

Van Dyke (reference 11) and others have pointed out that vorticity interaction is only one of several second-order boundary layer effects, and suggest the proper consideration of these additional effects would reduce Ferri's (reference 8) predictions somewhat. This observation does not explain the lower values given by the Nonsimilar Boundary Layer Program, however, since only the classical boundary layer equations were used. The effect shown is entirely due to the boundary condition applied at the outer edge of the boundary layer, namely,

$$\left(\frac{\partial u}{\partial y} \right)_{y \rightarrow \infty} \longrightarrow \text{Constant}$$

*Note that β of equation (2.8) is very nearly equal to the parameter A of equation (2.10) for hypersonic flight, since $1_e \approx u_\infty^2/2$.

**These results are not conveniently displayed in the format of figure 2-2.

rather than

$$\left(\frac{\partial u}{\partial y}\right)_{y \rightarrow \infty} \rightarrow 0,$$

the condition applied in no-vorticity calculations.

The present authors feel that the Nonsimilar Boundary Layer Program result, being a more complete calculation, is less likely to contain any hidden errors, and recommend the use of the Nonsimilar Boundary Layer Program curve of figure 2-2. However, once Γ is calculated the reader can easily obtain numerical results for both methods.

C. Infinite Cylinder

The pressure in the immediate vicinity of the stagnation line of an unswept infinite cylinder was obtained by modified Newtonian theory, equation (2.4). An empirical curve, shown in figure 2-1, was used for the pressure distribution away from the stagnation line. It was observed that there was very little difference between the data from many different tests; hence a single curve was used for all calculations.

The velocity distribution on the unswept cylinder can be calculated using the same methods as were used for the hemisphere. The actual velocity distribution differs slightly from that on a hemisphere, however, since the two pressure distributions are not identical.

The inviscid flow over a swept cylinder can be calculated by resolving the flow into components normal and parallel to the cylinder axis. The flow normal to the cylinder can then be calculated by the same method used for unswept cylinders. The pressure, temperature, density, and circumferential velocity depend only on that component of the free stream flow normal to the cylinder. The parallel flow component is constant. The streamline pattern can be calculated from the velocity components by integrating the relationship

$$y(x) = \int \frac{dy}{dx} dx = \int \frac{v}{u} dx \quad (2.14)$$

where y is the distance of the streamline from the stagnation line (measured along the cylinder surface) and x is the distance measured along the cylinder stagnation line. The body geometry streamline divergence parameter r , due to geometry is equal to the cylinder radius. Since r is constant for all x , $r/r_1 = 1$ and there is no direct effect of r on the heating rate. There is of course a pressure gradient effect on heating through the parameter f . The total streamline divergence is then equal to that due to pressure gradients alone, so that equation (2.1a) reduces to

$$\frac{\Delta}{\Delta_i} = \frac{f}{f_i} \quad (2.15)$$

where Δ and f can both be obtained from the integral of equation (2.14).

D. Sharp Unyawed Cone

Shock-wave angles and flow-field properties for a sharp unyawed cone were obtained using the method-of-characteristics, reference 12. Since transverse-pressure gradients are zero for an unyawed cone the value of $f/f_1 = 1$. Hence, the expression for the streamline divergence parameter reduces to

$$\frac{r}{r_1} = \frac{\Delta}{\Delta_1} = \frac{x}{x_1} \quad (2.16)$$

E. Sharp Delta Wing

The delta wing presents a more difficult analytic problem than any of the other basic shapes discussed so far, and rigorous theoretical methods are available for only a few restricted cases. For sharp leading edge delta wings with the flow supersonic everywhere it can be shown that all flow properties must be constant along any straight line through the apex. At low angles of attack oblique shock theory can be applied to the region upstream of a Mach line on the lower surface through the apex. Oblique-shock theory is applied in the plane normal to the leading edge at an effective free-stream Mach number, M_n , and wedge angle which can be obtained from purely geometric calculations as follows

$$\delta_T = \tan^{-1} \left(\frac{\tan \alpha}{\cos \Lambda} \right) \quad (2.17)$$

and

$$M_n = M_\infty \sqrt{1 - \sin^2 \Lambda \cos^2 \alpha} \quad (2.17a)$$

where α is the angle of attack and Λ is the geometric sweep angle.

It is seen that for very highly swept delta wings, the effective wedge angle will be much larger than the angle of attack, so that shock detachment will occur at relatively low angles of attack. For very high angles of attack the flow at the leading edge is outward, (i.e., with the leading edge behaving as a trailing edge), and the flow field can be calculated by an extension of the blunt body method of integral relations (reference 7) as shown in reference 13. Such calculations have thus far been made only for ideal gases with constant specific heat ratios.

For most of the conditions of practical interest, however, neither of the above methods could be applied and approximate methods become necessary. It was still desirable that the methods be as valid as possible in the actual flight environment. Accordingly, emphasis was placed on developing approximate analytic methods for predicting delta wing pressure, velocity, and streamline patterns.

1. Sharp Delta Wing Pressure Method

The approximate analytic method devised for predicting delta wing pressures was a modified Newtonian method, in which the constant K of equation (2.4) was allowed to vary so as to obtain the best agreement with known exact solutions. This was done by first plotting wedge, cone, and blunt-body stagnation point theoretical results as shown in figure 2-3.

It is seen in figure 2-3 that for wedges and cones the coefficient K at first decreases with normal Mach number, and then increases rapidly to a limit fixed by shock detachment. The effect is seen to be less pronounced, and to occur at larger deflection angles for cones than for wedges. For both wedges and cones, K is always greater than 2.0. Blunt-body stagnation point values for K are seen to behave in an opposite manner, being always less than 2.0, but increasing slowly with normal Mach number. (This behavior is consistent with the previous expression for K given for blunt bodies, equation (2.5)). For delta wings, it is to be expected that the wedge curves will apply in the leading edge region at low angles of attack, as previously discussed. At very large angles of attack, approaching 90 degrees, it is to be expected that the blunt body curve would be more applicable. In the intermediate range K would be expected to vary more or less smoothly between the wedge and blunt body curves.

Shock detachment is caused by the inability of attached flows to satisfy mass conservation requirements. For the sharp-delta wing, the phenomenon of shock detachment would not be expected to occur in the same sense as for a wedge or unyawed cone since mass is conserved by flow outward over the leading edge. The existence of outflow at the delta wing leading edge at very high angles of attack also implies that at some intermediate angle the flow must be just parallel to the leading edge, and so would correspond closely to cone flow. The curve of K for the delta wing would therefore be expected to begin at the wedge curve, fair through the cone curve, and terminate on the blunt-body curve.

Such a family of curves was drawn, and is presented in figure 2-4 which was used for all delta wing calculations in this report. The upper branch is based on a formula given by hypersonic small-disturbance theory,

$$C_P = \frac{\gamma + 1}{2} + \sqrt{\left(\frac{\gamma + 1}{2}\right)^2 + \left(\frac{2}{M_\infty \sin \delta}\right)^2} \quad (2.18)$$

which was used primarily because it gives a curve of the desired shape. The curve shown was calculated for $\gamma = 1.1$, a value which was selected because it leads to the desired curve, and not because $\gamma = 1.1$ is considered realistic. (A value of 1.1 is clearly unrealistic in comparison to wind tunnel data.) The lower branch is faired so that K approaches a value of 2.0 as the Mach number approaches infinity, varying as follows

$$K = 2 - \frac{2.2}{M_\infty} \quad (2.19)$$

for Mach numbers greater than 10.

Although the fairings of figure 2-4 are somewhat arbitrary, the development just given is preferable to a purely empirical approach, since all the required exact solutions can be made for flight conditions.

The major objective of figure 2-4 is to predict delta wing pressures; however, it is also expected to provide reasonable predictions for almost any shape, since it agrees well with both slender and blunt-body results.*

2. Velocity and Streamline Pattern

The inviscid velocity component parallel to the delta wing centerline was calculated by the following expression:

$$\frac{u_e}{u_\infty} = 1 - \alpha^2/5600 \quad (2.20)$$

where α is the wing angle of attack in degrees. Equation (2.20) was obtained in the same manner as the pressure curve described previously by an examination of cone and wedge theory. For two-dimensional nonreacting flow, the inviscid velocity depends only on the shock wave angle and density ratio, and is given by:**

$$\frac{u_2}{u_\infty} = \sqrt{\cos^2 \theta_s + \frac{\rho_\infty}{\rho_2} \sin^2 \theta_s} \quad (2.21)$$

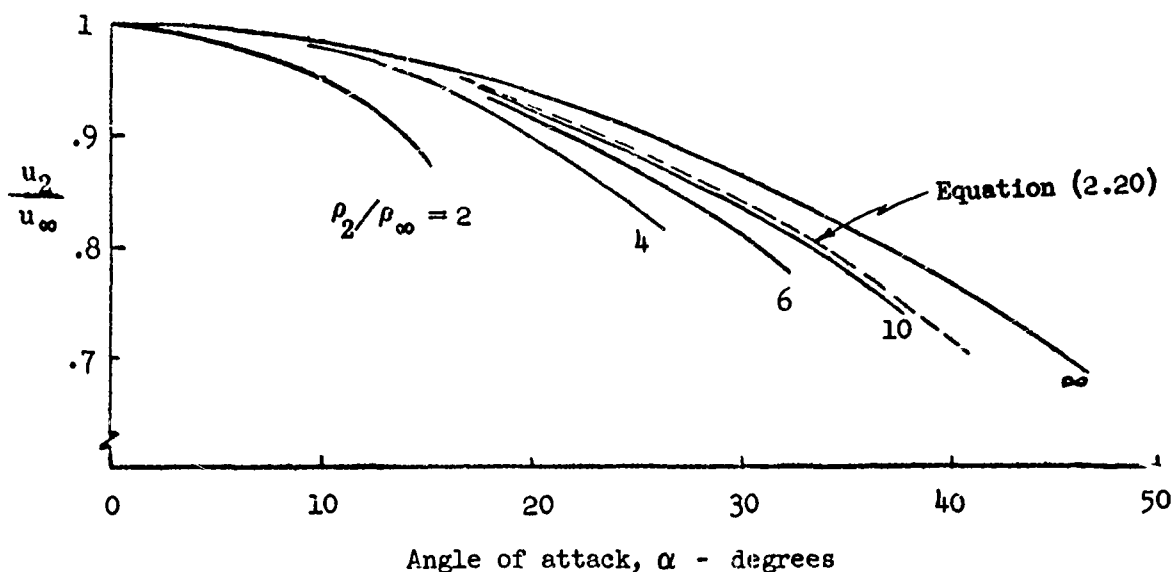
where θ_s is the shock wave angle in degrees. The wing angle of attack is found by the following equation

$$\theta_s - \alpha = \tan^{-1} \left(\frac{\rho_\infty}{\rho_2} \tan \theta_s \right) \quad (2.22)$$

*Figure 2-4 can not be expected to apply to interfering flow fields, however, since one of the effects of interference can be to increase the local dynamic pressure.

**Equations (2.21) and (2.22) are obtained by resolving the flow into components normal and parallel to the shock. In crossing the shock the normal velocity component is reduced in proportion to the reciprocal of the density ratio. The parallel component is unaffected.

Some typical results for various values of the density ratio are shown below:



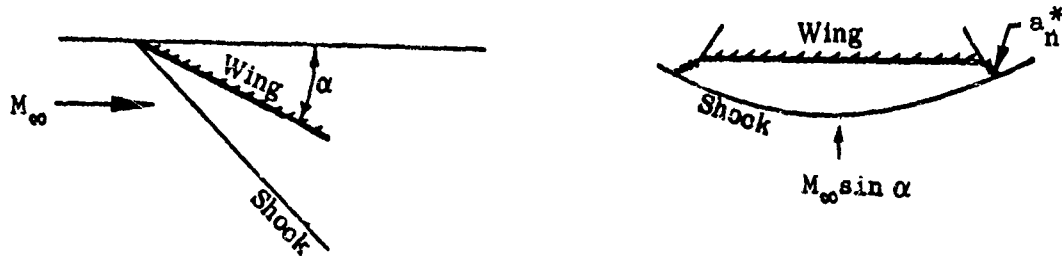
Equation (2.20) is also shown for comparison.

As shown in the above sketch the velocity increases with density ratio at constant α to an upper limit which equation (2.21) shows to be a cosine function. For cones no rigorous, simple formula is available, since the velocity varies as the flow compresses within the shock layer. However, the velocity changes during this compression are slight, and equation (2.21) is nearly correct for cones as well as wedges. The value of $\theta_s - \alpha$ for cone flow is only about one-half the wedge value given by equation (2.22)*, however, so that the cone curves would be expected to lie about midway between the wedge and cosine curves.

It is seen that the velocity ratios are fixed within fairly narrow limits for density ratios greater than about 5. In hypersonic flight density ratios less than 5 can occur only at small wedge deflection angles (less than about 11 degrees at Mach 20) where the effect of density ratio is seen to be small. Equation (2.20) was therefore chosen as a close approximation for hypersonic flight for angles of attack up to 40 degrees or more.

* This result is obtained by applying a mass balance to the cone shock layer, assuming that surface velocities are equal to the wedge values.

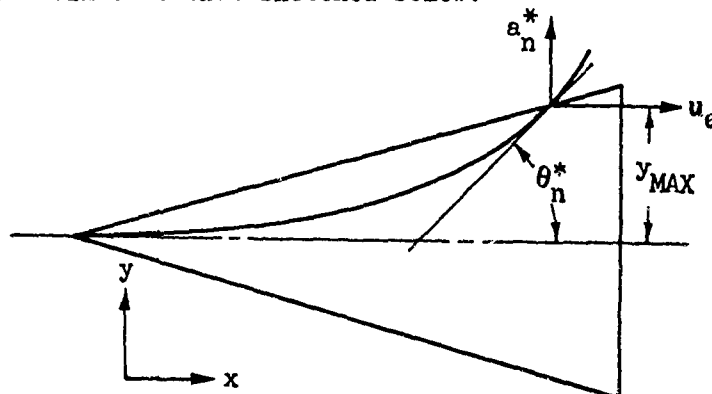
The spanwise velocity component for sharp delta wings is obtained by a crossflow theory. As shown in the following sketch, in the crossflow plane the delta wing appears as a sharp-cornered blunt body for which the velocity at the corner must be equal to the local sonic velocity, a_n^* (the detailed derivation of reference 13 leads to the same conclusion).



The local sonic velocity a_n^* is calculated from the Mach number component appearing in the crossflow plane, and is given by

$$a_n^* = a_\infty \left[\frac{2 + (\gamma - 1) (M_\infty \sin \alpha)^2}{2 + (\gamma - 1)} \right]^{1/2} \quad (2.23)$$

At the centerline the spanwise velocity component is zero but increases with distance away from the centerline. Superimposing the spanwise component onto the axial flow component (equation (2.20)) leads to a streamline qualitatively similar to that sketched below.



The leading edge streamline angle, θ_n^* , with respect to the centerline is calculated from the following equation:

$$\tan \theta_n^* = \frac{a_n^*}{u_e} \quad (2.24)$$

using equation (2.20) for the axial velocity component u_e .

It will be noted that this method predicts outflow even at zero angle of attack. This inconsistency was avoided by modifying equation (2.23) to:

$$a_n^* = a_\infty M_\infty \sin \alpha \sqrt{\frac{\gamma - 1}{\gamma + 1}} \quad (2.25)$$

This modification is equivalent to neglecting the effect of the free stream static temperature on a_n^* , and was used throughout this report.

The distribution of the spanwise velocity component cannot be calculated except for the few previously noted special cases for which complete flow field calculations can be made. However, the published calculations for the flat-faced blunt body show that the assumption of a linear distribution is conservative, i.e., overpredicts the spanwise component. Delta wing experimental data were similar, but more nearly linear than the blunt body theory would indicate. A linear distribution has therefore been assumed in the preparation of this report.

$$v_\theta = a_n^* \left(y / y_{MAX} \right) \quad (2.26)$$

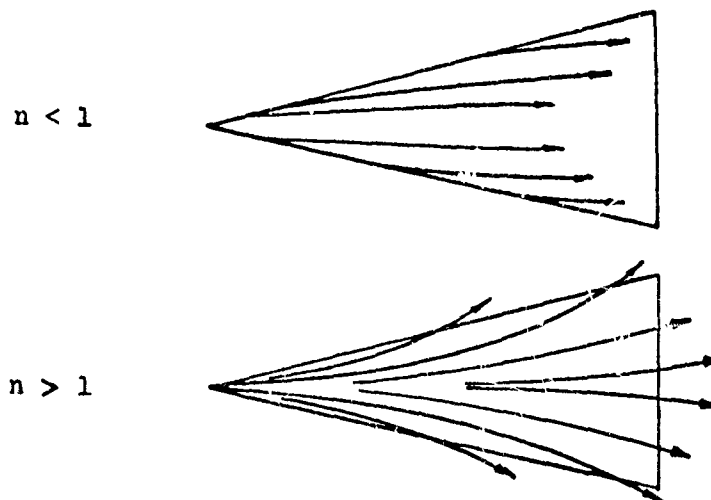
where y is the spanwise distance measured normal to and from the centerline and y_{MAX} is the leading-edge value of y . The streamline equation was obtained using equations (2.20) and (2.26) and is given by:

$$y = C x^n \quad (2.27)$$

where C is a constant for any particular streamline, and

$$n = \frac{a_n^*}{u_\theta \tan(90^\circ - \Lambda)} = \tan \theta^* \tan \Lambda \quad (2.28)$$

The streamline patterns corresponding to equation (2.27) fall into two classes, depending on the value of n . For n less than 1.0 the streamlines originate at the leading edge; for n greater than 1.0 all streamlines originate at the apex. The two types of patterns are sketched below:



Since the streamline divergence parameter Δ is proportional to y , it can be expressed using equation (2.27) as

$$\Delta/\Delta_i = (x/x_i)^n \cdot \frac{\sqrt{1 + (dy/dx)^2}}{(\sqrt{1 + (dy/dx)^2})_i} \quad (2.29)$$

Since the delta wing is taken to be flat, it is assumed that there is no three-dimensional effect due to body shape, so that $f/f_i = \Delta/\Delta_i$.

3. Heat Transfer Calculations

The sharp delta wing heating curves of Section VI were calculated using equation (2.29) together with pressure given by figure 2-4, the velocity components given by equation (2.20) and (2.26), and the $\rho_r \mu_r$ method of Appendix B. For the centerline of the sharp delta wing the three-dimensional flow effect can be calculated in closed form for laminar flow and is given by

$$h/h_{FP} = \sqrt{1 + 2n} \quad (2.30)$$

where n is defined by equation (2.28), and h_{FP} is the heat transfer coefficient for a flat plate evaluated using delta wing surface properties.

A similar expression can be derived for turbulent flow using the Blasius skin-friction law:

$$C_f = \frac{.0592}{Re^{.2}} \quad (2.31)$$

The resulting expression for the three-dimensional effect is:

$$h/h_{FP} = \sqrt[5]{1 + \frac{5}{4}n} \quad (2.32)$$

Equation (2.32) is an approximation in that equation (2.31) is considered to be less accurate than the Karman-Schoenherr or Prandtl-Schlichting equations. However, as shown in Appendix B, the error introduced into equation (2.32) is small.

These simple forms (equations (2.30) and (2.32)) are possible only because the streamwise distance to a point on the centerline is unaffected by streamline divergence. For locations not on the centerline the streamwise distance depends on the streamline pattern, as may be seen from the previous sketches. The combined distance and flow divergence effects must be evaluated by integrating the boundary-layer equations along the streamline, as was done in the preparation of the design curves, figures 6-32 and 6-33.

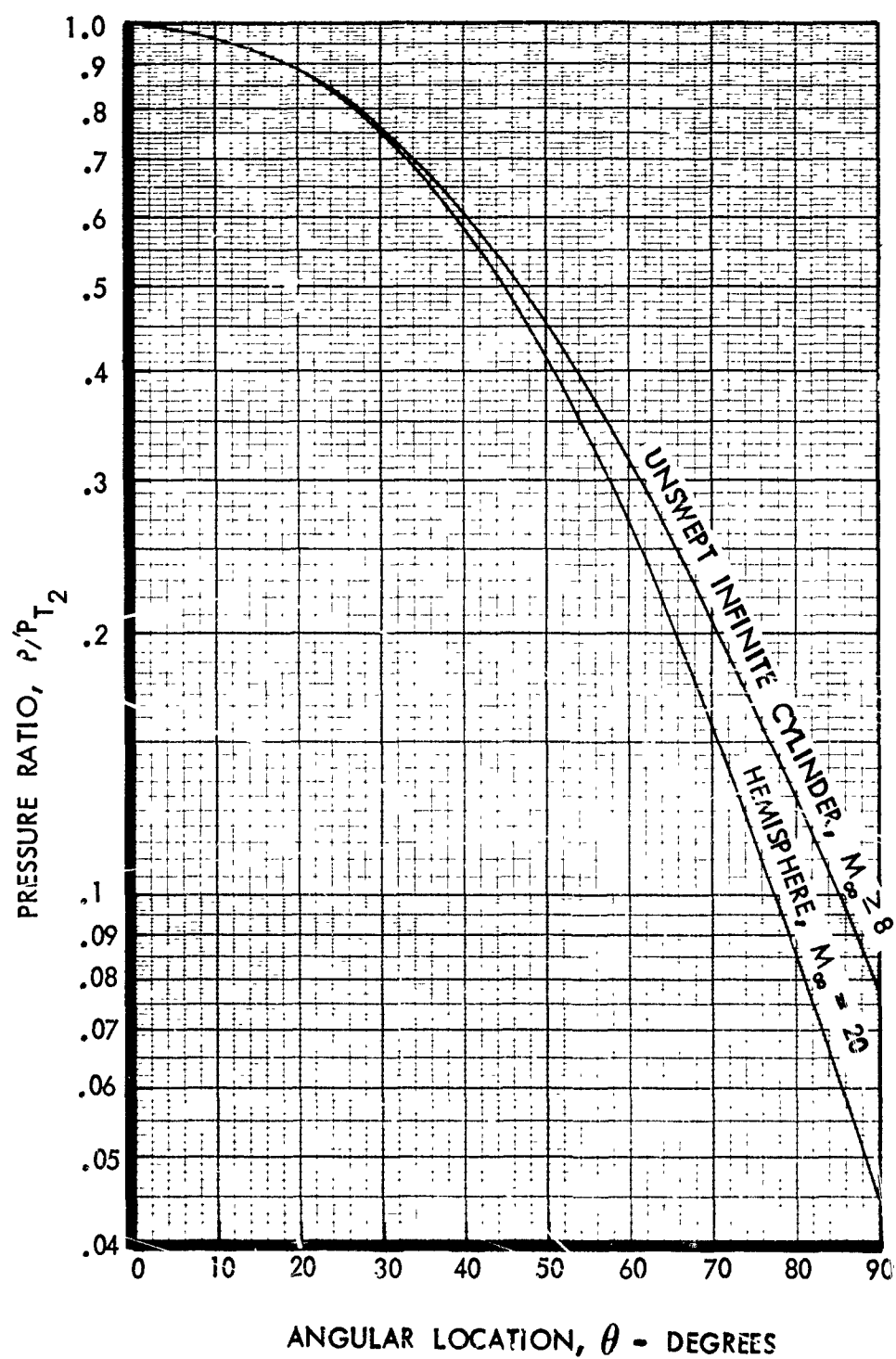


Figure 2-1: PRESSURE DISTRIBUTION ON HEMISPHERE AND UNSWEPT INFINITE CYLINDER

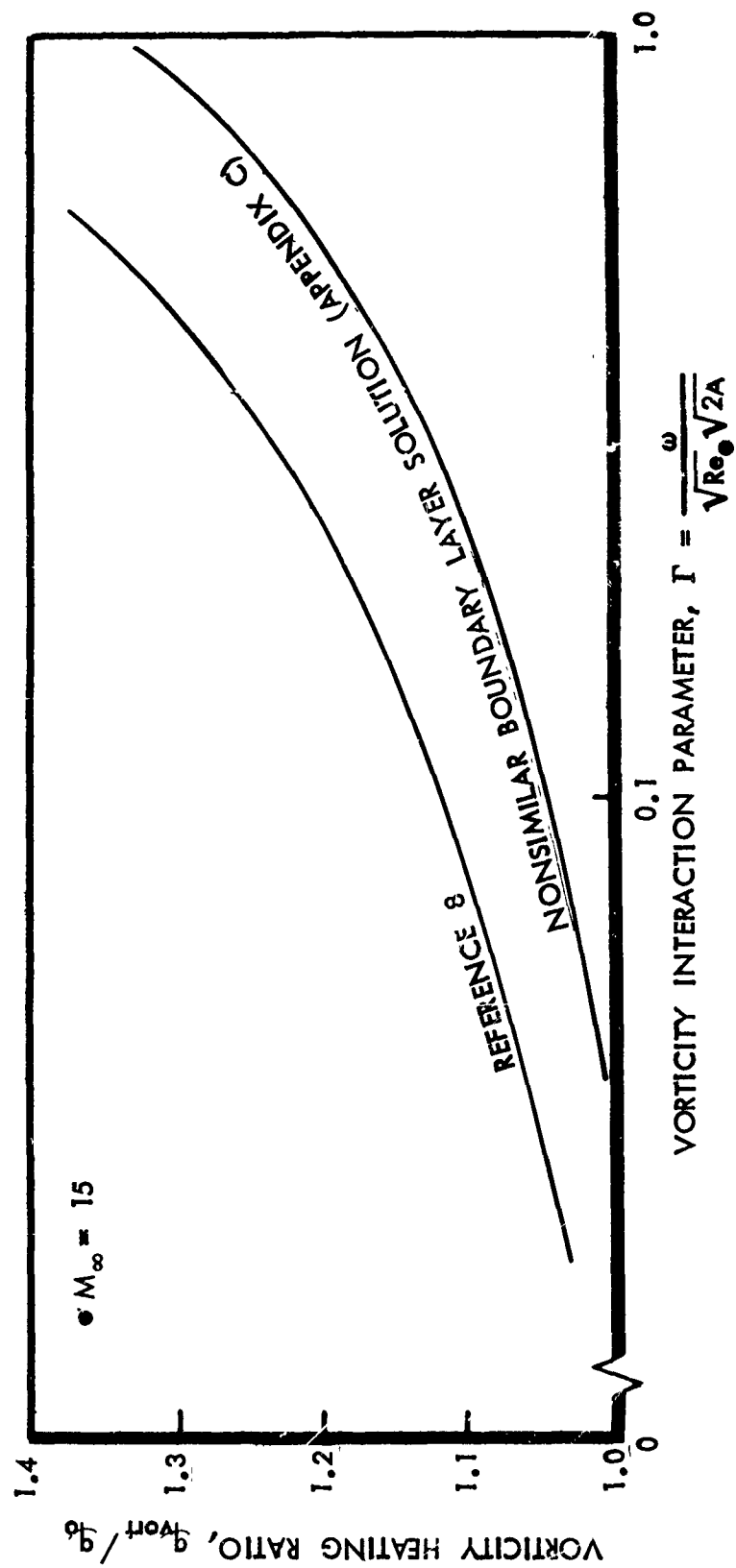


Figure 2-2: STAGNATION POINT VORTICITY INTERACTION EFFECT

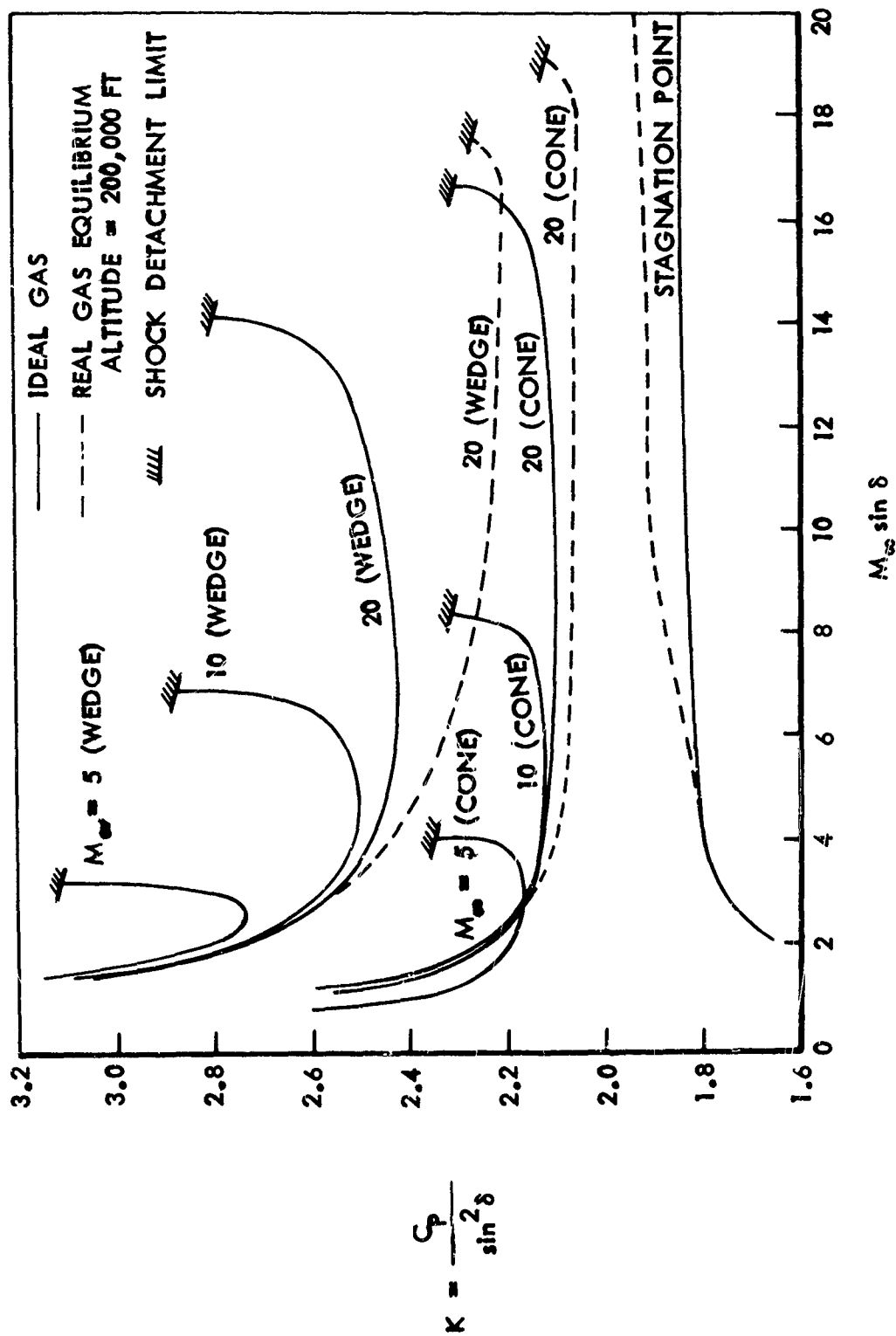


Figure 2-3: WEDGE, CONE, AND STAGNATION POINT PROPORTIONALITY CONSTANT

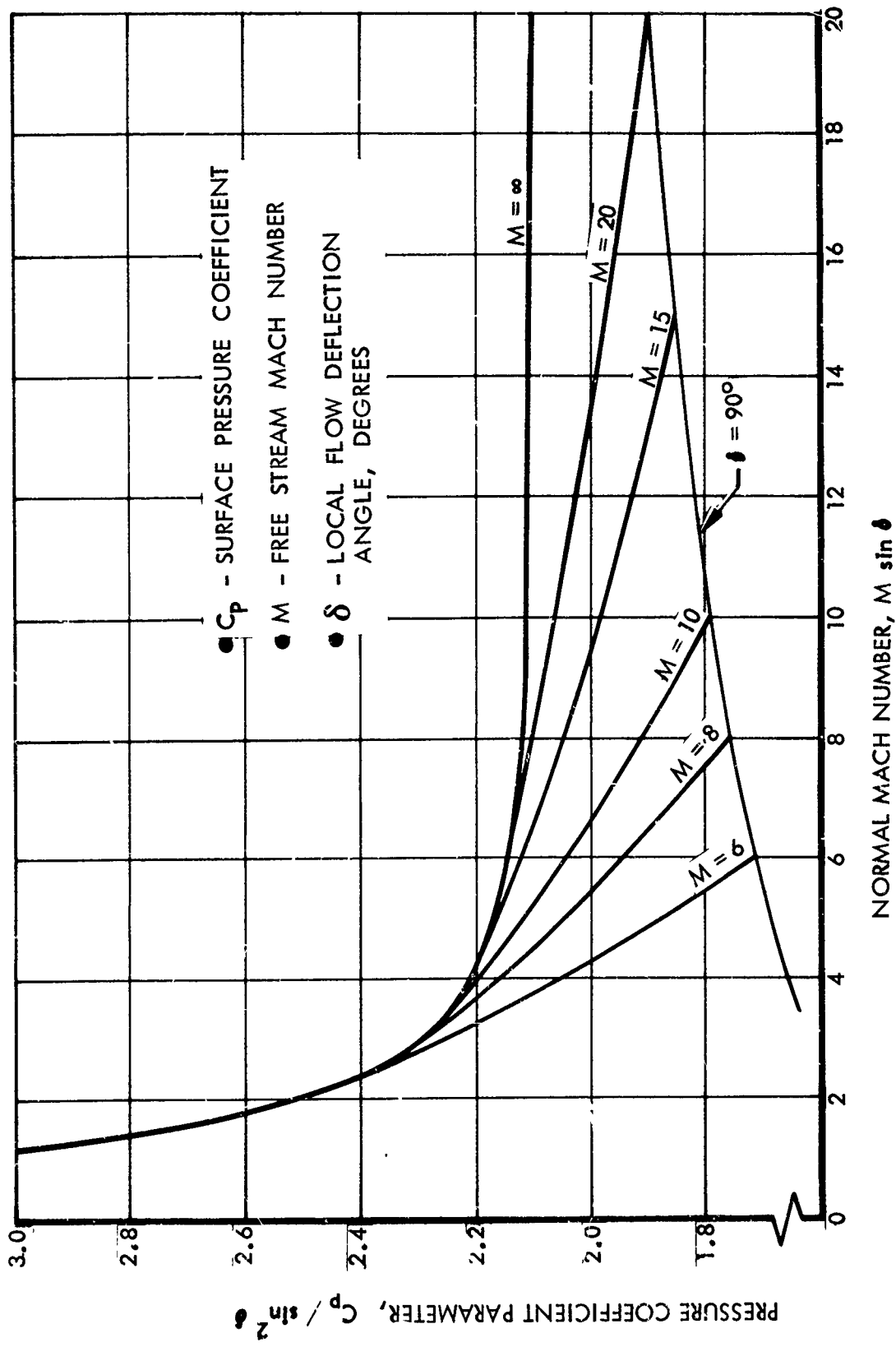


Figure 2-4: BOEING MODIFIED NEWTONIAN HYPERSONIC PRESSURE COEFFICIENTS

III. COMBINATIONS OF BASIC SHAPES

This section describes methods that were used to calculate the aerothermodynamic characteristics of three combinations of basic shapes, the hemisphere-cone, the blunt delta wing, and a flat plate with a trailing edge flap. The blunt delta wing is made up of a flat delta wing with cylindrical leading edges and a spherical cap. The spherical cap is of the same diameter, and tangent to, the cylindrical leading edges.

The examination of combined simple shapes illustrates the adjustments that must be made in applying basic methods to complex configurations. It will be seen that in some cases, as for example the slender blunted cone, the combined body has considerably different aerothermodynamic characteristics than would be indicated by an examination of each element separately.

A. Hemisphere-Cone

1. Local Flow Properties

Nose bluntness affects cone heating rates by altering the surface pressure distribution and by increasing the entropy of the flow at the boundary layer edge. Typical inviscid-flow blunt-cone pressure distributions are presented in figure 3-1. The values shown were calculated for a hemisphere-cone using the blunt body inverse method (reference 11) for the subsonic region and the method of characteristics for the remainder of the flow field. All calculations are for real-gas air in chemical equilibrium. Also shown are the sharp-cone pressure coefficients calculated using figure 2-4.

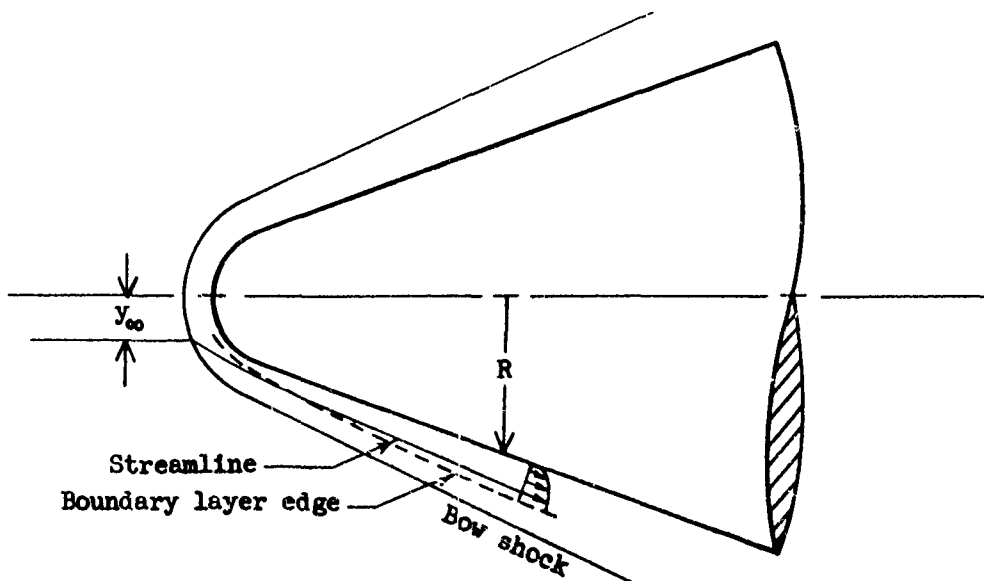
As shown in figure 3-1, the presence of the hemisphere affects the pressure distribution for considerable distances downstream, particularly at small cone angles. Theoretically, one expects that as the cone angle approaches zero the effect of nose bluntness will persist infinitely far downstream. At large cone angles, however, the effect is seen to be confined to a distance of a few nose diameters.

Figure 3-1 is applicable only for cones with hemispherical noses, but qualitatively similar behavior is to be expected for other nose shapes. The blast wave analogy proposed by Lin in reference 14 and applied by many others (see for example, the discussion in reference 5) indicates that for given free-stream conditions the distribution on a blunt cylinder aligned with the flow depends only on the nose drag coefficient and not on the details of the nose shape. This conclusion cannot be applied in the vicinity of the nose itself, however, since the analogy breaks down as the shock angle approaches 90 degrees. Since the bluntness effect extends such a short distance at large cone angles, the effect of nose shape on the details of the pressure distribution cannot be ignored in that case. However, it is seen that the overall effect is relatively small when the cone angle is large.

In contrast to the effect on pressure, the effect of bluntness on the entropy of the inviscid flow theoretically extends infinitely far downstream for all cone angles. The streamline at the cone surface reaches the stagnation point after having passed through the normal shock that exists ahead of all blunt bodies in supersonic flow. In crossing the shock much of the kinetic energy of the stream is transformed into internal energy, with the result that the surface streamlines on the blunt cone have a lower velocity and density than at corresponding locations on sharp cones, even though the static pressure may be nearly identical. These reductions in velocity and density lead to a reduction in the heating rate as well. The changes in local flow properties and the reduction in heating are commonly referred to as "bow shock effects."

In calculating the bow shock effect the local flow properties are obtained by isentropic expansion from the stagnation point to the local static pressure. Since this calculation requires knowledge of only the total enthalpy, stagnation point pressure, and the local pressure, it is seen that the magnitude of the bow shock effect does not depend on the nose shape or size, provided only that the nose is sufficiently blunt that there exists a detached shock wave.

The existence of a boundary layer on the cone modifies and reduces the bluntness effect.* A streamline actually entering the boundary layer may originate some distance away from the normal portion of the bow shock, as shown in the simplified sketch below:



* One of the implications of this statement is that the inviscid flow on a blunt cone does not approach as a limit the conditions of a local flow on a sharp cone as the bluntness is decreased to zero, although the discrepancy is confined to a vanishingly thin layer near the cone surface.

Since the mass flow within the boundary layer is given by

$$\rho_e u_e (\delta - \delta^*)$$

it is seen that y_∞ can be obtained without actually tracing the streamline. Applying a mass balance leads to:

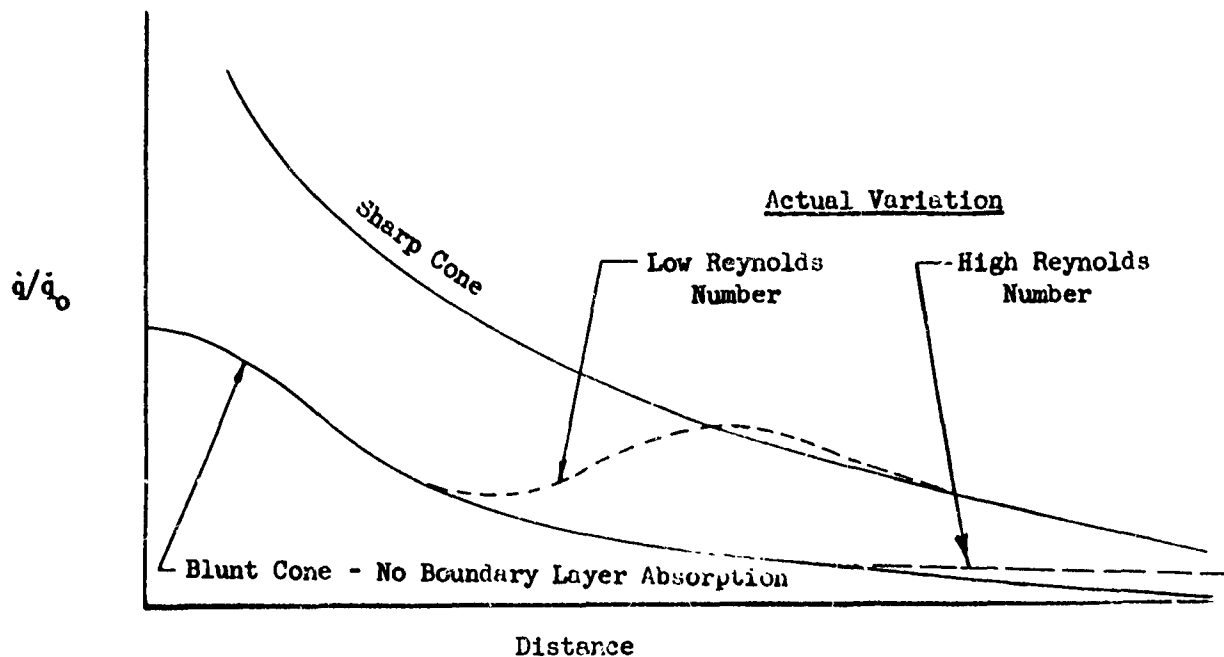
$$\rho_\infty u_\infty \pi y_\infty^2 = \pi [(R + \delta - \delta^*)^2 - R^2] \rho_e u_e \doteq 2 \pi R (\delta - \delta^*) \rho_e u_e \quad (3.1)$$

or

$$y_\infty \doteq \sqrt{2 R (\delta - \delta^*) \frac{\rho_e u_e}{\rho_\infty u_\infty}} \quad (3.2)$$

If the variation of the shock wave angle with y_∞ is known, the entropy just downstream of the shock can be obtained by oblique shock theory. Since the static pressure at the edge of the boundary layer is equal to that at the cone surface, all other flow properties can be obtained by isentropic expansion.

The actual variation in heating rate along the surface of a blunt cone, including the effect of the boundary layer mass absorption, follows the blunt cone theory initially and then increases toward the sharp cone theory. Some slight overshoot probably occurs as sketched below:



The boundary layer thicknesses δ and δ^* will be affected by the streamwise variation in edge flow properties, resulting in a difficult boundary layer calculation. Very little has appeared in the literature regarding the effect of such variation. Since the boundary layer is usually assumed to be "thin," it is to be expected that the variation in local flow properties will be gradual, and adequately accounted for by using the (varying) local properties in constant property boundary layer formulas. Such a procedure would account for the effect of changing levels, but not for the effects of flow property gradients. For any but the simplest shapes such a calculation is very difficult and the results far from certain.

In the present report, blunt cone heating rates are based on local flow properties calculated by isentropic expansion from behind a normal shock, and so represent the lower curve of the above sketch. Further information, including some experimental results for flat plate turbulent boundary layers, may be obtained from reference 15.

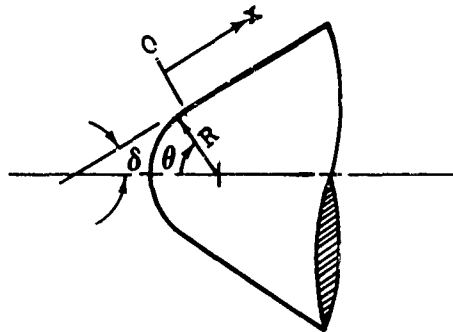
2. Streamline Divergence on a Blunt Cone

Bluntness does not change the fact that transverse pressure gradients are zero if the cone is unyawed. As a result, the value of $f/f_1 \equiv 1$ and by choosing the tangency point, or shoulder, of the hemisphere-cone combination as the location of the reference value equation (2.15) can be written:

$$\frac{\Delta}{\Delta_{SH}} = \frac{\sin \theta}{\sin \theta_{SH}} \quad x < 0 \quad (3.3a)$$

$$\frac{\Delta}{\Delta_{SH}} = 1 + \frac{x}{R} \tan \delta \quad x \geq 0 \quad (3.3b)$$

where δ , θ , and R are defined as shown:



B. Blunt Delta Wing

1. Local Flow Properties and Centerline Heating

On the blunt delta wing, as on the blunt cone, the hemispherical nose affects downstream pressures and through the entropy effect, all other flow properties. The evaluation of these effects is much more complex than for

the cone, varying with spanwise position as well as chordwise distance. In addition, bluntness affects the delta wing streamline patterns, and the wing in turn has an effect on the nose and leading edge flow. The calculation of the flow field surrounding a blunt delta wing is more difficult than for the sharp delta wing, since the previously mentioned condition of constant flow properties along ray lines can no longer be applied. In principle, the flow can be calculated by the method of characteristics for three dimensions, using blunt body theory to obtain the initial values. In practice, however, it was found that a large amount of computer time was required, and the computer results obtained showed indications of numerical instabilities.

This lack of exact theoretical methods for the blunt delta wing has required the use of approximate methods and empirical results. The bases for the approximate methods are the basic shape methods of the previous section. The empirical information is based on the results of an extensive series of delta wing tests that were conducted during the X-20 program covering a Mach number range from 6 to 22. The data from those tests has been reanalyzed under NASA contract and will be published as references 16, 17 and 18.

The effect of bluntness on centerline pressure distribution is shown in figure 3-2. These curves were obtained by matching empirical results from the X-20 tests to the hemisphere method previously given. Also shown in figure 3-2 are sharp delta wing values obtained from figure 2-4. The blunt delta wing pressures are appreciably higher than those for the sharp delta wing for at least three nose diameters, and for angles of attack greater than approximately 30° , do not fall into sharp delta wing values. The solid curves of figure 3-2 have been used for the heat-transfer curves of Section VI.

Near the centerline the effect of nose bluntness on entropy can be calculated as described in the discussion of hemisphere-cones. However, calculations show that the effect of the highly swept leading edges on downstream entropy levels is much less than for the hemisphere, and has a much smaller effect on the heating rates. The proper evaluation of bluntness effects on a delta wing therefore requires a detailed knowledge of the beginning of each streamline that wets the surface, a knowledge that at present does not exist. Since the bluntness effect reduces downstream heating rates, it is conservative to neglect the bluntness effect except at the centerline, where the surface streamlines are known to have come through the hemisphere shock. The curves presented in this report for blunt delta wing centerline heating are based on normal shock entropy, as were the blunt cone curves. The method used for calculating spanwise distributions for blunt delta wings will be described following a discussion of streamline methods.

Bluntness effects on the streamline patterns were experimentally investigated by an oil-flow technique. A mixture of oil and lampblack was spread uniformly over the surface of test models before they were subjected to the hypersonic tunnel flow. Patterns were seen to develop that indicate the direction of the surface shear force. These patterns were then either photographed or transferred to vellum paper by direct contact. An analysis was made of the relation of these observed shear force patterns to the streamline directions in the external flow which led to the conclusion that the surface shear patterns always indicate more outflow than actually exists in the external flow. The argument leading to this conclusion may be summarized as follows:

1. A fluid particle in the external flow describes a curved path such that the centrifugal force acting on the particle is in equilibrium with the transverse pressure gradient.
2. The same transverse pressure gradient acts on particles within the boundary layer, since the pressure is constant through the boundary layer.
3. Since the velocity of the particles within the boundary layer is less than those in the external flow, the centrifugal force will not match the external pressure gradient unless the path of the particles within the boundary layer has a smaller radius of curvature than that in the external flow.

Hence, the surface oil flow patterns (which reflect the surface shear forces) will indicate more curvature than exists in the external flow. This conclusion would apply in either laminar or turbulent flow. The oil flow results showed that bluntness greatly reduced the amount of outflow, with the streamlines being nearly parallel to the centerline in proximity to the nose even at high angles of attack. Since outflow increases the heating rates by thinning the boundary layer, it is conservative to use sharp delta wing streamline methods on the blunt delta wing. This has been done in preparing this report. Since the heating rate calculation involves streamwise integration of the boundary-layer momentum equation beginning at the stagnation point (as described in Appendix B) delta wing streamline assumptions do not affect the prediction at the hemisphere shoulder. It is also to be expected that far downstream where the wing span is much greater than the leading edge radius the sharp delta wing streamline method should be applied. Thus, the use of sharp delta wing streamline methods in the region just downstream of the nose results in a prediction that begins at sharp delta wing values. Far downstream the prediction approaches the same asymptotic values as would be calculated using a method based on estimated blunt wing streamlines, but the prediction would be conservative in the intermediate region.

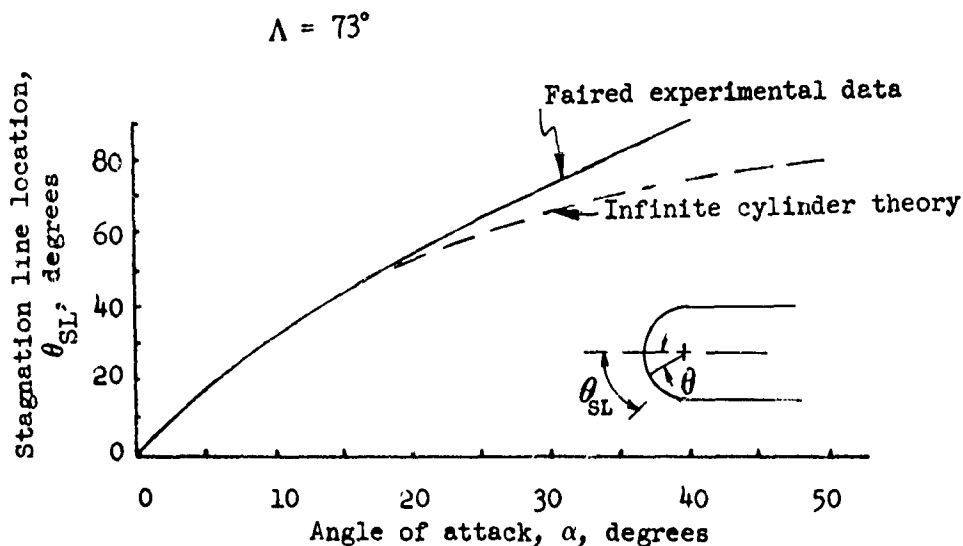
Using the sharp delta wing streamline prediction method, the streamline parameter Δ in the vicinity of the centerline is given by

$$\frac{\Delta}{\Delta_1} = \left(1 + \frac{x}{R} \cos \Lambda\right)^n \quad (3.4)$$

where R is the nose radius, x is measured along the centerline, beginning at the tangency point between the nose cap and the plane surface and is given by equation (2.28).

2. Blunt Delta Wing, Leading Edge and Nose Heating

The blunt delta wing discussion has thus far considered nose and leading edge effects on the delta-wing flow field. As long as the wing flow field is entirely supersonic, both normal and tangential to the leading edge in the plane of the wing, it is to be expected that the flow over the nose and leading edges will be unaffected by the lower surface. The sonic points on both the leading edge and nose are about 45 degrees from the stagnation point, so that the lower surface should begin to affect the leading-edge flow field when the effective angle of attack given by equation (2.16) reaches 45 degrees. Such an effect on the location of the leading-edge stagnation line was observed in the delta-wing tests as illustrated in the sketch below:



The upper curve is a faired curve representing oil flow data measured on an unyawed 73-degree swept blunt delta wing at Mach numbers of 6.0 and 8.08. The lower curve can be computed using equation (2.17), since θ_{SL} is numerically equal to δ_T . The curves show that at angles of attack less than about 15° the lower surface has no influence on leading-edge stagnation-line location. However, as the angle of attack is increased, lower-surface pressure influences the location of the stagnation line indicating that it will reach the shoulder at a lower angle of attack than predicted by the infinite cylinder theory.

During the X-20 program an approximate method was developed that predicts the angle of attack for which the stagnation line is located at the shoulder. The method is based on the observation that when the stagnation line is on the leading edge shoulder the velocity in the plane normal to the leading edge axis is zero at the leading edge shoulder. In this crossflow plane the velocity at the shoulder was estimated by superimposing the previously described delta wing outflow velocity onto the leading edge velocity distribution. Closest agreement with data obtained during the X-20 experimental program occurred when the circumferential velocity distribution on the cylinder was calculated by

$$v(\theta) = \left(\frac{\partial v}{\partial \theta} \right)_{SL} \theta \quad (3.5)$$

where θ is measured from the zero angle of attack stagnation line. The velocity gradient $(\partial v / \partial \theta)_{SL}$ was calculated from

$$\left(\frac{\partial v}{\partial \theta} \right)_{SL} = \beta \left(\frac{u_{\infty, n}}{R} \right) \frac{dx}{d\theta} \quad (3.6)$$

where $\beta = \frac{\partial v}{\partial x} \frac{R}{u_{\infty, n}}$ (which depends only on the normal Mach number) was calculated for the true normal Mach number as given by equation (2.17a). The normal velocity $u_{\infty, n}$ is calculated as if for zero angle of attack by

$$u_{\infty, n} = u_{\infty} \cos \Lambda \quad (3.7)$$

Setting the shoulder value of v equal to the delta-wing outflow velocity as given by equation (2.25) leads to:

$$\tan \alpha = \frac{\pi}{2} \left(\frac{\gamma + 1}{\gamma - 1} \right)^{1/2} \beta \cos \Lambda \quad (3.8)$$

Equation (3.8) gives that angle of attack at which the leading-edge stagnation line is located at the leading-edge shoulder. Stagnation line locations in this report have been approximated by using equation (2.17) for angles of attack up to 15° and then fairing a line to the value obtained using equation (3.8).

A second lower-surface effect on the leading edge that was first noted early in the X-20 program was a reduction in stagnation-line heating rates. Such a reduction is to be expected when it is noted that at very high angles of attack equation (2.24) predicts that the flow near the leading edge is outward. In that case the leading edge behaves as a trailing edge, and a reduction in heating is to be expected. No reliable methods were developed for predicting the magnitude of the reduction, however, since there was little effect on the X-20 operating envelope.

At about 45° angle of attack the delta-wing lower surface influences the subsonic portion of the nose hemisphere flow field, and a similar reduction in stagnation point heating is to be expected. However, the effect is expected to be small, and no evaluation of this effect was made during the X-20 program.

3. Blunt Delta Wing Spanwise Heating Rate Distribution - Leading Edge

Stagnation line locations shown in the charts of Section VI were determined using the method just described. Stagnation line heating rates were determined by infinite cylinder theory for flight conditions at angles of attack less than 20 degrees. The aforementioned reduction in heating rates at the stagnation line in comparison to infinite cylinder theory is based on a 73-degree swept delta wing data and is purely empirical.

The blunt delta wing heating curves shown in Section VI from the stagnation line around the leading edge and onto the surface were defined by the data of reference 16. The actual magnitude of the heating rate ratios presented, however, were shifted in order to fair smoothly into theoretical centerline values.

C. Deflected Flap

1. Compression

Flaps deflected into a stream compress the oncoming flow and often cause the boundary layer ahead of the flap to separate. Effects of flow separation and reattachment on aerodynamic heating can be large and extremely complex. In most cases predictions must be based on approximate methods. The difficulty of providing useful heat-transfer information for actual design is made somewhat easier by the fact that maximum values are usually of most interest.

Aerodynamic heat transfer through a laminar separated region was analyzed in reference 19 by an extension of boundary layer theory. That calculation indicated that the average heat transfer in a separated region is reduced by about 50 percent as compared to attached flow heat transfer for the same local flow properties at the boundary layer outer edge. This result has been verified in tests of reference 20 for cavity-type flow and tests of reference 21 for forward-facing step flow. The results of reference 20 indicate that the same reduction might apply to turbulent flow. Test data of reference 21, however, indicate an increase in heating for separated transitional and turbulent flow over forward-facing steps.

The prediction of reattachment heating is difficult because of large pressure gradients that exist throughout the reattachment region. Calculations (reference 22) have been made for laminar boundary layer flow at reattachment; however, a prior knowledge of the reattachment pressure gradient is required. Since regions of separated flow and locations of reattachment are practically impossible to predict for complex configurations, an approximate method was developed during the X-20 program to predict the upper bound of reattachment heating. This method relates the maximum inviscid pressure rise on the deflected flap to a maximum heating rise at the point of reattachment as follows:

$$\frac{h_{MAX}}{h_{UNDISTURBED}} = \frac{P_{MAX}}{P_{UNDISTURBED}} \quad (3.9)$$

This approximate result is based on the relation:

$$h = \frac{\text{constant}}{\text{Pr}^{2/3}} \frac{\rho^* \mu^{*1/n} u_e}{\left[\int_0^x \rho^* \mu^* u_e dx \right]^{1/(n+1)}} \quad (3.10)$$

which is a slight generalization of an equation shown in reference 23. In equation (3.10) n is 1 for laminar flow and 4 for turbulent flow. The superscript * denotes evaluation at the reference temperature, defined by Eckert (reference 24) as:

$$T^* = 0.5 T_W + 0.28 T_e + 0.22 T_{AW}$$

To evaluate the effect of a sudden compression on h as predicted by equation (3.10), we write

$$\frac{h_+}{h_-} = \frac{(\rho^* \mu^{*1/n} u_e)_+}{(\rho^* \mu^{*1/n} u_e)_-} \frac{\left[\int_0^{x_+} \rho^* \mu^* u_e dx \right]^{1/n+1}}{\left[\int_0^{x_-} \rho^* \mu^* u_e dx \right]^{1/n+1}} \quad (3.11)$$

where the subscripts + and - indicate evaluation just downstream and just upstream, respectively, of a sudden compression. If the compression occurs over a very short distance, the two integrals must be nearly equal, since

$$\int_0^{x_+} \rho^* \mu^* u_e dx = \int_0^{x_-} \rho^* \mu^* u_e dx + (x_+ - x_-) \rho^* \mu^* u_e + \dots$$

and for small values of $(x_+ - x_-)$

$$\int_0^{x_+} \rho^* \mu^* u_e dx \doteq \int_0^{x_-} \rho^* \mu^* u_e dx \quad (3.12)$$

so that

$$\frac{h_+}{h_-} \doteq \frac{(\rho^* \mu^{*1/n} u_e)_+}{(\rho^* \mu^{*1/n} u_e)_-} \doteq \frac{[P_e (\mu^{*1/n}/T^*) u_e]_+}{[P_e (\mu^{*1/n}/T^*) u_e]_-} \quad (3.13)$$

In this expression the change in pressure are dominant. The changes in the reference temperature T^* are small because T_W and T_{AW} do not change appreciably. In addition, the changes in T^* and μ^* tend to compensate. Referring to equation (2.20), it is found that the ratio of local to free-stream velocity is approximately unity for angles of 30 degrees or less.

Neglecting the "small" differences in velocity and temperature leads to:

$$\frac{[P_e (\mu^{*1/n}/T^*) u_e]_+}{[P_e (\mu^{*1/n}/T^*) u_e]_-} \doteq \frac{(P)_+}{(P)_-} \quad (3.14)$$

Immediately downstream of the compression the heating rate begins to decrease as the integral in equation (3.10) increases. Hence,

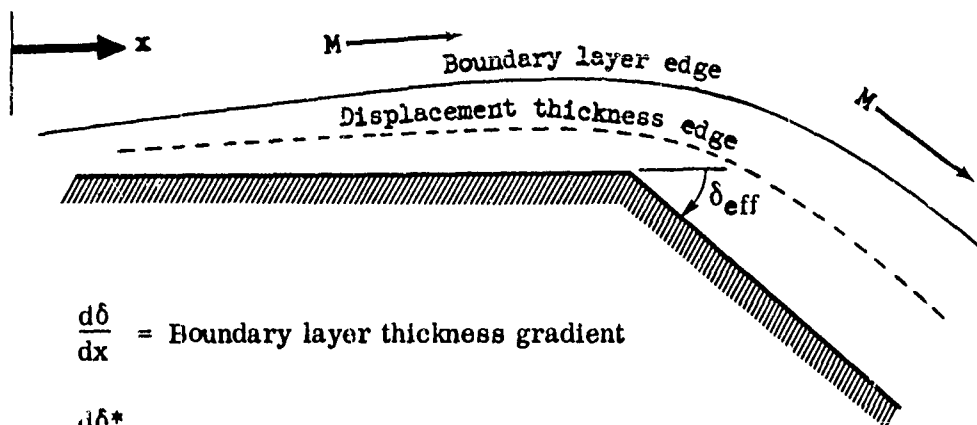
$$\frac{h_+}{h_-} \doteq \frac{h_{MAX}}{h_{UNDISTURBED}} \doteq \frac{P_+}{P_-} = \frac{P_{MAX}}{P_{UNDISTURBED}} \quad (3.9)$$

Since no assumption has been made regarding boundary layer state, equation (3.9) applies in either laminar or turbulent flow. Equation (3.9) would also be applicable in the presence of flow separation provided that no appreciable increase in the integral of equation (3.11) occurred over the separated region. Since the integral represents the effect of wall shear on the boundary layer growth, it seems reasonable that the small shear forces in the separated region are also negligible. In the case of separation the subscripts + and - would refer to conditions just ahead of separation and just downstream of reattachment. Although the development of equation (3.9) involves several gross approximations, it has been used in the absence of any better method. Comparisons of equation (3.9) with experimental data are presented in reference 17.

2. Expansion

Aerodynamic heating rates to flaps in an expanding flow field, while less than those obtained on compression surfaces, may be required for design. The presence of the boundary layer complicates the flow field by creating a displacement effect that changes the effective expansion angle. To determine this angle in a two-dimensional flow field, boundary-layer growth must be taken into account.

Consider the flow illustrated in the following sketch:



$$\frac{d\delta}{dx} = \text{Boundary layer thickness gradient}$$

$$\frac{d\delta^*}{dx} = \text{Displacement thickness gradient}$$

In the absence of a boundary layer the effective turning angle is δ_{eff} and the flow properties at the wall can be determined using the Prandtl-Meyer equation

$$\delta_{\text{eff}}]_1^2 = -\Delta\nu]_1^2 = \frac{1}{2} \int_{H_1}^{H_2} \left(\frac{2H}{a^2} - 1 \right)^{1/2} \frac{dH}{H} \quad (3.15)$$

where H is the difference between total and local enthalpy and a is the speed of sound evaluated using local enthalpy.

In the presence of a boundary layer, equation (3.15) is valid only for that portion of the turning angle external to the boundary layer. The effective expansion angle is given approximately by

$$\Delta\nu = \delta_{\text{eff}} - \frac{d\delta^*}{dx} \quad (3.16)$$

Equation (3.16) was used in preparing this report. However, this equation is exact only if the boundary-layer edge flow properties are constant. No exact simple formulation exists if the external flow properties are not constant due to the existence of nonisentropic flow within the boundary layer.

Consistent values of $\Delta\nu$ and δ^* were obtained by an iterative process in which equation (3.15) was first used to calculate pressure neglecting the boundary layer effect on turning angle. The displacement thickness was then determined using the Nonsimilar Boundary Layer Program. Equation (3.16) was then used to determine a new turning angle. This process was repeated until further changes were negligible.

Since the iteration process is lengthy the following approximate closed form relationship was fitted to the numerical results:

$$\frac{h_{\text{EXP}}}{h_{\text{HL}}} = \left(\frac{P}{P_{\text{HL}}} \right)^m \left(\frac{x_{\text{HL}}}{x} \right)^n \quad (3.17)$$

where h_{EXP} is the heat transfer coefficient on the expanded surface, h_{HL} is the heat transfer coefficient at the hinge line, P/P_{HL} is the inviscid pressure ratio across the expansion wave, x_{HL}/x is the ratio of the distance to the hinge line to the distance from the leading edge of the flat plate. For laminar flow n is 0.5 and for turbulent flow n is 0.2. The exponent m has a value of approximately 0.8 for laminar flow and approximately 0.9 for turbulent flow. However, due to the fact that equation (3.17) involves several approximations, m was conservatively assumed equal to 0.8 for both laminar and turbulent flow.

Use of equation (3.17) is limited to two-dimensional sharp-flat-plate-flap combinations at angles of attack greater than zero degrees.

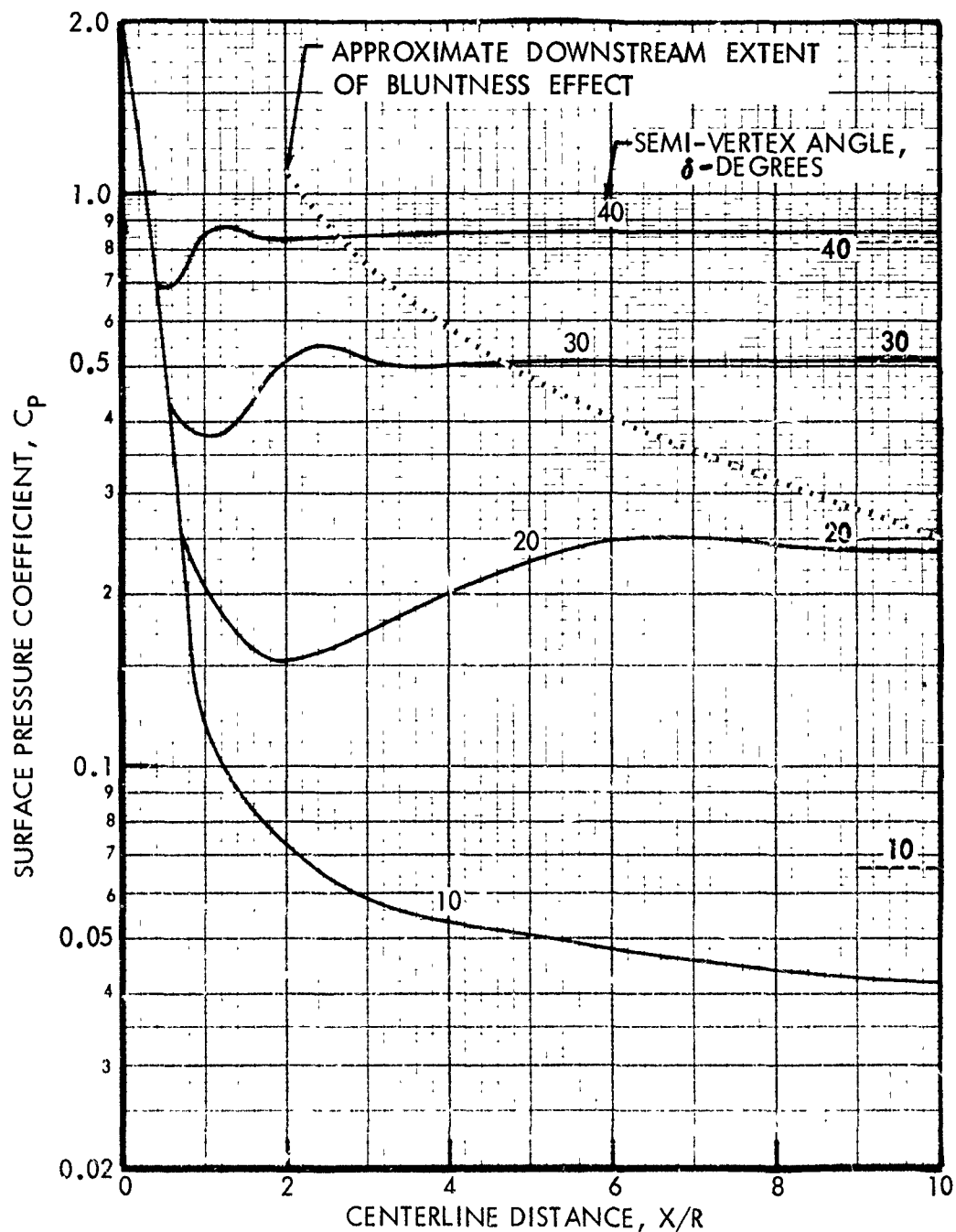
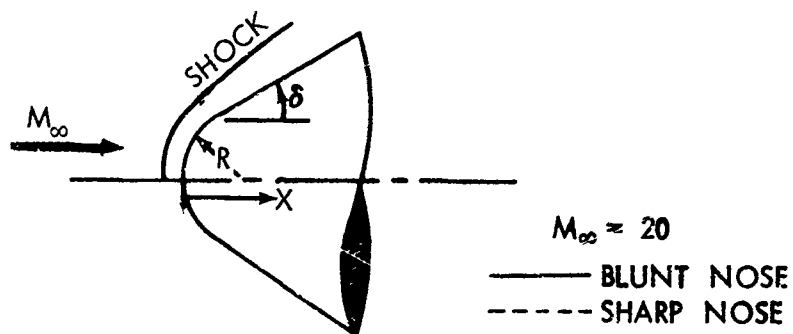


Figure 3-1: UNYAWED BLUNT CONE SURFACE PRESSURE

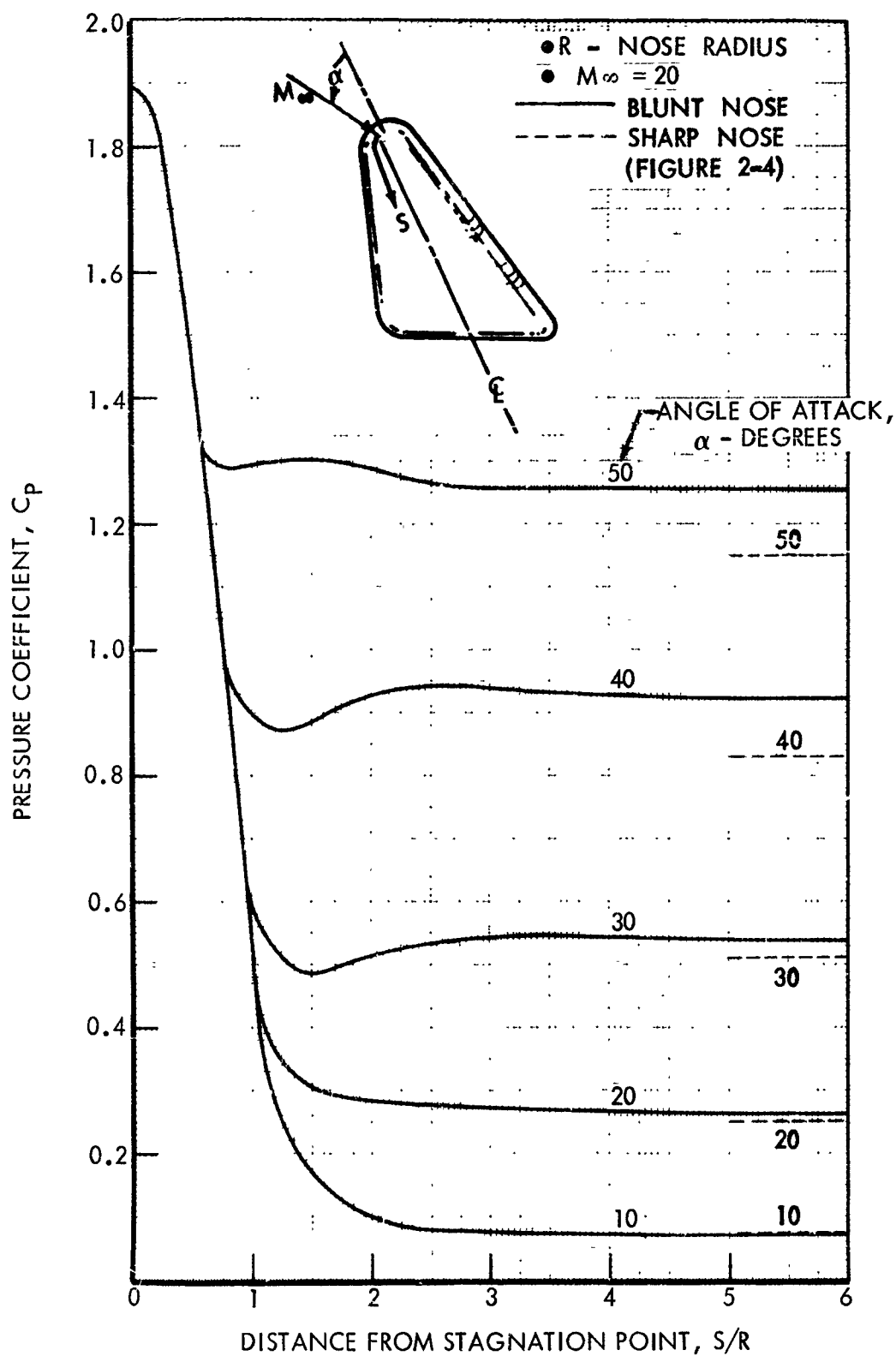


Figure 3-2: BLUNT DELTA WING LOWER SURFACE CENTERLINE PRESSURE

IV. SURFACE CONDITION EFFECTS

In general it is not to be expected that the surface panels of a re-entry vehicle will have the ideally smooth surfaces assumed in the basic heat transfer analysis. Roughnesses resulting from manufacturing tolerances which may allow protruding fasteners, panel mismatch, and panel surface curvature can cause flow field disturbances. The severe thermal environment may lead to buckling of surface panels; further, shallow corrugations or surface waves may be required to control the orientation of skin buckling that results from thermal expansion. It is also unlikely that perfect sealing can be provided at panel joints and particularly at the hingelines of movable control surfaces. Leakage at such points can bleed off the relatively cool air in the lower part of the boundary layer and so cause increased heating rates.

In the X-20 program the Nonsimilar Boundary Layer Program, Appendix C, was used to calculate the effects of leakage and shallow surface waves on laminar heating rates. The results of those calculations are described in this section. For all other roughness effects it was necessary to rely on experimental results. The surface roughness tests were not completed at the termination of the X-20 program, nor was the analysis completed of those tests that had been made. The results available at the time led to the following conclusions:

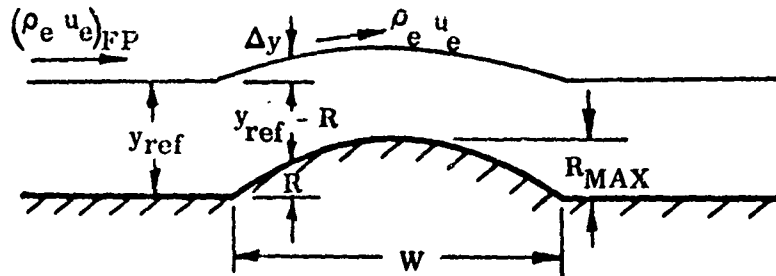
1. Forward facing steps are not acceptable for design.
2. An allowance of 20 percent for the effect of aft facing steps was required.
3. Where notches were unavoidable, they should be combined with aft facing steps.

A detailed test of aft facing step and notch configurations was in progress at the time of the termination of the X-20 contract. The results of the surface roughness tests are being reanalyzed by The Boeing Company under contract to NASA, and will be published in reference 18.

A. Shallow Surface Waves

Calculations of viscous interaction effects on the pressure and boundary layer over a shallow wave were made by combining the results of linearized theory and the Nonsimilar Boundary Layer Program. An inverse method was employed using linearized theory for the pressure distribution, and the Nonsimilar Boundary Layer Program to calculate laminar boundary layer profiles. A method essentially the same as the one used in this report was developed by Baxter and Flugge-Lotz, reference 25.

The parameters entering the calculation are shown in the sketch below.



A distribution of pressure was assumed and Δy found from linear theory with the aid of equation (4.1):

$$C_P = \frac{2}{\sqrt{M_e^2 - 1}} \left(\frac{d(\Delta y)}{dx} \right) \quad (4.1)$$

Using the Nonsimilar Boundary Layer Program the effect of the assumed pressure distribution on the boundary layer can be accurately calculated. Then the height of the surface wave corresponding to the assumed pressure distribution is given by:

$$R = y_{ref} + \Delta y - \delta_{FP}^* - \left[\frac{(\rho_e u_e)_{FP}}{\rho_e u_e} \right] (y_{ref} - \delta_{FP}^*) \quad (4.2)$$

When the results of many such calculations were examined it was found that the following equations could be used to predict the maximum laminar heating rates:

$$\frac{\Delta \dot{q}_{MAX}}{\dot{q}_{FP}} = \frac{1}{2} \left\{ -K_1 + [K_1^2 + 4K_2]^{1/2} \right\} \quad (4.3)$$

where

$$K_1 = \left[1 + ABC + (R/\delta_{FP}^*) (BCD - 1) \right] / [AC + R/\delta_{FP}^* (BC)] \quad (4.4)$$

$$K_2 = (R/\delta_{FP}^*) B / [AC + R/\delta_{FP}^* (CD)]$$

and

A, B, C, and D are defined as

$$A = \left[\frac{y_{ref}}{\delta_{FP}^*} - 1 \right] \left[1 - \frac{(\rho_e u_e)_{FP}}{\rho_e u_e} \right] / \frac{\Delta P}{P_{FP}} \quad (4.5a)$$

$$B = \left(\frac{\dot{q}_{MAX} - \dot{q}_{FP}}{\dot{q}_{FP}} \right) / \left(\frac{\delta_{FP}^* - \delta_{MIN}^*}{\delta_{MIN}^*} \right) \quad (4.5b)$$

$$C = \left(\frac{P_{MAX} - P_{SM}}{P_{SM}} \right) / \left(\frac{\dot{q}_{MAX} - \dot{q}_{SM}}{\dot{q}_{SM}} \right) \quad (4.5c)$$

$$D = \frac{1}{\gamma \pi} \frac{[M_e^2 - 1]^{1/2}}{M_e^2} \frac{W}{R} \quad (4.5d)$$

The following numerical evaluations of the parameters A, B, and C were made through correlation of Nonsimilar Boundary Layer Program results.

$$A = \frac{0.3}{0.78 + 0.84 l_w/l_o}$$

$$B = 2.5 (0.78 + 0.84 l_w/l_o)$$

$$C = \frac{1}{(0.78 + 0.84 l_w/l_o)}$$

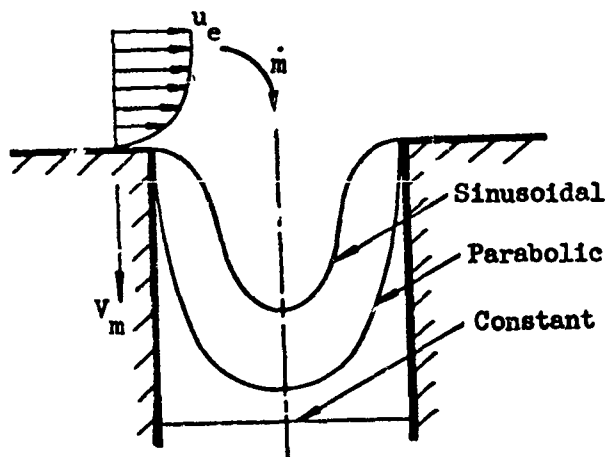
Curves are given in Section VI that provide numerical results in laminar flow based on equations (4.3), (4.4) and (4.5).

No analytical method had been developed to predict the effect of surface waves in turbulent flow.

B. Leakage

The effect of leakage on laminar heating rates was also calculated with the Nonsimilar Boundary Layer Program. Calculations were made for constant, parabolic, and sinusoidal leakage velocity distributions.

The leakage velocities assumed are illustrated by the following sketch:



where \dot{m} is the rate at which mass leaves the boundary layer, V_m is the leakage velocity, and u_e is the boundary layer edge velocity. Downstream laminar heating rates were computed using the Nonsimilar Boundary Layer Program. The results were well correlated by the following equations independently of the distribution of V_m :

$$\frac{\dot{q}}{\dot{q}_{NL}} = 1 + \frac{0.494 L}{(X/X_L - 1)^{2/3}} \quad (4.6)$$

$$L = \dot{m} (\rho_w \mu_w u_e X_L^2 H_L)^{-1/3} \quad (4.7)$$

$$\text{where } H_L = \frac{\dot{q}_{NL}}{I_{AW} - I_w} \quad (4.8)$$

The definitions of the above terms are shown in figure 4-1. Equation (4.6) was used to prepare the leakage effect curve of Section VI.

For turbulent flow no analytical method existed for predicting the effect of leakage on heating rates.

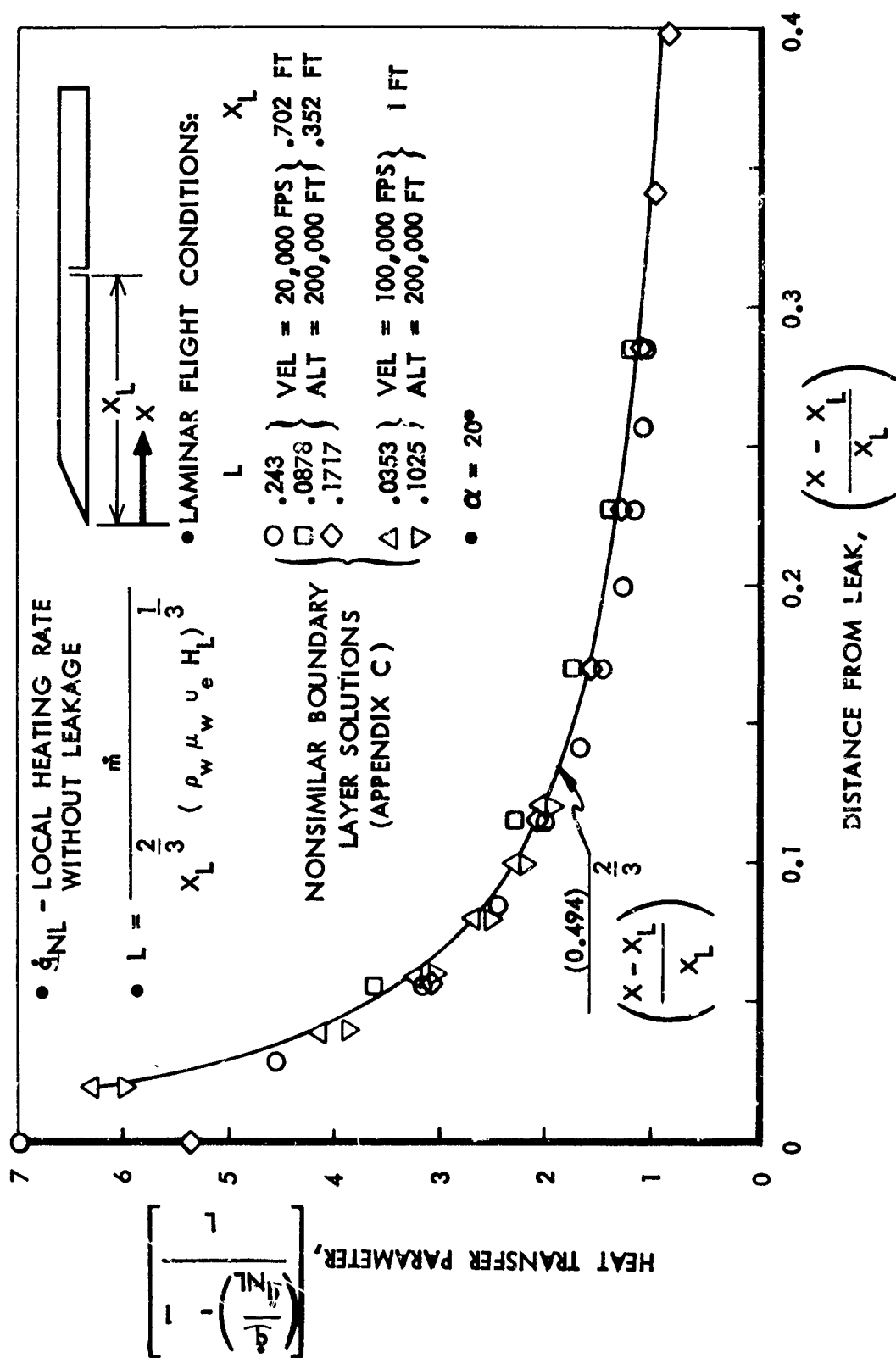


Figure 4-1: EFFECT OF LEAKAGE ON LAMINAR HEAT TRANSFER

V. APPLICATION TO COMPLEX CONFIGURATIONS

The aerothermodynamic environment of a re-entry vehicle is highly configuration and trajectory dependent, and no set of generalized rules can be expected to insure an accurate and thorough analysis. Rather, each vehicle must be examined individually and the adequacy of the analysis will depend in good part on the experience and care of the engineer making the study. However, when properly applied the charts of the following section can provide good initial estimates of heating rates for typical hypersonic vehicle configurations being considered today. As a minimum the following steps should be taken:

1. Make preliminary estimates by dividing the vehicle into geometric elements corresponding as closely as possible to the shapes discussed in Sections II and III, and apply the corresponding curves of Section VI.
2. Examine the relation of each element to the others. If an element is within the flow field of another a detailed calculation of the local flow should be made to determine the local pressure increase. Then multiply the previous estimate of the local heating rate by the pressure ratio so obtained. (This calculation is particularly applicable to local re-entrant corners, such as deflected trailing edge flaps.)
3. Estimate the location of shock waves to determine if any will impinge on any other part of the configuration. There is no simple method for calculating the effects of such impingements in all cases, but in the absence of more definitive information it should be assumed that a significant heating rate increase will result.
4. Examine each location at which the heat protection system changes in any way, and look for any design feature that could interfere with the action of the heat protection system. For example, on a radiantly cooled vehicle, examine each location at which the material temperature limit changes, and look for radiation blockage by nearby configuration components.
5. Estimate the effect of the surface condition during re-entry on smooth body heating. No simple theory exists for any roughness element different than a wave. The rule followed for the X-20 was to try and eliminate grooves and steps where possible and attempt to control the orientation of surface buckling.

It is emphasized that the above are only the preliminary steps, with the course of further analysis dependent on the results of these initial calculations. For example, step 2 may lead to unnecessarily conservative values, but will highlight potential problem areas. Thus, on the highly swept delta

wing glider shown in figure 5-1, step 2 in the above procedure would direct attention to the elevons and canopy, while step 3 would indicate that the fin may be critical at low angles of attack. On the hypersonic airbreather shown in figure 5-2 the critical regions indicated would be the wing leading edge at its juncture with the body and at the impingement point of the body shock wave, the entire cowl, the tip fins, and the interior of the engine where re-radiation of heat is blocked by the enclosed geometry. Two examples from the X-20 program that illustrate the need of detailed analysis will now be described.

A. Control Surface Gap

If aerodynamic flaps are to be used for control they must be allowed to move freely. It was found in the X-20 studies that free movement could be provided only by preventing contact between the outboard edge of the elevon and the fin. When due allowance for thermal and load deformations had been made it was found that a sizeable gap existed between the two surfaces, and that flow through the gap would occur at many flight conditions. Although the resulting aerodynamic heating was not severe, excessive temperatures occurred because the heated surfaces, being in close proximity, were unable to re-radiate effectively. Thus it became necessary to obtain accurate heating rate information for the inside of the gap.

Since it was unlikely that an analytical investigation alone would lead to an acceptable fin-elevon design, a series of tests were conducted specifically to solve this problem. A large number of fin lower edge shapes, elevon outboard edge shapes, and gap widths were tested to determine the combined effects of aerodynamic heating and improved radiation view factor on gap temperatures. The analysis of experimental data and radiation view factors indicated that the point of maximum surface temperature occurs very near the point of minimum fin-elevon separation for fins and elevons having cylindrical surfaces, and near the junction of the entrance and plane sections for parallel fin-elevon surfaces. Gap width was found not to affect pressure distributions as long as the flow was not choked by boundary layer growth.

The above information forms a basis for the analysis in this report which considers the flow fields associated with the three gap configurations presented in figure 5-3.

Maximum temperature will occur on these gap configurations approximately 90° from the shoulders indicated on figure 5-3. The pressure distribution used in calculating a heating rate distribution by the ρ_r/μ_r method is shown in figure 2-1. Stagnation conditions were based on the normal velocity components,

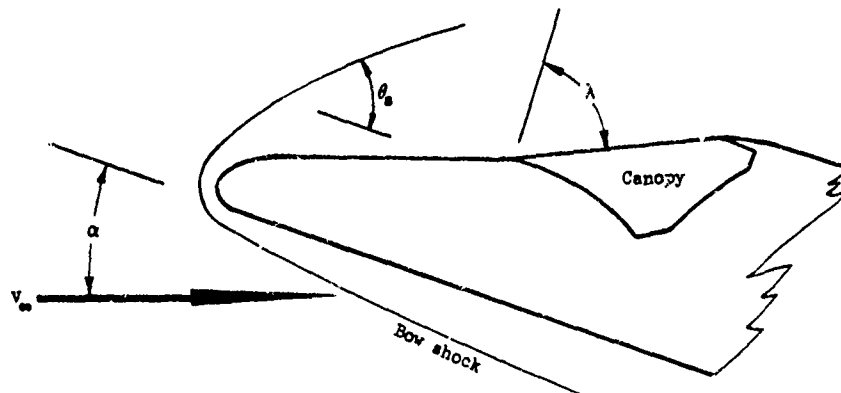
$$V_n = V_\infty \sin \alpha \quad (5-1)$$

where V_∞ is the stream velocity and α is the vehicle angle of attack. The heating rate 90° from the shoulder is used for the design chart shown in Section VI.

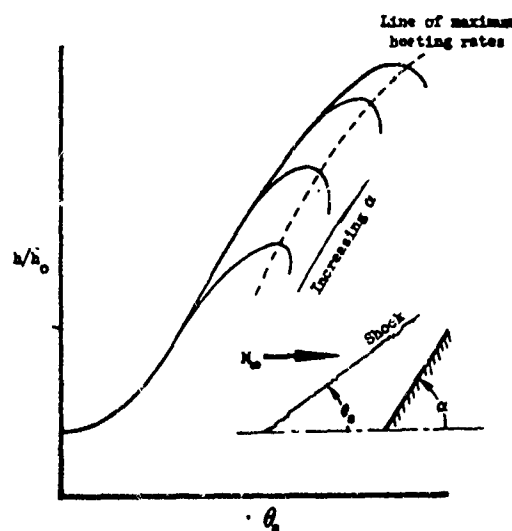
B. Fin Leading Edge and Canopy Interference Effects

The vehicles illustrated in figures 5-1 and 5-2 have vertical fins that are to be used for aerodynamic control and canopies forming the cockpit area. Experimental data obtained during the design of the X-20 indicated that at low angles of attack, fin leading-edge and canopy heating rates would be considerably higher than predicted by swept-infinite-cylinder theory or local oblique-shock theory based on free-stream conditions. The higher heating rates are attributed to the shock wave generated by the wing surface interfering with the leading edge and canopy surface flow field.

The exact nature of the interference effect has not been established, even at the present time. However, based on the results of the calculations described below, it appears that the primary effect is the change in local flow properties caused by the wing shock envelope. The flow field is illustrated below:



The effect on the canopy heating rate was estimated by using oblique shock theory to calculate local flow properties just downstream of the shock. The canopy heating rate was then calculated with infinite cylinder theory using the local flow properties. It was found that for each angle of attack the effect of the oblique shock varied such that there was a most unfavorable angle, as illustrated below:



Since the bow shock is curved, it was assumed that at some point the most unfavorable angle would occur, and that therefore, the maximum canopy heating rate would be given by the maxima of the above family of curves. Good agreement with test data was obtained by this method.

It will be noted that for given free-stream conditions the final result depends only on the true sweep angle, λ , of the canopy, (since the angle of the shock is assumed to take on all possible values) and thus can be plotted as a single curve. The curve so obtained was also applied to fin leading edges, and again good agreement with test data was obtained. The agreement with the fin data may be fortuitous, however, since the effect of sweeping the initial shock in the planform view was not considered.

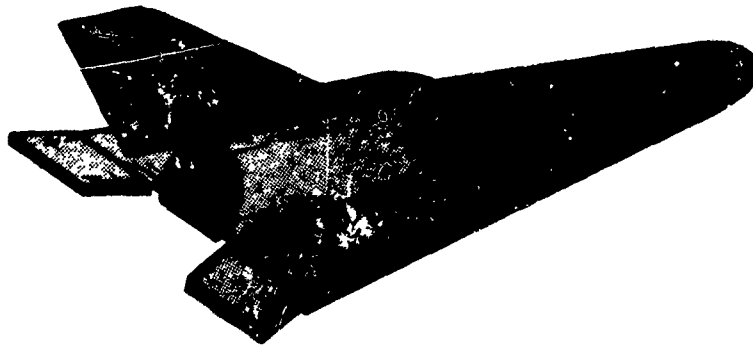


Figure 5-1: RE-ENTRY VEHICLE

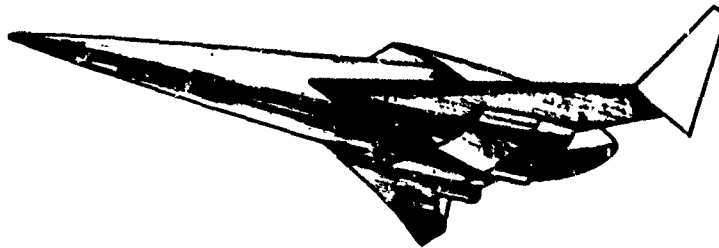


Figure 5-2: HYPERSONIC CRUISE VEHICLE

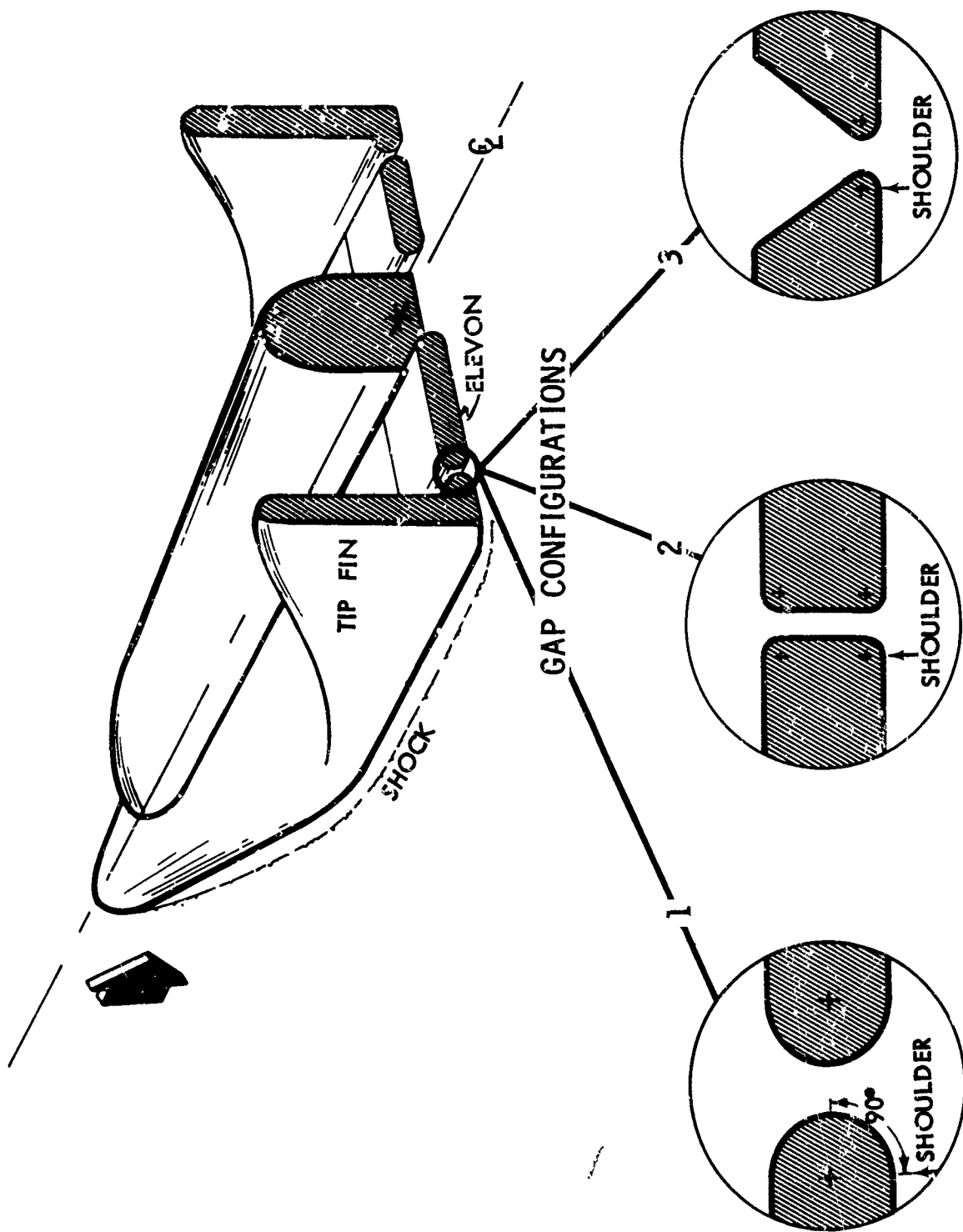


Figure 5-3: CONTROL SURFACE GAP GEOMETRY

VI. DESIGN CHARTS

This section contains charts that provide numerical values of heating rates to the geometric elements and methods discussed in Sections II, III, IV and V. As stated in Section II, calculations were made assuming the flow to behave as a continuum and to be in chemical equilibrium. All charts showing altitude were developed using the U. S. Standard Atmosphere, 1962. Other gas properties have been determined using references 1, 2, and 26.

A. Method of Presentation

Heating rates are presented in terms of equivalent heat-transfer coefficients and recovery temperatures defined by

$$h = \frac{\dot{q}}{T_{AW} - T_w} \quad (6.1)$$

where \dot{q} is the local heating rate T_w is the local wall temperature and T_{AW} is the recovery temperature defined as

$$T_{AW} = \frac{i_{AW}}{c_p} = \frac{i_{AW}}{0.24} \quad \text{°R} \quad (6.2)$$

where i_{AW} is the recovery enthalpy and c_p is the specific heat at constant pressure for a perfect gas. Defining h and T_{AW} in this manner is equivalent to assuming that the specific heat of air at the wall temperature is always

$$C_{P_w} = 0.24 \quad \text{Btu/lbm} \quad (6.3)$$

While in reality this assumption is usually not true, the error in making this approximation is small because of the large difference between recovery enthalpy and wall enthalpy for hypersonic flight conditions. In addition, the assumption is always conservative, in that its use always results in slightly higher values of heating rate. Finally, use of equation (6.2) allowed structural designers to easily obtain equilibrium wall temperatures for radiation cooled structures using the simplified thermal balance relationship

$$\dot{q}_{RAD} = \dot{q} \quad (6.4a)$$

$$\text{or } \epsilon \sigma (T_{w_{eq}})^4 = h (T_{AW} - T_{w_{eq}}) \quad (6.4b)$$

where ϵ is the surface emissivity, σ is the Stefan-Boltzmann constant and \dot{q}_{RAD} is the heat flux lost through radiation when the wall temperature has reached equilibrium.

Heating rates, \dot{q} , were calculated assuming a wall temperature of 2000 °R. This temperature was chosen because it represents the order of temperature one can expect on nonrefractory materials during the most critical part of lifting re-entry. Correction charts are presented that allow heat-transfer coefficients to be obtained for other wall temperatures.

B. Reference Conditions

Heat transfer coefficients, as represented by equation (6.1), were calculated for all of the elements considered in Section II, III, IV and V at the two flight conditions* shown in Table I.

<u>REFERENCE FLIGHT CONDITIONS</u>		
	Laminar	Turbulent
Altitude	240,000 ft.	180,000 ft.
Velocity	20,700 fps	18,700 fps

TABLE I

This table represents the design conditions most critical for the X-20.

Distribution functions were formed for each geometry by normalizing local values of heat transfer coefficient by a reference value calculated at the appropriate flight condition for laminar or turbulent flow. Distribution functions formed in this way are relatively weak functions of altitude below about 280,000 feet and velocity between 8,000 to 26,000 fps. For laminar flow, the reference value, h_0 , chosen was the stagnation point of a 1-foot-radius hemisphere. Laminar heating rates for all of the geometric elements (i.e., sharp plates, sharp and blunt cones etc.) considered in Sections II, III, IV and V have been normalized by this value and are presented in terms of altitude. Other altitude and velocity combinations are then obtained by multiplying distribution functions by the appropriate reference value.

*For laminar flow the "altitude-velocity" chosen is in the region of chemical nonequilibrium flow. The effect of chemical nonequilibrium on heating is not taken into account in this document. However, it is expected to be small and favorable.

No unique way has been found to normalize all turbulent heating rates by the same reference value and keep the resulting ratio relatively insensitive to altitude and velocity. As a result, in turbulent flow two methods were used to find reference values for normalizing local heat transfer coefficients.

The first is used in conjunction with sharp flat plates, sharp cones, sharp delta wings, yawed infinite cylinders and control surface gaps. Reference values correspond to turbulent stagnation line heating rates for a 60° swept infinite cylinder with a 1-foot radius. This reference value was used exclusively during the design of the X-20 and was designated at that time as the "Turbulent Reference Heat Transfer Coefficient," h_{RT} . This nomenclature has been retained in this report.

Development of the second method was completed during the compilation of this report. It is used in determining reference values to normalize turbulent heating rates on the hemisphere, unyawed infinite cylinder, blunt cone and blunt delta wing. This method utilizes the relationship between laminar and turbulent flow inherent in the $\rho_r \mu_r$ method. This expression, developed in Appendix B, is

$$\frac{h_T}{h_L} = \frac{0.185 R_r^{1/2}}{0.332 [\log_{10} (R_r + 3000)]^{2.584}} \quad (6.5)$$

where R_r is the reference Reynolds number,* defined in Appendix B as

$$R_r = \frac{\rho_r \mu_r u_e x_{eq,L,o}}{\mu_o^2 F_x^2} \frac{x_{eq,L,o}}{x_{eq,L}} \quad (6.6)$$

Equation (6.5) is shown in Appendix B to be valid in the Reynolds number range between 0.003 million and 100 million.

Absolute values of laminar or turbulent heat-transfer coefficients are then obtained at altitudes and velocities different than shown in Table I through the use of the appropriate reference value using the relationship

$$h = \left(\frac{h}{h_{ref}} \right) h_{ref} \quad (6.7)$$

where the subscript ref signifies "o" for laminar flow and "RT" for turbulent flow.

*Called reference because of its special significance to the $\rho_r \mu_r$ method.

C. Reference Condition Charts

1. Recovery Temperature

The equivalent recovery temperature, equation (6.2) has been evaluated over a range of velocities between 8,000 and 26,000 fps. It is presented in figure 6-1 as a function of free-stream velocity and the ratio of the recovery temperature to the stream total temperature

$$T_T = T_\infty + \frac{V_\infty^2}{2 c_{p,I}} \quad (6.8)$$

The ratio, T_{AW}/T_T , is shown over the range 0.85 (corresponding to flat plate incompressible laminar flow values at $\delta = 0$; reference 27.) to 1.0, the latter value being at the stagnation point.

2. Laminar Reference Heat-Transfer Coefficient

The reference heat-transfer coefficient for laminar heating is the laminar heat transfer coefficient, h_0 , at the stagnation point of a 1 foot radius hemisphere. It is shown in figure 6-2. Wall temperature corrections are shown in figure 6-3 as a function of free-stream Mach number, M_∞ . Radius corrections may be made with the equation:

$$\frac{h}{h_0} = \left(\frac{R_0}{R} \right)^{1/2} \quad (6.9)$$

where h is the stagnation point heat transfer coefficient for a sphere of radius R and h_0 is the reference laminar heat transfer coefficient for a sphere of radius $R_0 = 1$ foot.

3. Turbulent Reference Heat Transfer Coefficient

Absolute values of the reference heat-transfer coefficient for turbulent heating, h_{RT} , are presented in figure 6-4. These curves represent the turbulent stagnation-line heat-transfer coefficient for a 60° swept, 1-foot-radius infinite cylinder. Wall temperature corrections are shown in Figure 6-5. Figure 6-4 can be used to determine turbulent stagnation line heating rates for 60° swept cylinders of radii different than 1 foot by using the correction factor shown in figure 6-6. This correction is, however, dependent on the reference Reynolds number at the stagnation line. To avoid confusion, this particular evaluation of equation (6.6) was designated, R_R , and is presented in figures 6-7 and 6-8 as a function of altitude and velocity.

D. Geometric Elements

1. Hemisphere

The laminar design curve for the hemisphere is shown in figure 6-9. Wall temperature corrections may be obtained from figure 6-3 and a radius correction by equation (6.9).

Turbulent design curves for the hemisphere are normalized by the laminar value as described above.

Local reference Reynolds number, equation (6.6), at the location of maximum turbulent heating is presented in figure 6-10 in terms of altitude and velocity for a hemisphere of $R = 1$ foot. The reference Reynolds number for a hemisphere of radius R can be found by the equation

$$R_{r\text{MAX}} = (R) (R_{r\text{MAX}})_{R=1\text{ft}} \quad (6.10)$$

where $R_{r\text{MAX}}$ is obtained from figure 6-10. The location of maximum turbulent heating is shown in terms of local reference Reynolds number in figure 6-11. Local heat transfer coefficients normalized to the maximum turbulent values are presented in terms of the local angular location in figure 6-12. A slight Mach number dependency is noted. Finally, the level of turbulent heating is determined by figure 6-13 which relates the maximum turbulent heat-transfer coefficient, h_{MAX} , to the laminar stagnation-point value, h_{SP} . Figure 6-13 is based on a correlation that is a function only of the local reference Reynolds number, $R_{r\text{MAX}}$, provided that the pressure distribution in the vicinity of maximum turbulent heating is based on modified Newtonian theory, equation (2.4). For local reference Reynolds numbers in the range 0.01 million to 1 million, the correlation for $(h_{\text{MAX}}/h_{\text{SP}})$ can be expressed by the equation.

$$\frac{h_{\text{MAX}}}{h_{\text{SP}}} = 0.0844 R_{r\text{MAX}}^{0.283} \quad (6.11)$$

Vorticity Interaction Effects on Stagnation Point Heating

Design curves for modifying stagnation point heating rates for vorticity interaction are shown on figures 6-14 and 6-15.

The vorticity interaction parameter, Γ , is obtained using the relationship

$$\Gamma = F_1 F_2 / \sqrt{\text{Re}_0} \quad (6.12)$$

where F_1 and F_2 are defined by figure 6-14 and

$$Re_o = \frac{\rho_o \sqrt{i_o} R}{\mu_o} \quad (6.13)$$

The parameters in equation (6.13) were defined in Section II as follows: ρ_o is density, μ_o is viscosity evaluated at stagnation conditions, i_o is stream total enthalpy, and R is the nose cap radius.

Figure 6-15 presents the ratio of heating with vorticity to heating without in terms of the vorticity interaction parameter Γ . Both the Non-similar-Boundary-Layer results and Ferri's results (reference 8) are shown on this figure allowing the reader to apply either method.

2. Infinite Cylinders

a) Swept Infinite Cylinders

Design curves for laminar stagnation line heat-transfer coefficients are shown in figure 6-16. Circumferential heat-transfer distributions for laminar flow are presented in figure 6-17 for sweep angles between zero and 80 degrees. Turbulent stagnation line heat-transfer coefficients presented in figure 6-18 are normalized using the turbulent reference heat transfer coefficient h_{RT} . Circumferential heat-transfer distributions are shown in figure 6-19 over the same range of sweep angles as in the laminar case except that the zero degree sweep (unswept cylinder) case has been deleted from this curve.

b) Unswept Infinite Cylinders in Turbulent Flow

The method described under turbulent heat-transfer distribution on a hemisphere also applies to the unswept infinite cylinder although the charts are different. The reference Reynolds number at the location of maximum turbulent heating on the unswept cylinder is shown in figure 6-20 for an unswept infinite cylinder 1 foot in radius. The differences between the infinite cylinder and the hemisphere are primarily due to changes in x_{eq} and are on the order of 2 to 2.5 times larger for the unswept cylinder. The local reference Reynolds number for an unswept cylinder of radius R may be found using equation (6.10) after R_{MAX} is obtained from figure 6-20.

Figure 6-21 shows the variation in the location of maximum turbulent heating with R_{MAX} . From figure 6-22 the turbulent heating distribution can be obtained in terms of the maximum turbulent heat-transfer coefficient h_{MAX} .

The lower curve in figure 6-13 relates the maximum turbulent heat-transfer coefficient on an unswept infinite cylinder to the stagnation point heat-transfer coefficient of a hemisphere having the same radius as that of the cylinder. For reference Reynolds numbers in the range 0.01 million to 1

million the correlation of h_{MAX}/h_{SP} can be expressed by the equation

$$\frac{h_{MAX}}{h_{SP}} = 0.0613 R_{r_{MAX}}^{0.283} \quad (6.14)$$

Comparing equations (6.11) and (6.14), and remembering that R_r is 2 to 2.5 times larger for the cylinder than for the hemisphere, we see that turbulent heating rates on an unswept cylinder are approximately 10% less than on a sphere of the same diameter.

3. Sharp Flat Plates

Design curves for laminar and turbulent heating on the sharp flat plate are shown in figure 6-23. The laminar heat-transfer coefficient $h_{FP,L}$ has been computed for $x = 1$ foot. For turbulent flow the heat-transfer coefficient $h_{FP,T}$ is presented for $x = 10$ feet.

The wall temperature correction is shown in figure 6-24 and applies also to sharp unyawed cones and sharp delta wings.

The distance correction, shown in figure 6-25 except for low angles of attack, is given by:

$$\frac{h_x}{h_m} = (x_m/x)^n \quad (6.15)$$

where h_x is the heat-transfer coefficient at a distance x and h_m is the heat-transfer coefficient at distance x_m . For laminar flow $n = 0.5$, $x_m = 1.0$ foot and $h_m = h_{FP,L}$. For turbulent flow $n = 0.2$, $x_m = 10$ feet and $h_m = h_{FP,T}$.

The exponent on the ratio (x_m/x) is a variable that is dependent upon the reference Reynolds number, equation (6.6).

Figure 6-25 also applies to unyawed sharp cone and sharp delta wing distance corrections.

4. Unyawed Cones

a) Sharp cones

Design curves for laminar and turbulent heating on unyawed sharp cone surfaces are shown in figure 6-26. The laminar heat-transfer coefficient $h_{SC,L}$ on the sharp cone is for $x = 1$ foot and for turbulent flow the heat-

transfer coefficient $h_{SC,T}$ is for $x = 10$ feet. The wall temperature and distance corrections are shown in figures 6-24 and 6-25 respectively.

b) Blunt cones

Design curves for laminar heating on an unyawed blunt cone having a hemispherical nose cap are shown in figure 6-27. A noticeable "bump" is noted in this curve just aft of the nose cap-cone junction. This "bump" corresponds to the region for which perturbations in the pressure distribution have occurred as was shown in Section III, figure 3-1. These effects damp out more rapidly at large semi-vertex angles of the cone.

Wall temperature effects are given by figure 6-3 for the stagnation point region of the hemispherical nose cap and figure 6-24 for the conical surface.

Turbulent heating rates are presented using the second method of Section VI-B. The local reference Reynolds number at the point of maximum turbulent heating on a 1-foot-radius nose is determined using figure 6-10. For nose cap radii different than 1 foot, modify $R_{r_{MAX}}$ using equation (6.10).

Figure 6-28 presents local reference Reynolds numbers at a distance x from the stagnation point. The ratio defined by equation (6.5) for blunt cones is shown in figure 6-29. Absolute turbulent heat-transfer coefficients at the location S are then determined from the relationship.

$$h_{BC,T} = \left(\frac{h_{BC,T}}{h_{BC,L}} \right) \left(\frac{h_{BC,L}}{h_{SP}} \right) \left(\frac{h_{SP}}{h_o} \right) h_o \quad (6.16)$$

where the ratio $(h_{BC,T}/h_{BC,L})$ is defined by figure 6-29, the ratio $(h_{BC,L}/h_{SP})$ is defined by figure 6-27, (h_{SP}/h_o) is defined by equation (6.9) for the radius used to determine $R_{r_{MAX}}$, and h_o is the laminar reference heat-transfer coefficient shown in figure 6-2.

5. Delta Wings

a) Sharp Delta Wings

Design curves for laminar and turbulent heating on a 70° swept sharp delta wing are shown in figure 6-30. The laminar heat-transfer coefficient $h_{DW,L}$ is for $x = 1$ foot, and the turbulent heat-transfer coefficient, $h_{DW,T}$ is for $x = 10$ feet. The wall temperature and distance correction factors are shown in figures 6-24 and 6-25, respectively. Corrections for the effect of sweep on centerline heating can be made using the curves of figure 6-31. Spanwise heat transfer distribution curves are given in figures 6-32 and 6-33 for laminar and turbulent flow, respectively, in terms of a ratio of local heat-transfer coefficient, h_ξ , to the coefficient at the centerline, $h_{\xi=0^\circ}$. The effective gamma used for streamline calculations was equal to 1.2.

b) Blunt Delta Wings

Laminar heating design curves are presented in figure 6-34 for obtaining values on the centerline of a 73°* swept blunt delta wing. As noted in Section III, nose bluntness effects were neglected and are not included on this figure. Correction factors for sweep effects on centerline heating are presented in figure 6-35.

Spanwise laminar heating distributions are shown in figures 6-36 and 6-37. As noted in Section III, these are semi-empirical distributions that have been determined using data (reference 16) measured in proximity to equivalent centerline locations of $S/R = 17$ and 27 , in conjunction with theoretical centerline heating rates calculated using the $\rho_r \mu_r$ method, Appendix B, and semi-empirical leading-edge stagnation-line locations determined using the faired curve shown in Section III-B-2.

Leading-edge sweep angle influences spanwise heating distributions. For the range of sweep angles of most interest in hypersonic flight (usually between 65° and 80°) a first order approximation can be made using information available on design charts appearing in this document. The following procedure is suggested:

(1) At the Leading Edge

Establish a new stagnation line location using figure 6-38 and effective sweep angle using figure 6-39. Determine the percentage difference between laminar stagnation line heating rates for swept infinite cylinders, figure 6-17, having effective sweep angles corresponding to geometric sweep angles of 73° and the one being investigated. Shift the stagnation line location shown on figure 6-36 or 6-37 to the new value and modify the stagnation line heating rate ratio by the percentage difference in heating rates previously determined for swept infinite cylinders. Construct a new distribution curve in proximity to the stagnation line using the slopes shown on figure 6-36 or 6-37.

(2) At the Centerline

Modify the values at the centerline using the sweep correction curves of figure 6-35. Construct a new distribution curve similar to the one shown on figure 6-36 or 6-37 depending on S/R .

For leading-edge sweep angles less than 73° centerline heating rates decrease whereas the stagnation-line heating rates increase. For leading-edge sweep angles greater than 73° centerline heating rates increase but stagnation line heating rates decrease. For either situation modify the leading edge distribution curve of figure 6-36 or 6-37 to intersect the new lower-surface heating distribution curve.

To establish laminar spanwise heating distributions for centerline values

*This sweep angle was chosen because the bulk of the delta wing models used during the X-20 test program had this sweep, and the data obtained from that program was used to substantiate the method and provide spanwise distributions.

of S/R different than those shown on figures 6-36 and 6-37 the following procedure is suggested. The value at the centerline for the S/R of interest is established using figure 6-34. Construct a new lower surface heating distribution curve parallel to the one shown in figure 6-36 or 6-37 (using the figure having an S/R closest to the one desired) until it intersects the leading edge distribution curve shown.

Turbulent heating rates to the centerline of the delta wing can be obtained using the second reference method which is similar to the procedure used with a blunt cone. The reference Reynolds number at the location of maximum turbulent heating on the hemispherical nose is obtained from figure 6-10 and is used in conjunction with figure 6-40 to determine the local reference Reynolds number on the lower surface centerline at a distance S from the stagnation point. The relation between the turbulent and laminar heat transfer coefficient is determined using figure 6-29. The laminar surface heat transfer coefficient is related to the laminar stagnation point heat transfer coefficient by figure 6-34. Finally the turbulent heat transfer coefficient h_T is calculated by the relationship

$$h_T = (h_T/h_L) (h_L/h_{SP}) (h_{SP}/h_o) h_o \quad (6.17)$$

where h_o is obtained from figure 6-2. The value for (h_{SP}/h_o) is determined using equation (6.9).

6. Deflected Flaps

Design curves for maximum laminar heating on deflected flap surfaces attached to sharp flat plates are shown in figure 6-41. That portion of the curves that is dashed is outside the range for which the "upper limit" theory discussed in Section III is applicable. Use of these curves within the dashed range should be made with caution. For a positive deflection the maximum heat-transfer coefficient h_F may occur anywhere on the flap; generally, if flow separation has occurred, h_F is near the point of flow reattachment. The heat-transfer coefficient h_{HL} is the laminar heat transfer coefficient calculated just ahead of the hinge line of the flap with the assumption that no flow separation has been caused by the deflected flap. The value of the hinge line heat-transfer coefficient h_{HL} may be evaluated by sharp flat-plate heat-transfer methods, figures 6-23 through 6-25.

For a negative deflection, h_F is an approximate heat transfer coefficient at the hinge line assuming that the expansion has already occurred. Aft of the hinge line the heating decay follows the relation on the following page

$$h \sim (1/x)^n \quad (6.18)$$

where $n = 0.5$ for laminar flow and 0.2 for turbulent flow.

Maximum turbulent heating rates were normalized using the laminar values for the same local boundary-layer conditions. This method† is consistent with the second turbulent reference method described in Section VI-B. Values are presented in figure 6-42.

7. Surface Conditions

a) Waves

Heat transfer design curves for a particular type of roughness, shallow surface waves, are shown in figures 6-43 and 6-44, in terms of a wave height parameter, E/δ^* . The displacement thickness δ^* may be evaluated by the use of the displacement-thickness heating parameter $h\delta^*$ shown in figure 6-45 and a value for the heat-transfer coefficient h for a smooth surface. The latter is found using figure 6-23. The derivation of the product $h\delta^*$ can be found in Appendix D.

b) Leakage (Mass Removal Through an Orifice at the Surface)

Leakage effects on sharp flat plate laminar heating at all angles of attack in terms of the distance downstream of a leak are shown on figure 6-46. The heat-transfer parameter is shown in terms of a nondimensional heat-transfer ratio and a nondimensional mass flow ratio, L , as defined in Section IV.

8. Control Surface Gaps

Design curves for laminar and turbulent heating at the most critical location on a fin for representative tip-fin-elevon control-surface gaps (figure 5-3, Section V) are shown in figure 6-47. This location is 90° from the tip-fin shoulder. For the gaps shown in figure 5-3 this is the point of minimum fin-elevon separation. Maximum heating rates do not occur at this location. However, maximum temperatures do occur if the structure is radiation cooled, because the radiation view factor is at its minimum. For all of the gap shapes shown in figure 5-3 one design curve is applicable at each of the two flight reference conditions. The leading edge radius of the fin shown in this figure is equal to 1 foot. For radii different from 1 foot, corrections can be made to the heating rates using figure 6-6 for turbulent flow and equation (6.9) for laminar flow where h_0 is the reference heat-transfer coefficient for a radius of $R = 1$ foot, and R is the fin radius in feet.

†Use of this method for this combination of two-dimensional bodies considerably simplified the extrapolation-to-flight methods for this geometry that are presented in Section VII.

9. Canopy and Fin Leading Edges

Laminar and turbulent flow design curves for predicting canopy stagnation line heating rates are shown in figure 6-48. The curves shown were developed using the method described in Section V-B. Heat-transfer-coefficient ratios are shown in terms of the true sweep angle $(\alpha + \lambda)$.

Values for h_o are obtained from figure 6-2 and h_{RT} from figure 6-4. The radius of the leading edge shown is 1 foot. For radii different from this, a correction factor can be obtained using figure 6-6 for turbulent flow or equation (6.9) for laminar flow.

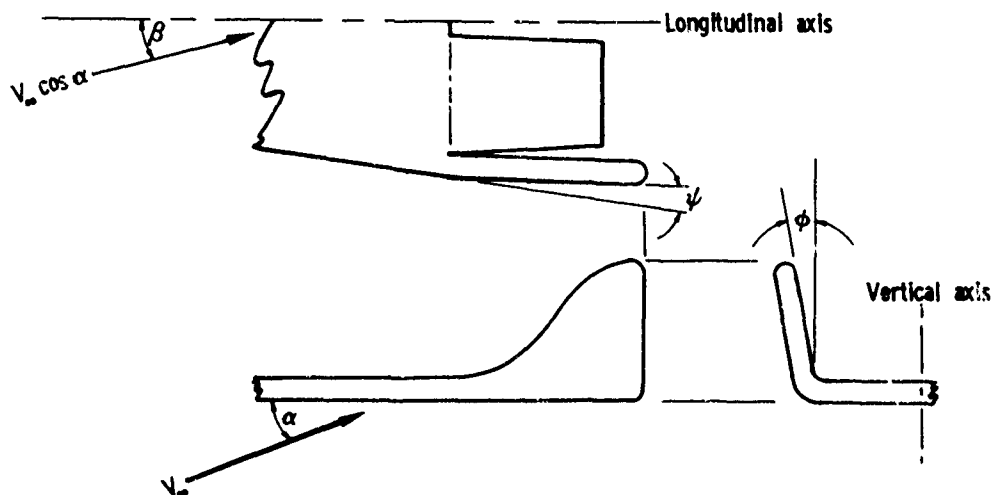
As noted in Section V, heating rates obtained using the above method were also applied to tip-fin leading edges during the X-20 program. Figure 6-48 can be used directly for this geometry by allowing the independent variable, $(\alpha + \lambda)$, to represent the effective sweep angle, Λ_{eff} , of the fin leading edge measured with respect to the vertical axis normal to the free stream velocity vector. This angle is defined by:

$$\begin{aligned} \cos \Lambda_{eff} = & \cos \alpha (\cos \theta_{SL} \cos (\psi + \beta) \cos \Lambda + \sin \theta_{SL} \sin (\psi + \beta)) \\ & + \sin \alpha \cos \theta_{SL} \sin \Lambda \end{aligned} \quad (6.19)$$

where Λ is the fin leading-edge geometric sweep angle and θ_{SL} is the location of the stagnation line as defined by:

$$\tan \theta_{SL} = \frac{\sin (\psi + \beta)}{\cos (\psi + \beta) \cos \Lambda + \tan \alpha \sin \Lambda} \quad (6.20)$$

The remaining angles are defined in the following sketch.



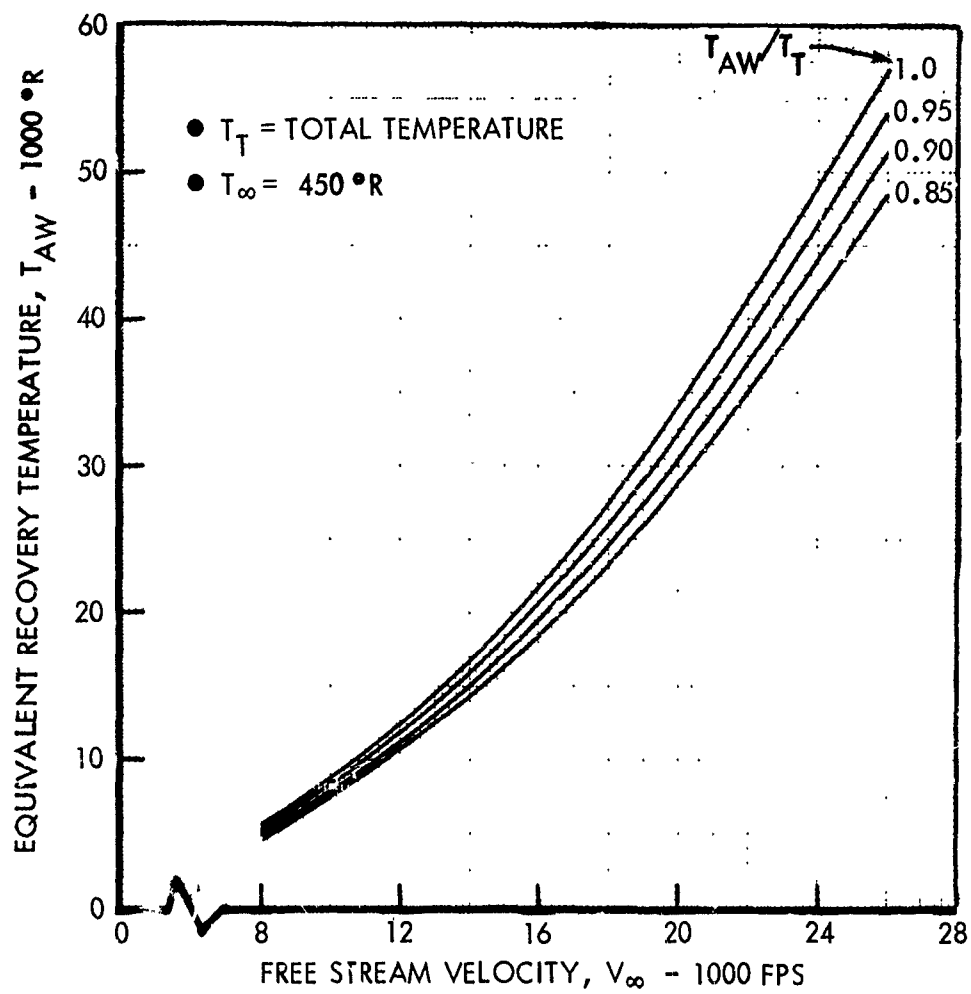


Figure 6-1: EQUIVALENT RECOVERY TEMPERATURE

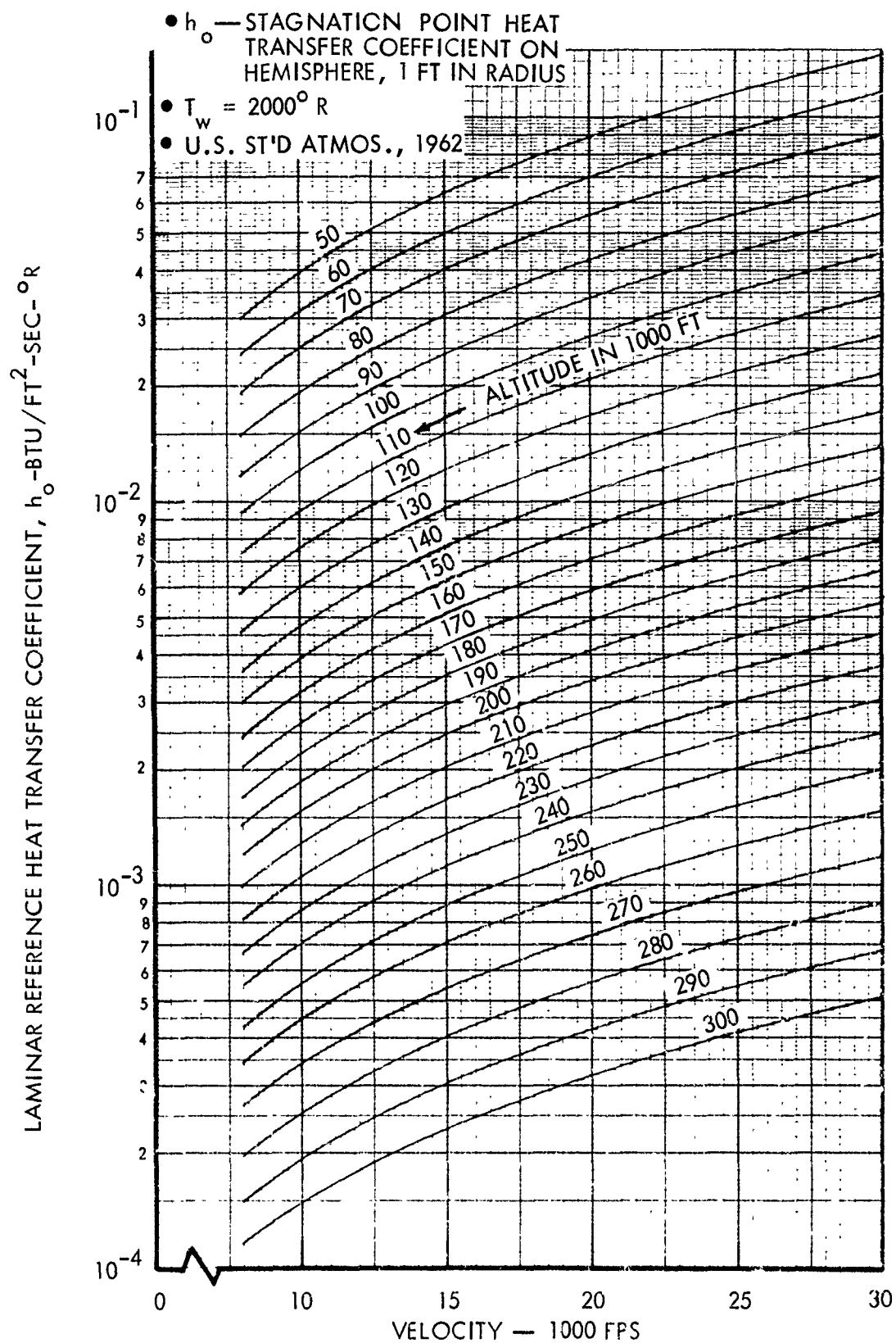


Figure 6-2: LAMINAR REFERENCE HEAT TRANSFER COEFFICIENT

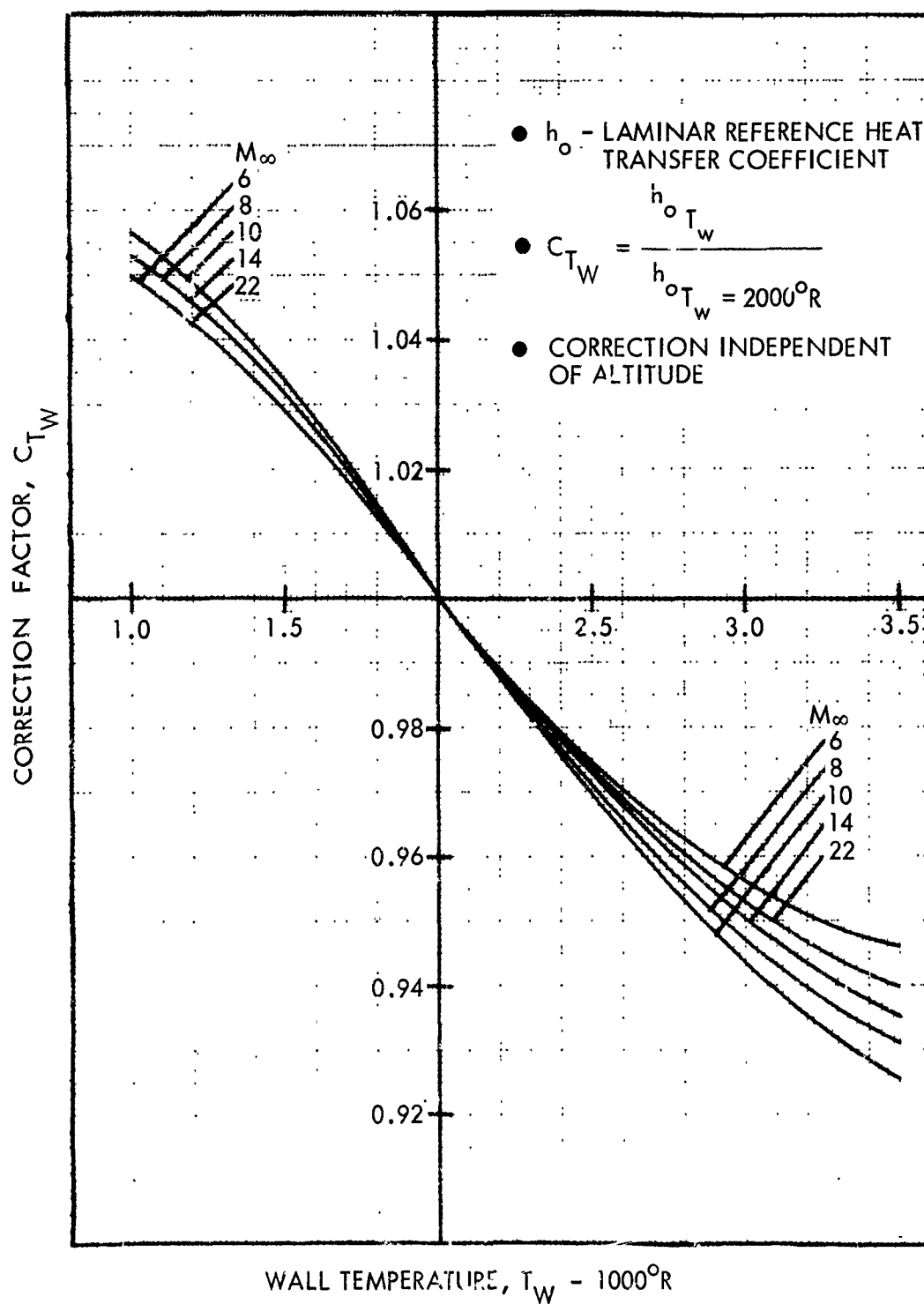


Figure 6-3: WALL TEMPERATURE CORRECTION FACTOR FOR LAMINAR REFERENCE HEAT TRANSFER COEFFICIENT

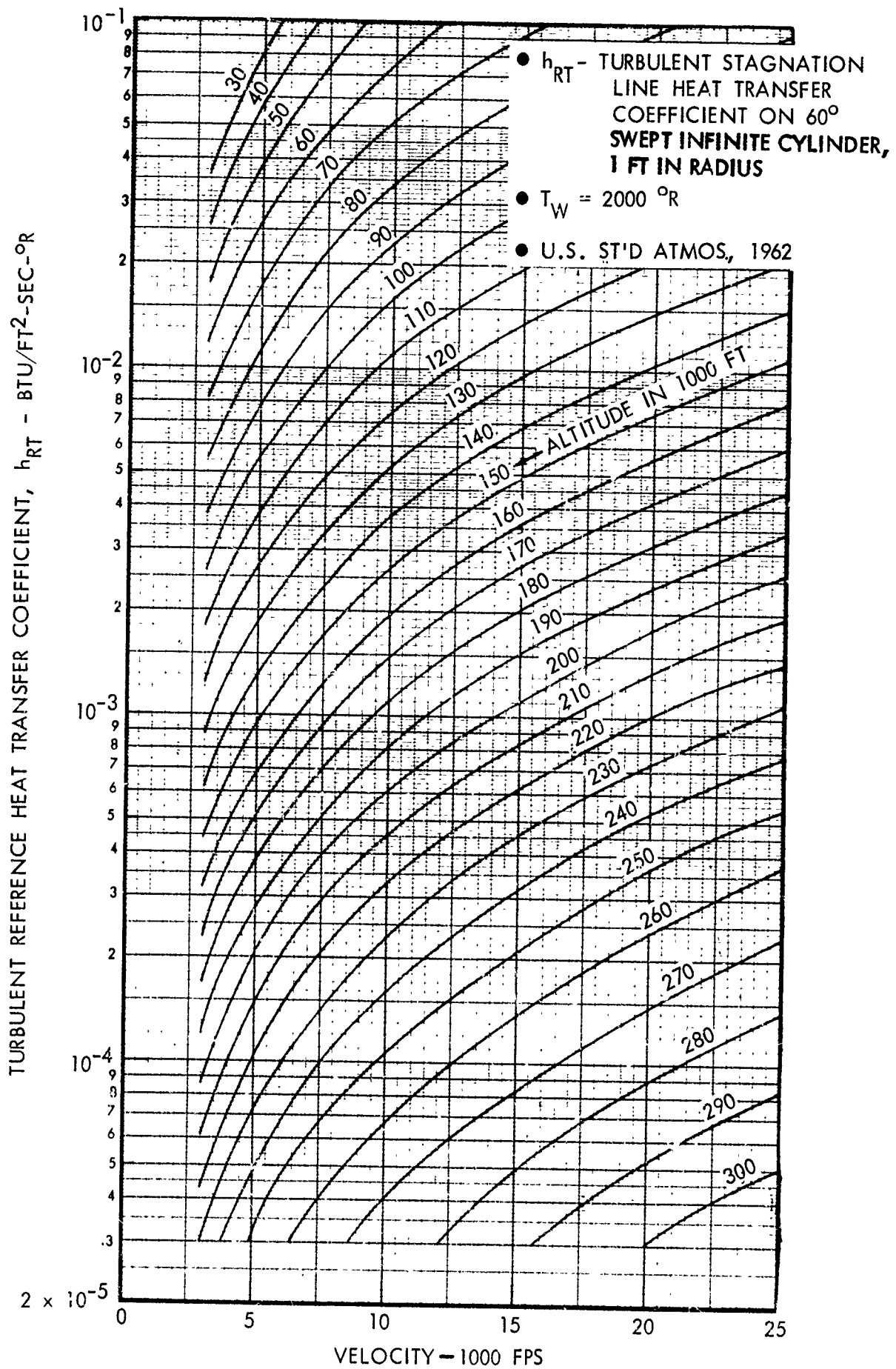


Figure 6-4: TURBULENT REFERENCE HEAT TRANSFER COEFFICIENT

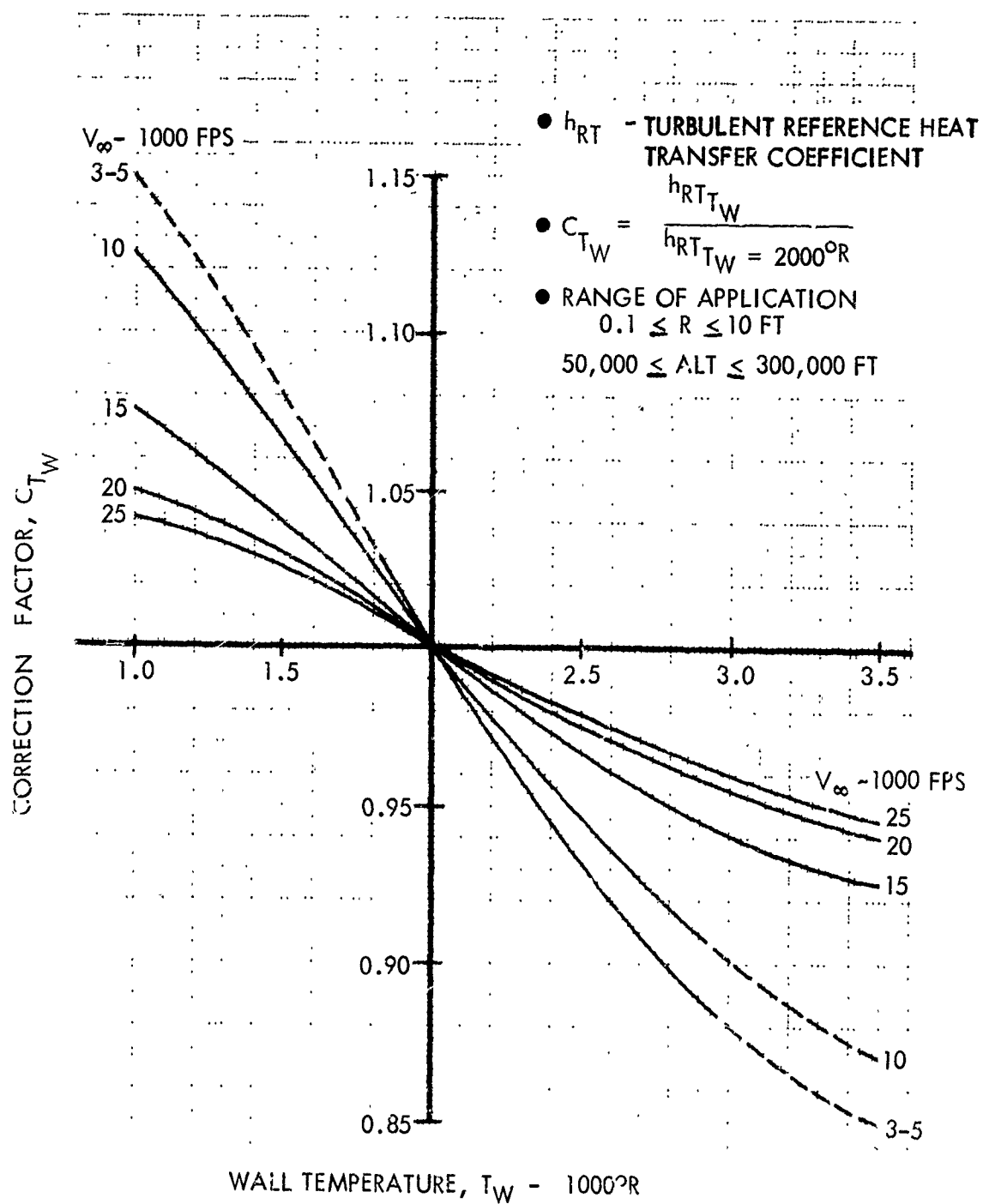


Figure 6-5: WALL TEMPERATURE CORRECTION FACTOR FOR TURBULENT REFERENCE HEAT TRANSFER COEFFICIENT

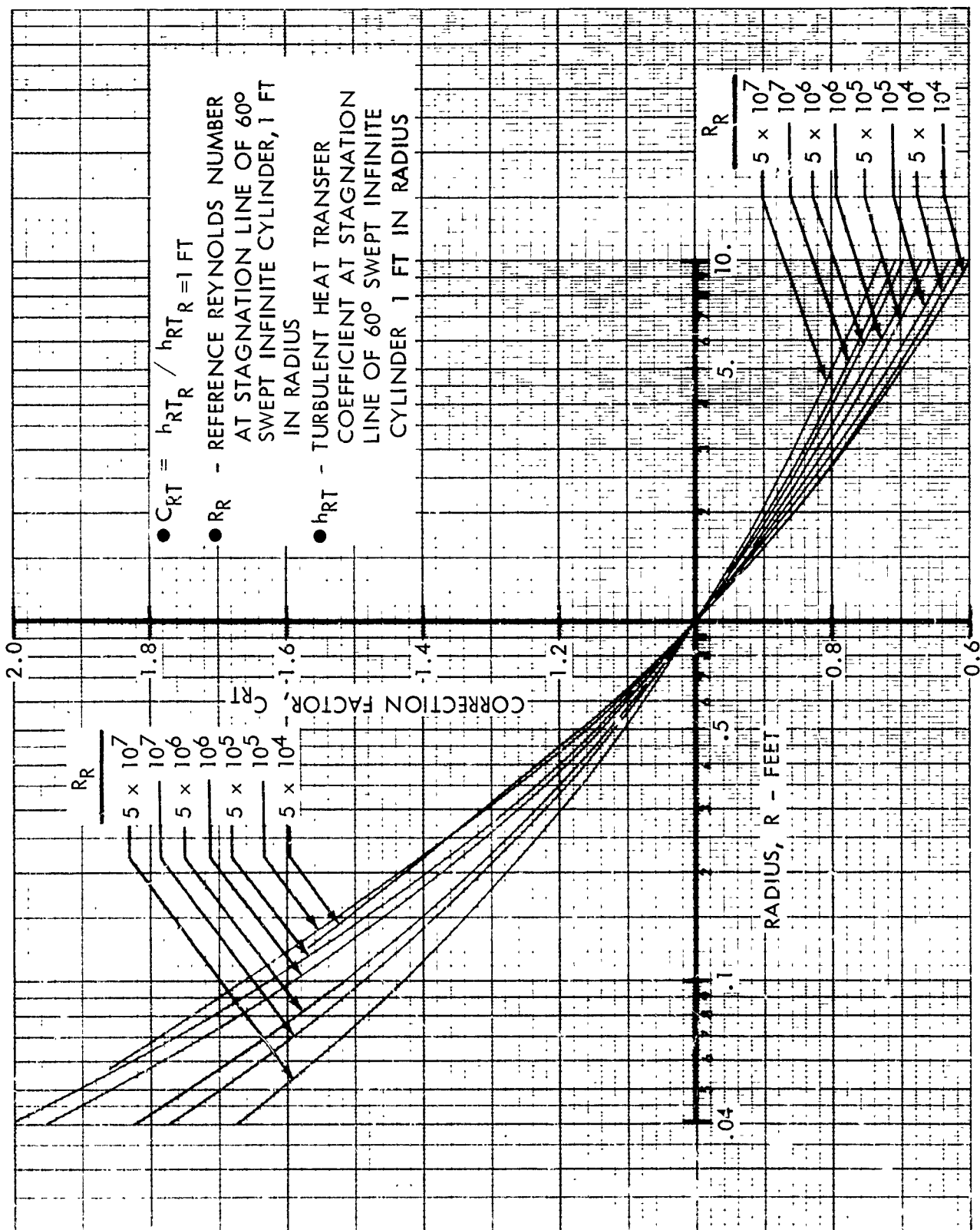


Figure 6-6: RADIUS CORRECTION FACTOR FOR TURBULENT REFERENCE HEAT TRANSFER COEFFICIENT

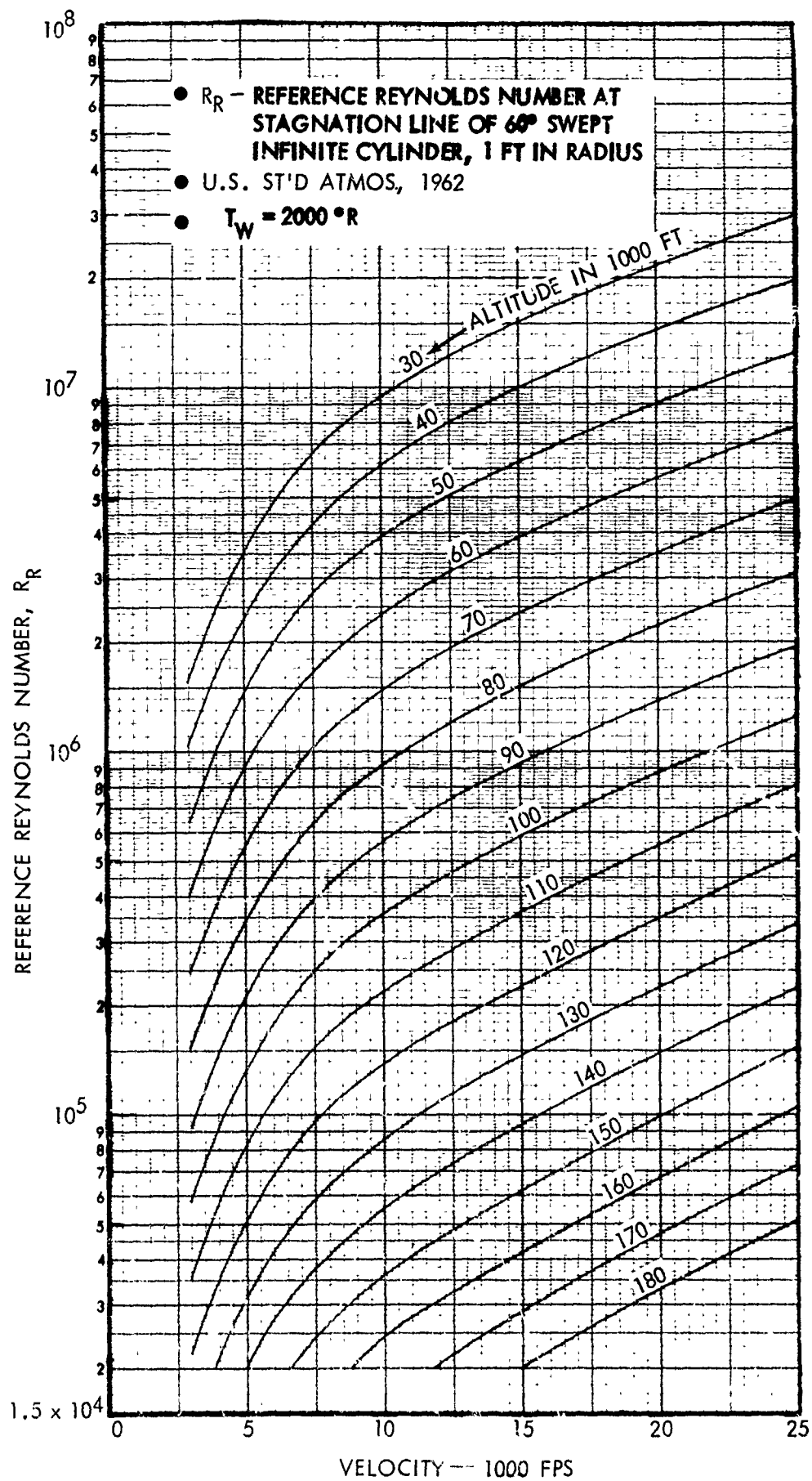


Figure 6-7: REFERENCE REYNOLDS NUMBER

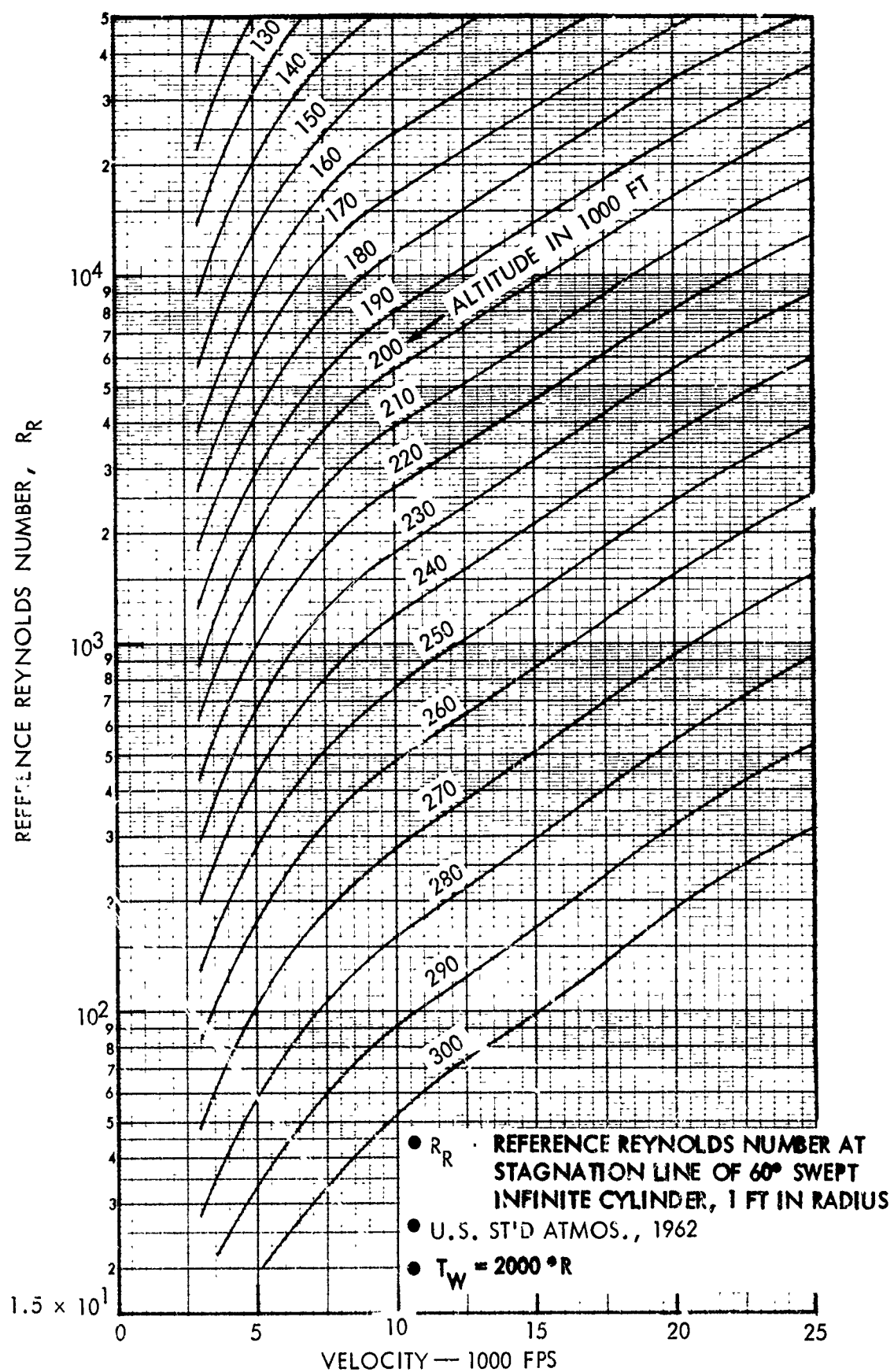


Figure 6-8: REFERENCE REYNOLDS NUMBER

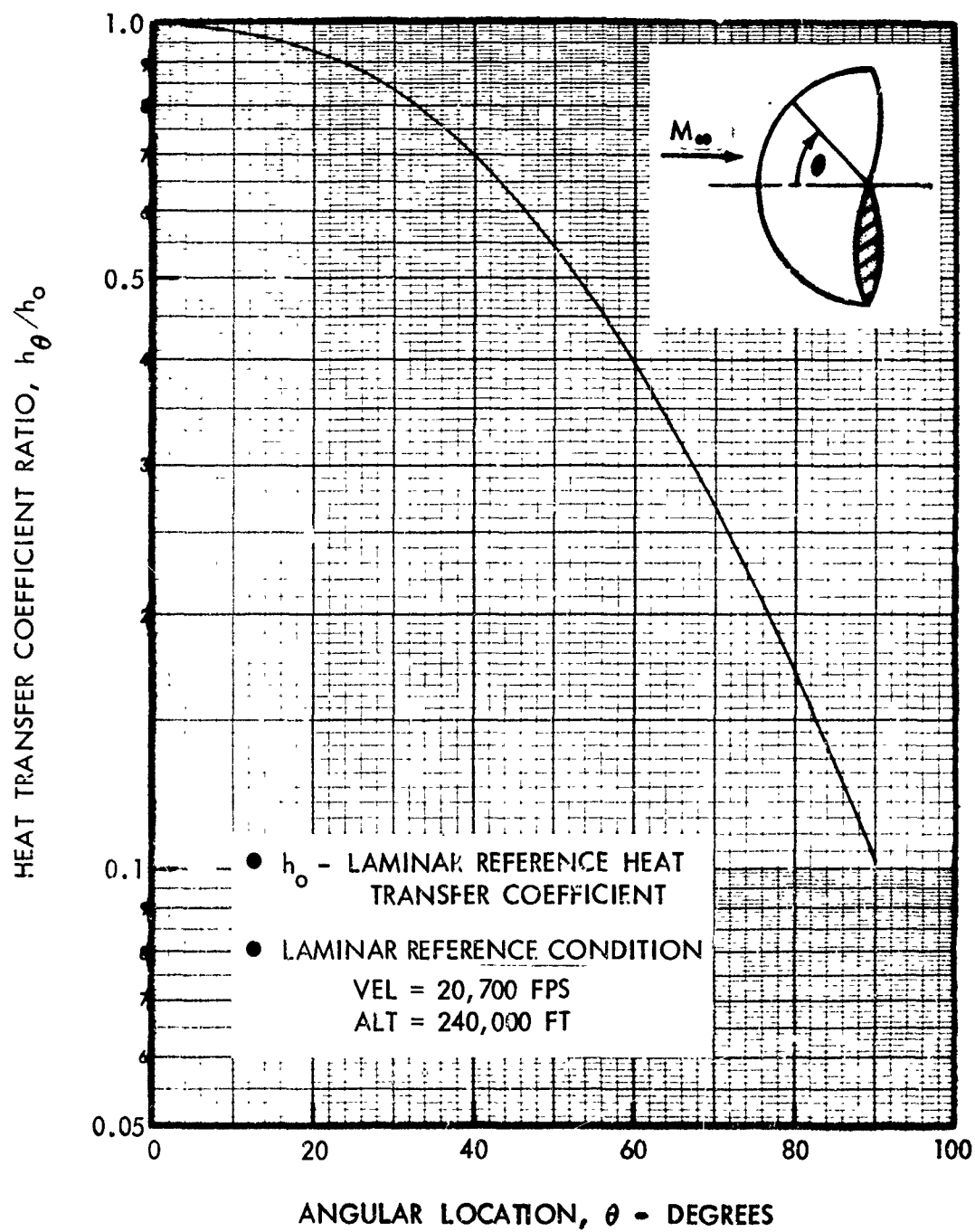


Figure 6-9: HEMISPHERE LAMINAR HEATING DISTRIBUTION

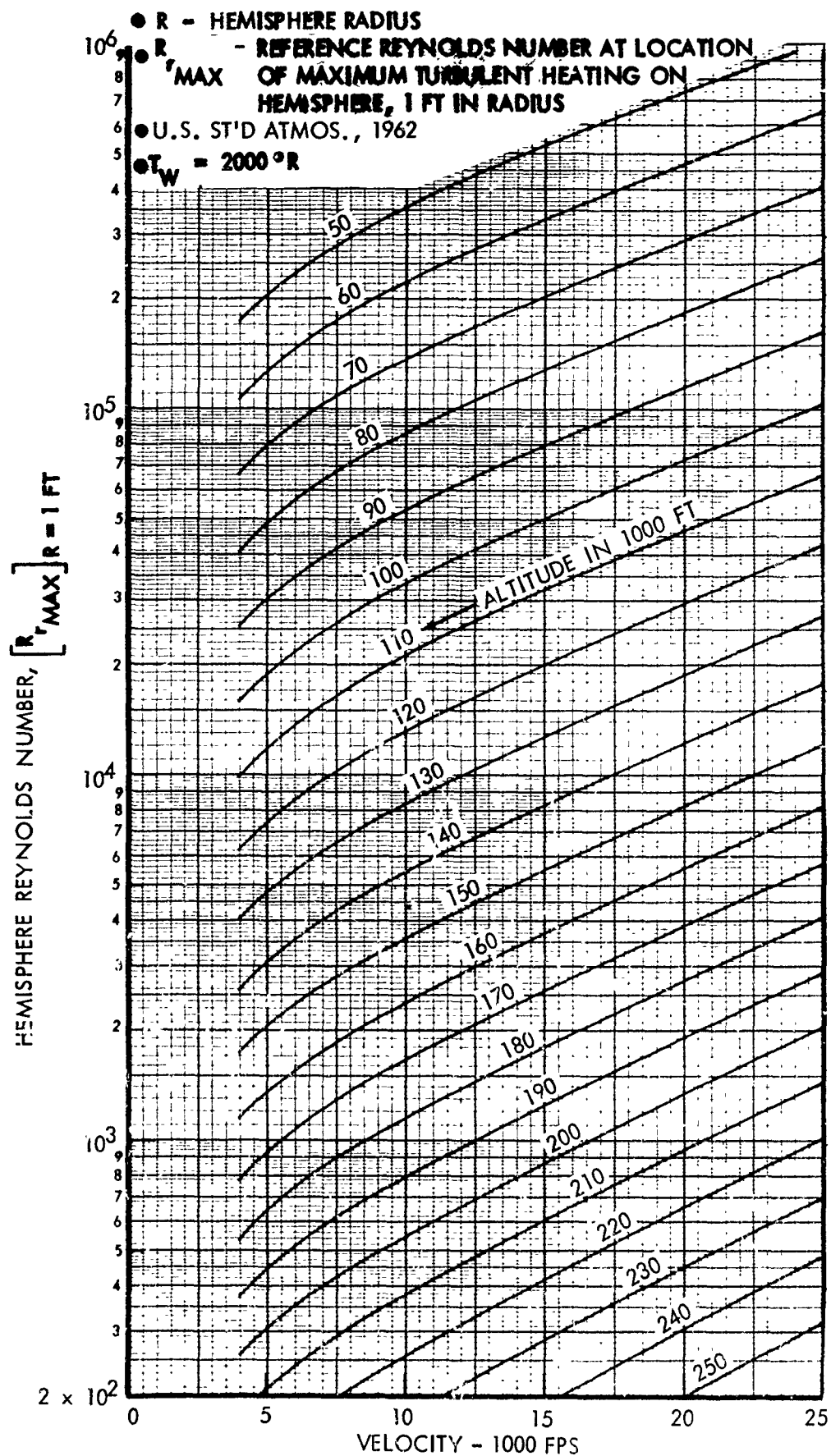


Figure 6-10: HEMISPHERE REFERENCE REYNOLDS NUMBER AT LOCATION OF MAXIMUM TURBULENT HEATING

- $R_{t\text{MAX}}$ - REFERENCE REYNOLDS NUMBER AT LOCATION OF MAXIMUM TURBULENT HEATING ON HEMISPHERE OF RADIUS R
- θ_{MAX} - ANGULAR LOCATION OF MAXIMUM TURBULENT HEATING MEASURED FROM STAGNATION POINT
- R - HEMISPHERE RADIUS

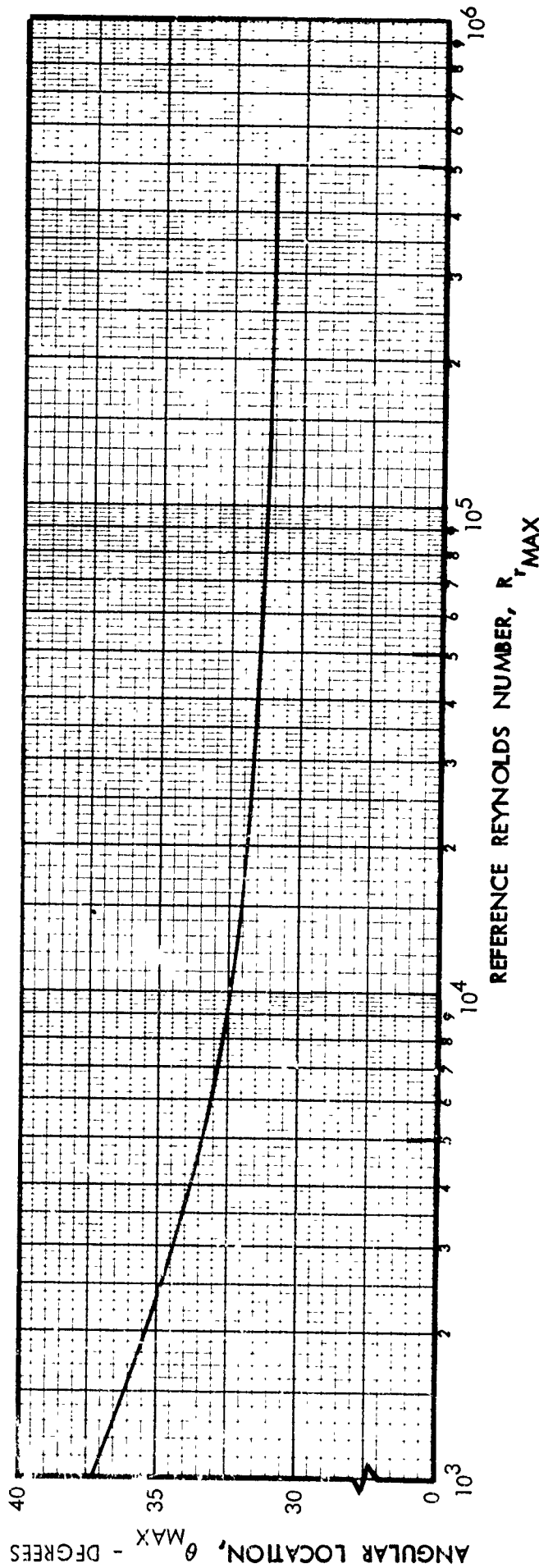
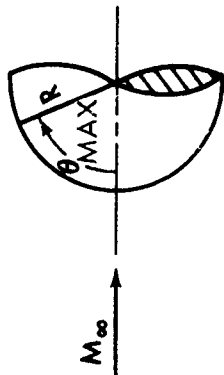


Figure 6-11: LOCATION OF MAXIMUM TURBULENT HEATING ON HEMISPHERE

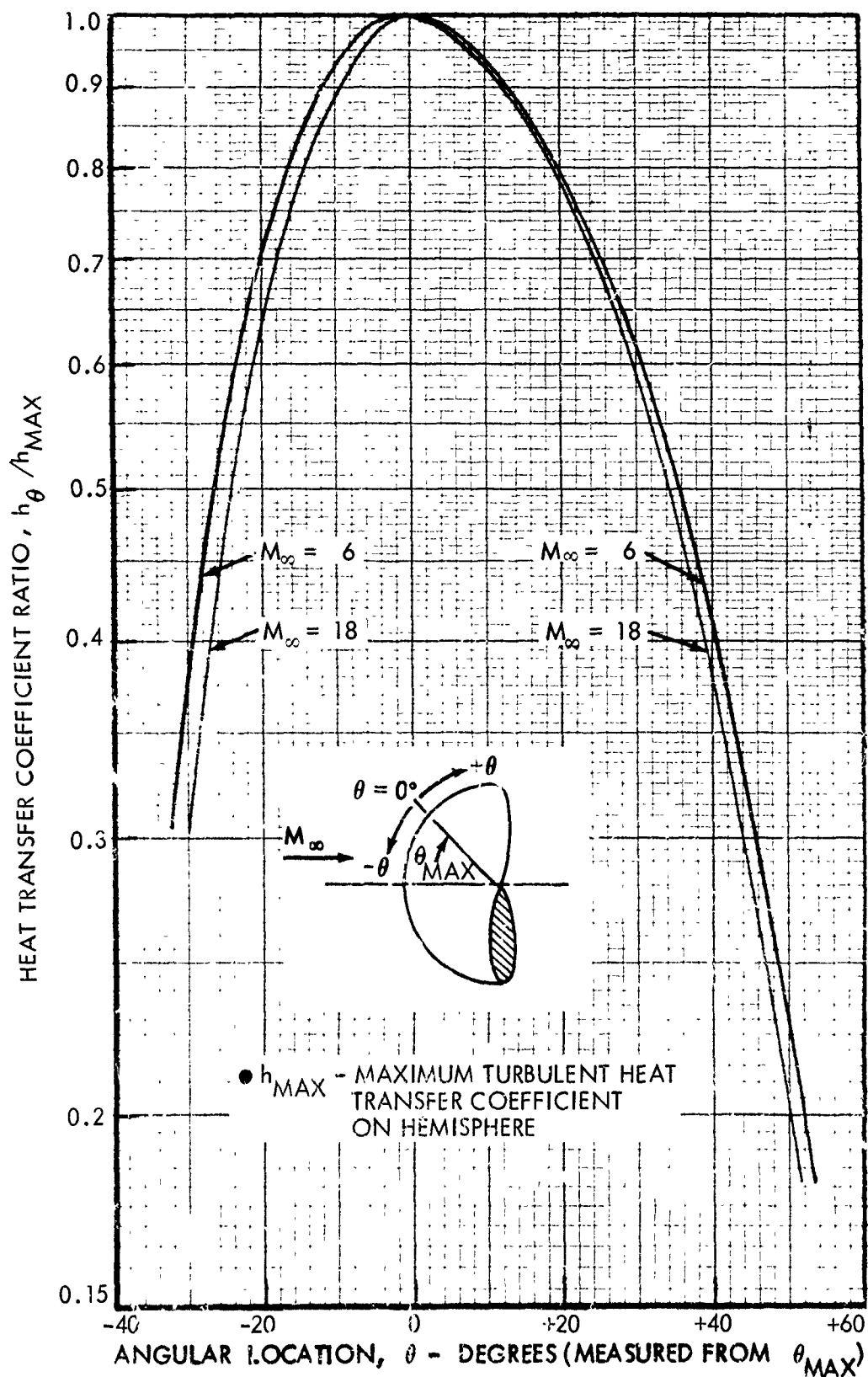


Figure 6-12: HEMISPHERE TURBULENT HEATING DISTRIBUTION

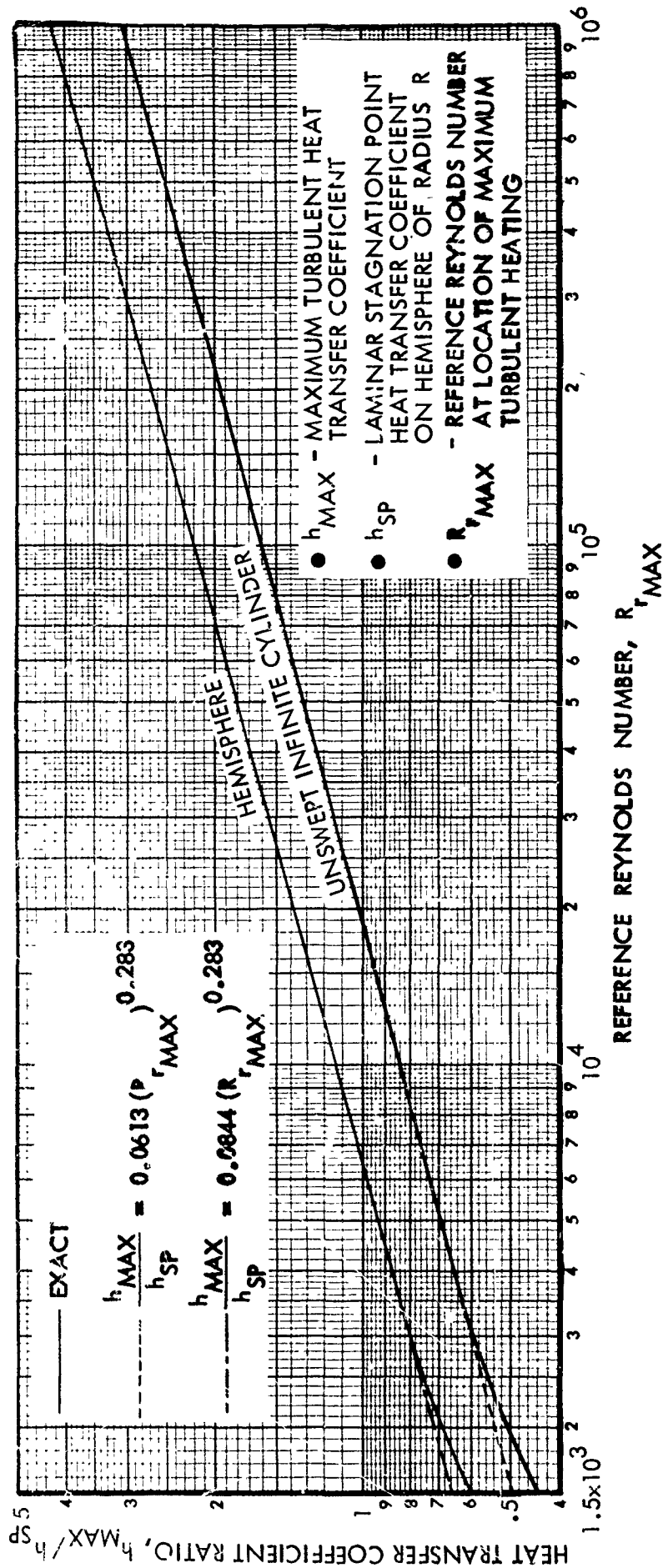


Figure 6-13: HEMISPHERE AND UNSWEPT INFINITE CYLINDER
MAXIMUM TURBULENT HEATING

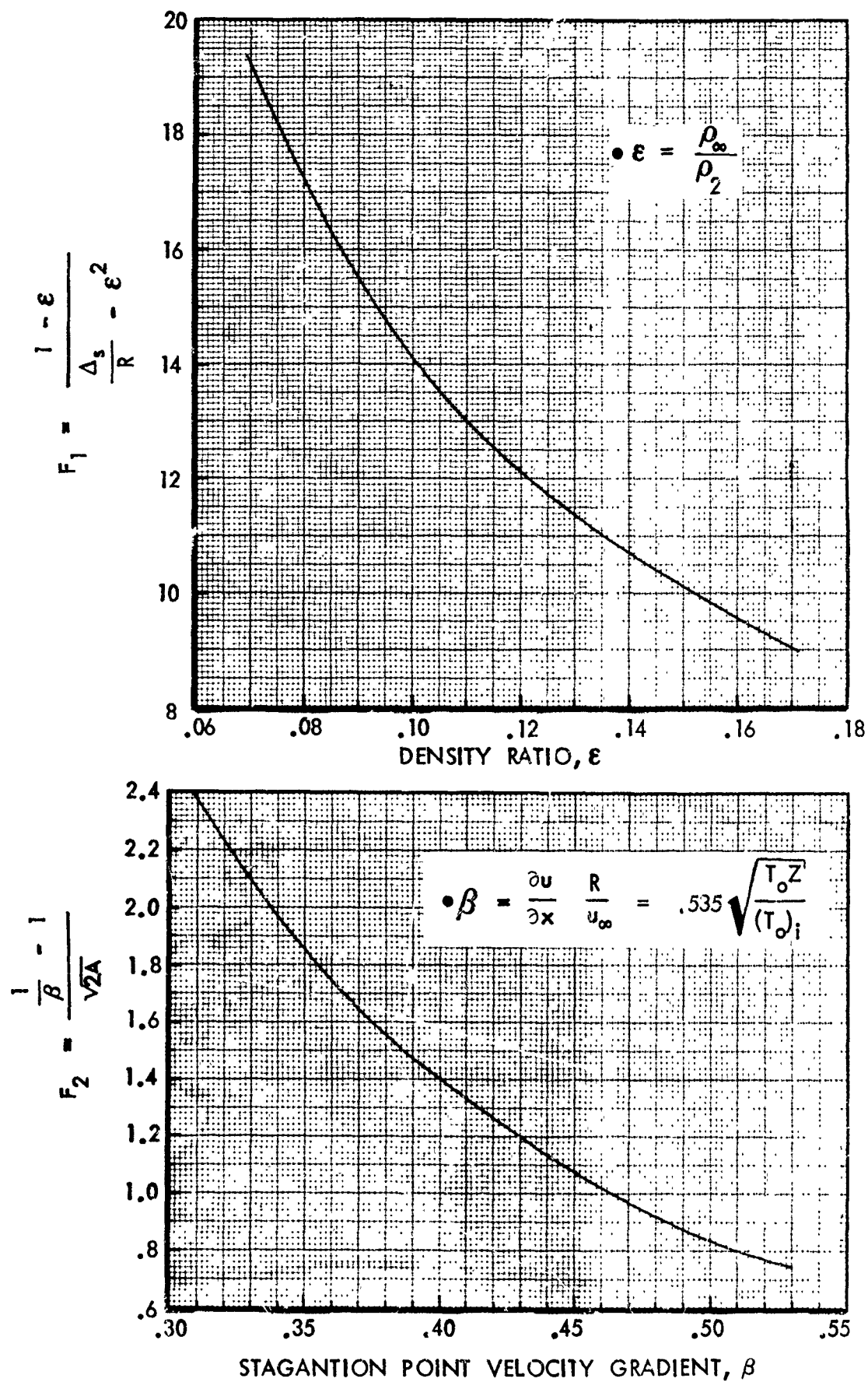


Figure 6-14: VORTICITY INTERACTION FUNCTIONS

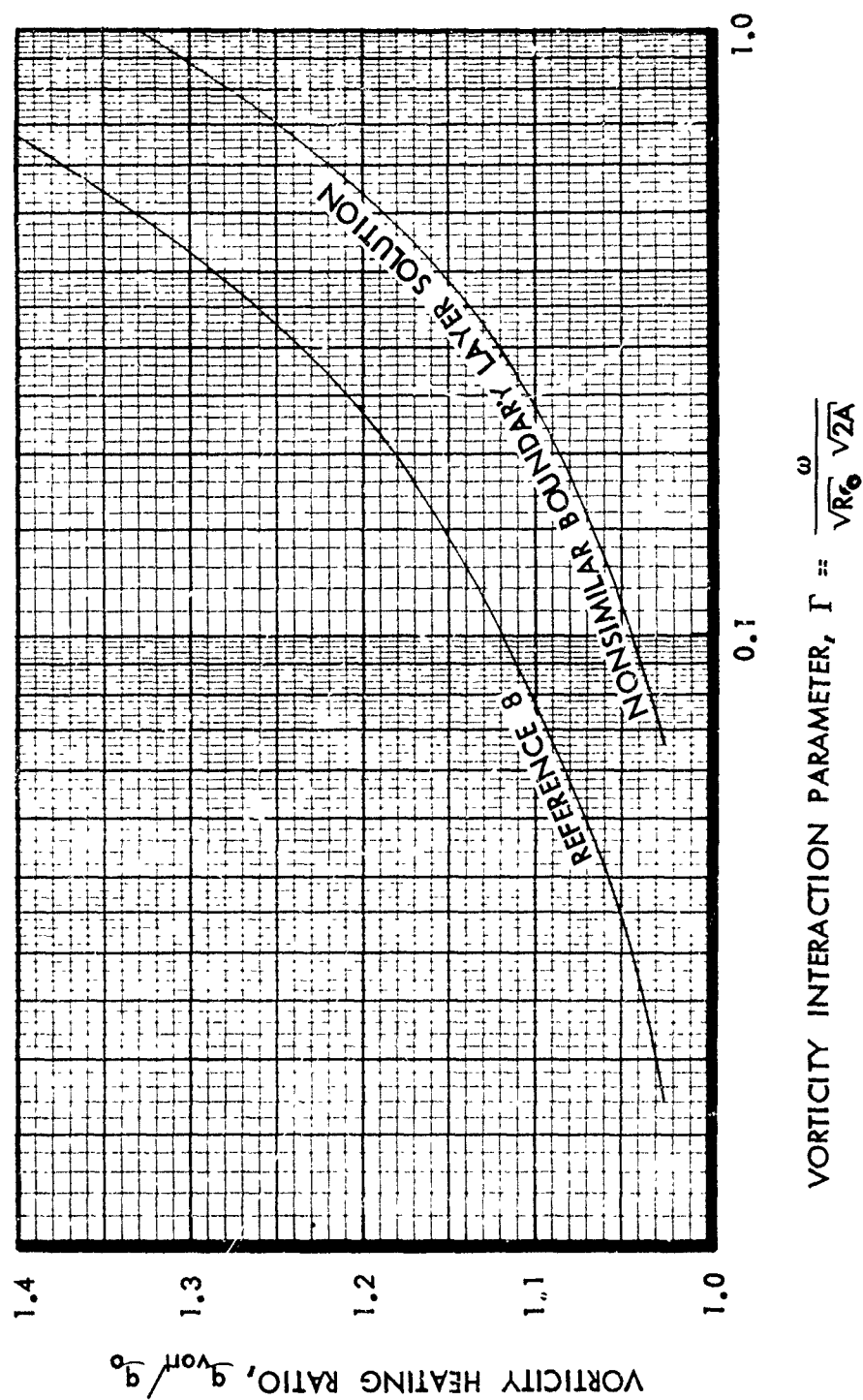


Figure 6-15: STAGNATION POINT VORTICITY INTERACTION EFFECT

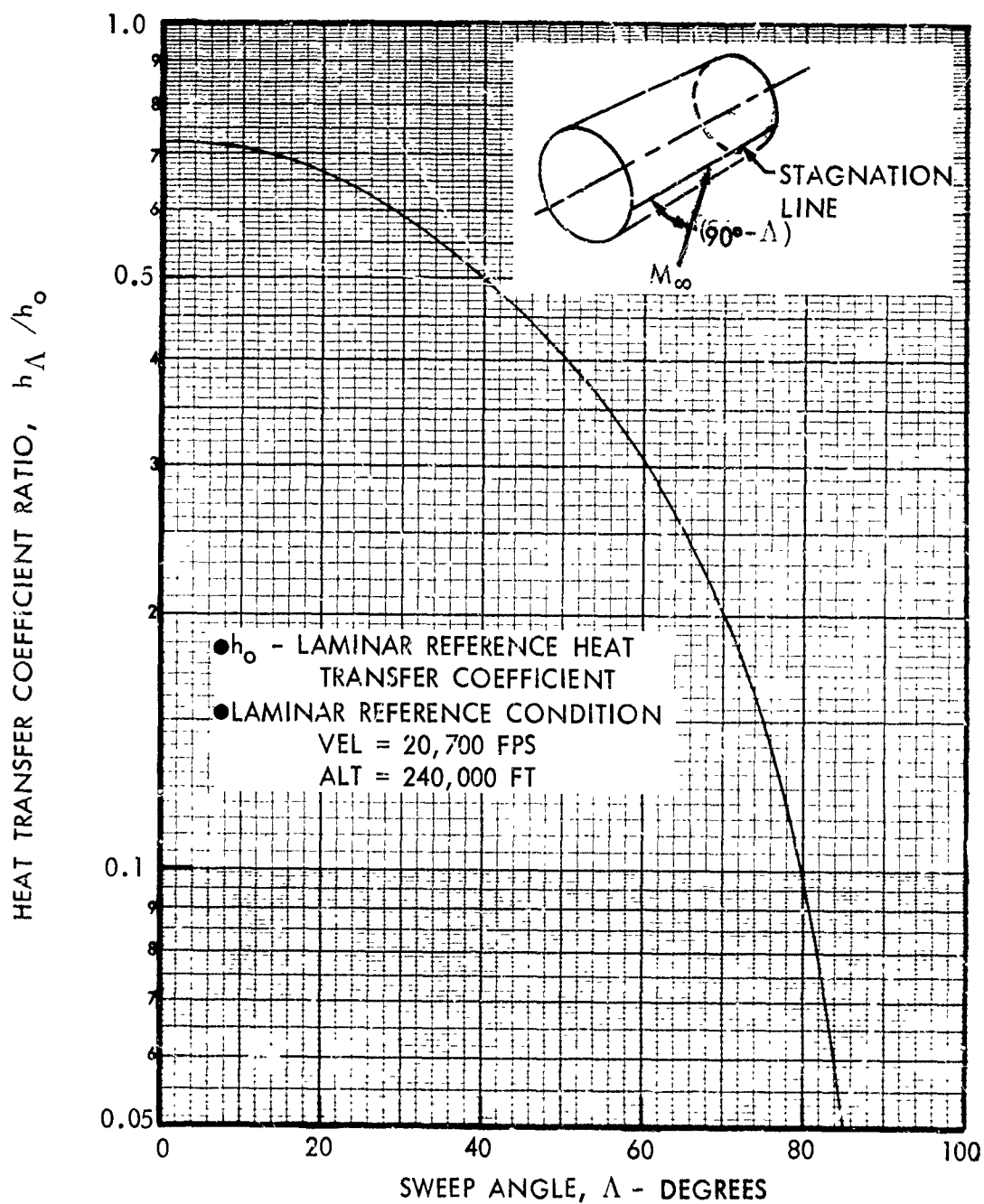


Figure 6-16: SWEPT INFINITE CYLINDER STAGNATION LINE LAMINAR HEATING

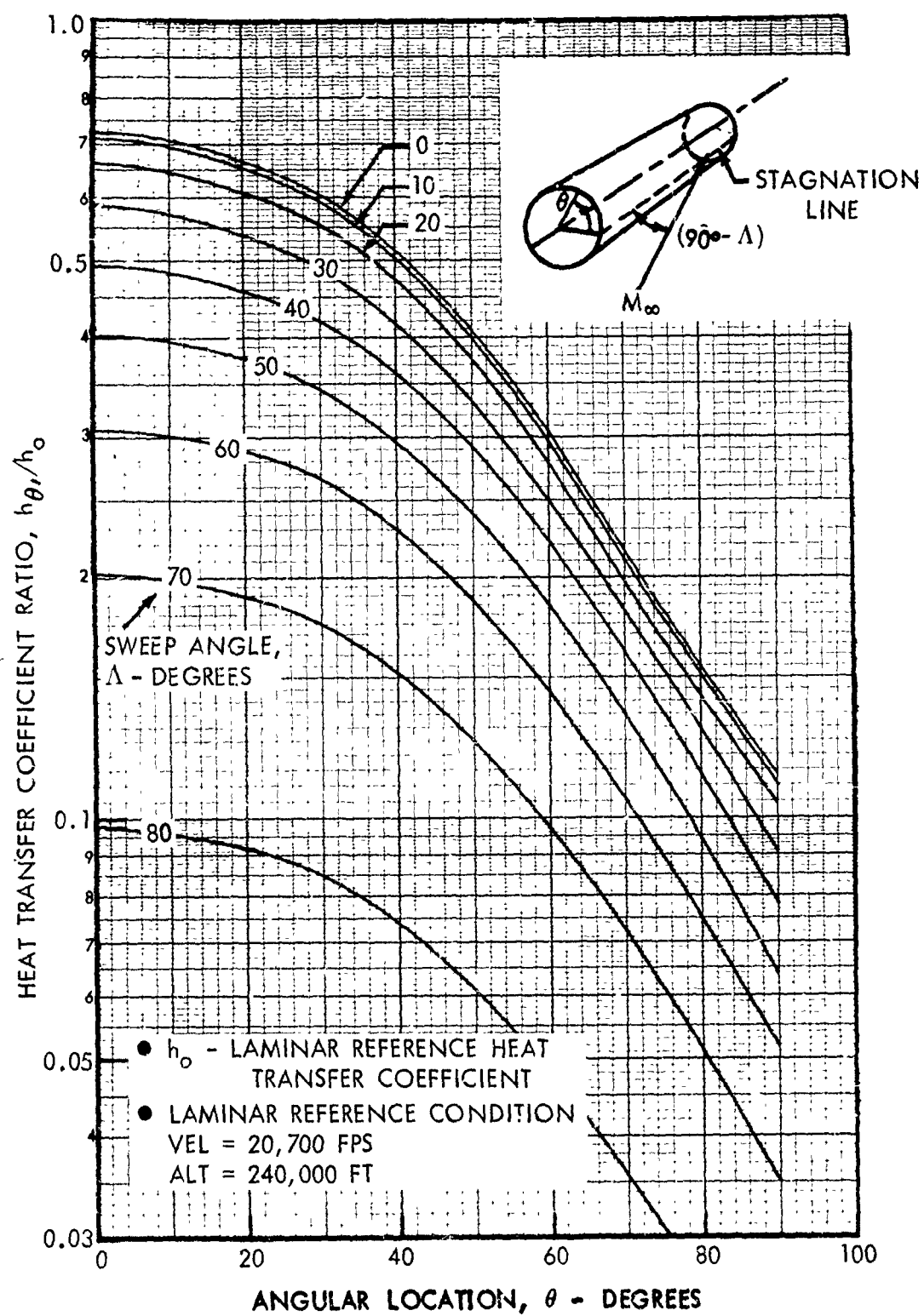


Figure 6-17: SWEPT INFINITE CYLINDER LAMINAR HEATING DISTRIBUTION

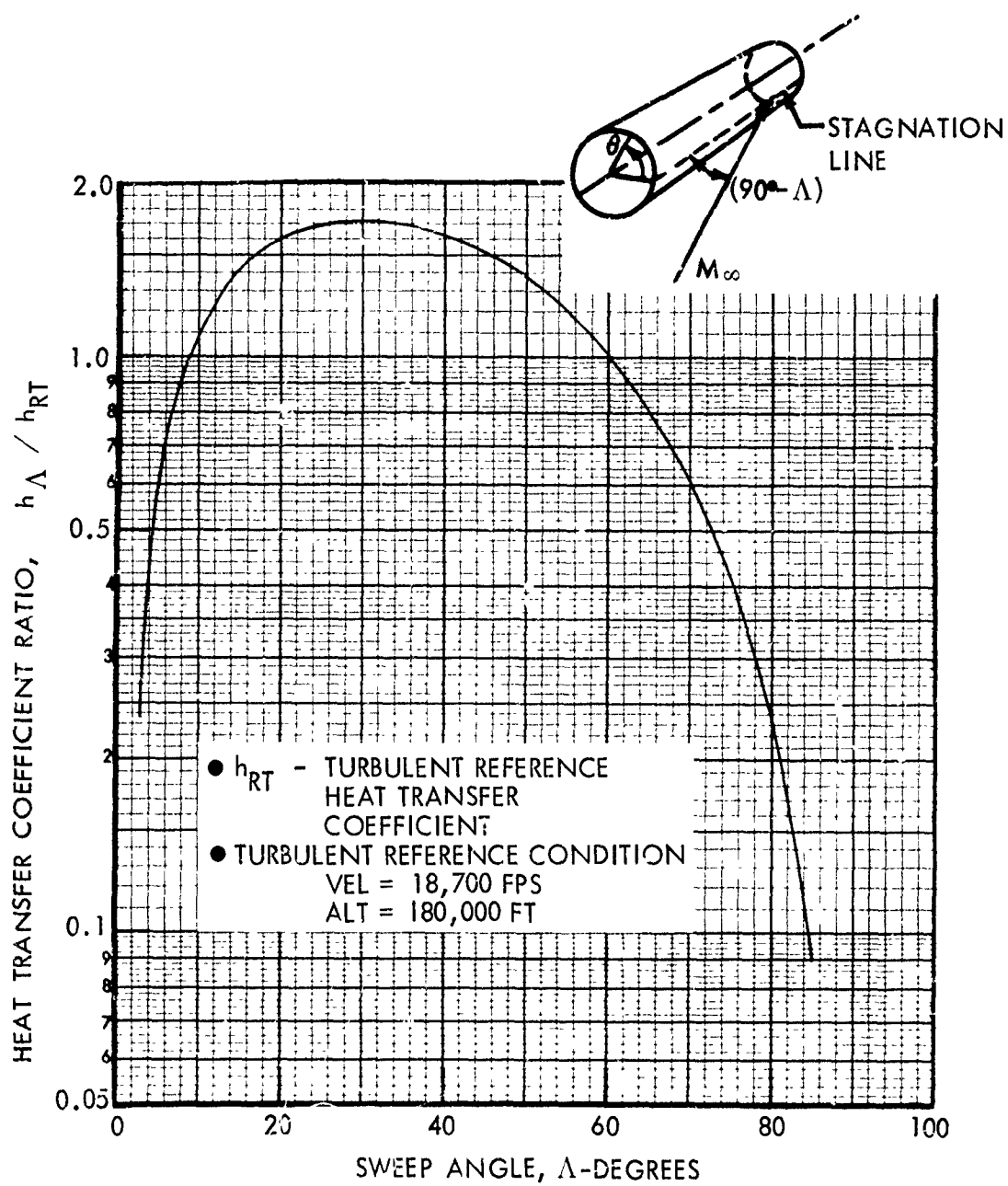


Figure 6-18: SWEPT INFINITE CYLINDER STAGNATION LINE
TURBULENT HEATING

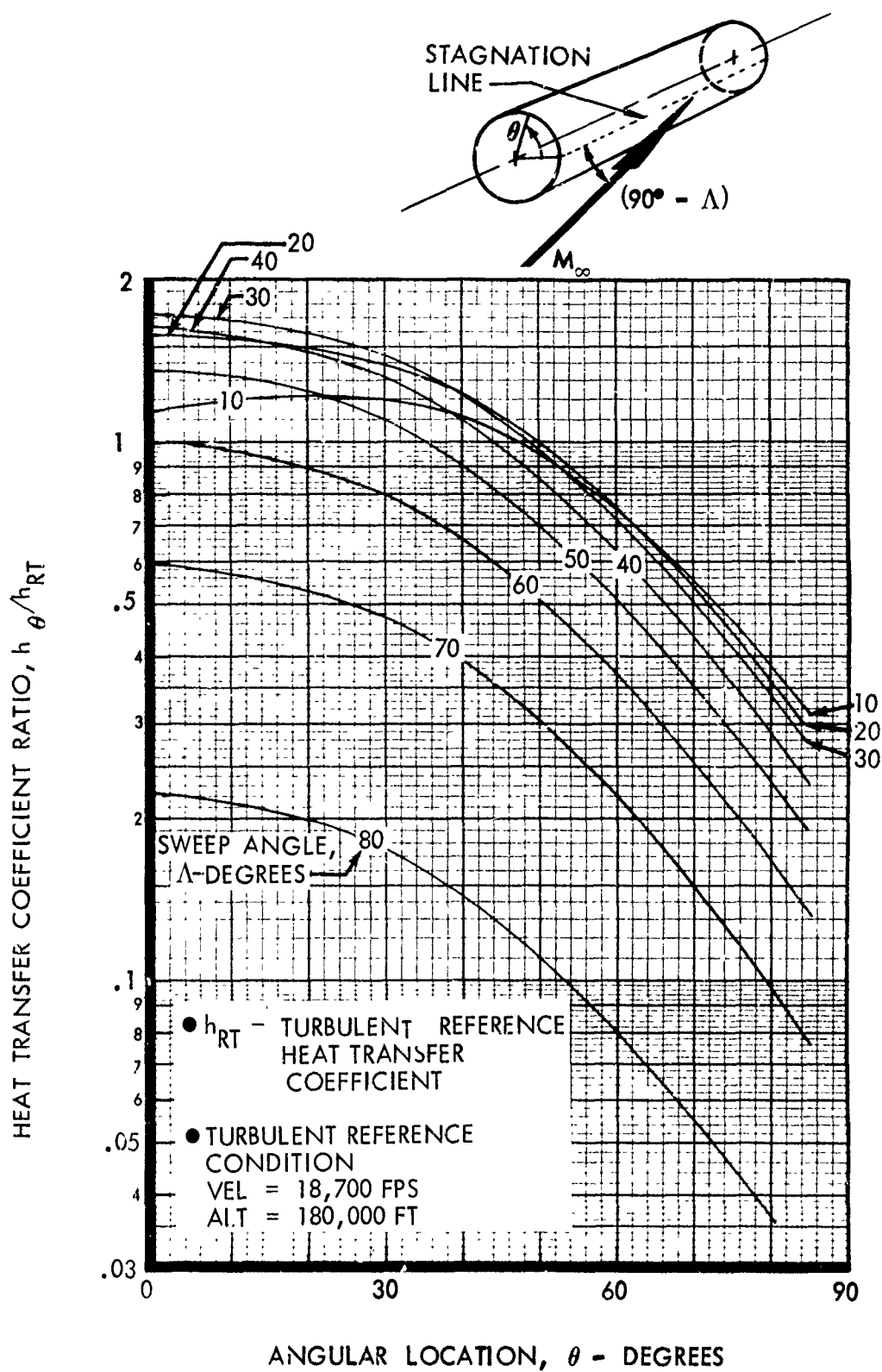


Figure 6-19: SWEEPED INFINITE CYLINDER TURBULENT HEATING DISTRIBUTION

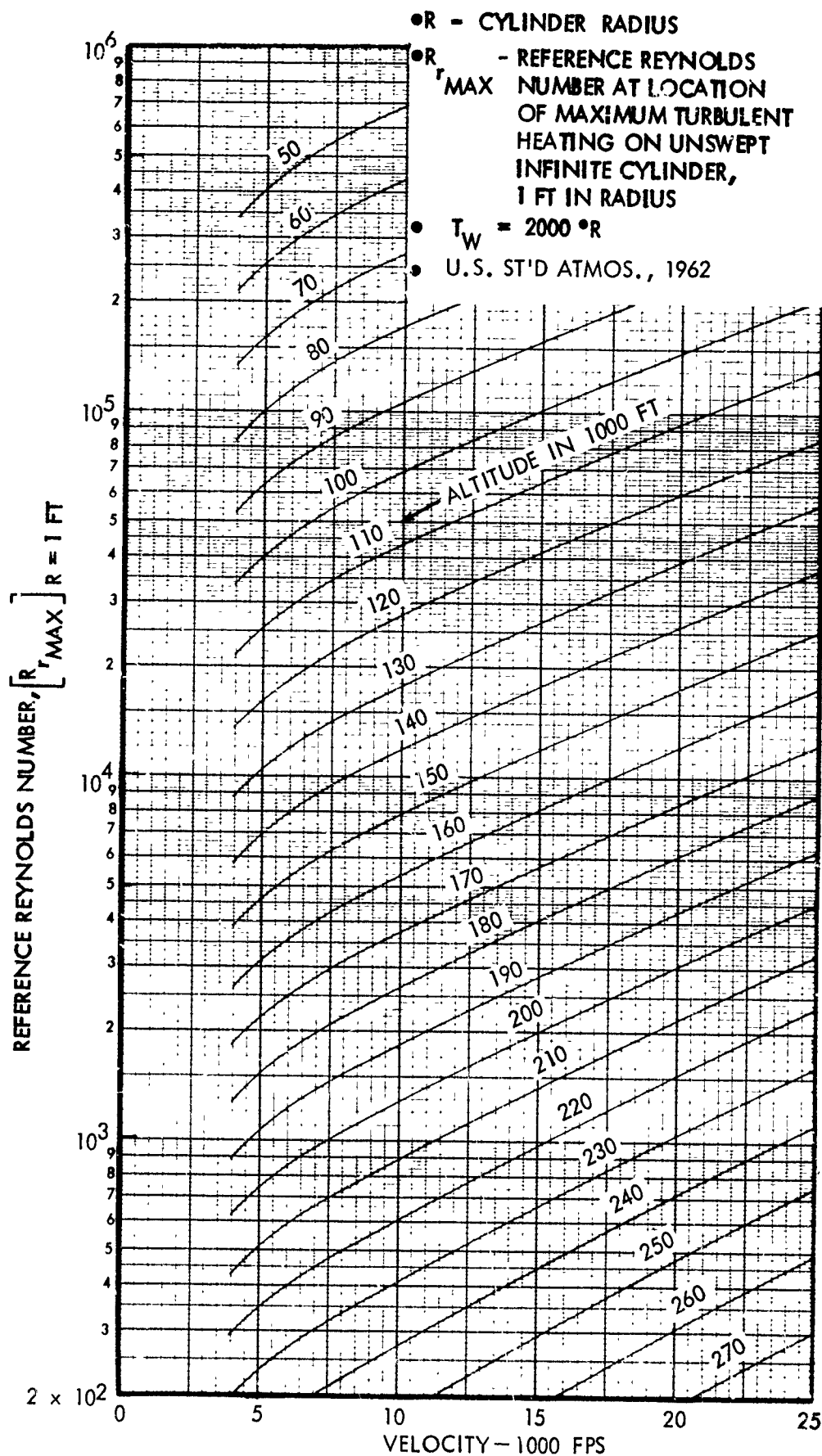


Figure 6-20: UNSWEPT INFINITE CYLINDER REFERENCE REYNOLDS NUMBER AT LOCATION OF MAXIMUM TURBULENT HEATING

- $R_{r,MAX}$ - REFERENCE REYNOLDS NUMBER AT LOCATION OF MAXIMUM TURBULENT HEATING ON UNSWEPT INFINITE CYLINDER OF RADIUS R
- θ_{MAX} - ANGULAR LOCATION OF MAXIMUM TURBULENT HEATING MEASURED FROM STAGNATION LINE
- R - CYLINDER RADIUS

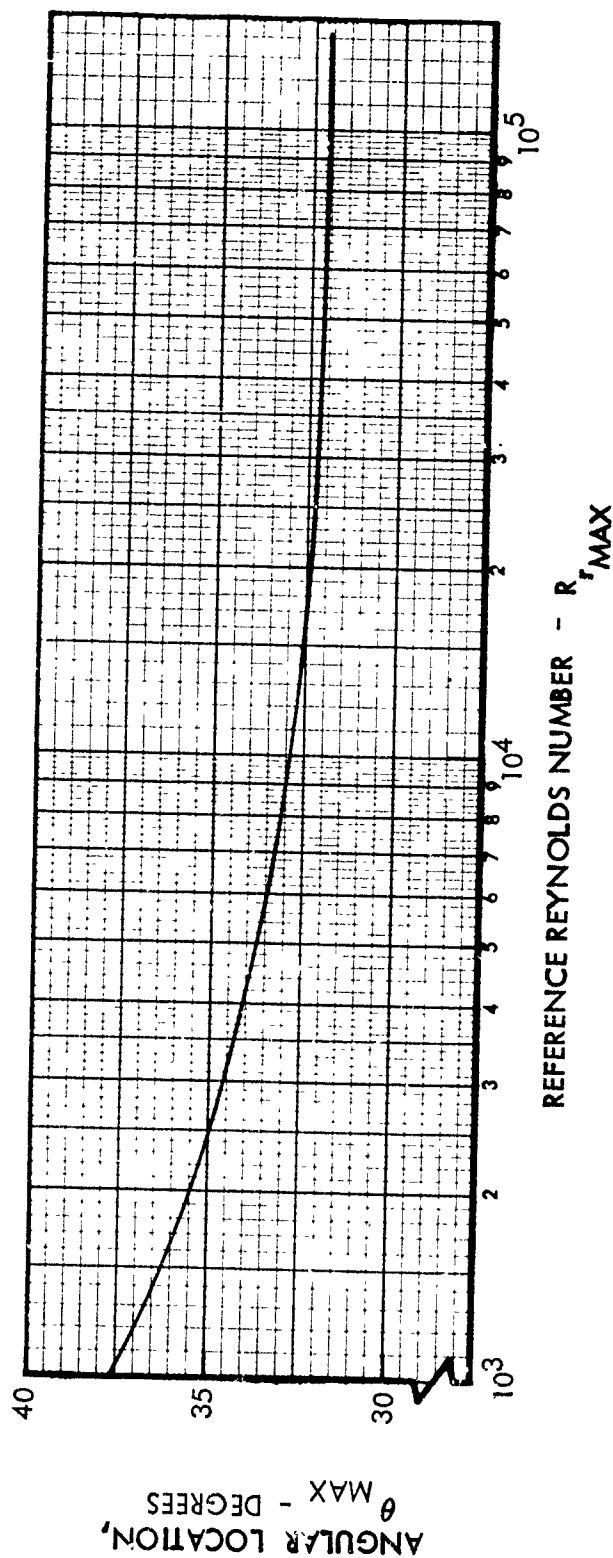
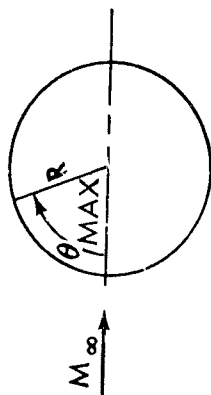


Figure 6-21: LOCATION OF MAXIMUM TURBULENT HEATING ON UNSWEPT INFINITE CYLINDER

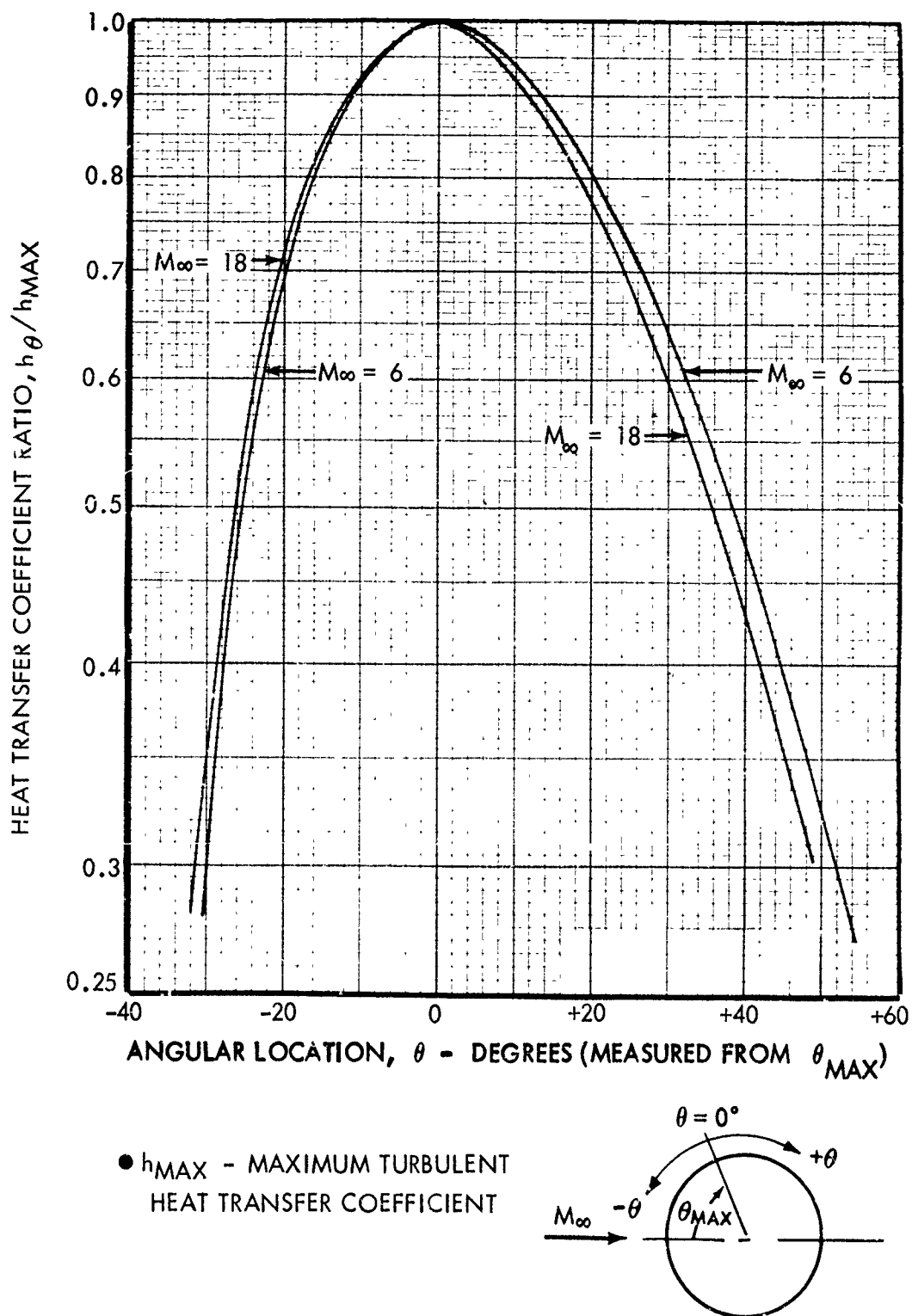


Figure 6-22: UNSWEPT INFINITE CYLINDER TURBULENT HEATING DISTRIBUTION

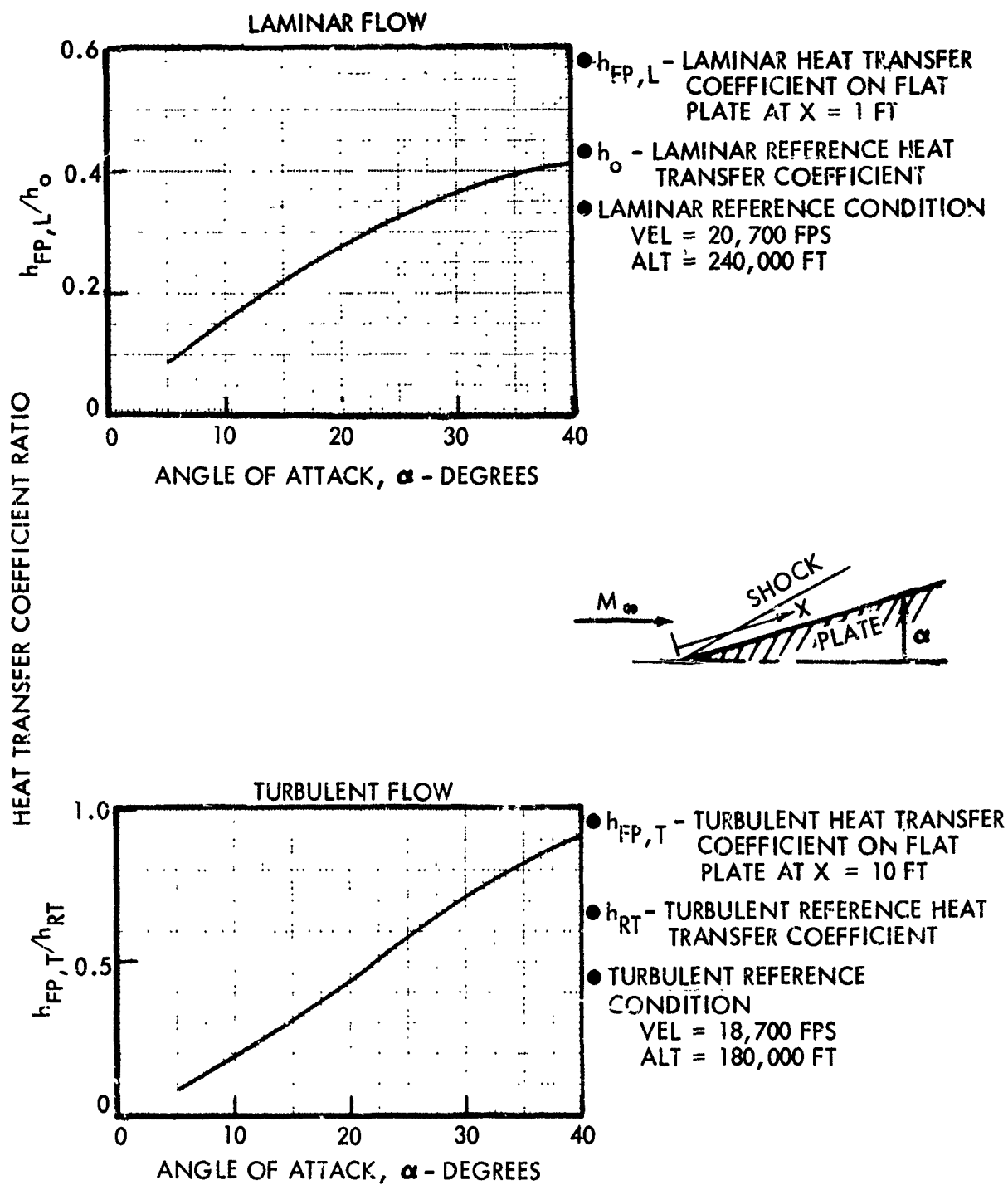


Figure 6-23: SHARP FLAT PLATE HEATING

$$\bullet C_{TW} = \frac{h_{TW}}{h_{TW} = 2000^{\circ}\text{R}}$$

- LAMINAR REFERENCE CONDITION
VEL = 20,700 FPS
ALT = 240,000 FT

- TURBULENT REFERENCE CONDITION
VEL = 18,700 FPS
ALT = 180,000 FT

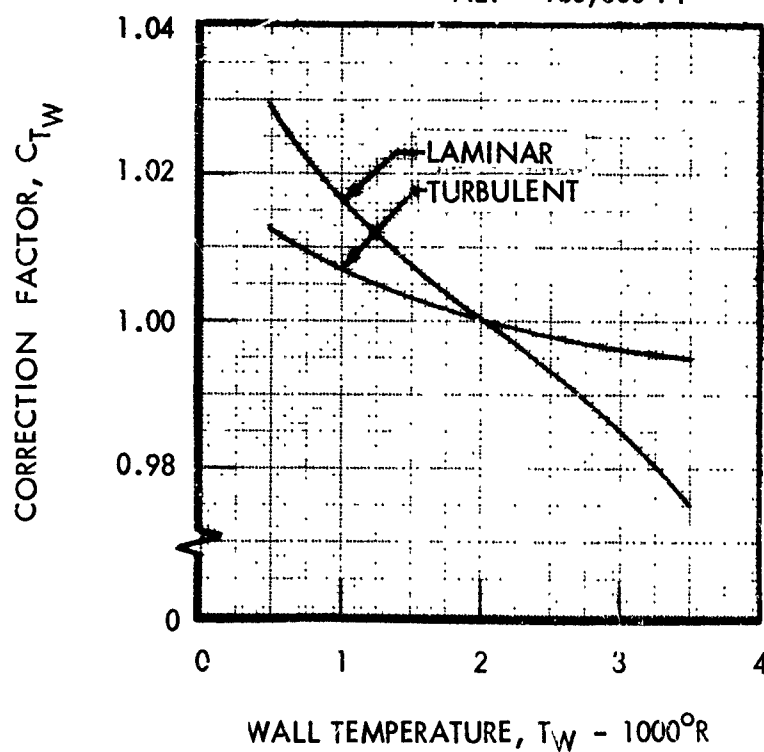


Figure 6-24: WALL TEMPERATURE CORRECTION FACTORS FOR SHARP FLAT PLATES, UNYAWED SHARP CONES, AND SHARP DELTA WINGS

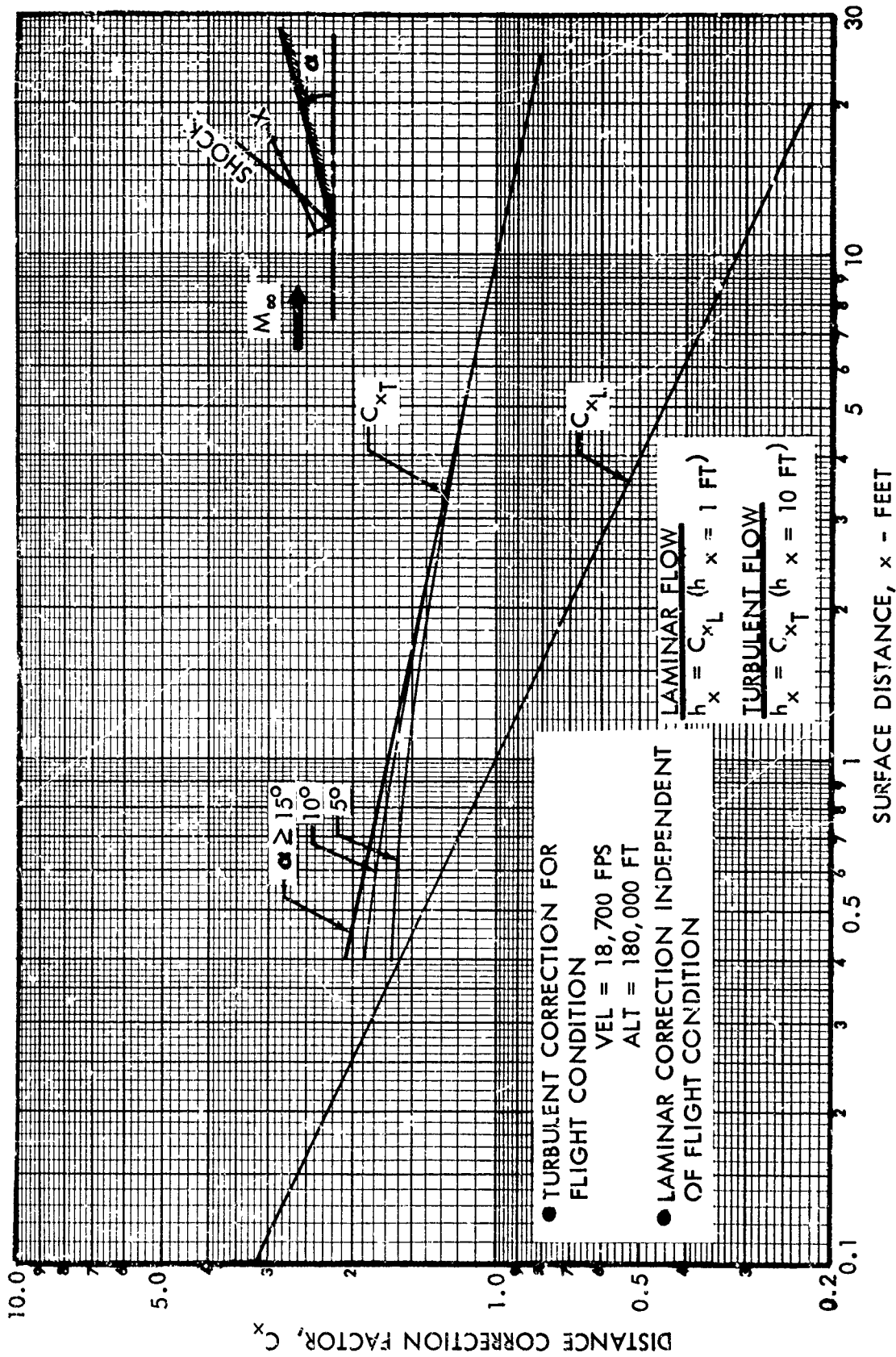


Figure 6-25: DISTANCE CORRECTION FACTORS FOR SHARP FLAT PLATES, UNYAWED SHARP CONES, AND SHARP DELTA WINGS

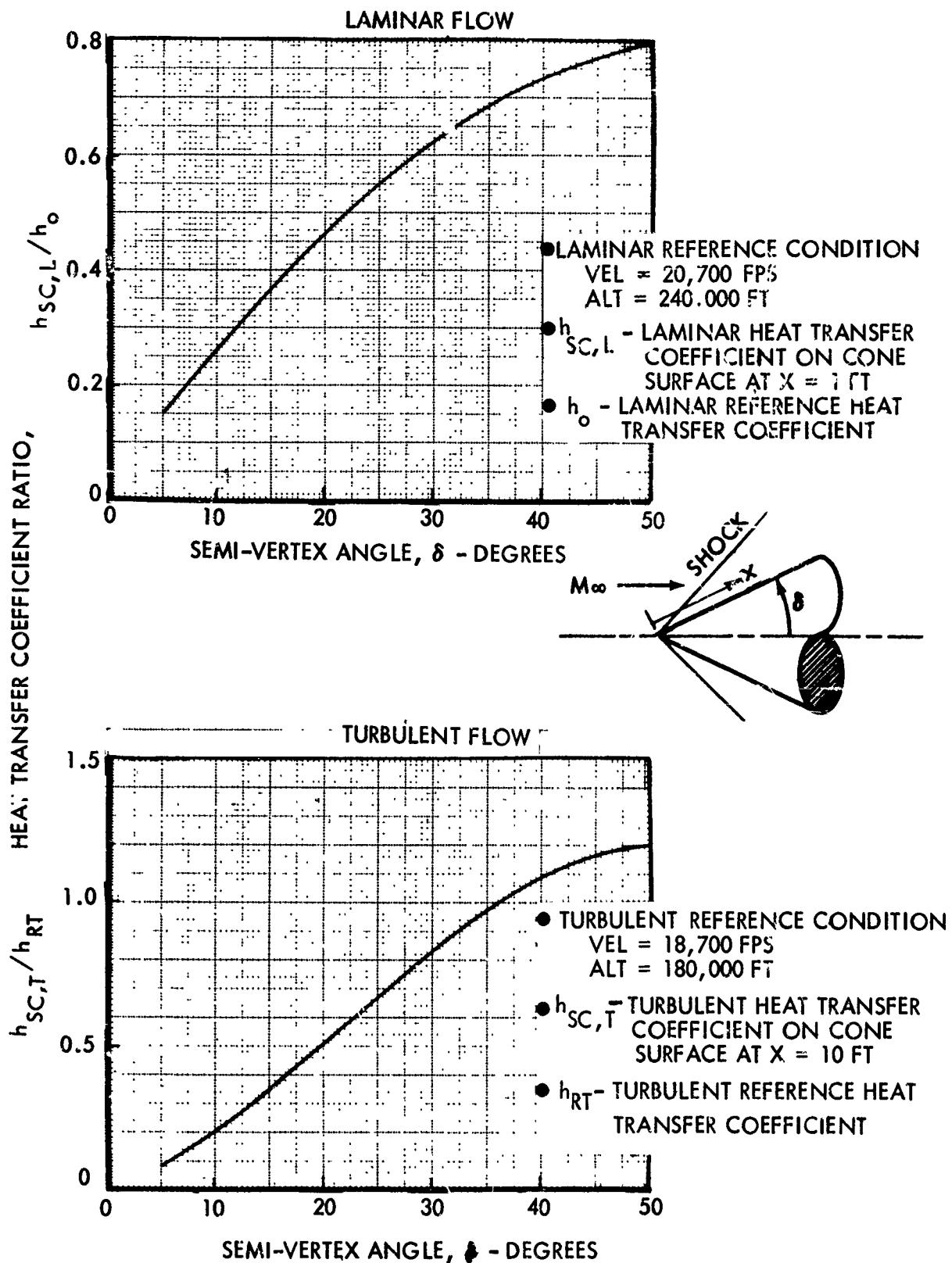


Figure 6-26: UNYAWED SHARP CONE HEATING

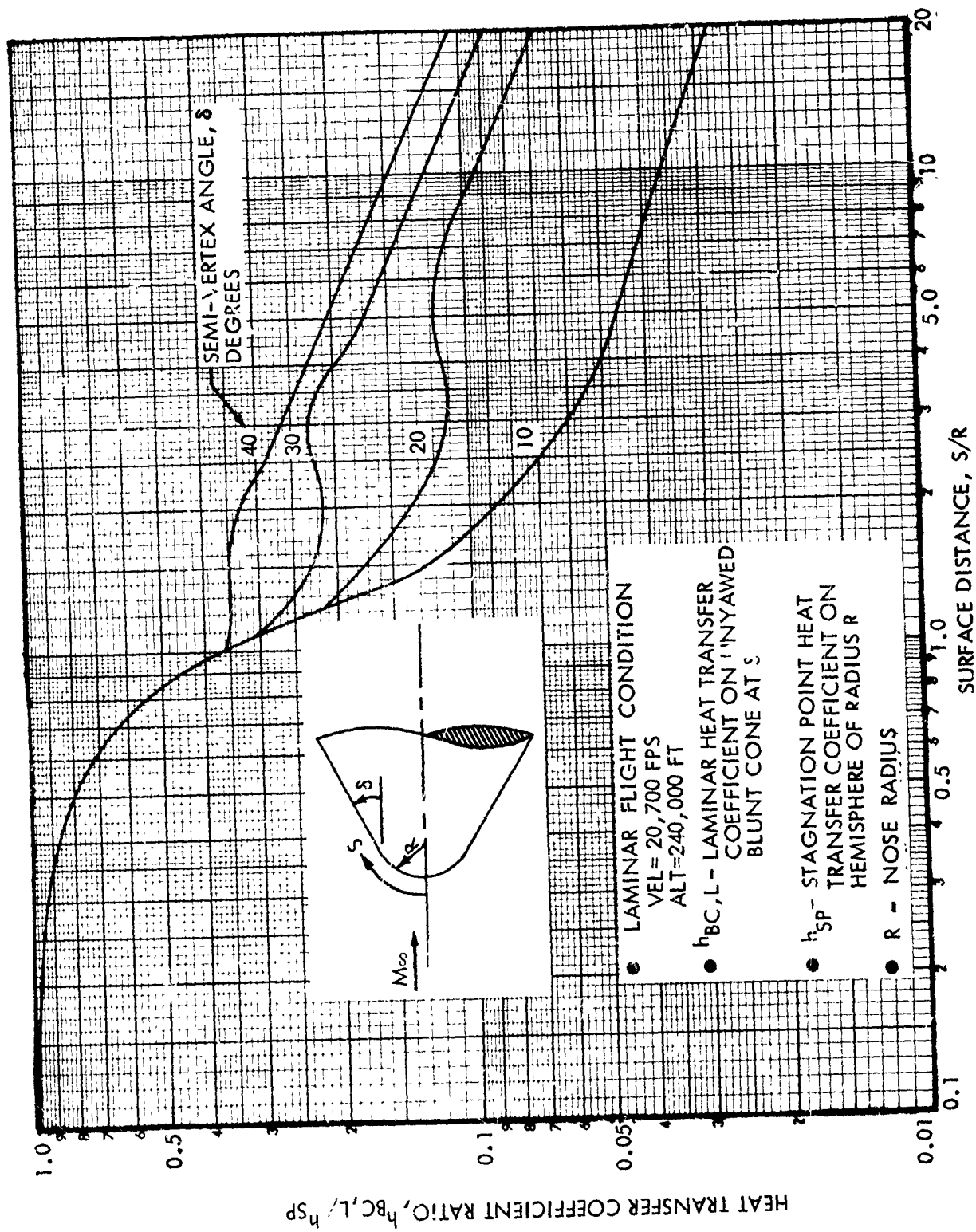


Figure 6-27: UNYAWED BLUNT CONE LAMINAR HEATING

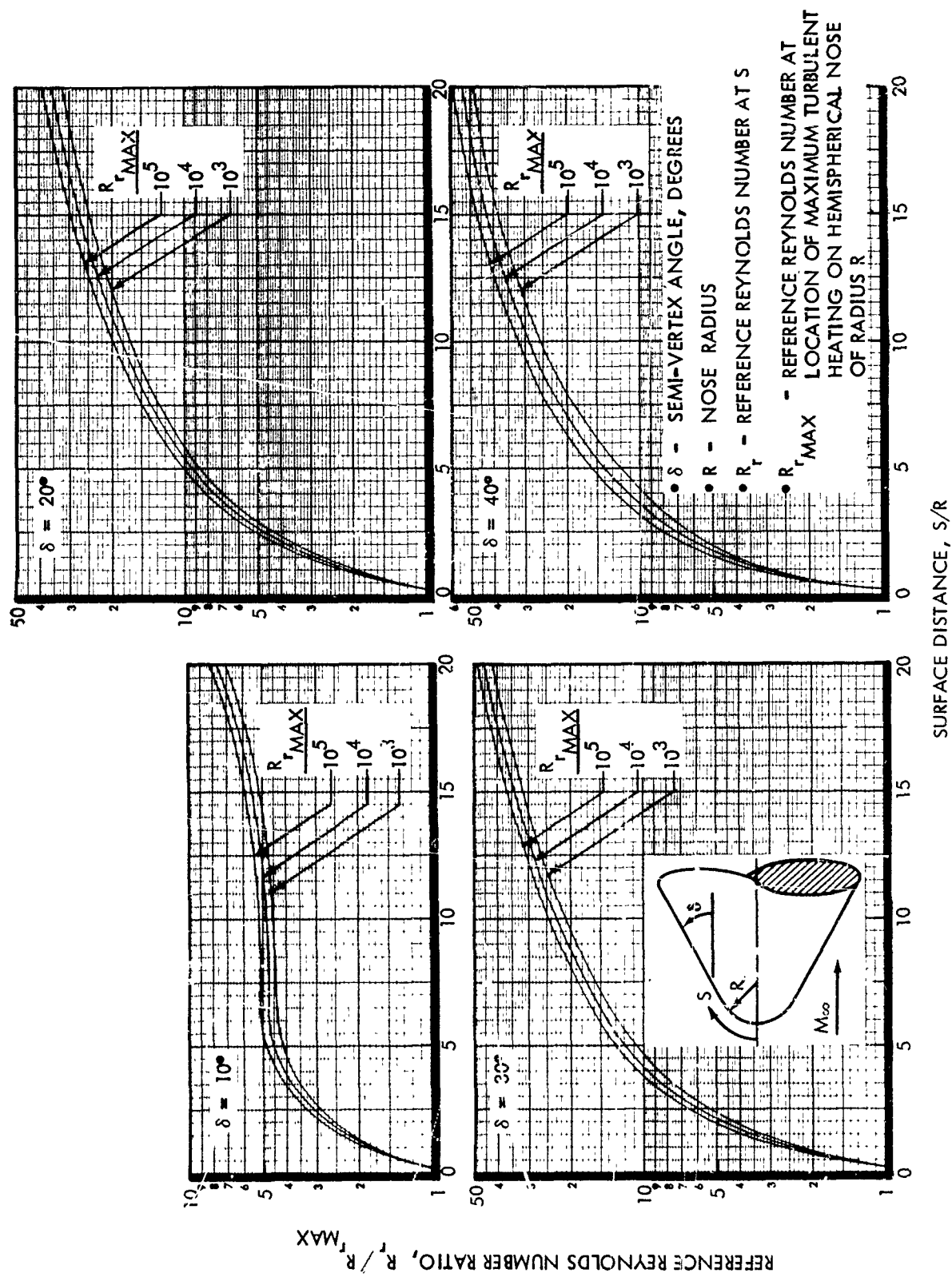


Figure 6-28: UNYAWED BLUNT CONE REFERENCE REYNOLDS NUMBER

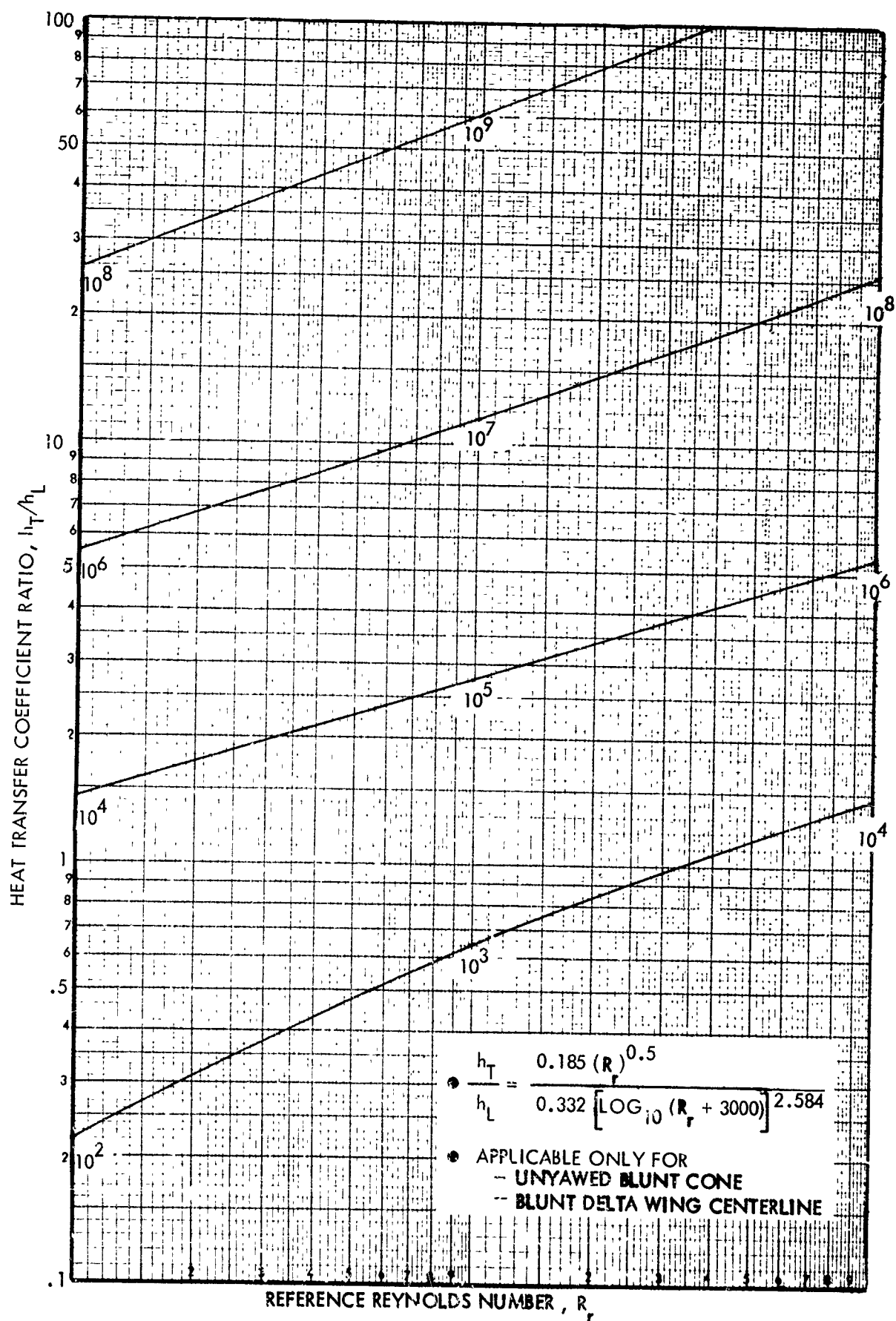


Figure 6-29: UNYAWED BLUNT CONE AND BLUNT DELTA WING
LAMINAR TO TURBULENT HEAT TRANSFER CORRELATION

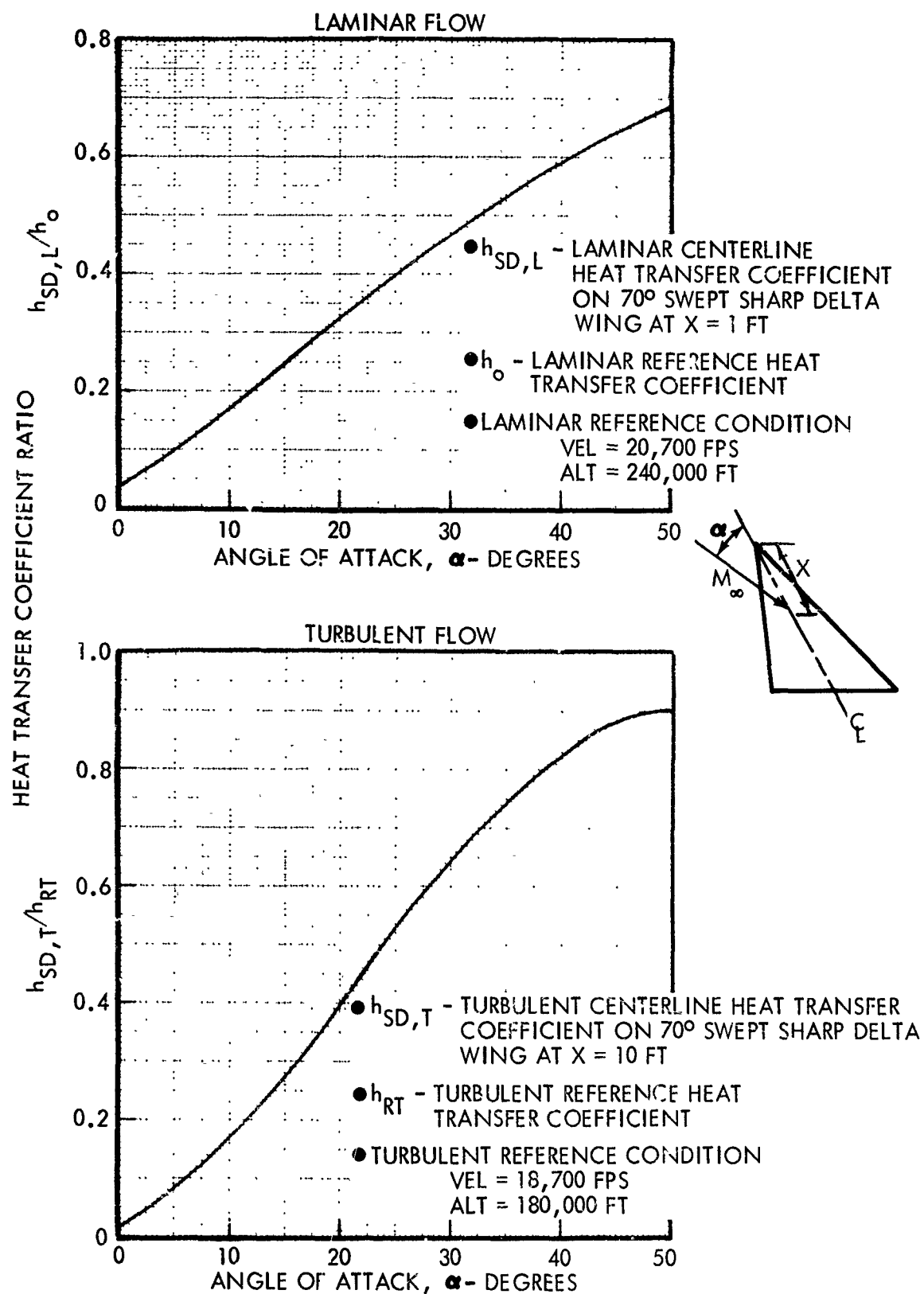


Figure 6-30: SHARP DELTA WING LOWER SURFACE CENTERLINE HEATING

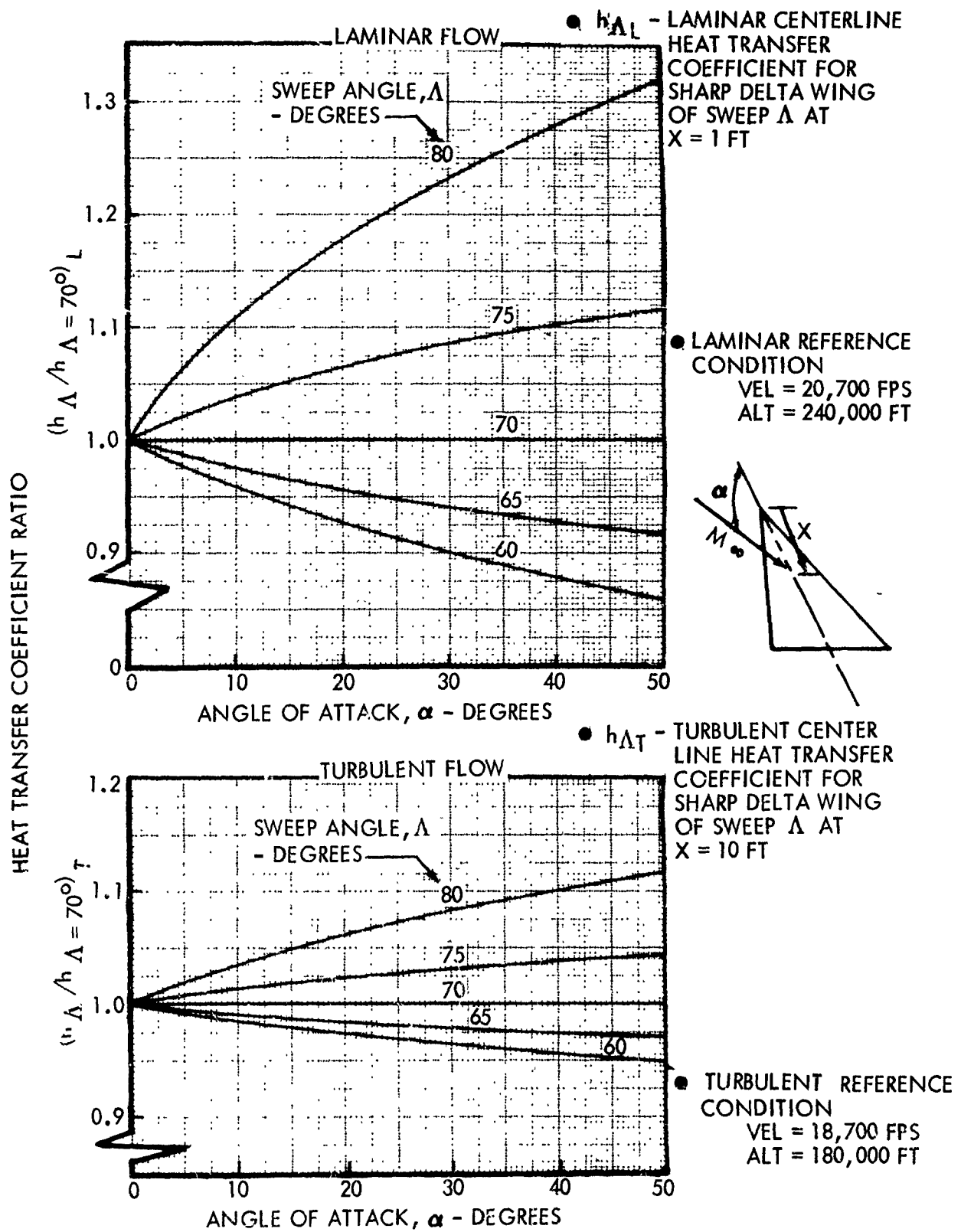


Figure 6-31: EFFECT OF SWEEP ON SHARP DELTA WING
LOWER SURFACE CENTERLINE HEATING

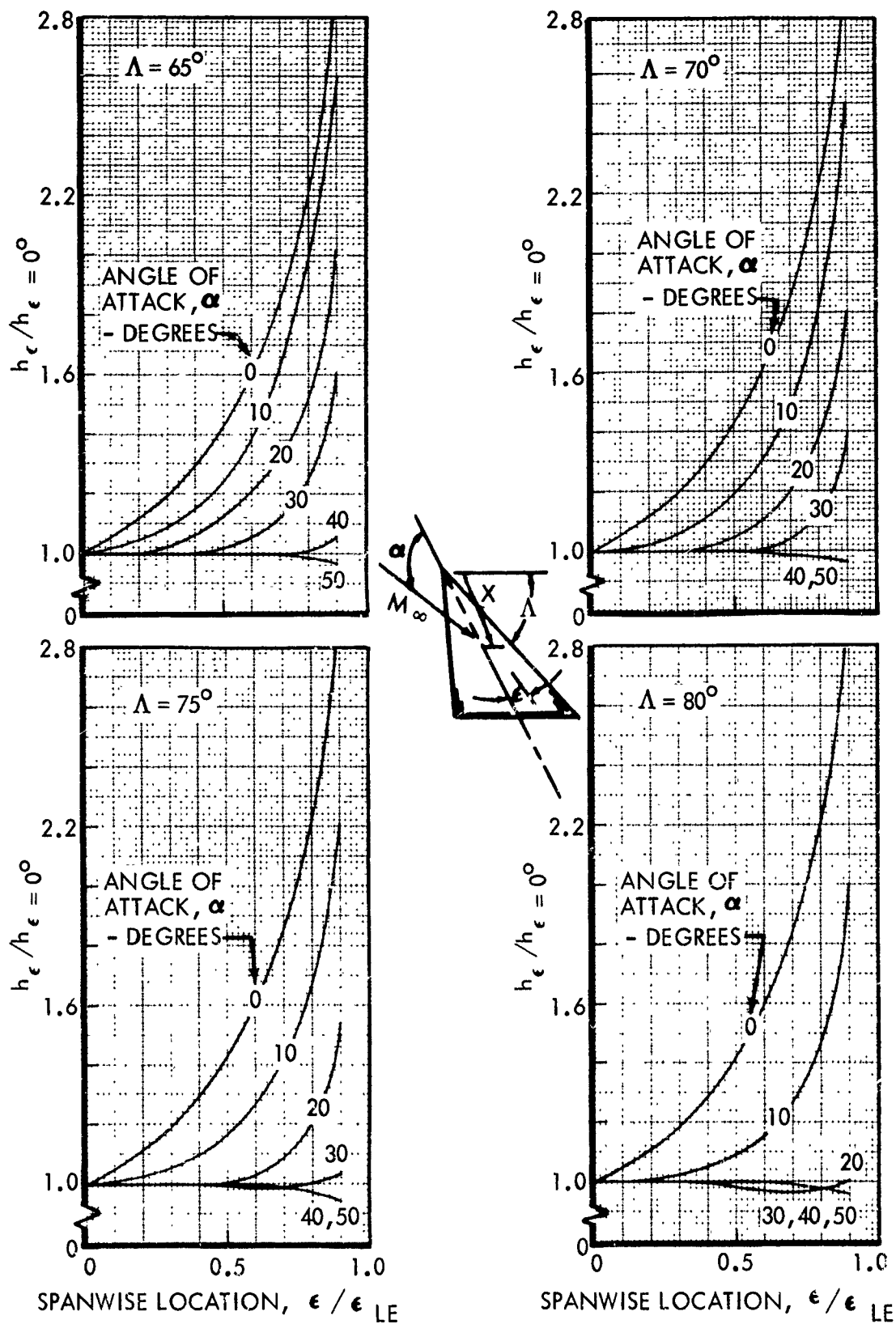


Figure 6-32: SHARP DELTA WING SPANWISE LAMINAR HEATING PARAMETER

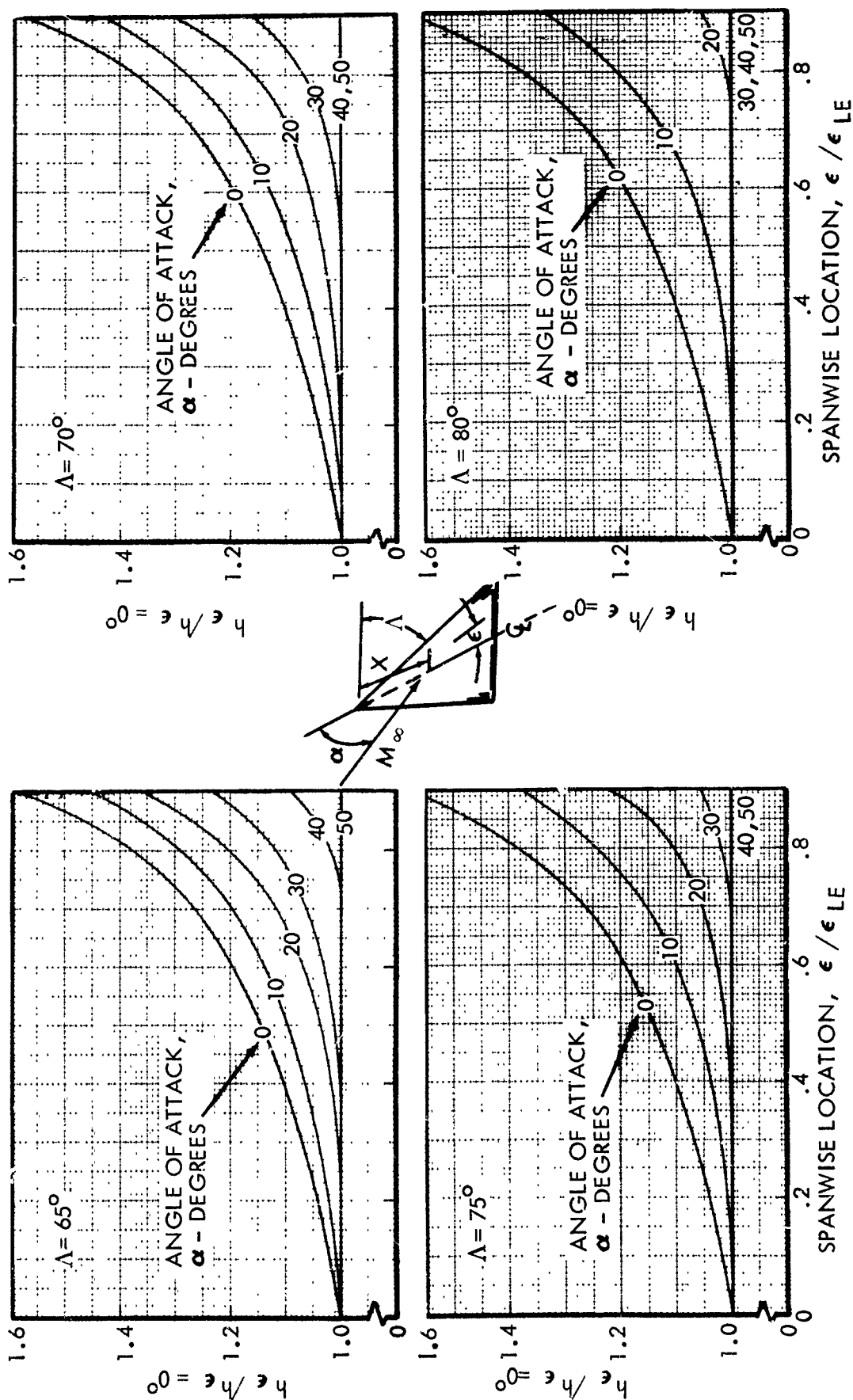


Figure 6-33: SHARP DELTA WING SPANWISE TURBULENT HEATING PARAMETER

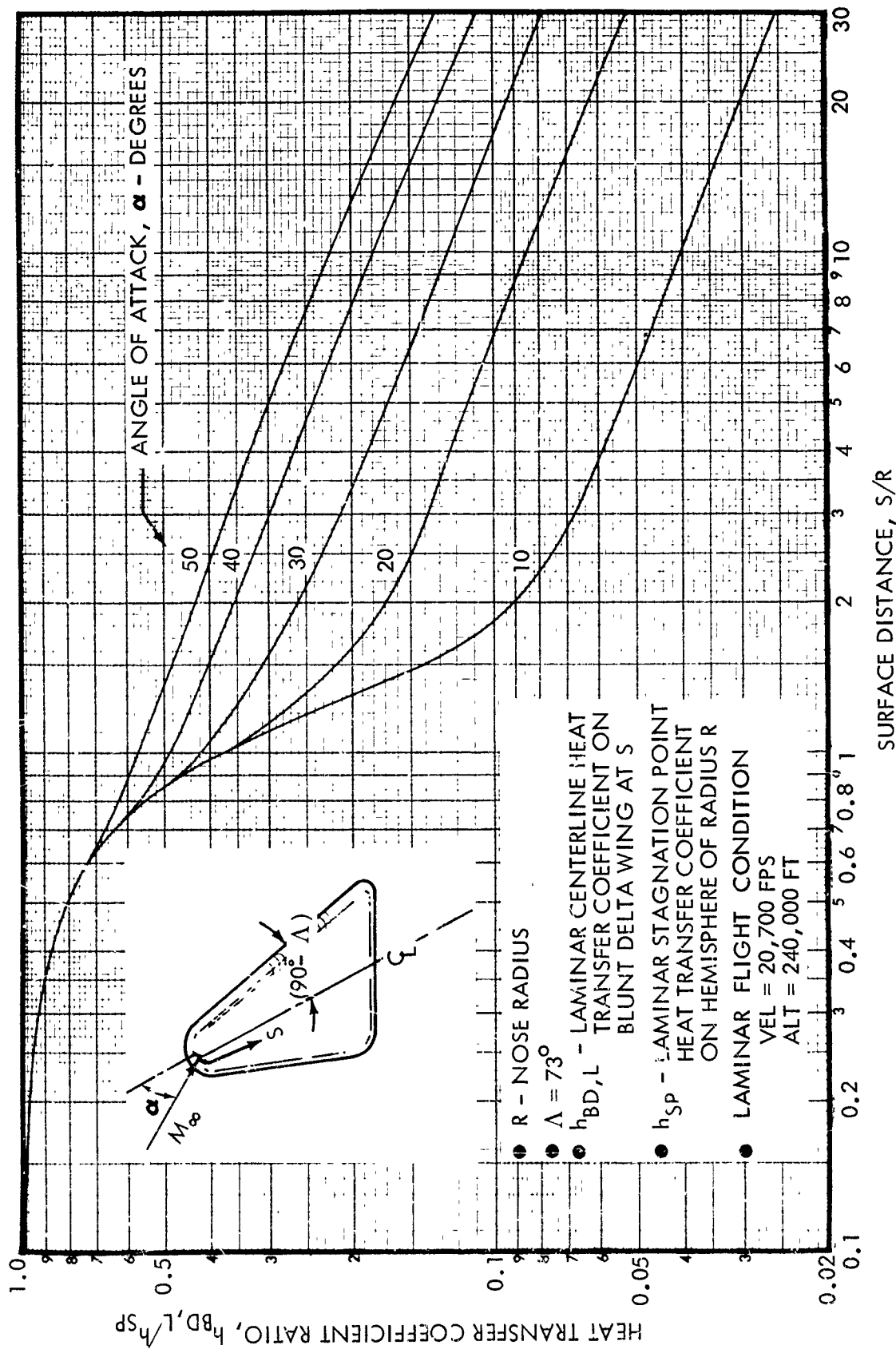


Figure 6-34: BLUNT DELTA WING LOWER SURFACE CENTERLINE LAMINAR HEATING

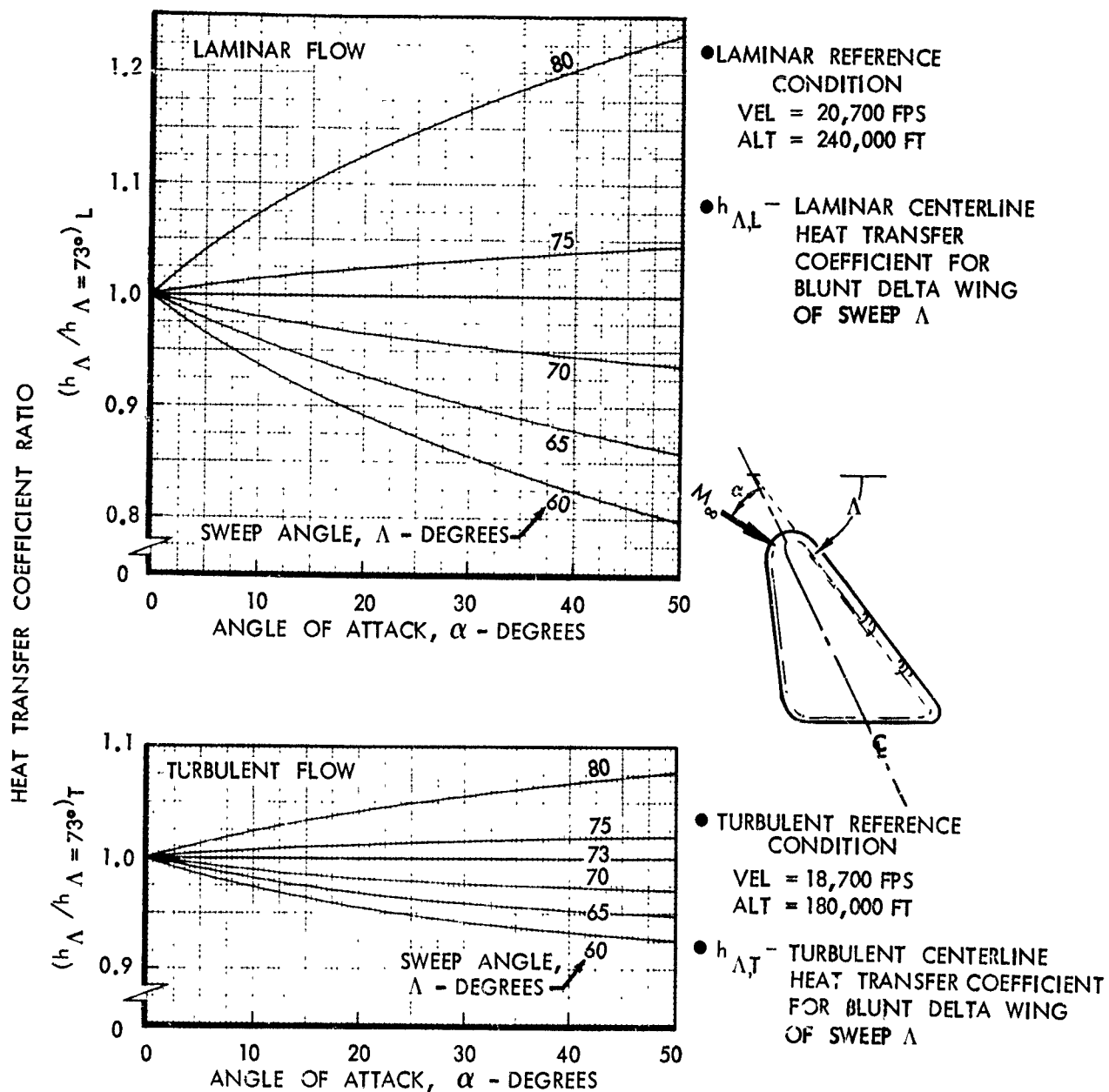


Figure 6-35: EFFECT OF SWEEP ON BLUNT DELTA WING LOWER SURFACE CENTERLINE HEATING

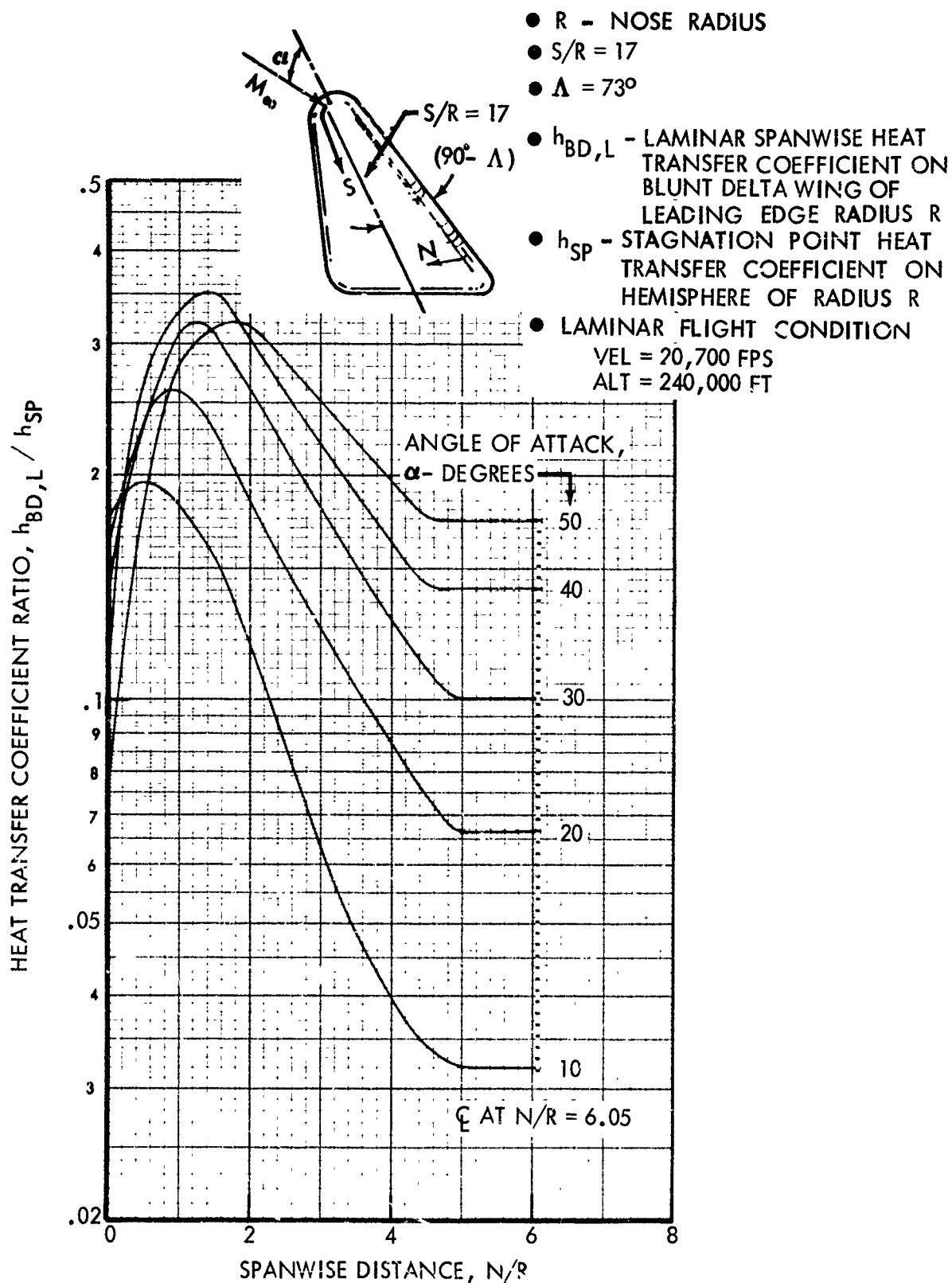


Figure 6-36: BLUNT DELTA WING LOWER SURFACE SPANWISE LAMINAR HEATING

- R - NOSE RADIUS
- $S/R = 27$
- $\Lambda = 73^\circ$
- $h_{BD,L}$ - LAMINAR SPANWISE HEAT TRANSFER COEFFICIENT ON BLUNT DELTA WING OF LEADING EDGE RADIUS R
- h_{SP} - STAGNATION POINT HEAT TRANSFER COEFFICIENT ON HEMISPHERE OF RADIUS R
- LAMINAR FLIGHT CONDITION
VEL = 20,700 FPS
ALT = 240,000 FT

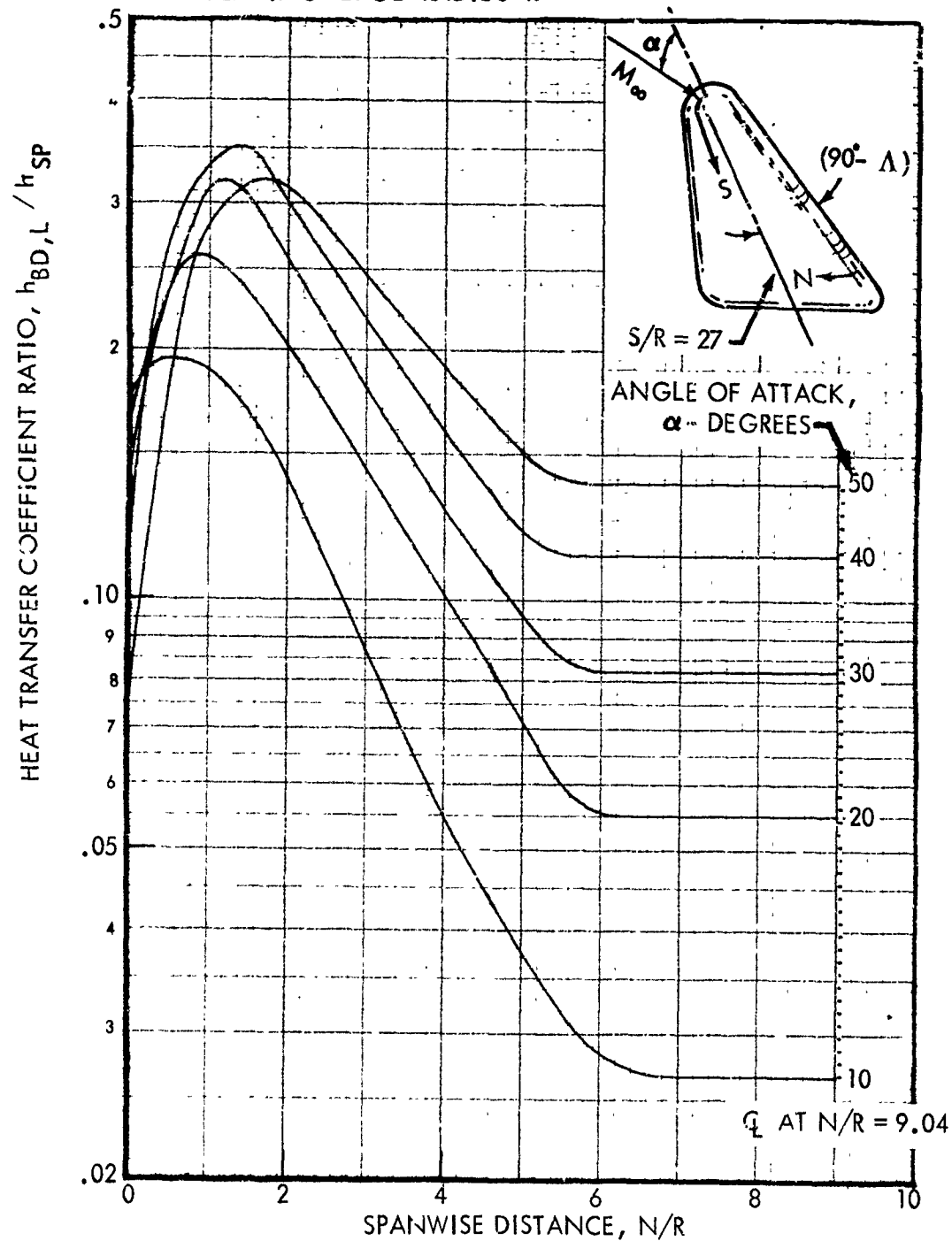


Figure 6-37: BLUNT DELTA WING LOWER SURFACE SPANWISE LAMINAR HEATING

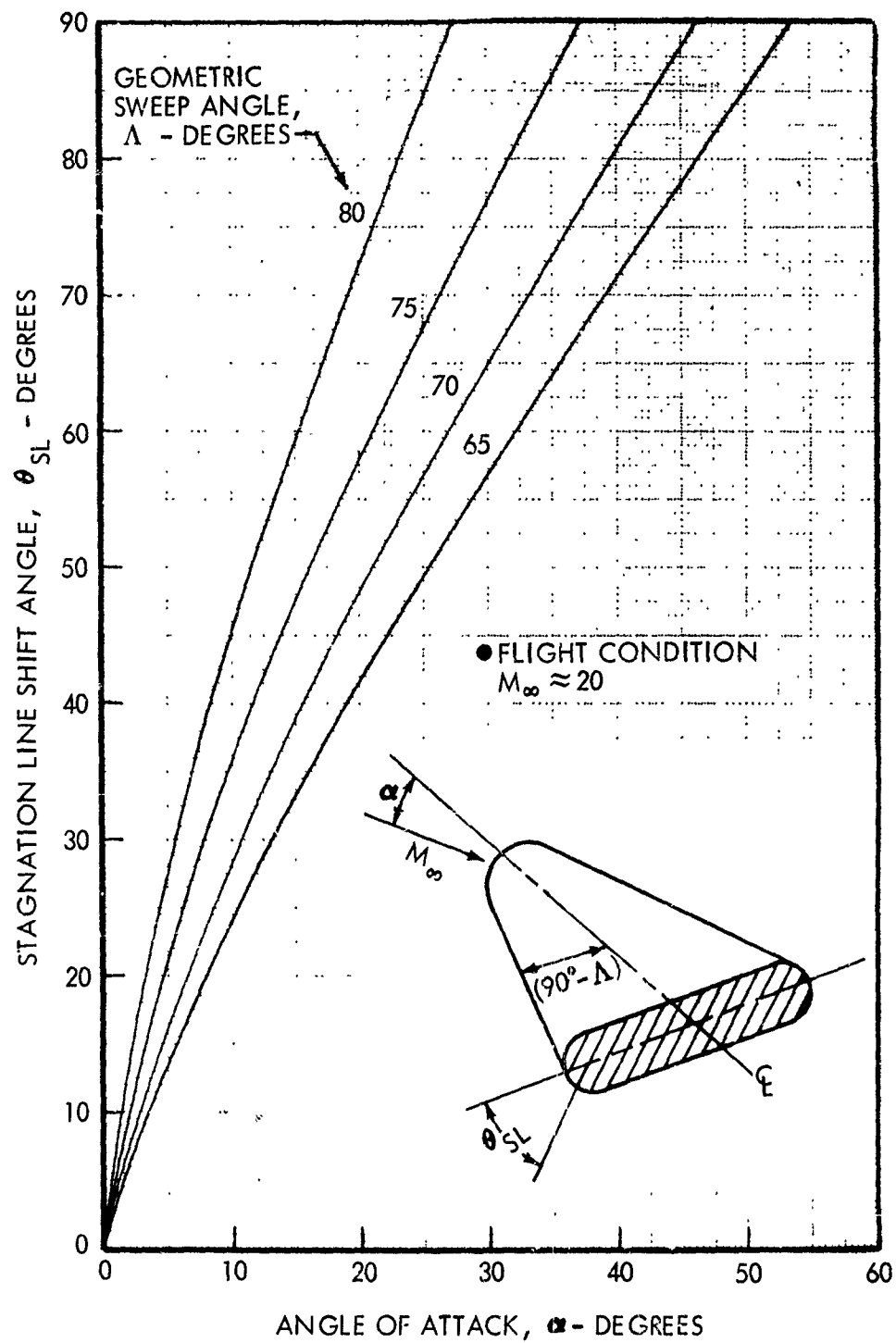


Figure 6-38: UNYAWED BLUNT DELTA WING LEADING EDGE STAGNATION LINE SHIFT

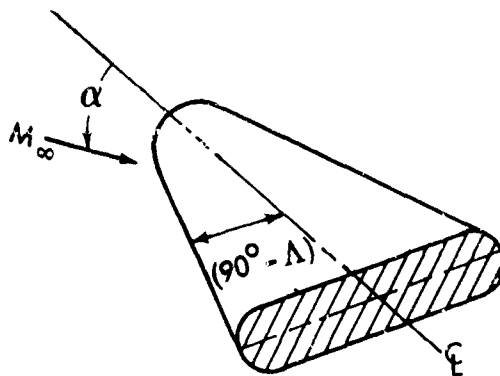
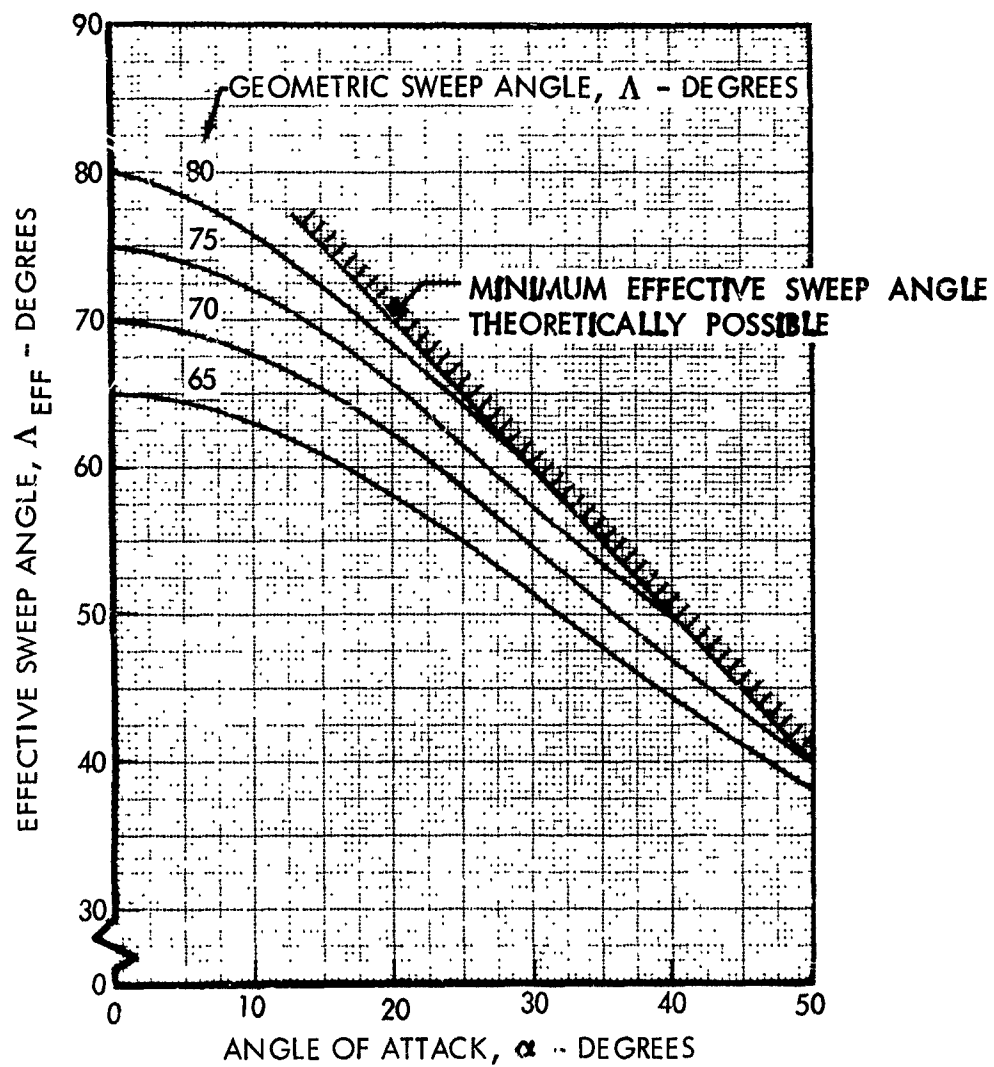


Figure 6-39: UNYAWED BLUNT DELTA WING LEADING EDGE EFFECTIVE SWEEP ANGLE

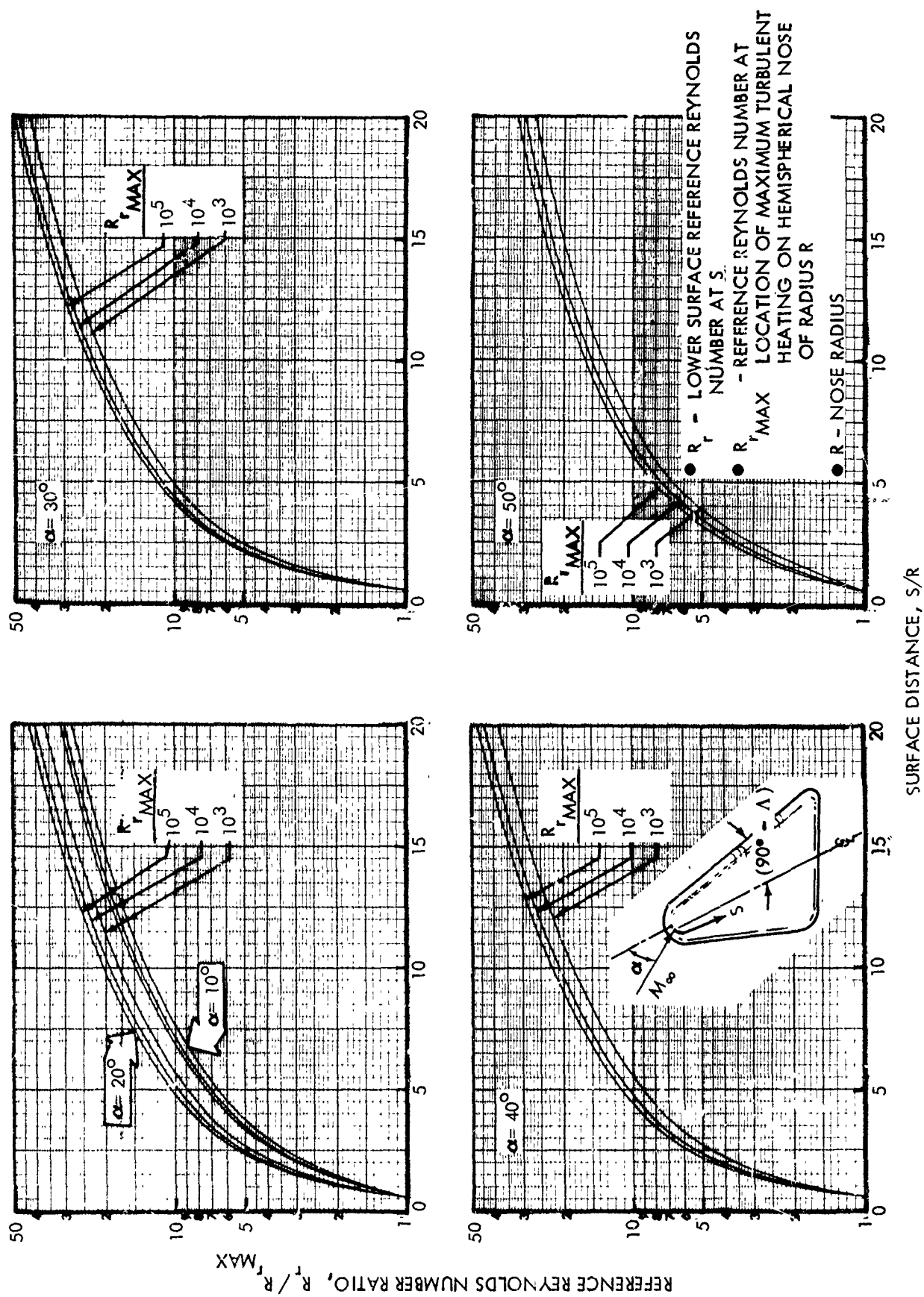


Figure 6-40: BLUNT DELTA WING LOWER SURFACE CENTERLINE REFERENCE REYNOLDS NUMBER

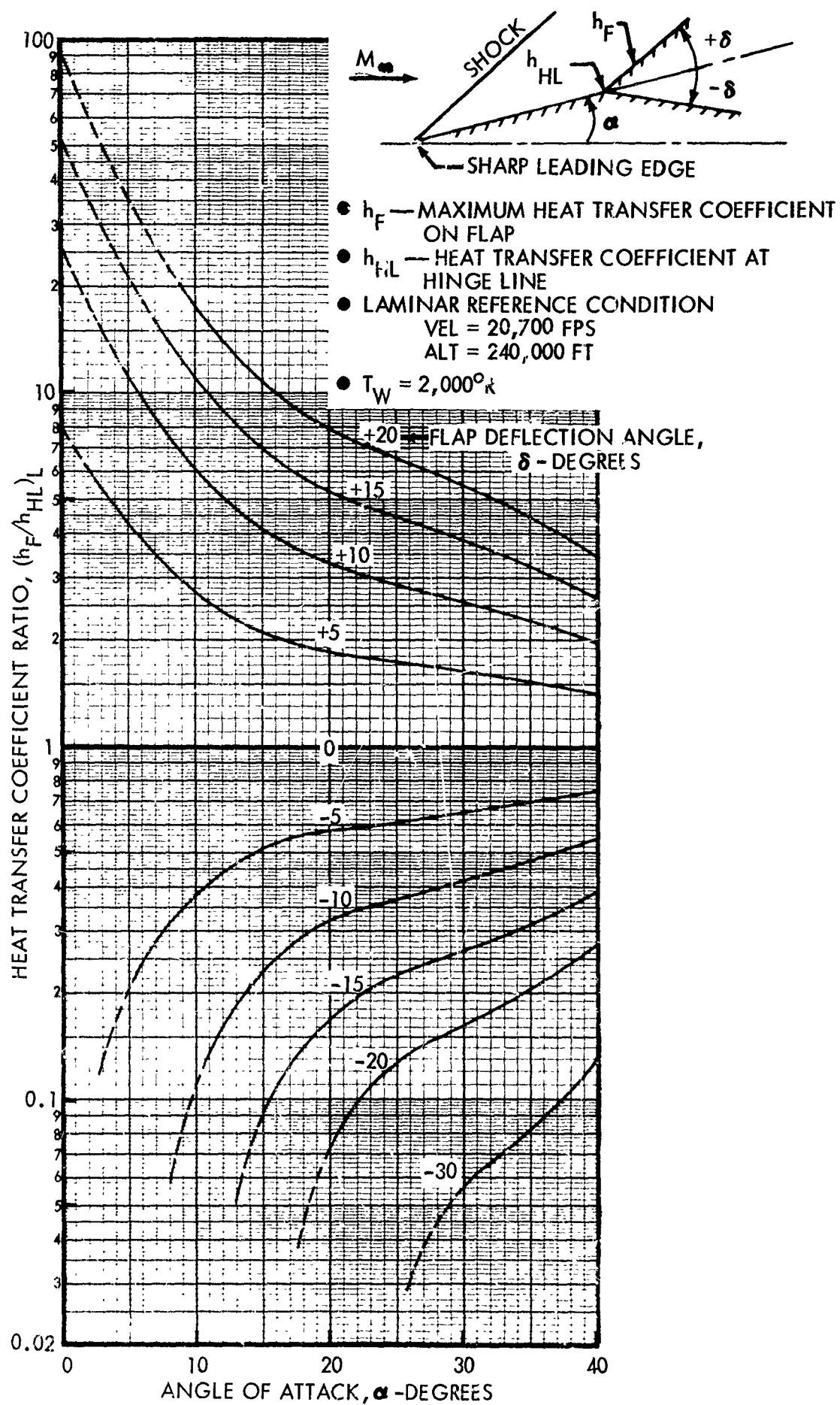


Figure 6-41: FLAP SURFACE MAXIMUM LAMINAR HEATING

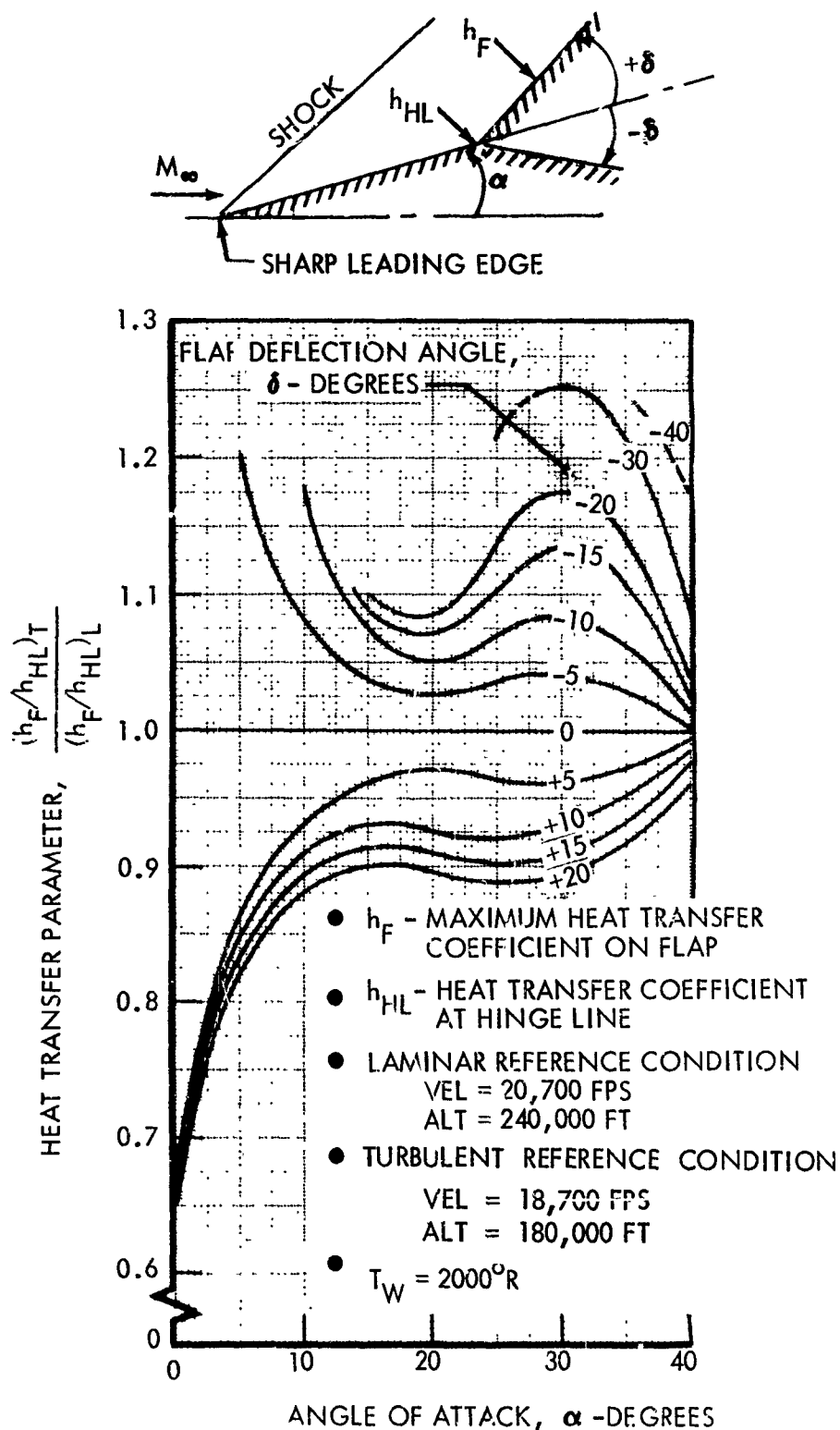


Figure 6-42: FLAP SURFACE MAXIMUM TURBULENT HEATING -- RATIO OF TURBULENT TO LAMINAR REFERENCE VALUES

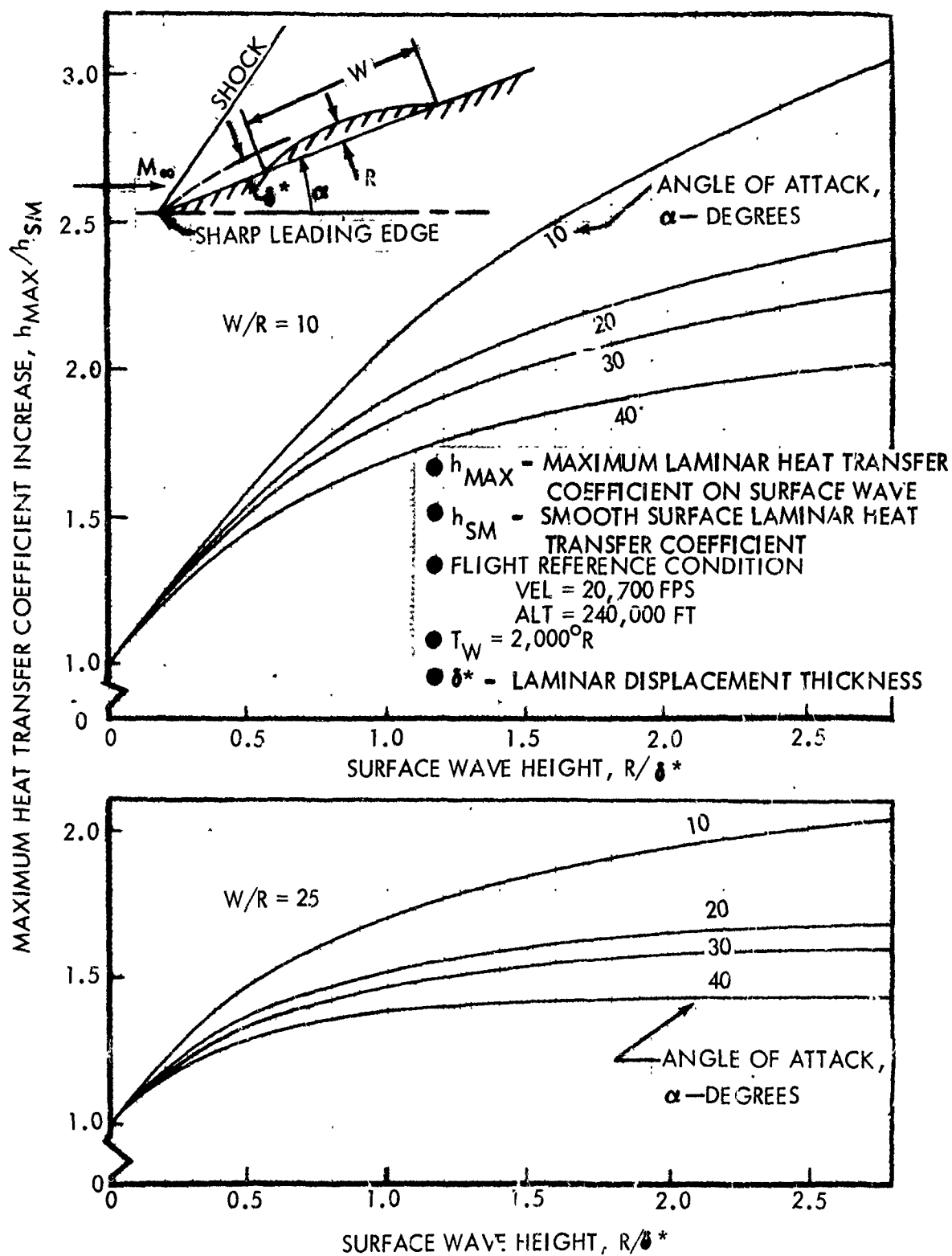


Figure 6-43: SURFACE WAVE LAMINAR HEATING

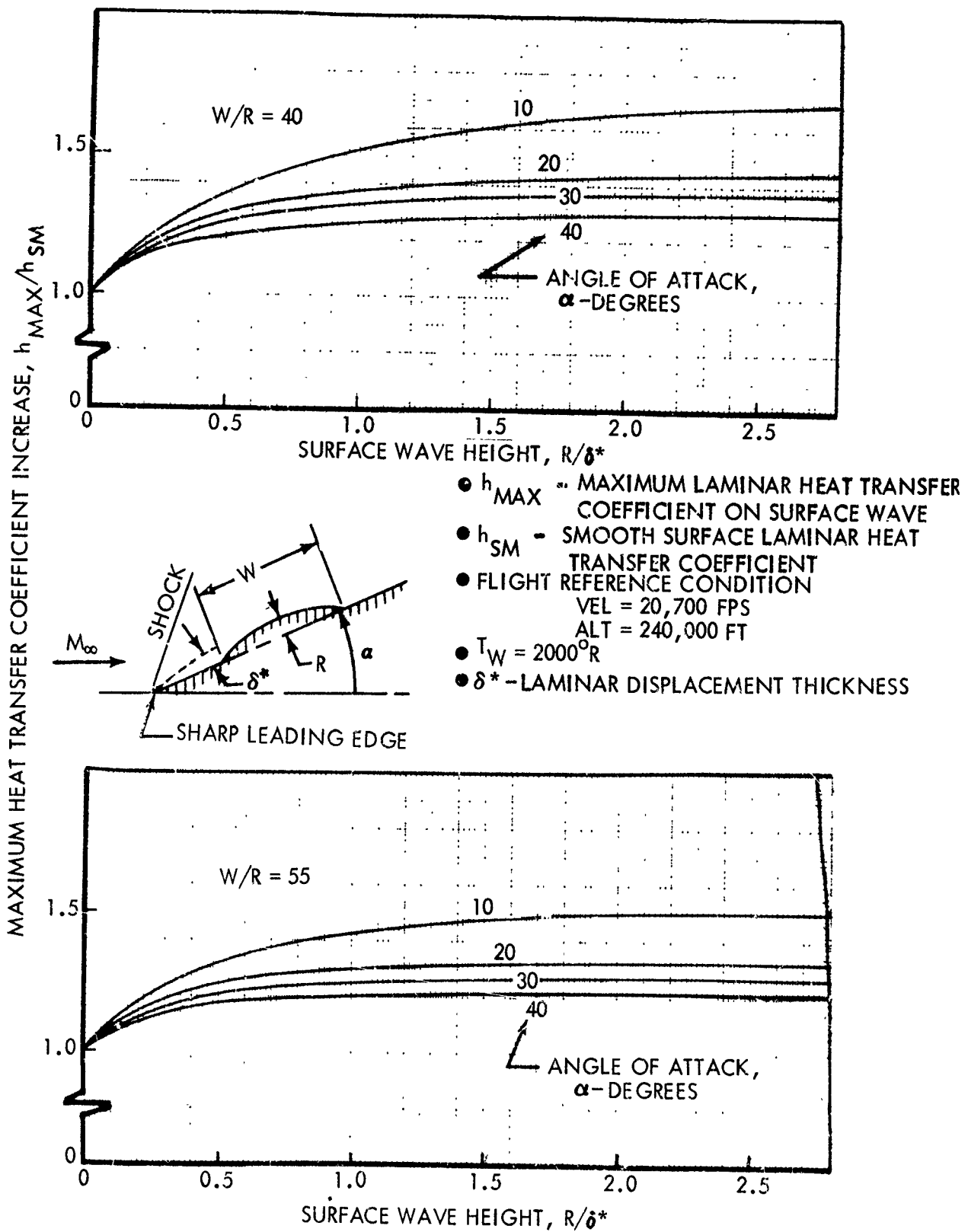


Figure 6-44: SURFACE WAVE LAMINAR HEATING

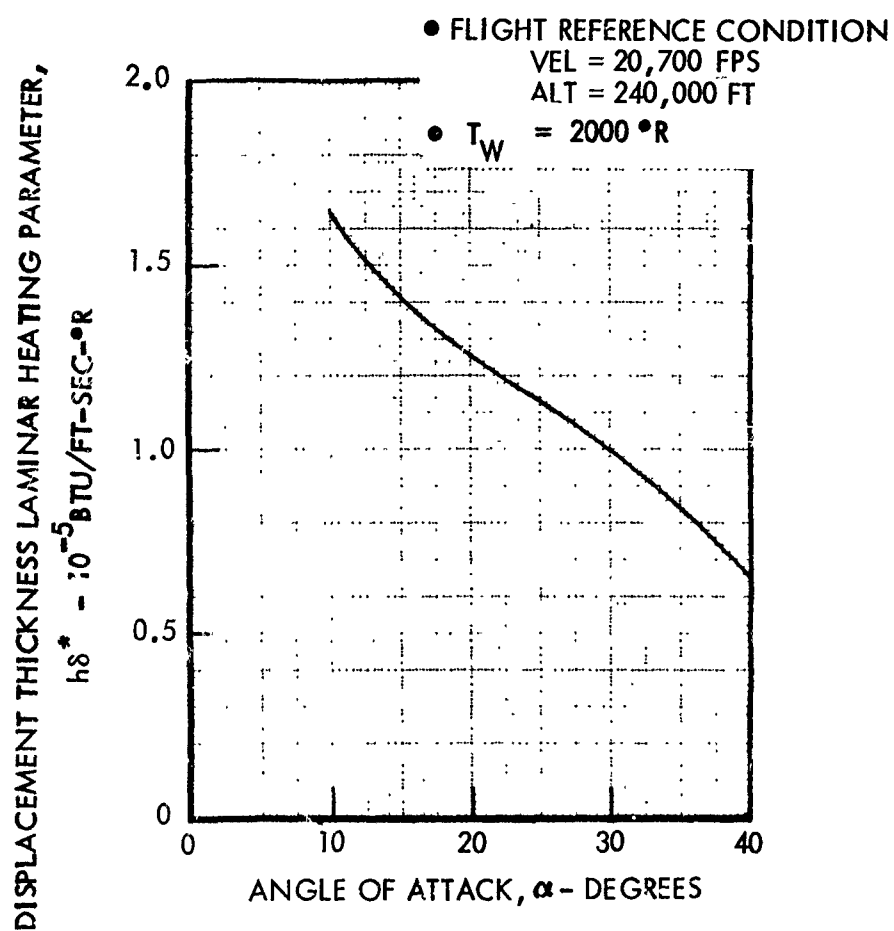
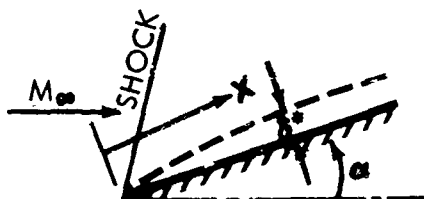


Figure 6-45: SHARP FLAT PLATE LAMINAR DISPLACEMENT THICKNESS HEATING PARAMETER

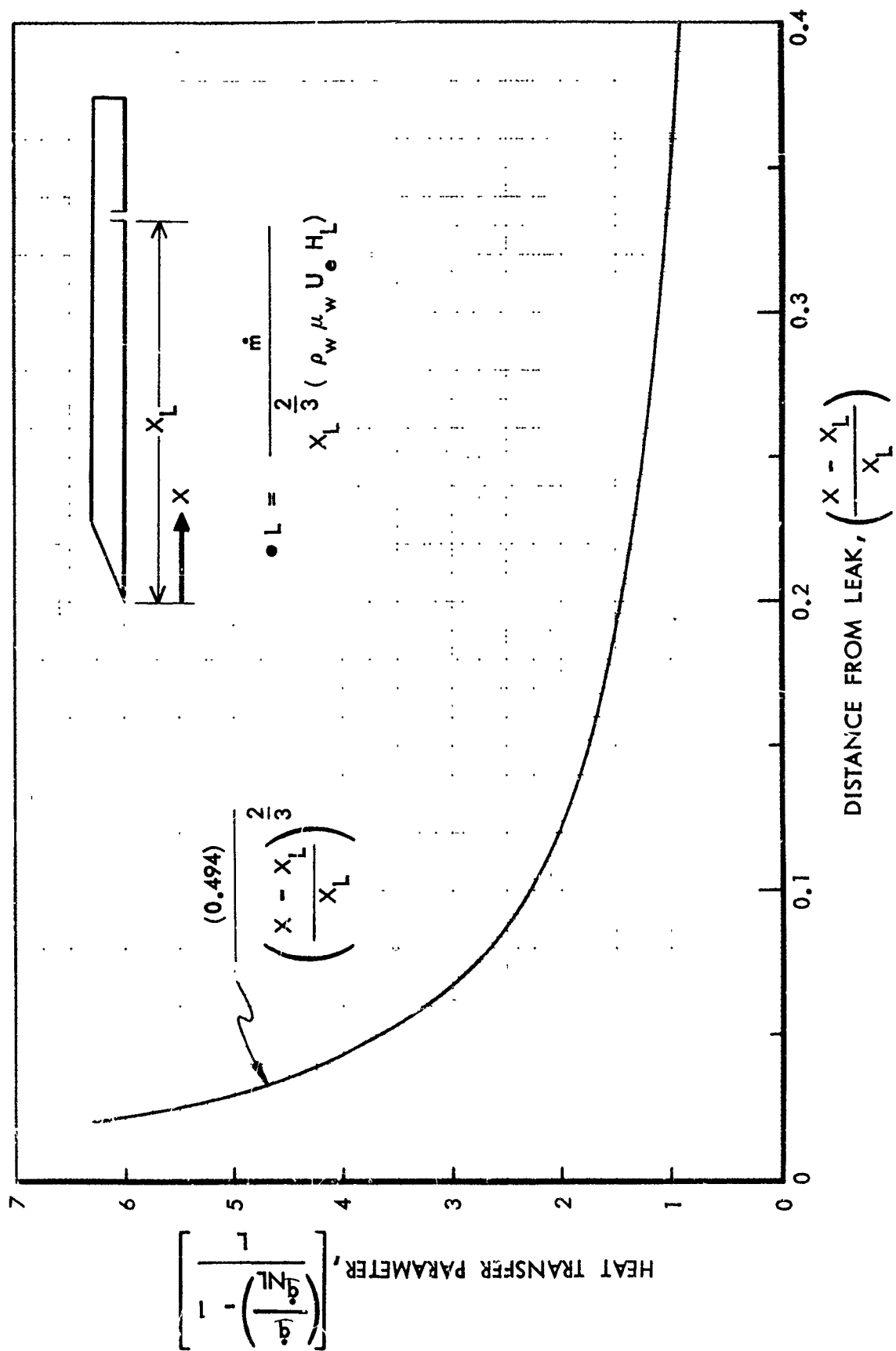


Figure 6-46: EFFECT OF LEAKAGE ON LAMINAR HEAT TRANSFER

- h_G - HEAT TRANSFER COEFFICIENT
90° FROM STAGNATION LINE
ON FIN SURFACE
- h_o - LAMINAR REFERENCE HEAT
TRANSFER COEFFICIENT
- h_{RT} - TURBULENT REFERENCE
HEAT TRANSFER COEFFICIENT
- LAMINAR REFERENCE CONDITION
VEL = 20,700 FPS
ALT = 240,000 FT
- TURBULENT REFERENCE CONDITION
VEL = 18,700 FPS
ALT = 180,000 FT

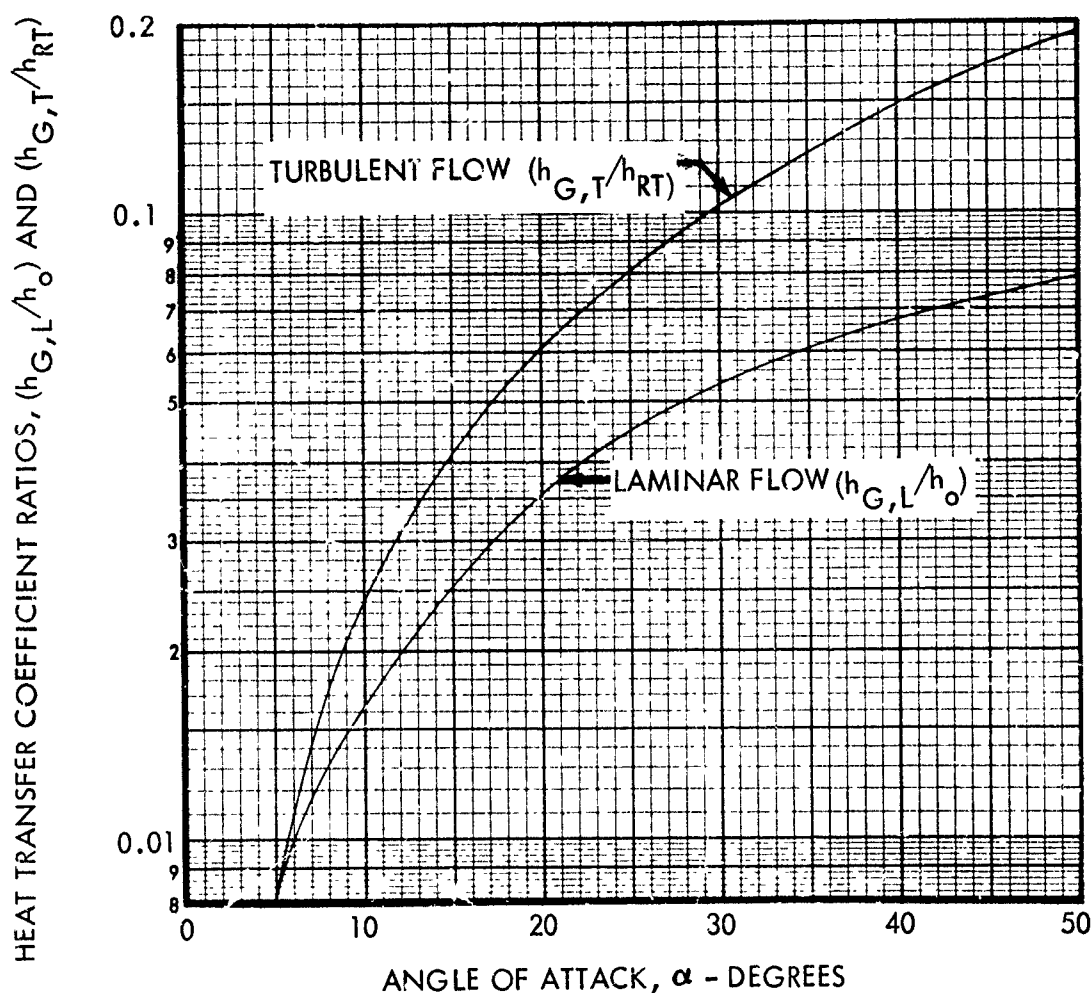
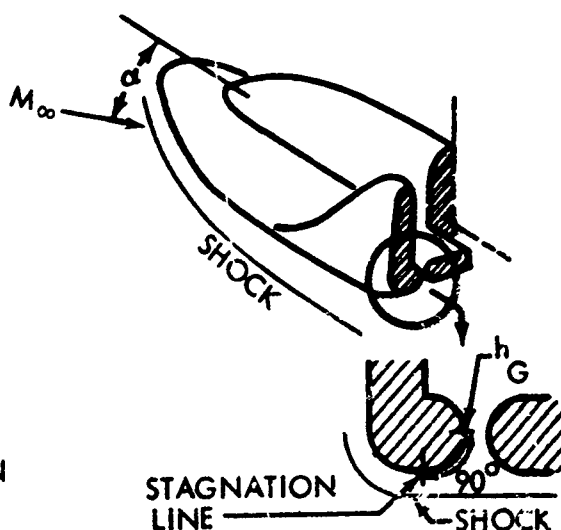


Figure 6-47: CONTROL SURFACE GAP HEATING (TIP FIN - ELEVON)

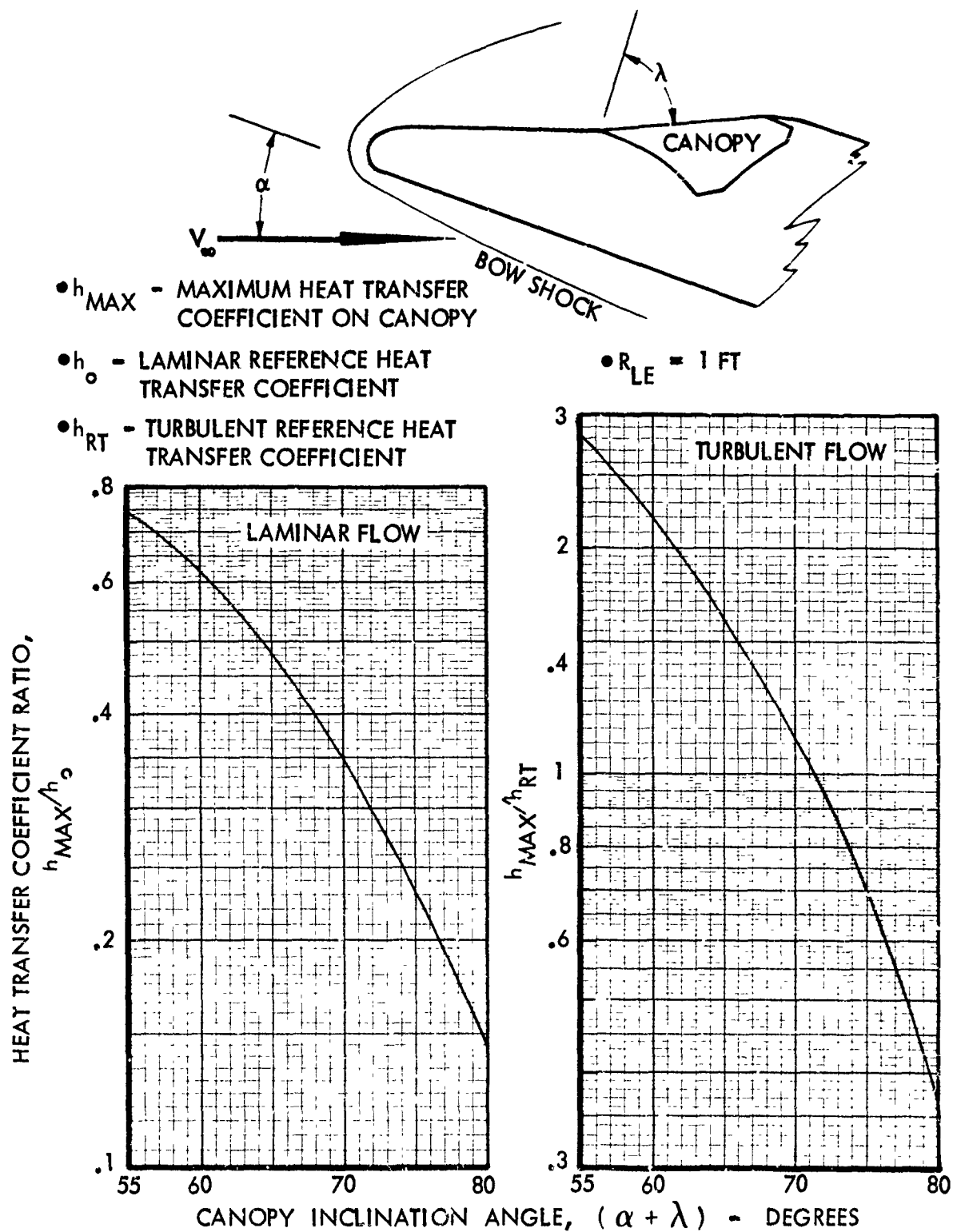


Figure 6-48: CANOPY INTERFERENCE - LAMINAR AND TURBULENT HEATING

VII. USE OF GROUND-FACILITY DATA IN DESIGN

Ground facilities presently being used in the design of hypersonic flight vehicles cannot simultaneously duplicate velocities and Mach numbers associated with re-entry. Ground-test data, however, are required to obtain detailed aerodynamic-heating distributions on complex configurations for which completely analytic solutions are not possible. To apply ground-test data in actual design, it is necessary to correct for the effects of any differences that exist between ground facility environment and flight conditions. Several examples of effects that might be expected are discussed in reference 28; a few specific examples are discussed in this section.

Also included in this section is a description of methods for correcting wind tunnel data to flight conditions. Charts are presented that provide the required correction factors for those geometric elements which could be investigated analytically. The purpose of these charts is to serve as a guide in extrapolating ground-test data to flight conditions for complex geometries. Since these charts provide a means of extrapolating wind-tunnel data to flight conditions, they will be referred to as "extrapolation-factor charts."

All charts presented in this section are based on the assumptions discussed in Section II and do not account for chemical nonequilibrium effects. In addition, chemical equilibrium is assumed to exist in ground-facility test sections both in the free stream and within the body shock wave.

A. Real-Gas Effects on Shock-Layer Properties

1. Pressures

Some effects of the differences between ground-test and flight-test conditions on inviscid-flow shock-layer properties can be determined from oblique-shock calculations for a two-dimensional flat plate. Real-gas effects on sharp-flat-plate pressure coefficients are shown in figure 7-1. Pressure coefficients in ground facilities having free-stream temperatures on the order of 100 °F, are compared to pressure coefficients that would be obtained at an altitude of 240,000 feet at the same Mach numbers. Viscous-inviscid interaction and separated-flow effects are not considered in Figure 7-1.

At high angles of attack, pressure coefficients for flight are seen to be lower than those in ground facilities at the same Mach number. This reduction in pressure is primarily caused by the higher enthalpy achieved in flight. At the higher enthalpies of flight real-gas effects increase the density jump across shock waves which thereby tend to lie closer to the body. Since the pressure experienced by the body is the reaction to flow deflections caused by the shock, the smaller shock envelope occurring in flight leads to lower pressures on the body.

Of course, for highly swept shock waves, the downstream temperature may be relatively low, even at hypersonic speeds, and so fail to induce any appreciable real-gas behavior. This explains the absence of any apparent differences in pressure coefficients for angles of attack less than about 10 degrees.

The conclusions drawn from figure 7-1 are not applicable to all geometries, however. An opposite trend can occur on a trailing-edge flap deflected into the stream, as illustrated in figure 7-2. At a 10-degree angle of attack, flap pressure coefficients for wind-tunnel conditions are shown to agree with those for flight conditions. When the flat plate is inclined at larger angles of attack, however, real-gas effects become noticeable and are often opposite of those for a flat plate. The departure from the flat-plate trend reflects the effect of shock layer flow properties on the pressure jump at the flap. The effective free stream for the flap is of course the flow within the plate shock layer. Although the static pressure of the local flow is reduced by real-gas effects, the aforementioned increase in the local density leads to a corresponding increase in the local dynamic pressure. As a result, the pressure jump at the flap is increased, causing the trends shown in figure 7-2.

The combined effect of Mach number and enthalpy differences on deflected flaps is illustrated in figure 7-3. The curves shown are for two specific wind tunnels and particular flight conditions, as noted. Negative flap deflections are seen to cause lower pressure coefficients in flight than in the wind tunnels, while positive deflections lead to higher values. Thus it is seen that the effect of flap deflection is always larger in flight than in the wind tunnel. Although figure 7-3 is drawn specifically for flat-plate flap combinations, similar trends are to be expected for flaps attached to sharp cones or delta wings.

Real-gas effects on stagnation point pressure are relatively small, as shown in figure 7-4.

2. Streamlines

The lack of enthalpy simulation in ground facilities has an effect on streamline patterns on swept infinite cylinders. The differences in the local streamline angle at each circumferential location on the surface of a 50° swept infinite cylinder are illustrated in figure 7-5 as a function of total enthalpy ratio. The local streamline angles were calculated using methods described in Section II.

3. Boundary Layer Properties

In flight, dissociation may occur within the boundary layer, altering the temperature, density, and velocity profiles. A comparison of flight and ground-facility gas-temperature profiles similar to those presented in reference 28 are shown in figure 7-6 for a flat plate at a 20-degree angle of attack. The profiles are shown as a function of η , the nondimensional distance normal to the wall. Considerable differences are seen not only in the levels of temperature but also in the ratio of peak temperature to boundary-layer-edge temperature. Part of the difference is due to the relatively higher wall temperature in the ground facilities and part to dissociation in the boundary layer in the flight case.

Displacement thickness is significantly affected by the changes in the density and velocity profiles in the boundary layer. The effect on displacement thickness is shown in figure 7-7. For the conditions indicated, the displacement thickness in the wind tunnel is approximately 50% higher than in flight.

4. Heating Rates

The resultant effect of the changes in boundary-layer characteristics on heat transfer shown in figures 7-6 and 7-7 can be illustrated by comparing a normalized surface heat-transfer coefficient at ground-facility conditions to a similar ratio at flight conditions. The resulting ratio, denoted by ζ and specifically defined in figure 7-8, has been calculated for several geometries. Values of ζ for a flat plate are shown in figure 7-8 as a function of angle of attack for two different facilities. Free-stream temperatures in these two facilities are nearly equal but the total enthalpy and the Mach Number are higher in the shock tunnel.

Similar information for a deflected flap is shown in figure 7-9. This figure illustrates differences in the heat-transfer parameter for a flap that is attached to a sharp flat plate at a 20-degree angle of attack.

Partial simulation effects on stagnation-line heat transfer for infinite-swept cylinders are illustrated in figure 7-10 as a function of sweep angle for two different ground facilities. Curves shown indicate that at large sweep angles opposite trends in the heat-transfer parameter can occur in tunnels having different energy levels and Mach numbers.

B. Extrapolation of Ground-Facility Heat-Transfer Test Data to Flight Conditions

Calculations of the type just described have been made in order to provide extrapolation factors that allow the correction of experimental ground-test heat-transfer data to flight conditions. The factors presented are calculated for the basic shapes discussed in Section II, but should serve as guides to the correction of data for more complex shapes.

The previously defined heat-transfer parameter ζ can be used to correct ground facility data to flight conditions. For example:

$$\begin{aligned} h_{L,FLT} &= \left(\frac{1}{\zeta_L} \right) h_{o,FLT} \left(\frac{h_L}{h_o} \right)_{WT} \\ h_{T,FLT} &= \left(\frac{1}{\zeta_T} \right) h_{RT,FLT} \left(\frac{h_T}{h_{RT}} \right)_{WT} \end{aligned} \quad (7.1)$$

For several of the basic shapes it was found that the major effect of Mach number on ζ is due to its effect on pressure. Accordingly, a compress-

ibility parameter Δ has been defined as follows:

$$\Delta = \left[\left(P/P_{T_2, f} \right)_{WT} / \left(P/P_{T_2, f} \right)_{FLT} \right]^n \quad (7.2)$$

where P is the local surface pressure, P_{T_2} is the stagnation-point pressure on a reference body, the subscript WT denotes ground-facility stream conditions and the subscript FLT refers to the flight reference condition. The subscript f indicates a sphere in laminar flow or a 60° swept cylinder in turbulent flow. The exponent n is (by definition) 0.5 in laminar flow and 0.8 in turbulent flow. Using Δ , the correction of wind tunnel data to flight conditions is made for example as follows:

$$h_{L, FLT} = h_o \left(\frac{\Delta}{\zeta} \right)_L \left(\frac{1}{\Delta_L} \right) \left(\frac{h_L}{h_o} \right)_{WT} \quad (7.3)$$

Curves of Δ and ζ/Δ for several basic shapes are presented in this section. For control surfaces extrapolation to flight conditions is made with a single chart without the use of a compressibility parameter. The basis for these charts is discussed in detail in the following sections.

1. Compressibility Parameter (Δ)

Compressibility-parameter charts applicable to hypersonic ground facilities are presented in figures 7-11 through 7-18. Free stream temperatures from $120^\circ R$ down to the liquifaction limit (which ranges from $60^\circ R$ to $90^\circ R$ depending on the pressure) were considered. The effects of enthalpy differences on Δ for the range of ground facilities indicated above is small and therefore not shown.

2. Extrapolation Factor (ζ/Δ)

Extrapolation factors corresponding to figures 7-11 through 7-18 are presented in figures 7-19 through 7-29. Also included in the group is the extrapolation factor for the hemisphere, figure 7-25. For the hemisphere, Δ is unity and $\zeta/\Delta = \zeta$. This is consistent with the assumption made in Section II that the pressure distribution is constant for all conditions.

The extrapolation factors were computed for the same range of conditions as for Δ . The effect of Mach number differences on ζ/Δ for the range of conditions studied is small and therefore not shown.

3. Correction Factors for Deflected Flaps.

The heat-transfer method employed in the analysis of deflected flaps is approximate and the extrapolation procedure described in the above paragraphs does not apply. Instead the extrapolation is made with the equation

$$\left(\frac{h_F}{h_{HL}}\right)_{FLT} = \zeta \left(\frac{h_F}{h_{HL}}\right)_{WT} \quad (7.4)$$

The extrapolation factor ζ for specific wind tunnel Mach numbers is presented in figures 7-30 and 7-31.

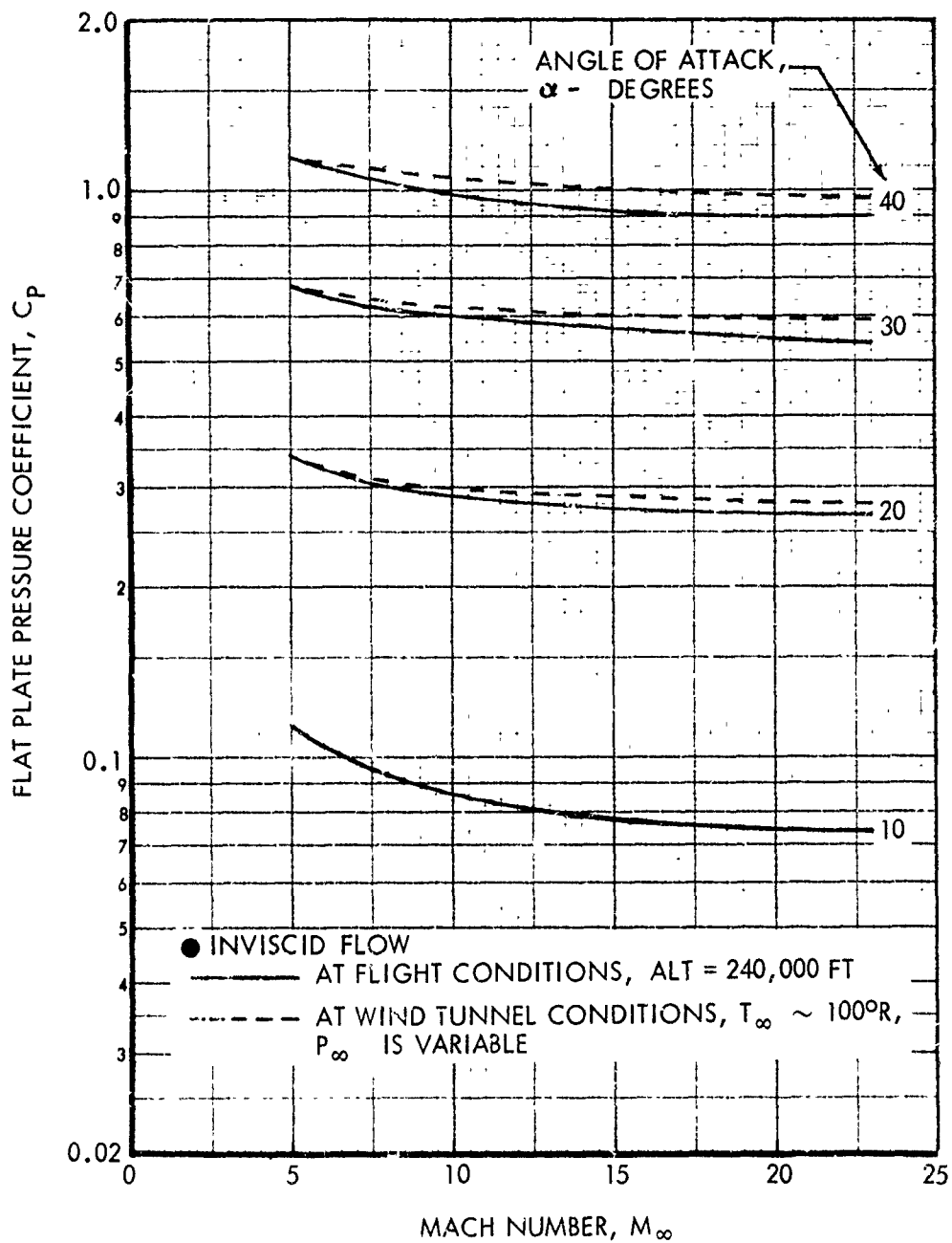


Figure 7-1: REAL GAS EFFECT ON SHARP FLAT PLATE SURFACE PRESSURE

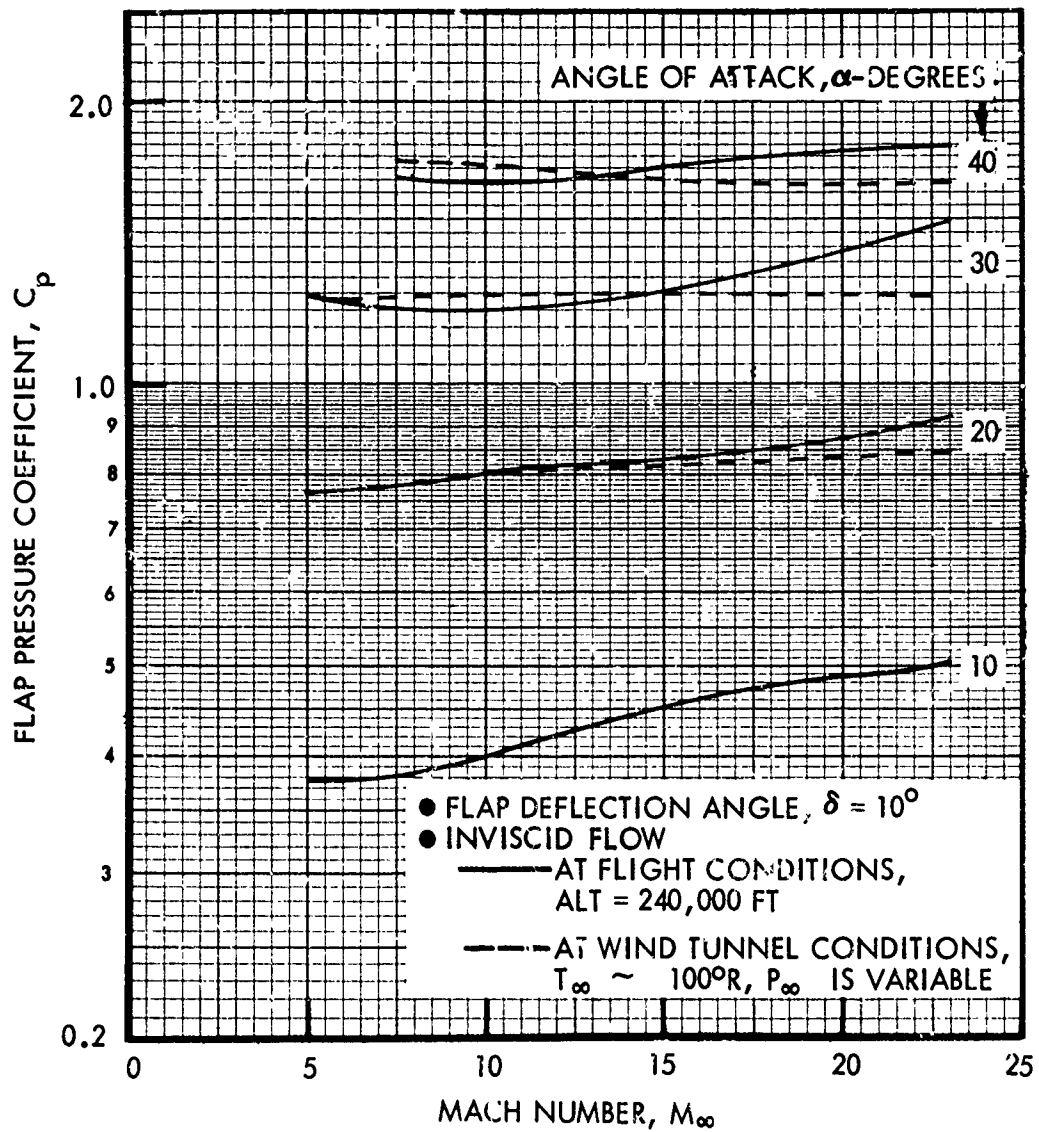
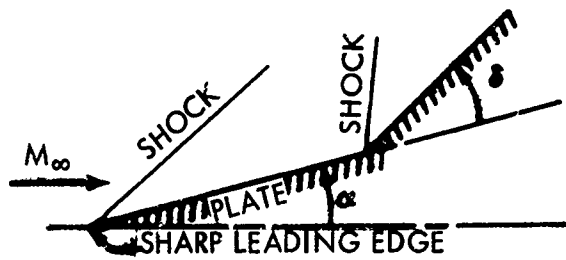


Figure 7-2: REAL GAS EFFECT ON FLAP SURFACE PRESSURE

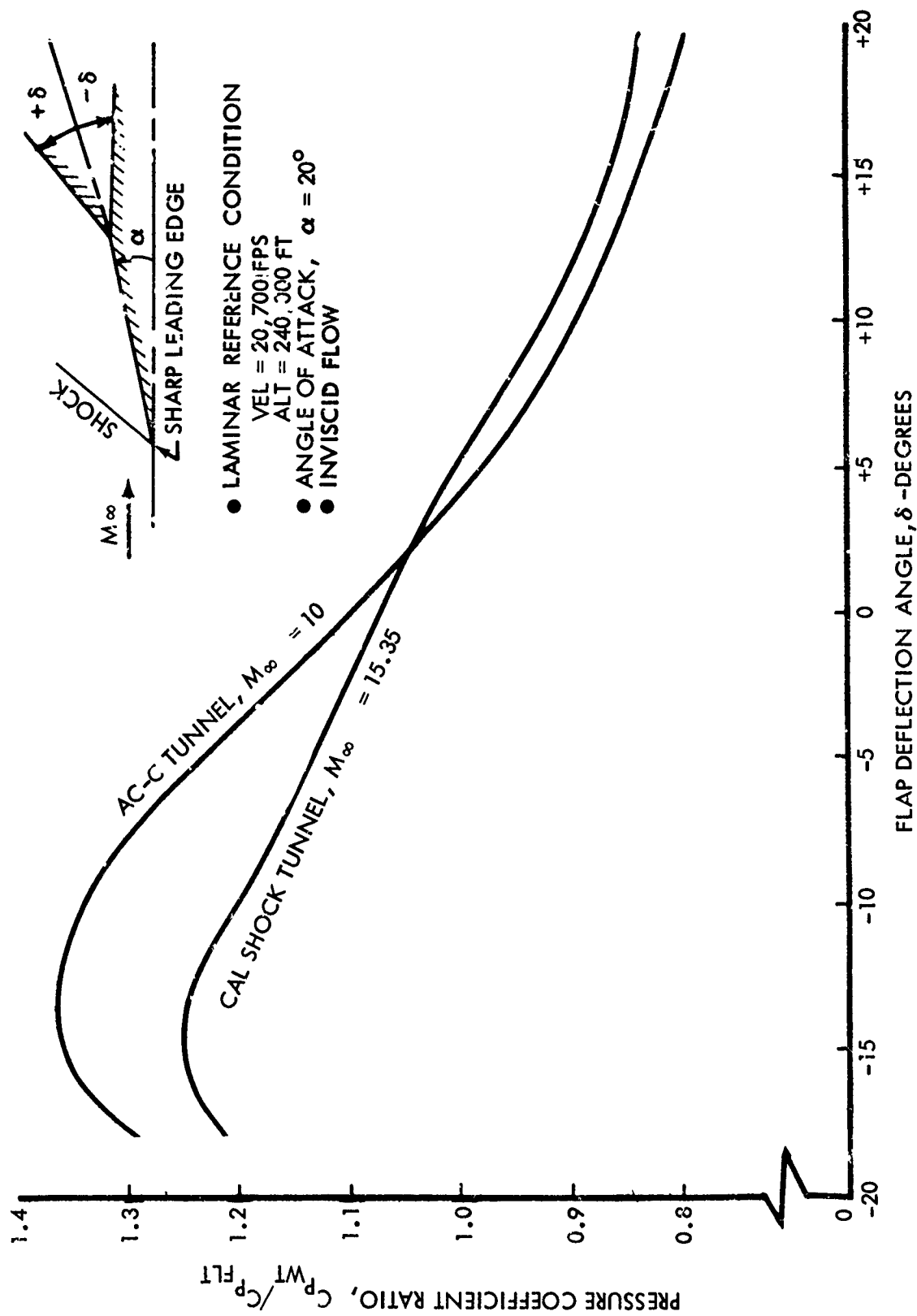


Figure 7-3: FLAP SURFACE PRESSURE COMPARISON

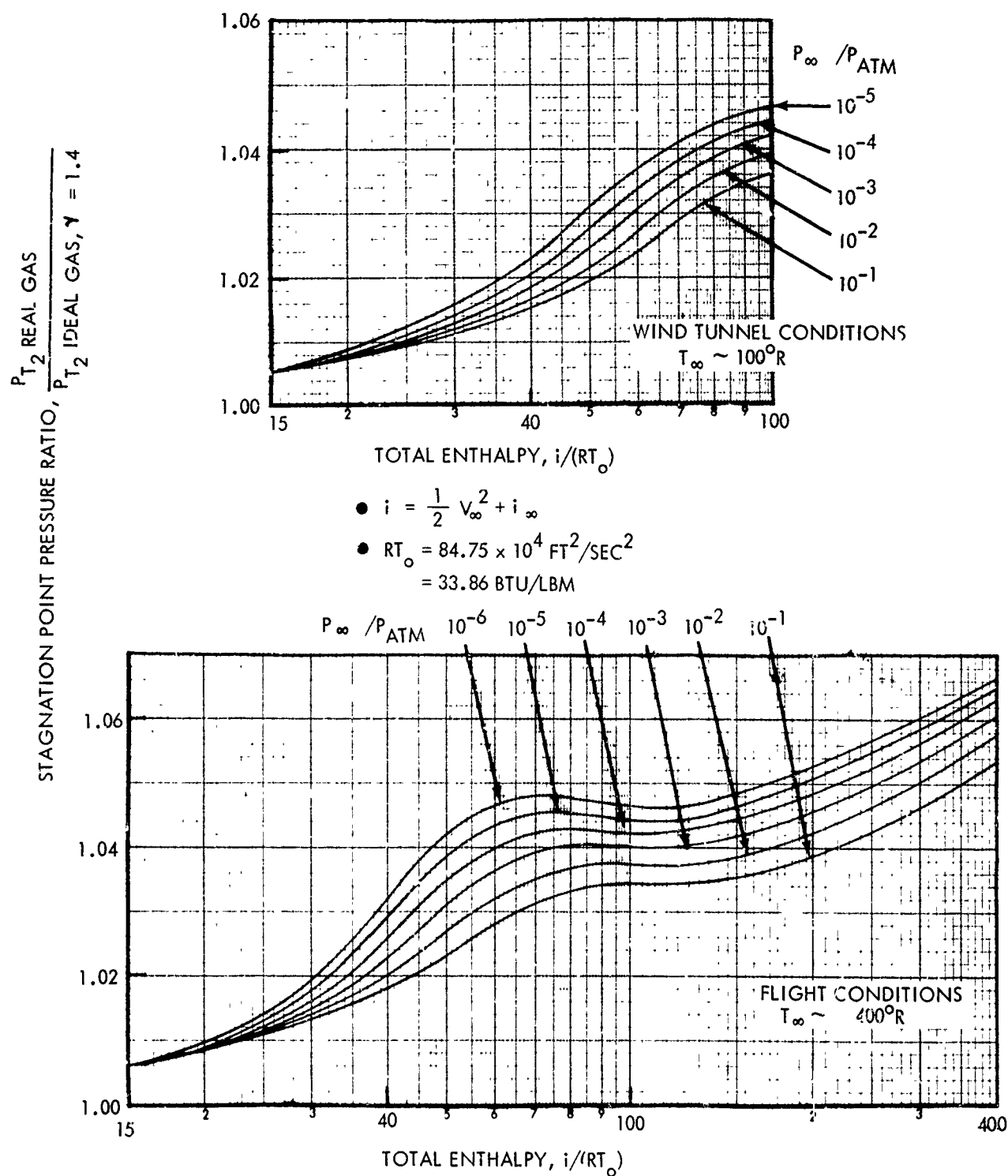


Figure 7-4: REAL GAS EFFECT ON STAGNATION POINT PRESSURE

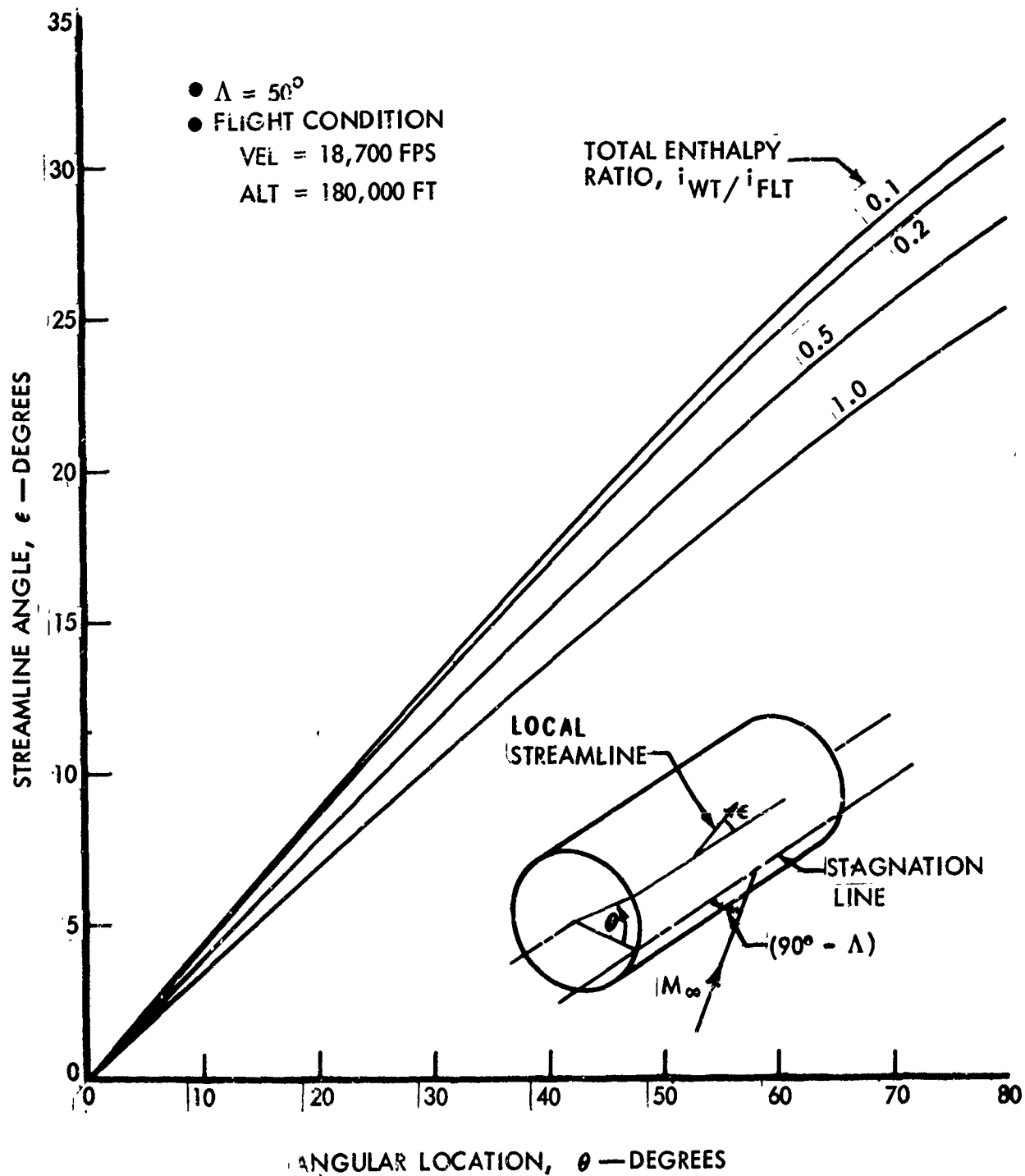


Figure 7-5: REAL GAS EFFECT ON STREAMLINE ANGLE FOR INFINITE SWEEP CYLINDER

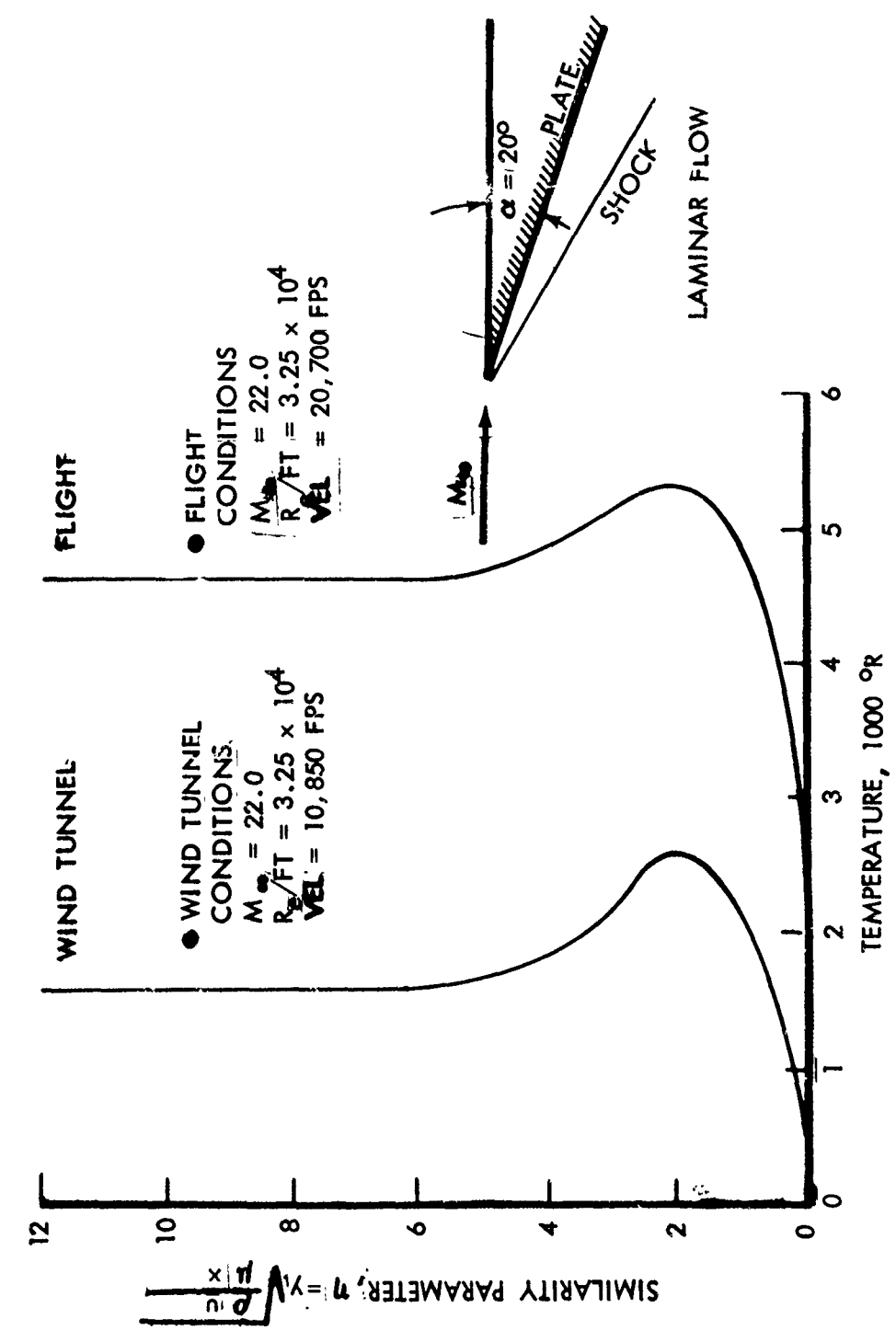


Figure 7-6: REAL GAS EFFECT ON SHARP FLAT PLATE BOUNDARY LAYER TEMPERATURE PROFILE

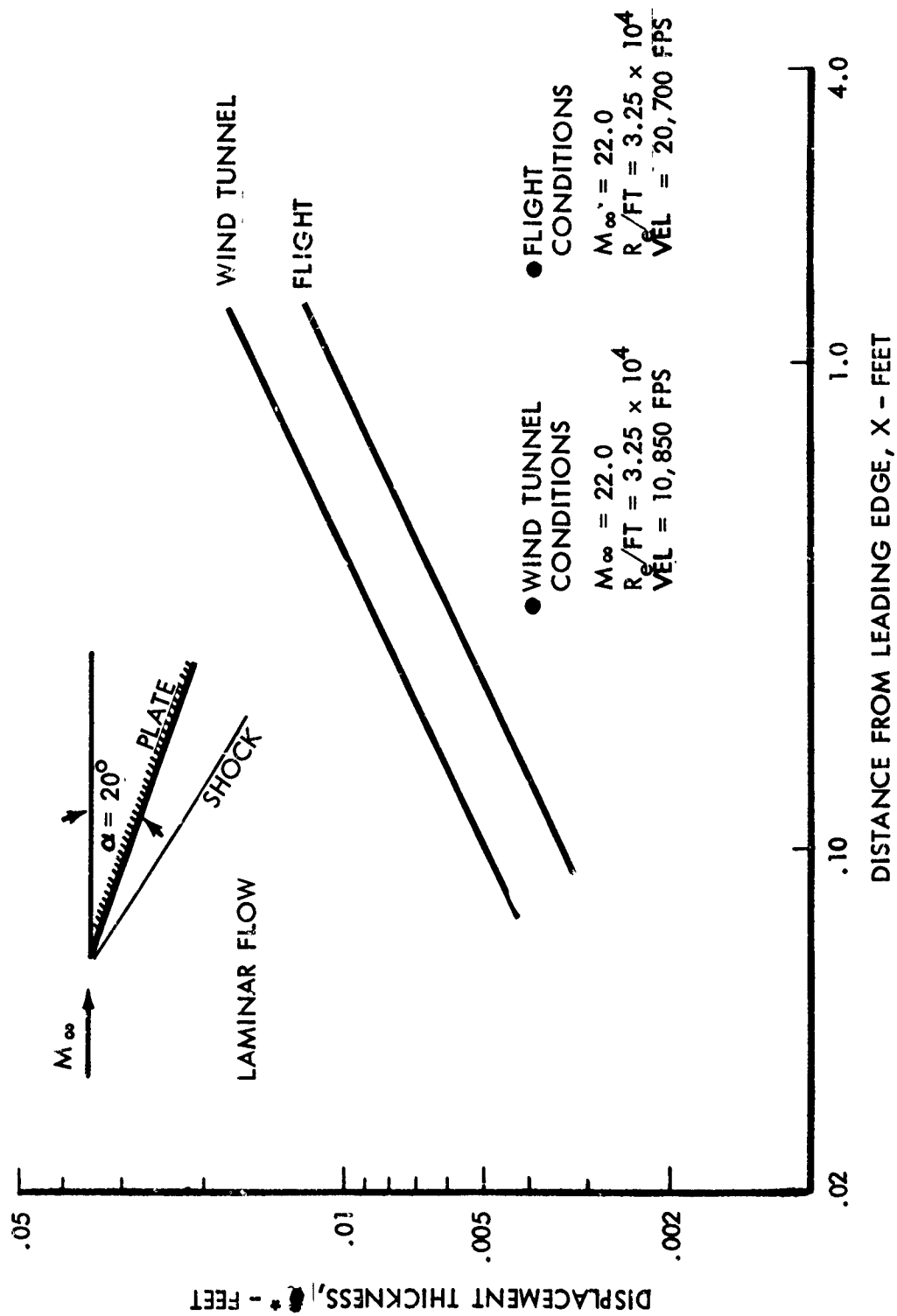


Figure 7-7: REAL GAS EFFECT ON SHARP FLAT PLATE BOUNDARY LAYER DISPLACEMENT THICKNESS

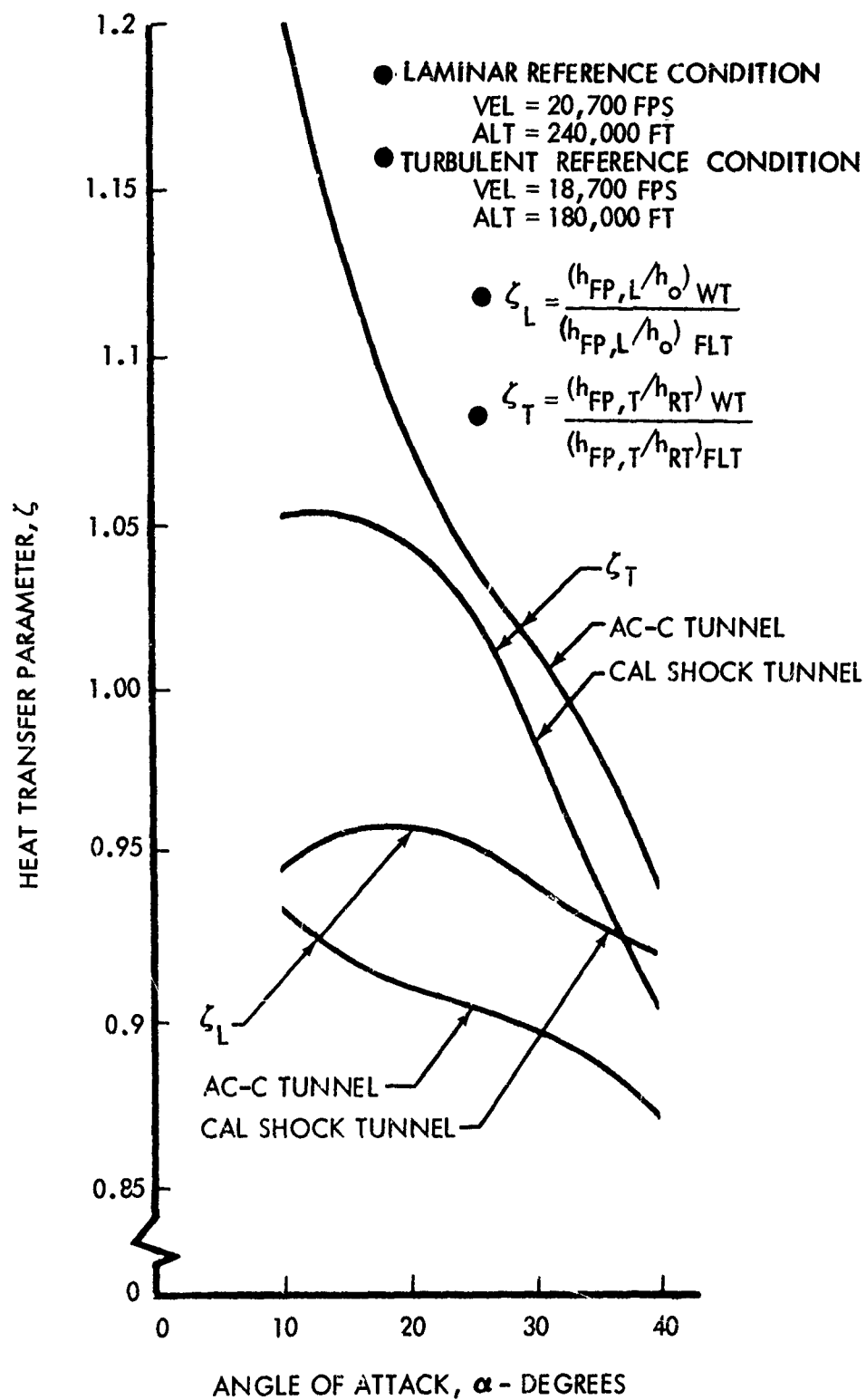


Figure 7-8: SHARP FLAT PLATE HEATING COMPARISON

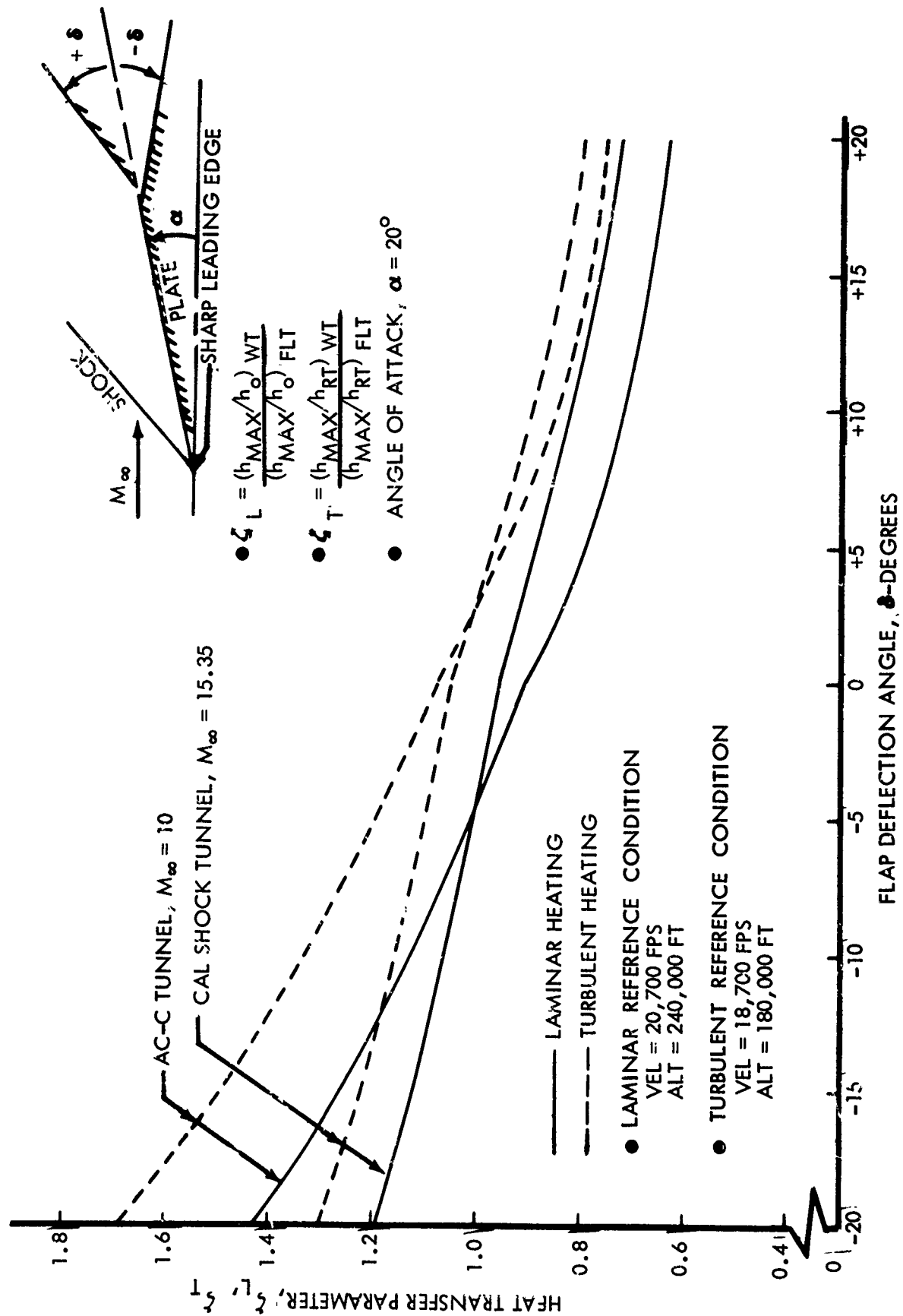


Figure 7-9: FLAP SURFACE HEATING COMPARISON

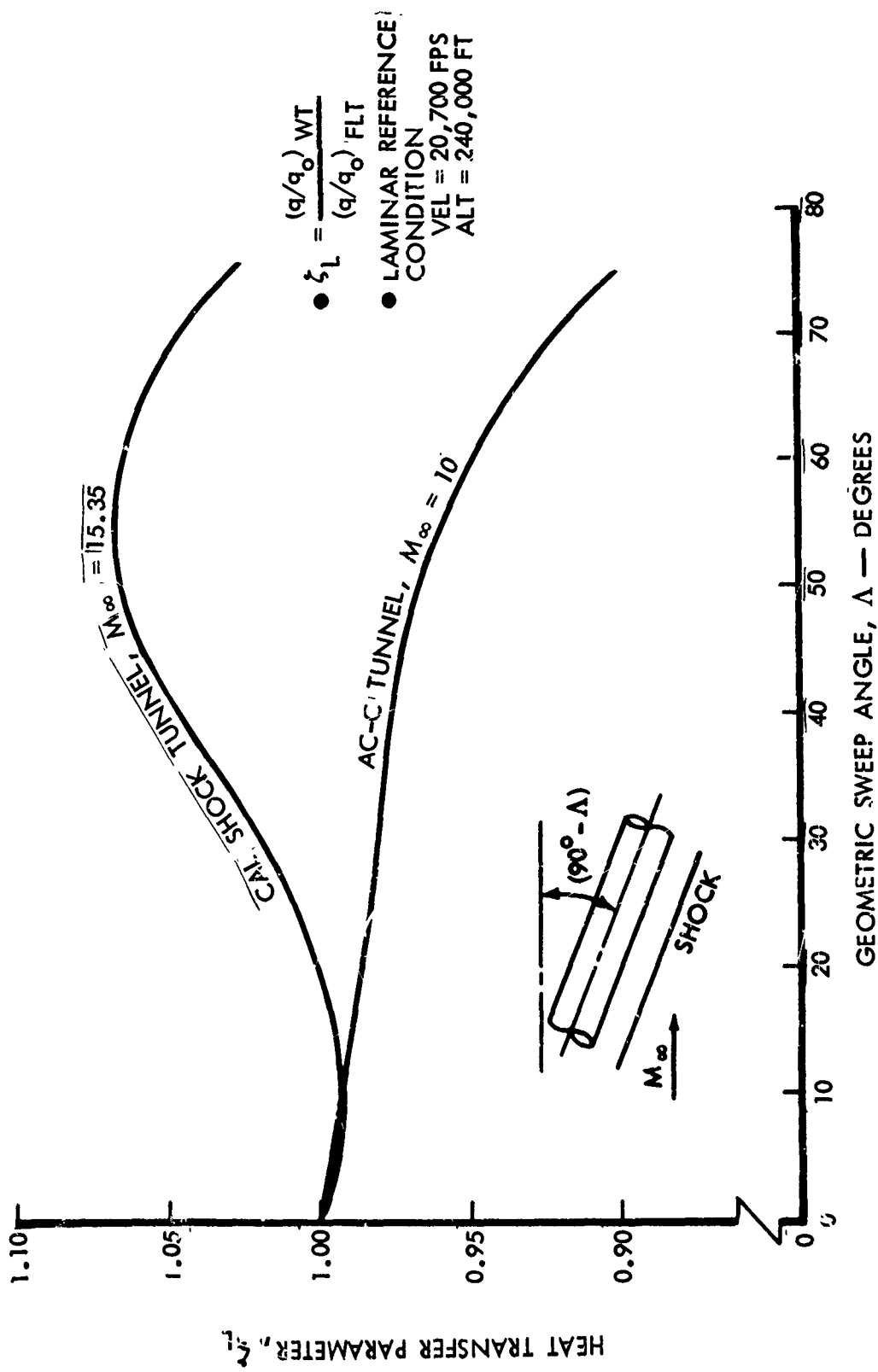


Figure 7-10: SWEEP INFINITE CYLINDER HEATING COMPARISON

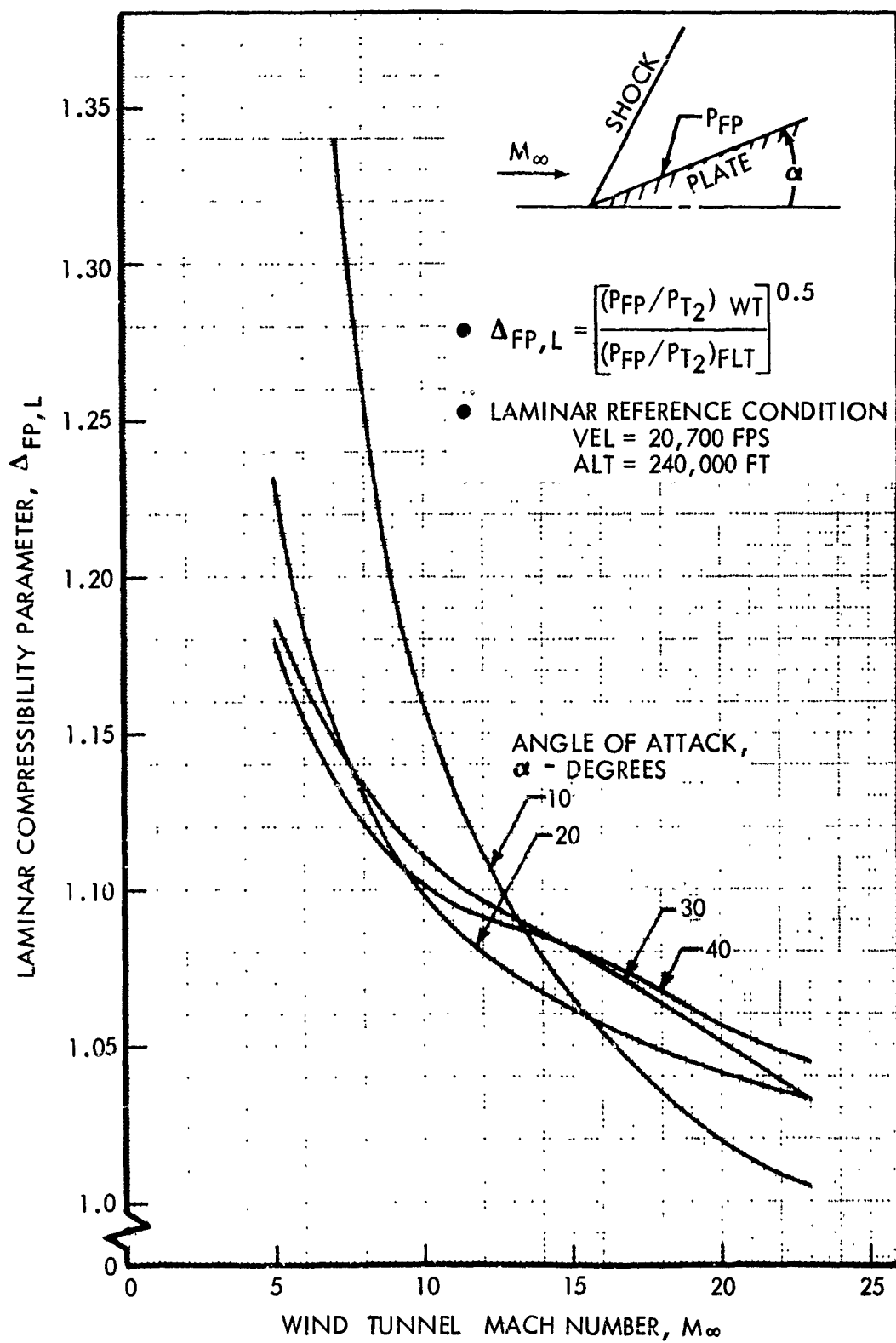


Figure 7-11: SHARP FLAT PLATE LAMINAR COMPRESSIBILITY PARAMETER

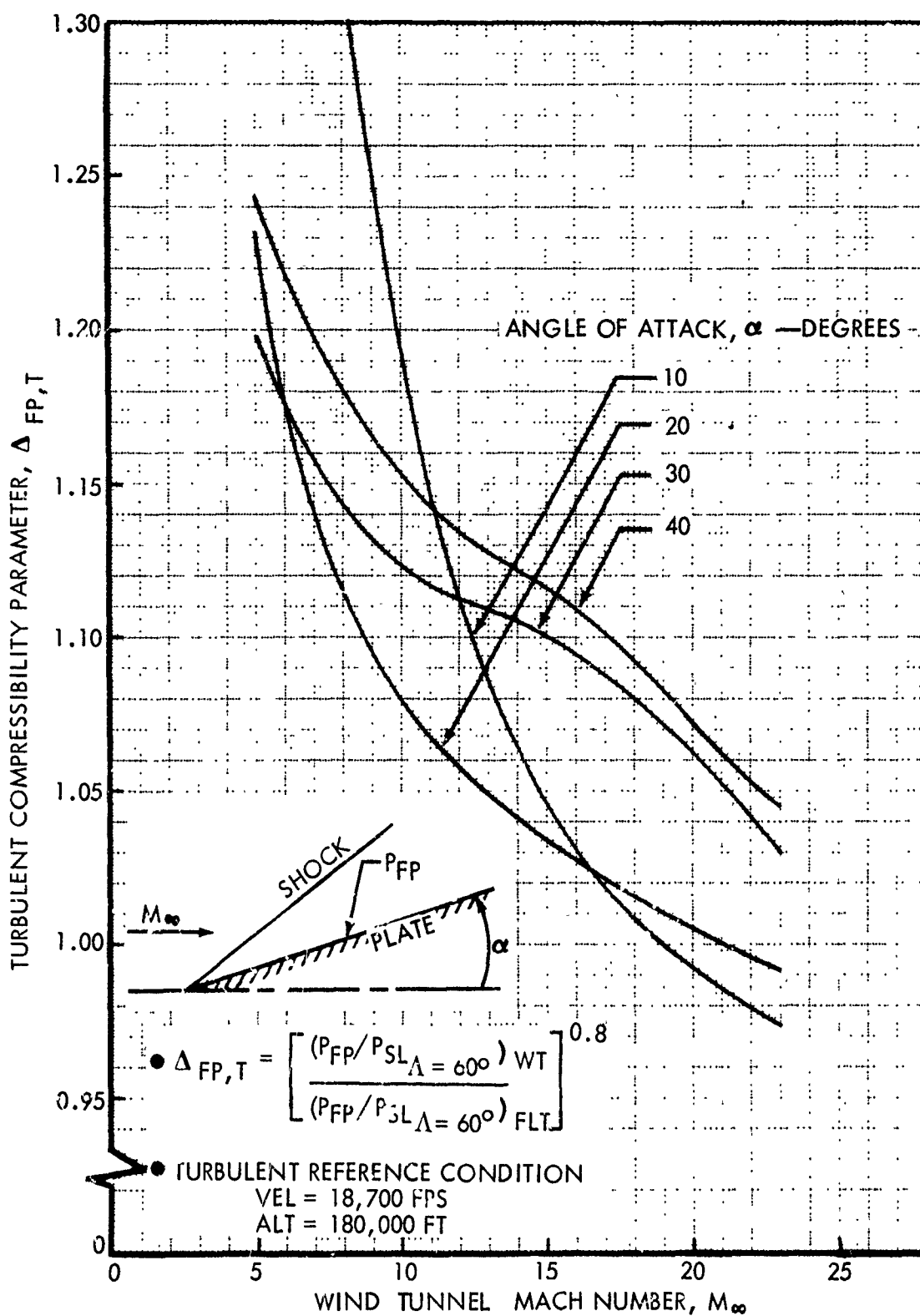


Figure 7-12: SHARP FLAT PLATE TURBULENT COMPRESSIBILITY PARAMETER

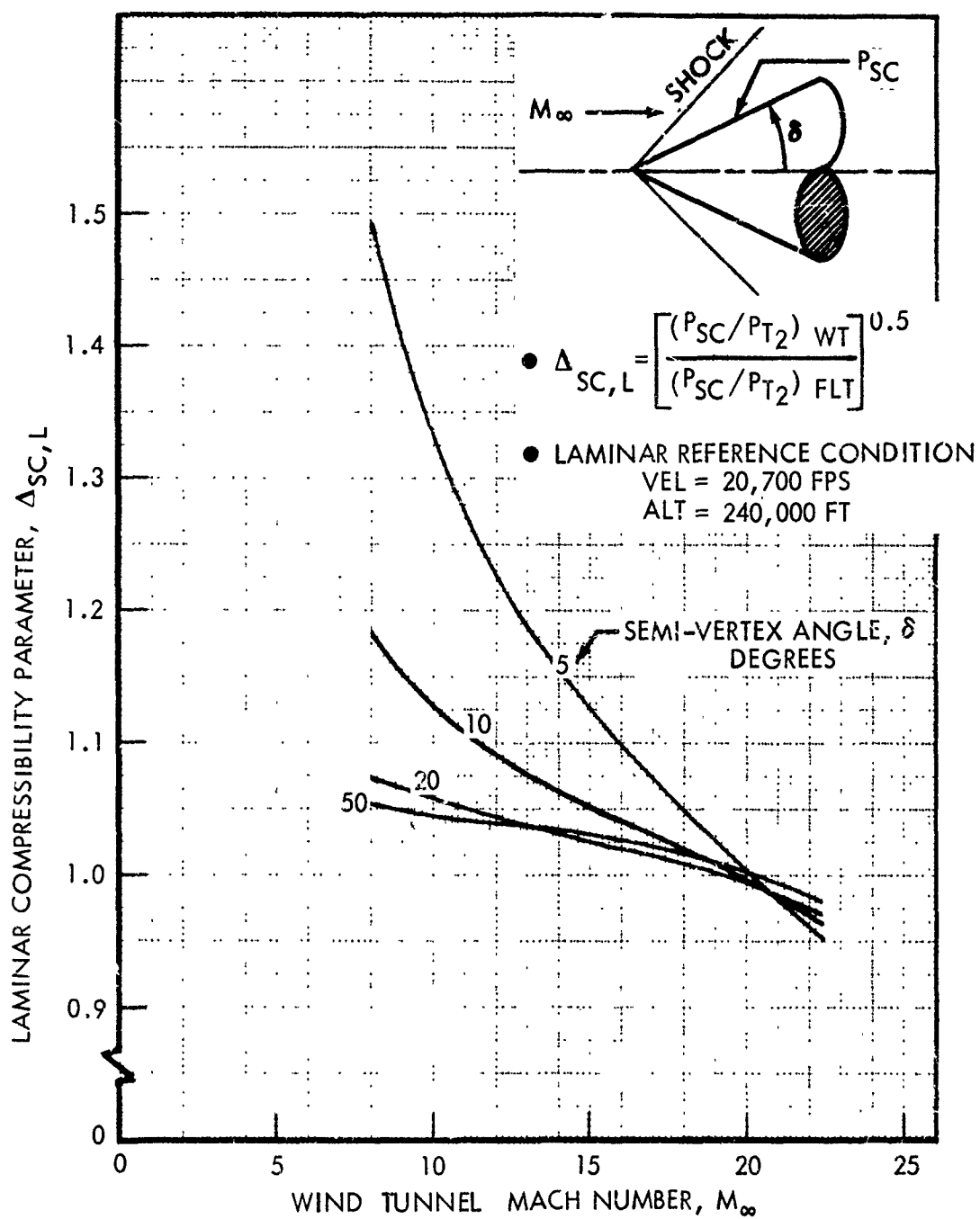


Figure 7-13: UNYAWED SHARP CONE LAMINAR COMPRESSIBILITY PARAMETER

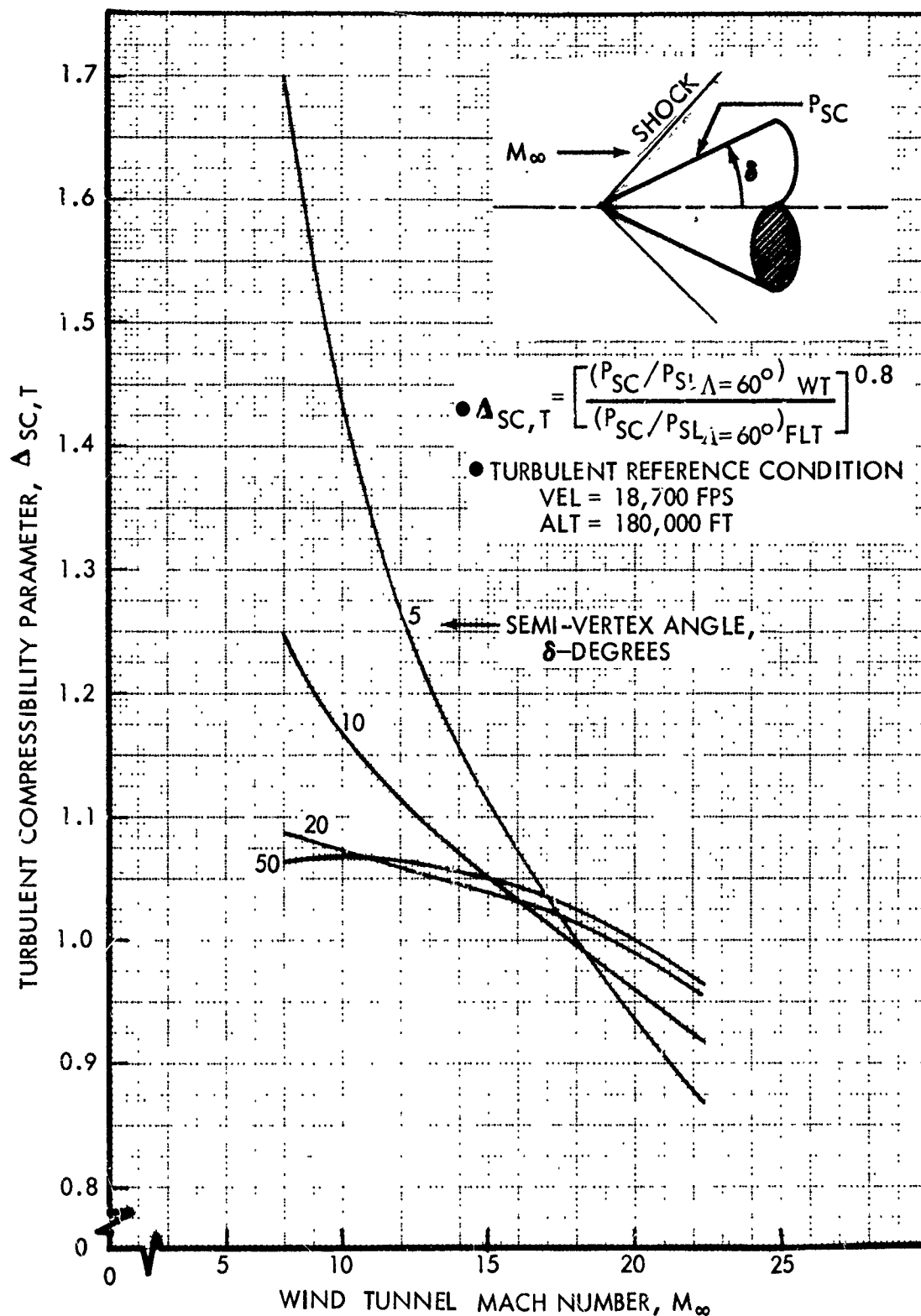


Figure 7-14: UNYAWED SHARP CONE TURBULENT COMPRESSIBILITY PARAMETER

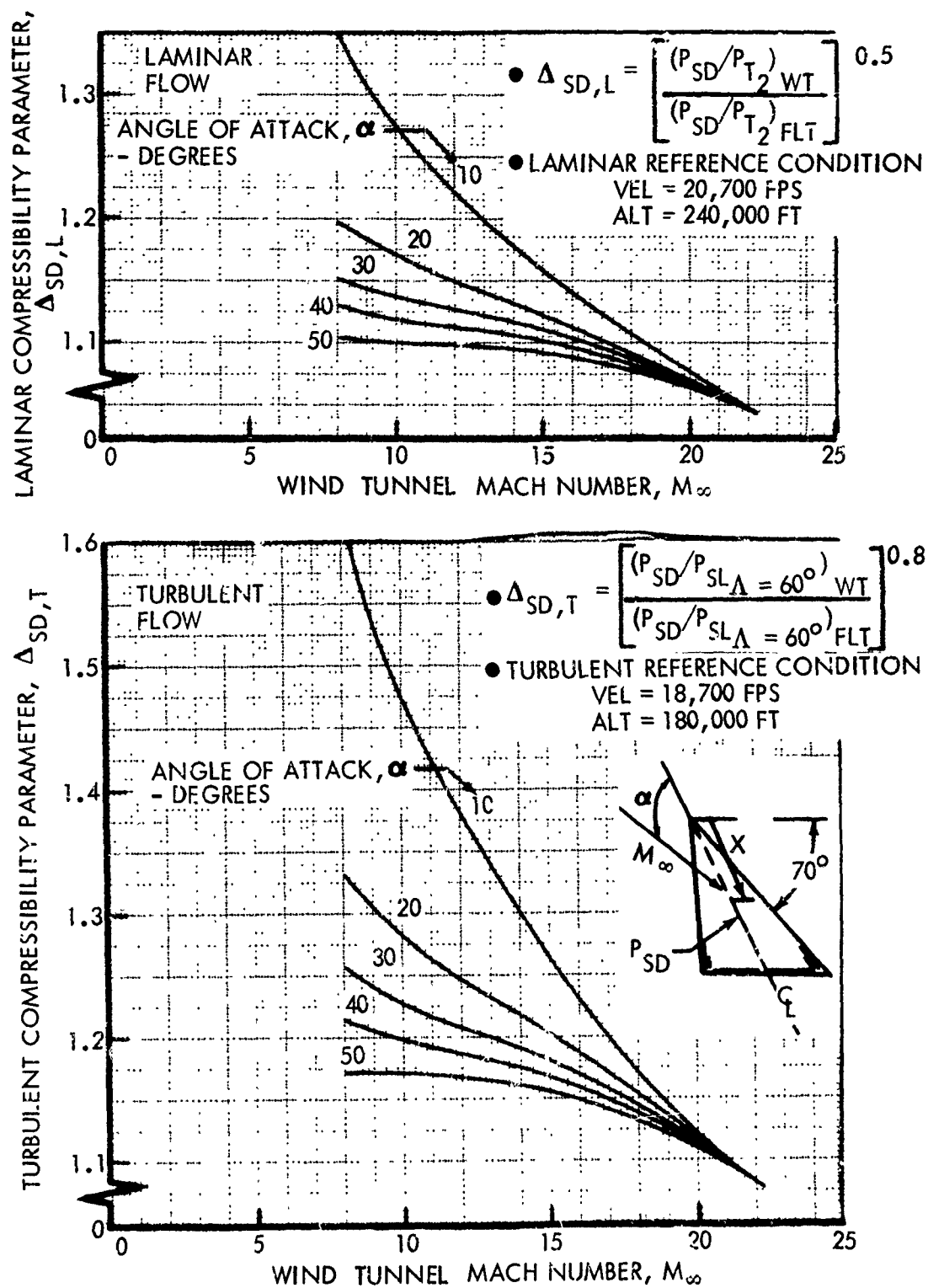


Figure 7-15: SHARP DELTA WING COMPRESSIBILITY PARAMETERS

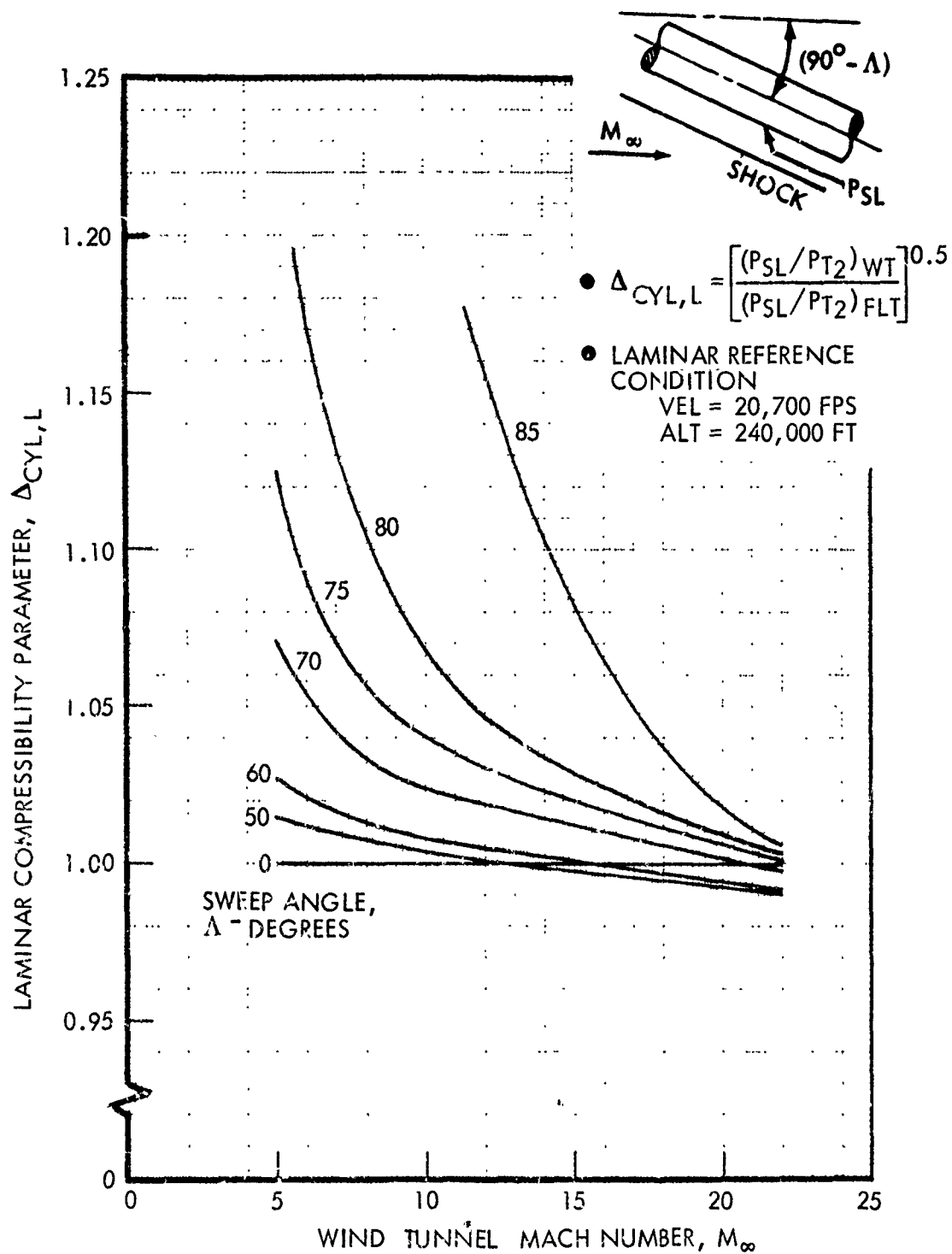


Figure 7-16: SWEPT INFINITE CYLINDER LAMINAR COMPRESSIBILITY PARAMETER

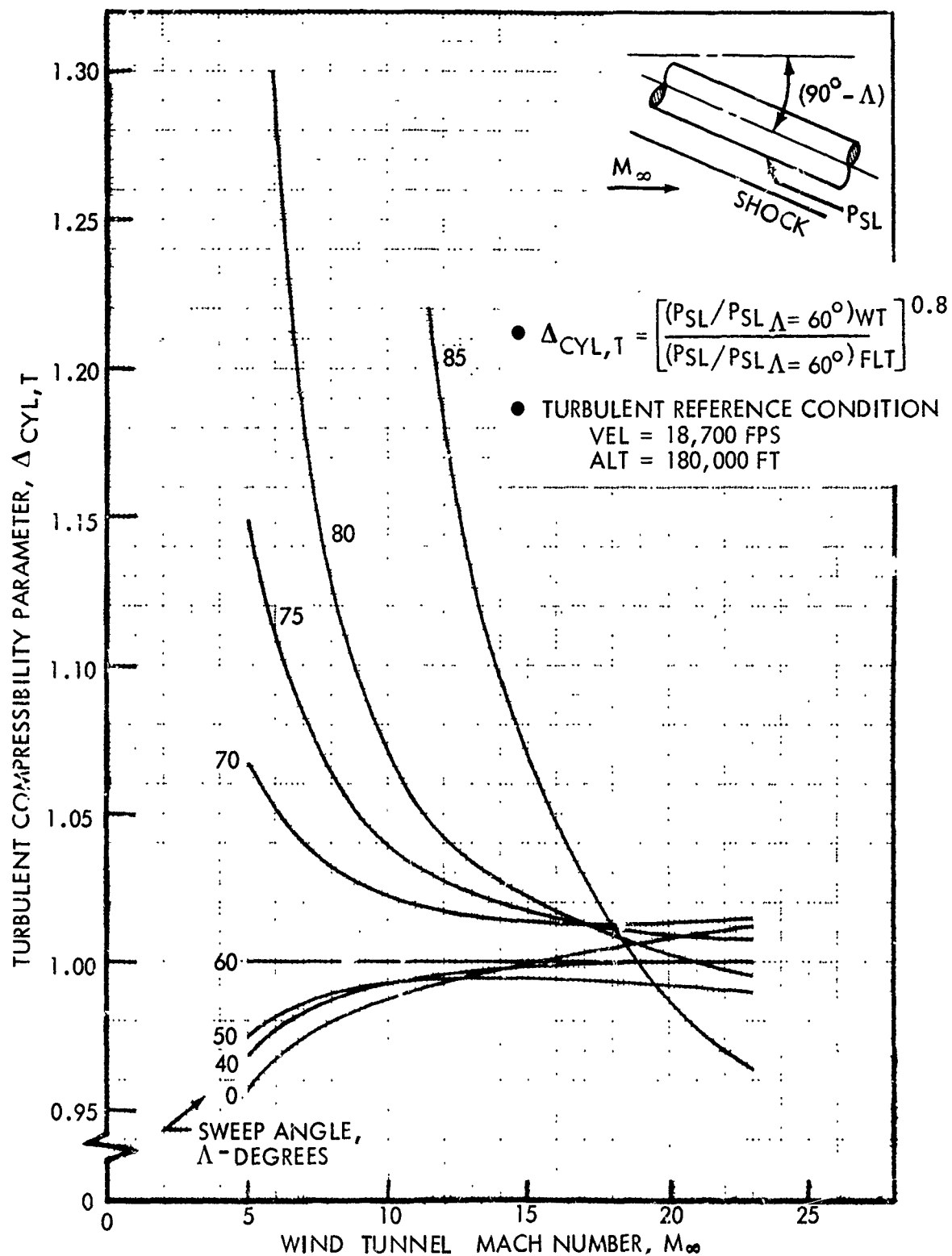


Figure 7-17: SWEPT INFINITE CYLINDER TURBULENT COMPRESSIBILITY PARAMETER

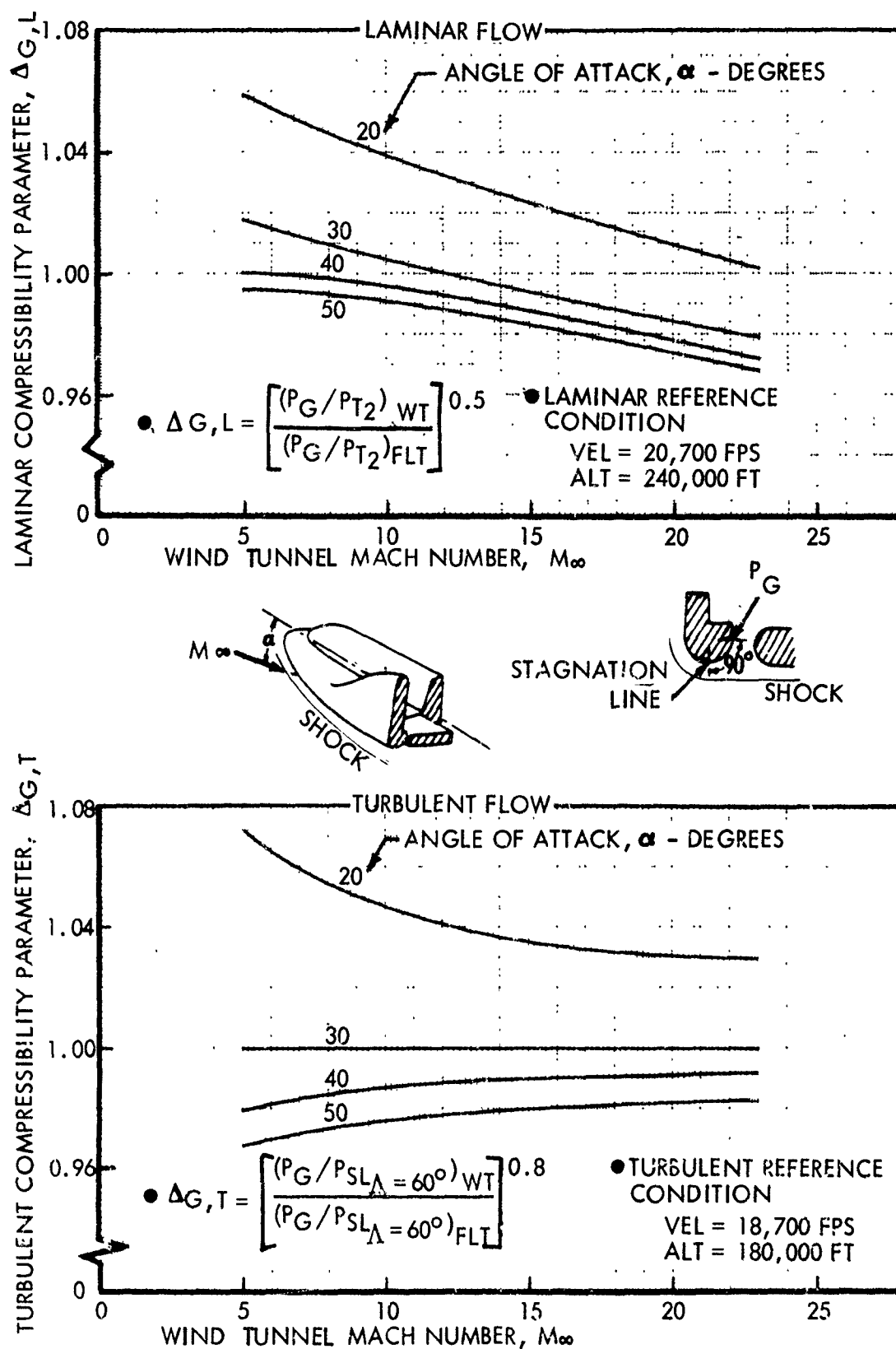


Figure 7-18: CONTROL SURFACE GAP COMPRESSIBILITY PARAMETERS

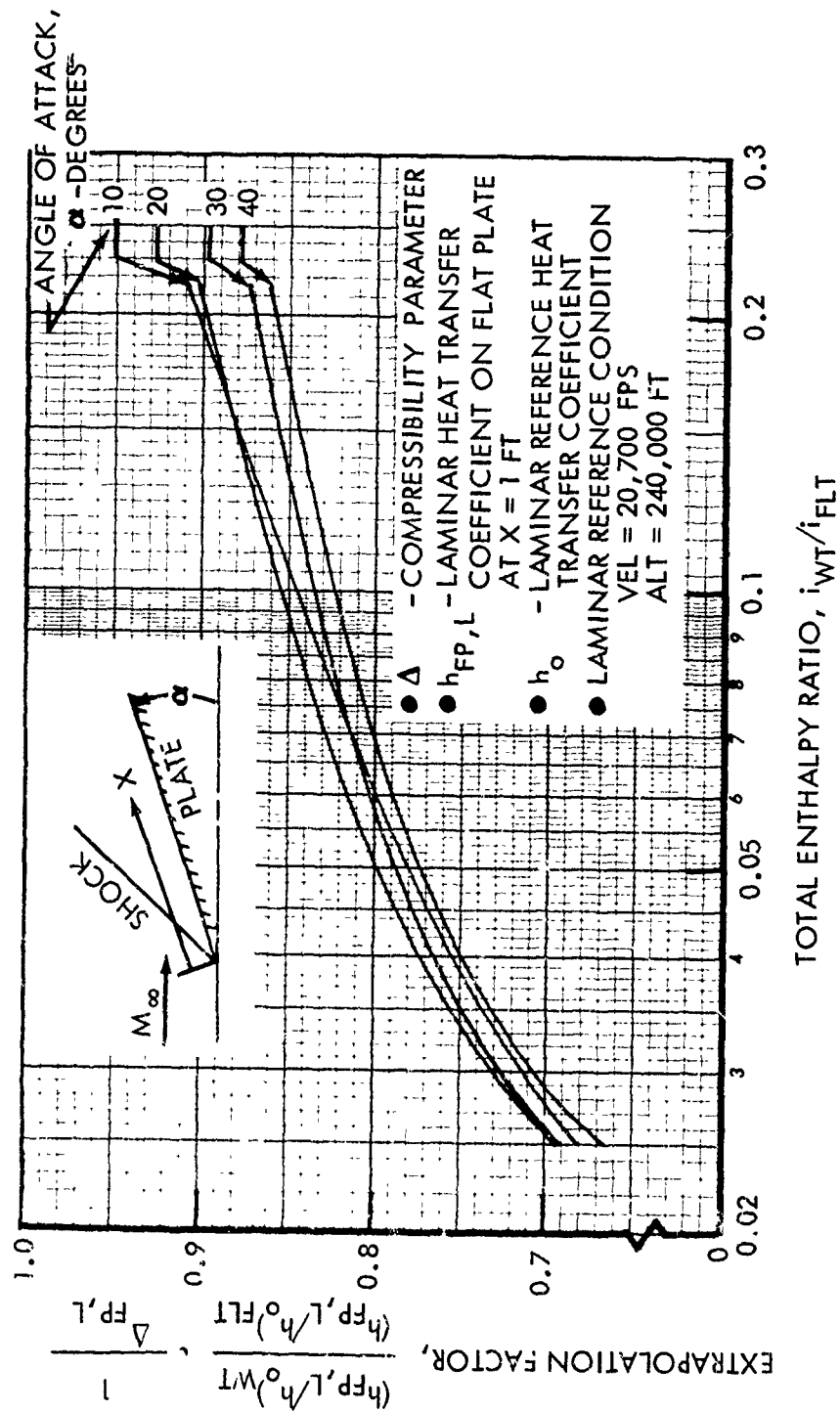


Figure 7-19: SHARP FLAT PLATE LAMINAR HEATING EXTRAPOLATION FACTOR

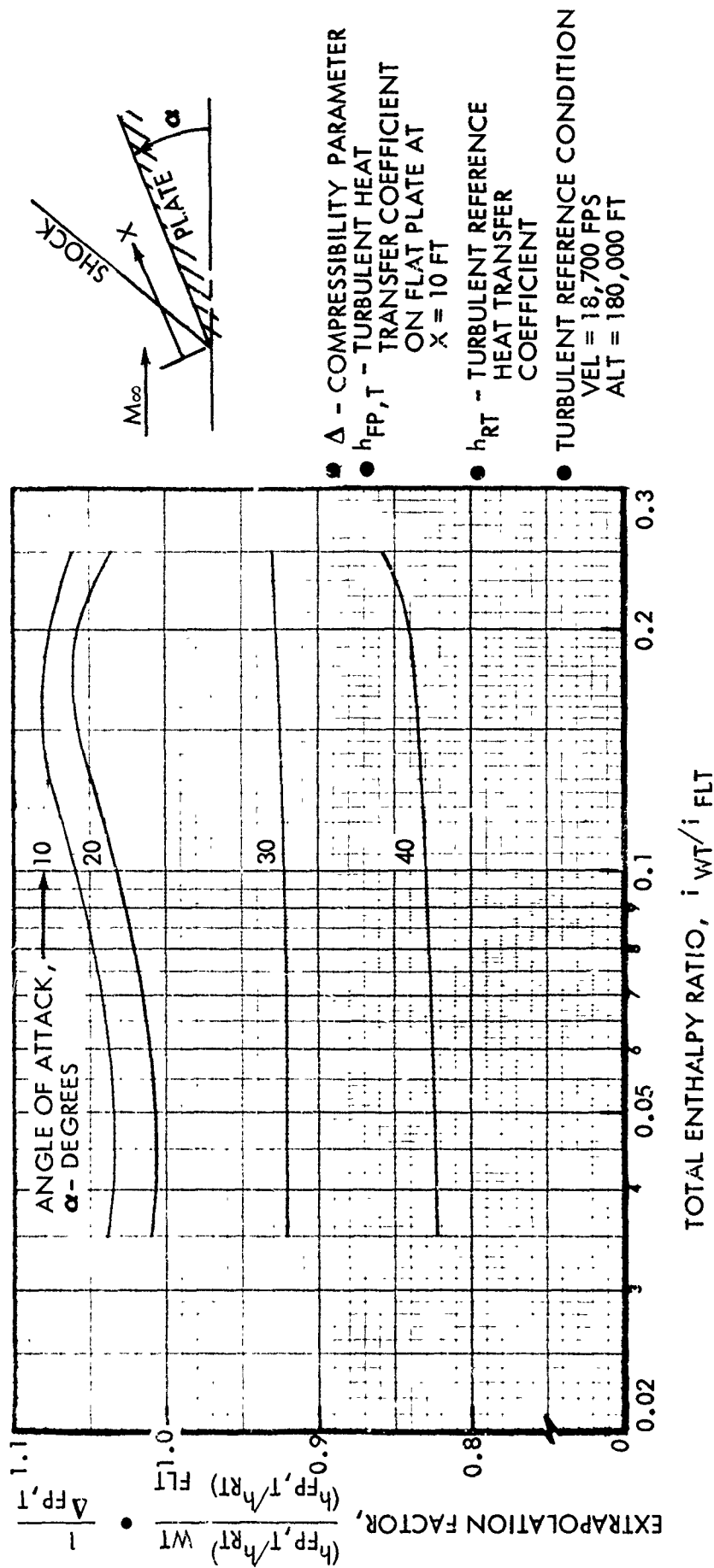


Figure 7-20: SHARP FLAT PLATE TURBULENT HEATING EXTRAPOLATION FACTOR

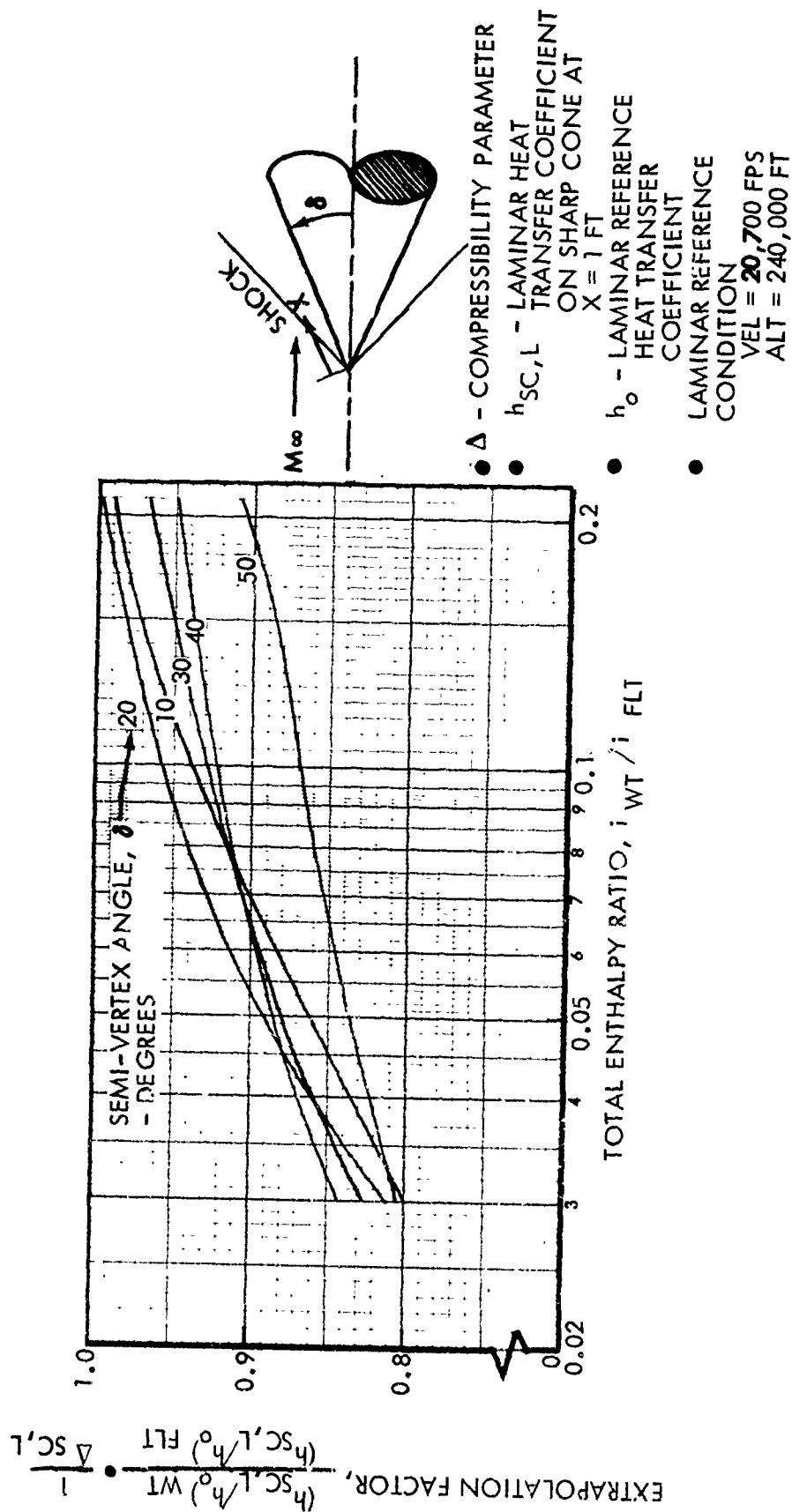


Figure 7-21: UNYAWED SHARP CONE LAMINAR HEATING EXTRAPOLATION FACTOR

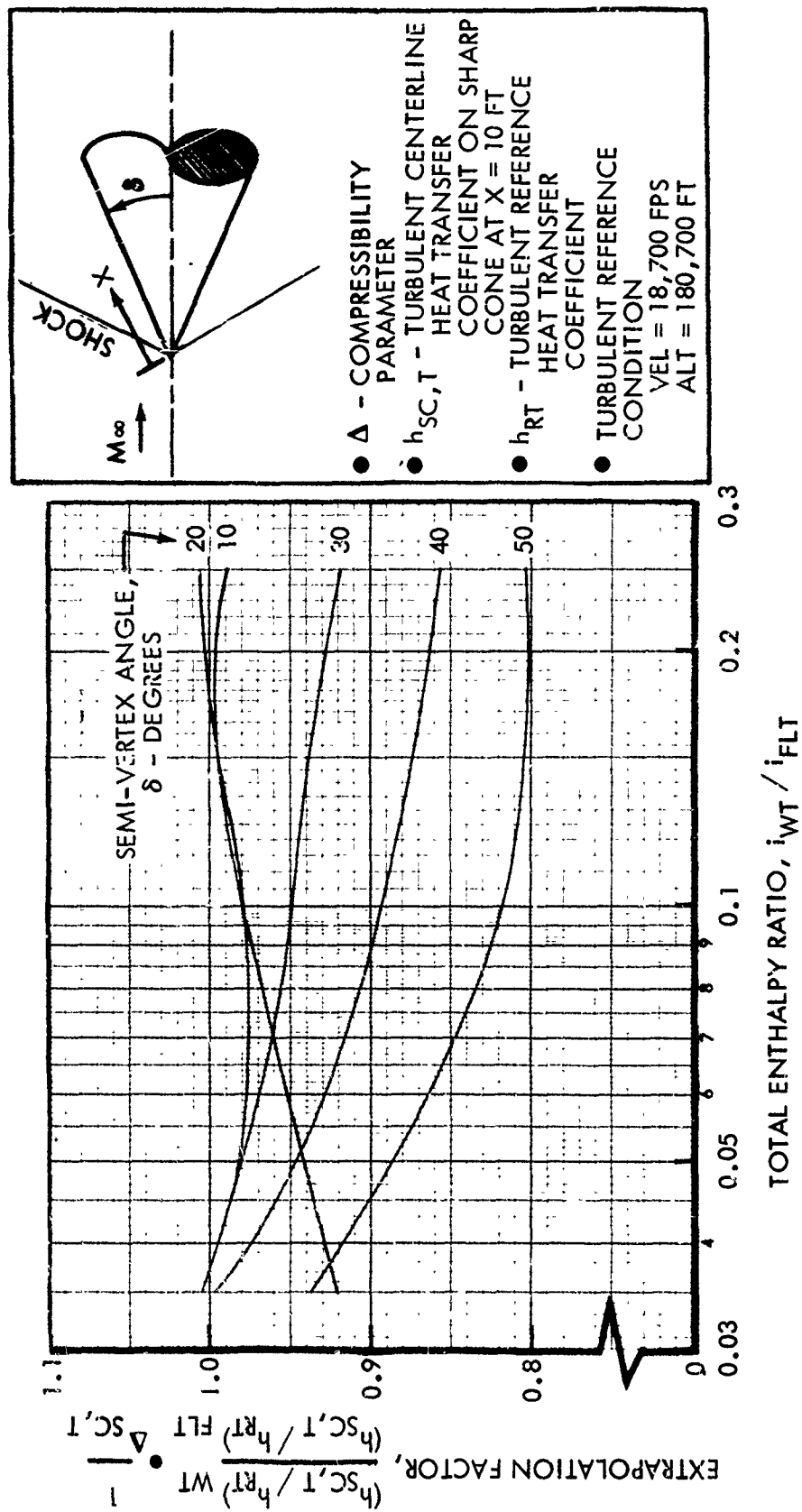


Figure 7-22: UNYAWED SHARP CONE TURBULENT HEATING EXTRAPOLATION FACTOR

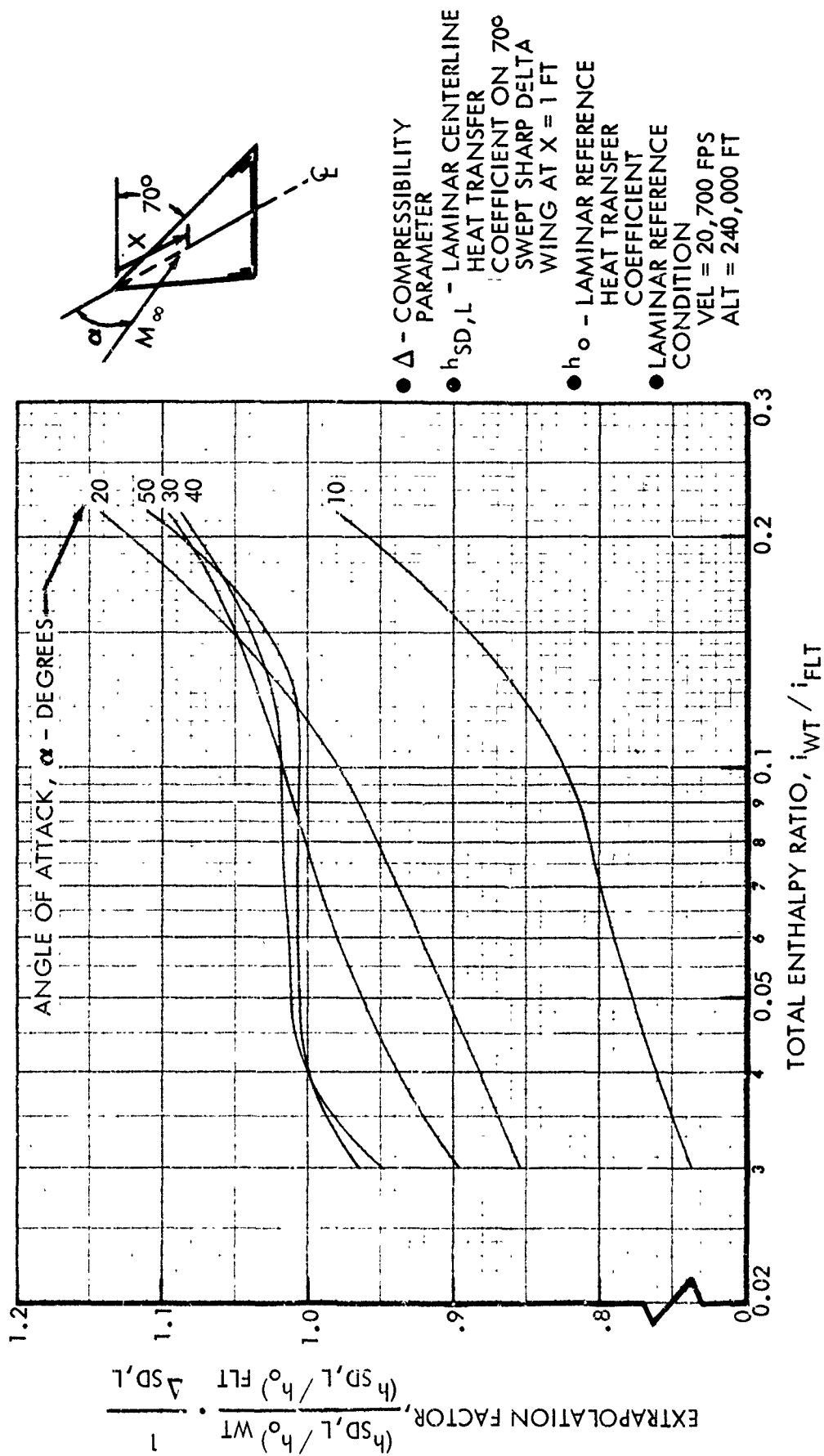


Figure 7-23: SHARP DELTA WING LAMINAR HEATING EXTRAPOLATION FACTOR

- Δ - COMPRESSIBILITY PARAMETER
- $h_{SD,T}$ - TURBULENT CENTER LINE HEAT TRANSFER COEFFICIENT ON 70° SWEEP SHARP DELTA WING AT $X = 10$ FT
- h_{RT} - TURBULENT REFERENCE HEAT TRANSFER COEFFICIENT
- TURBULENT REFERENCE CONDITION
VEL = 18,700 FPS
ALT = 180,000 FT

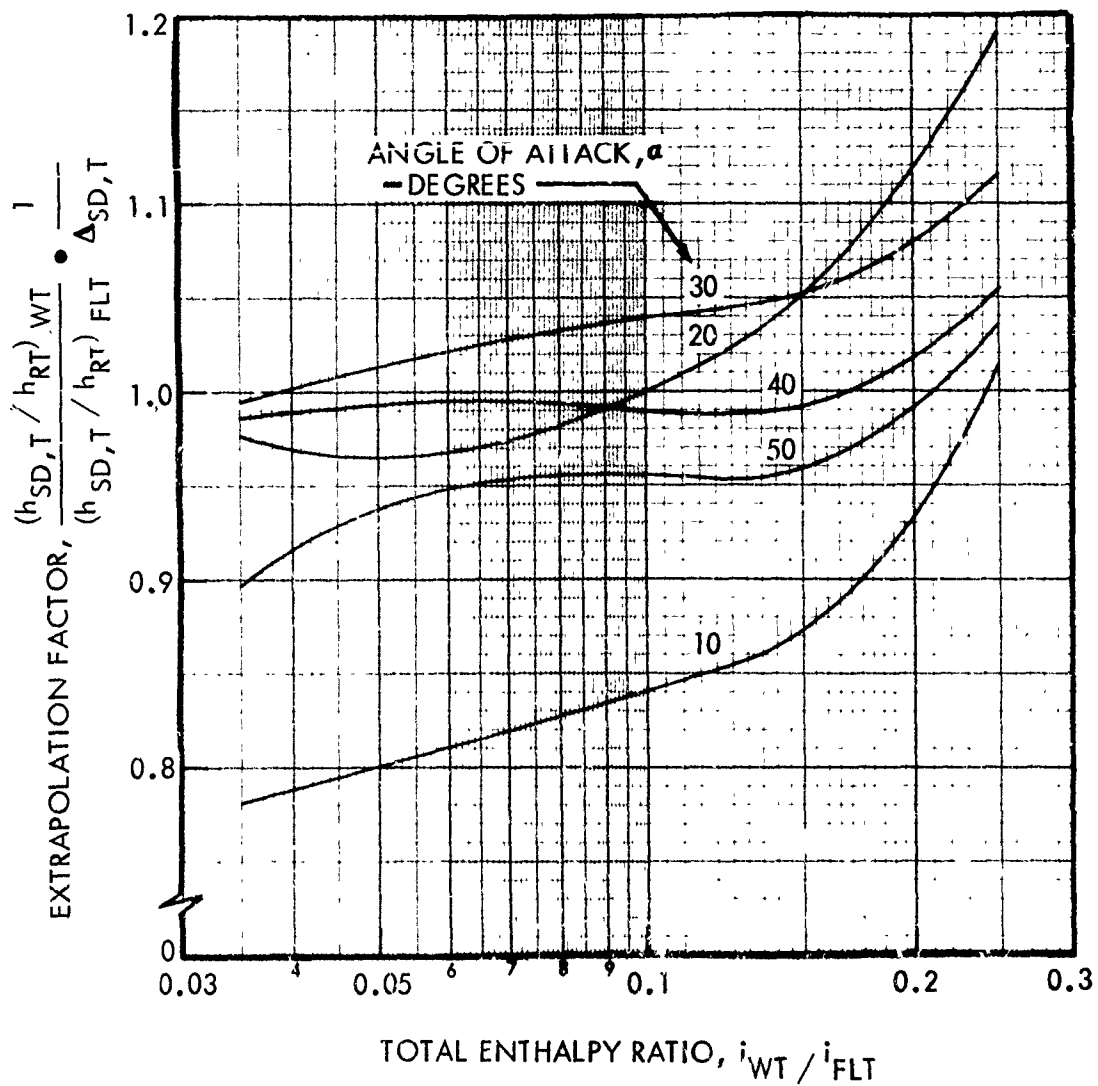
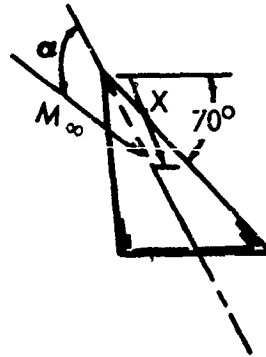


Figure 7-24: SHARP DELTA WING TURBULENT HEATING EXTRAPOLATION FACTOR

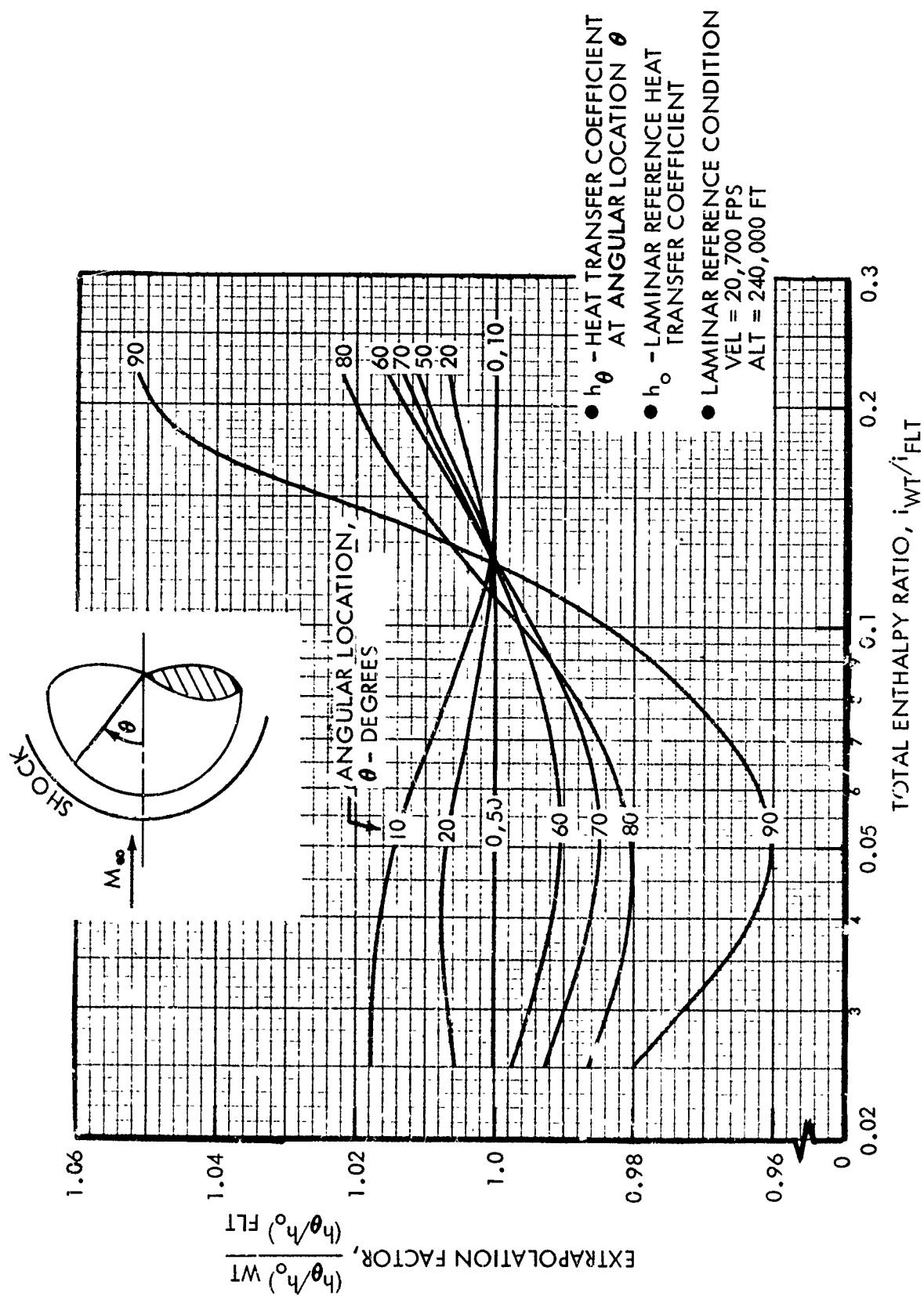


Figure 7-25: HEMISPHERE LAMINAR HEATING EXTRAPOLATION FACTOR

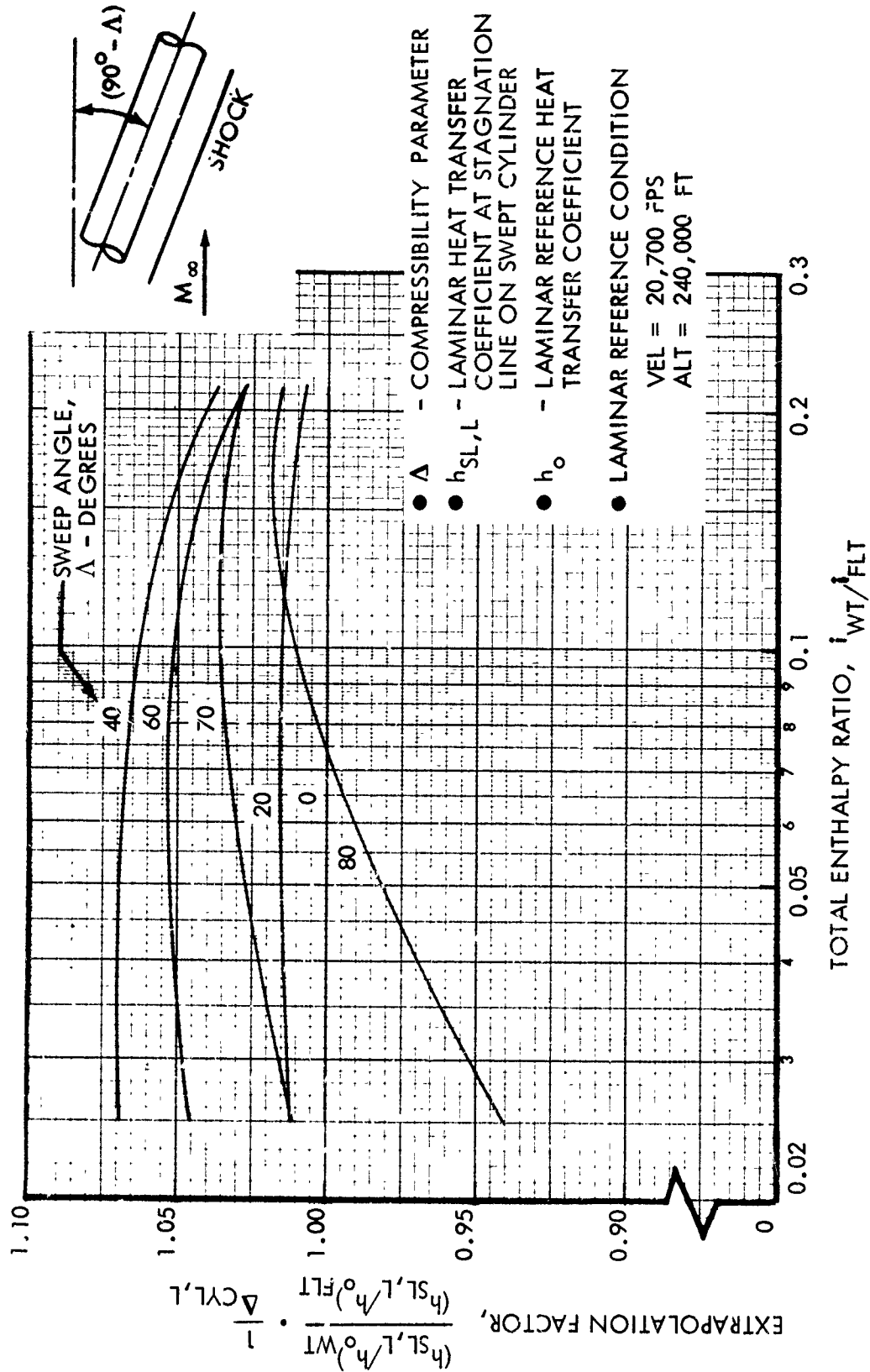
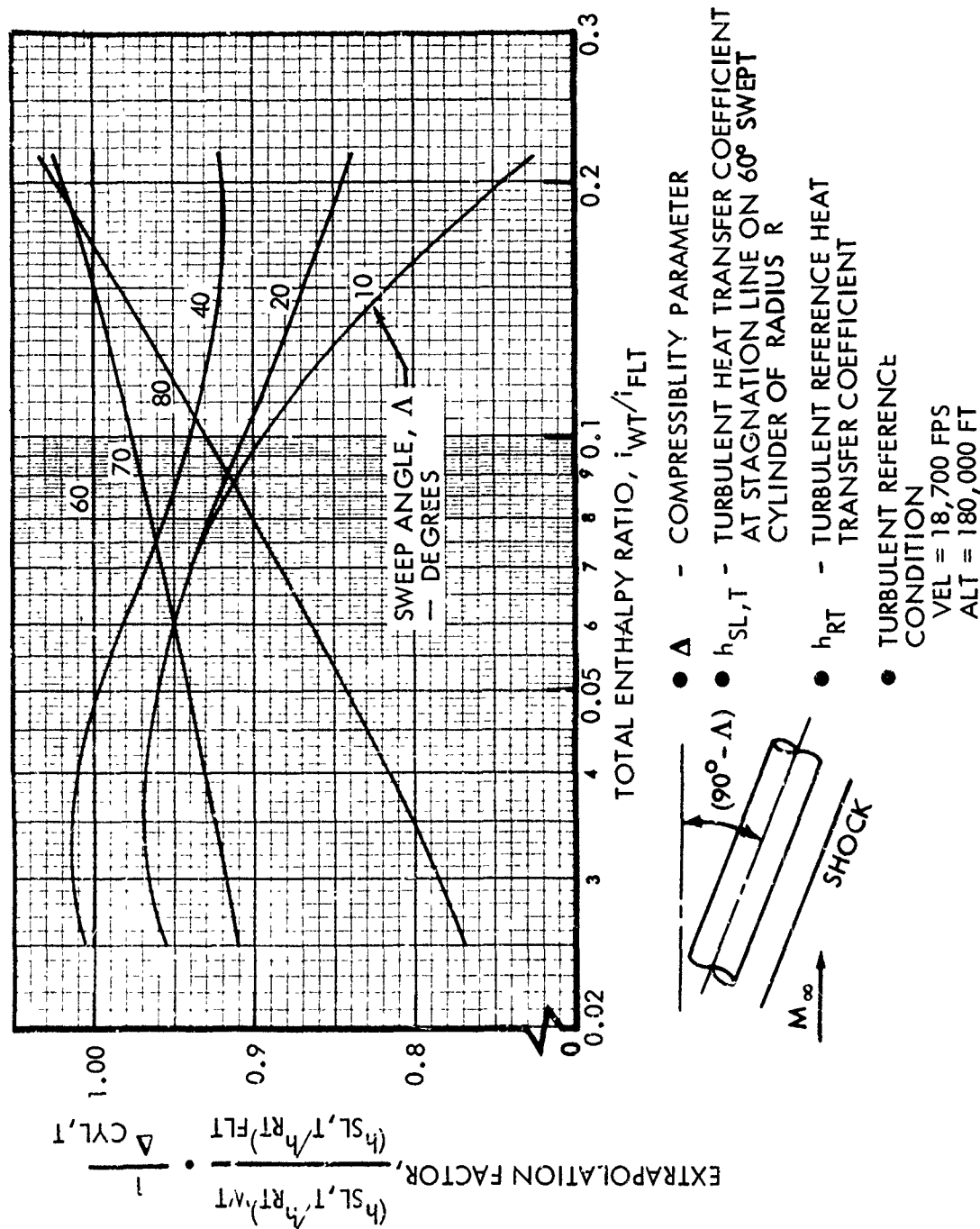


Figure 7-26: SWEEP INFINITE CYLINDER LAMINAR HEATING EXTRAPOLATION FACTOR



137 Figure 7-27: SWEEP INFINITE CYLINDER TURBULENT HEATING EXTRAPOLATION FACTOR

- Δ - COMPRESSIBILITY PARAMETER
- $h_{G,L}$ - LAMINAR HEAT TRANSFER COEFFICIENT ON FIN SURFACE 90° FROM STAGNATION LINE
- h_o - LAMINAR REFERENCE HEAT TRANSFER COEFFICIENT
- LAMINAR REFERENCE CONDITION
VEL = 20,700 FPS
ALT = 240,000 FT

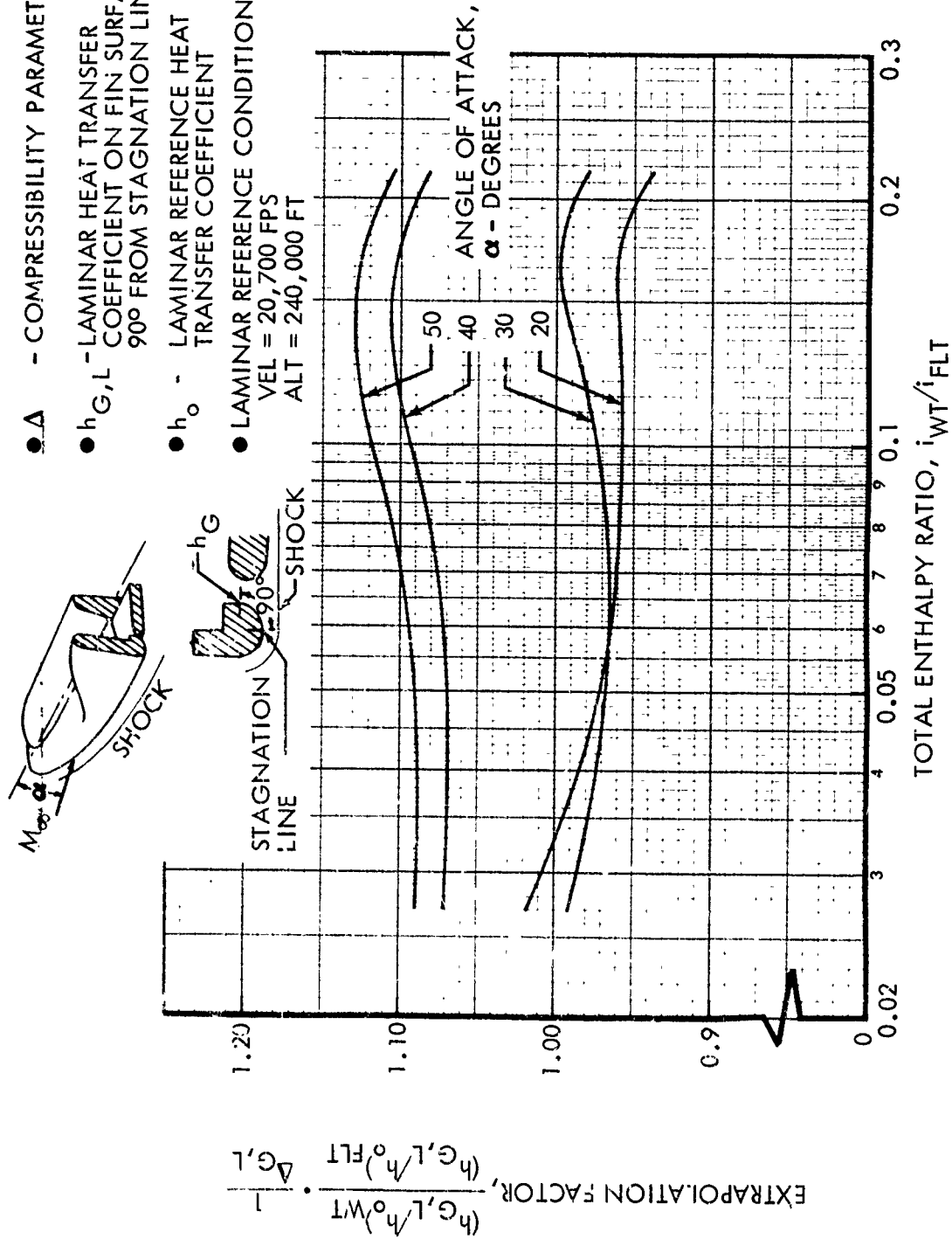


Figure 7-28: CONTROL SURFACE GAP LAMINAR HEATING EXTRAPOLATION FACTOR

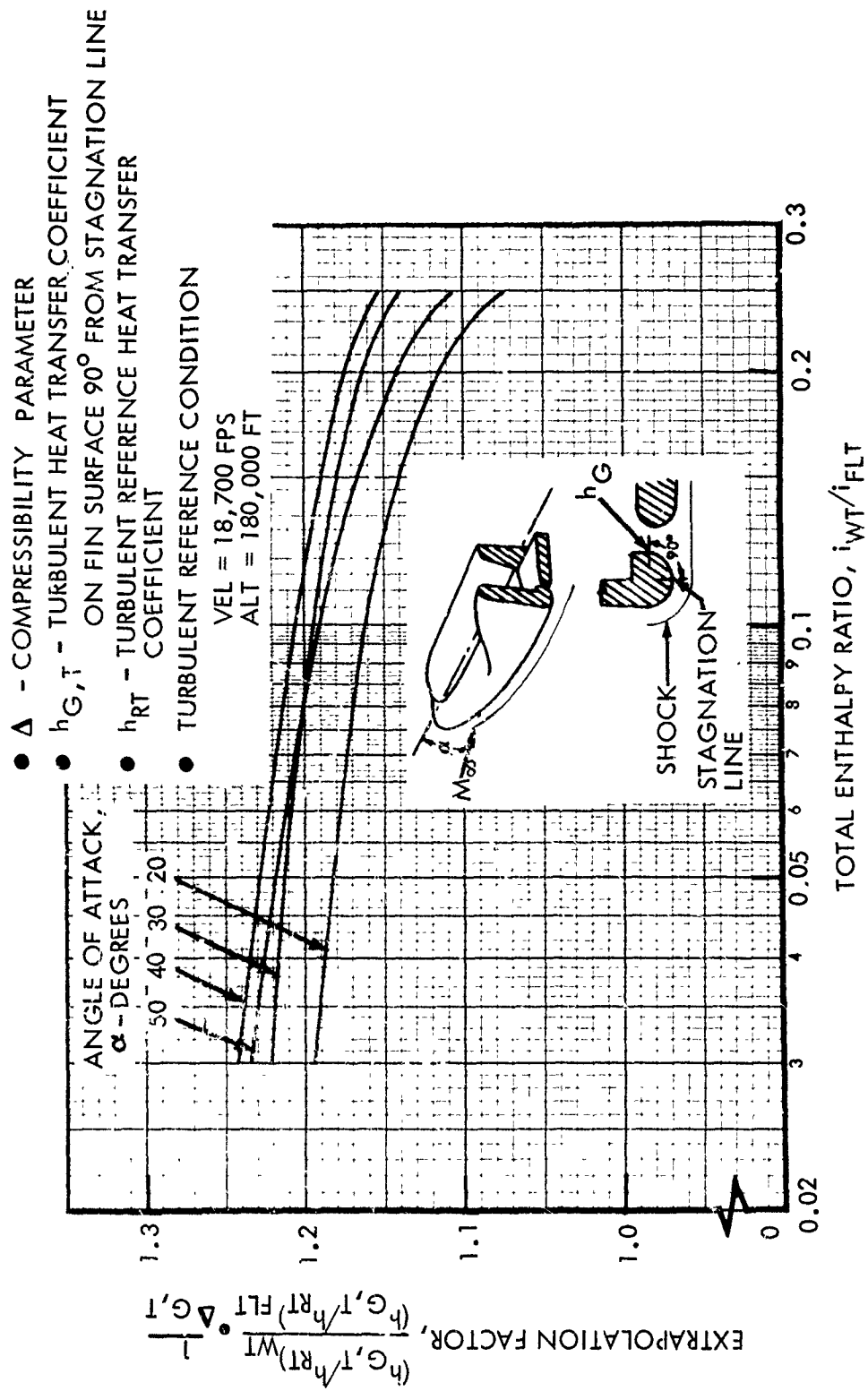


Figure 7-29: CONTROL SURFACE GAP TURBULENT HEATING EXTRAPOLATION FACTOR

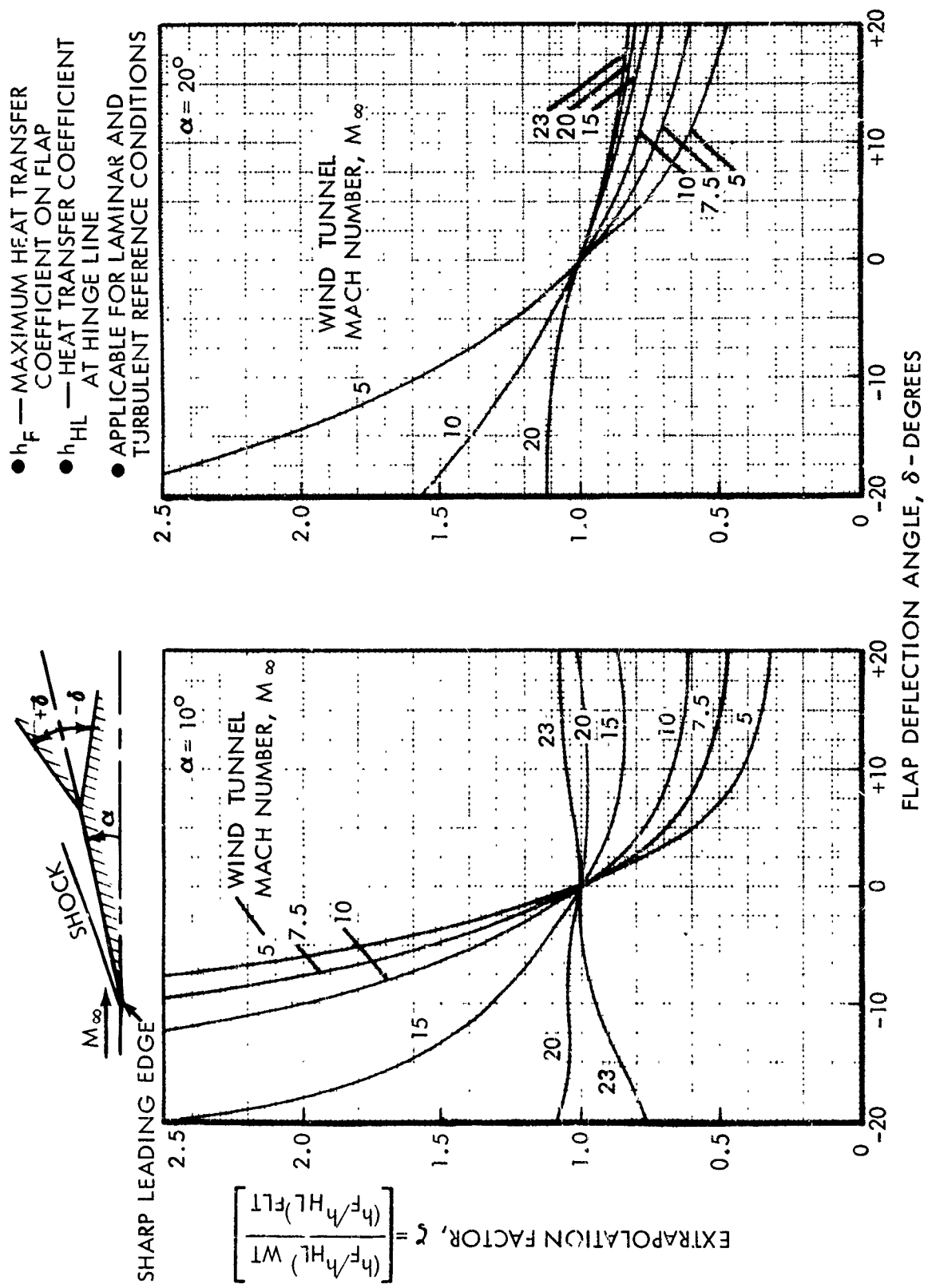
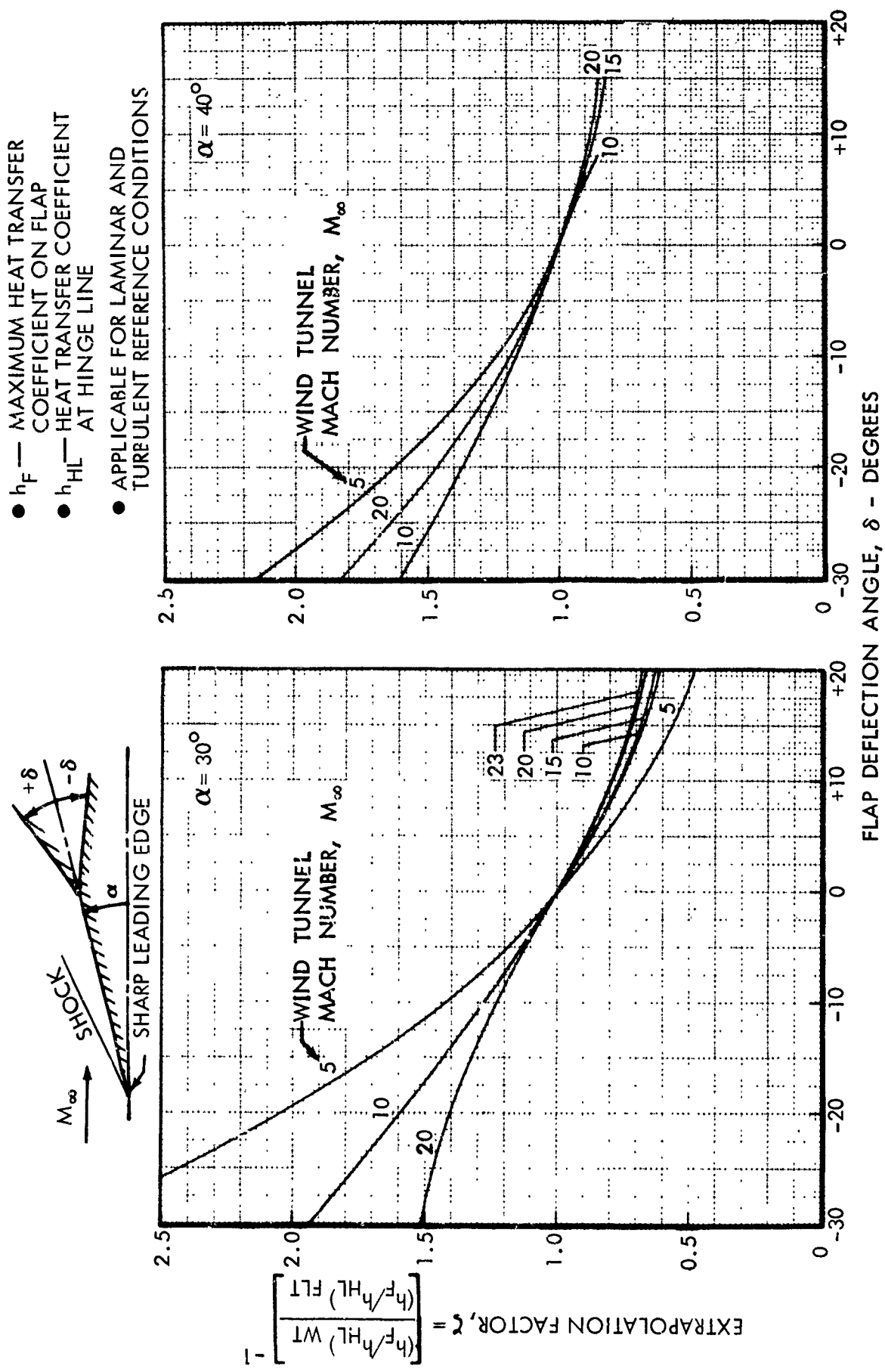


Figure 7-30: FLAP SURFACE HEATING EXTRAPOLATION FACTOR



- h_F — MAXIMUM HEAT TRANSFER COEFFICIENT ON FLAP
- h_{HL} — HEAT TRANSFER COEFFICIENT AT HINGE LINE
- APPLICABLE FOR LAMINAR AND TURBULENT REFERENCE CONDITIONS

Figure 7-31: FLAP SURFACE HEATING EXTRAPOLATION FACTOR

APPENDIX A

SIMPLIFIED EQUATIONS

Simplified equations have been developed for modified Newtonian pressure coefficients, figure 2-4, reference heat transfer coefficients, figures 6-2 and 6-4, reference Reynolds number, figures 6-7 and 6-8, and the local reference Reynolds numbers at the location of maximum turbulent heating, figure 6-10 and 6-20. Heat-transfer coefficients have the units, Btu/ft²-sec-°R.

The pressure coefficient equation was developed for $\gamma = 1.1$ and does not apply to wind tunnel conditions. All other equations for both wind-tunnel and flight conditions were developed from numerical results using the $\rho_r \mu_r$ method, Appendix B. The 1962 U. S. Standard Atmosphere defines the flight conditions.

The accuracy of the equations in general is $\pm 4\%$ or better. Simplified equations applicable to wind tunnels have been developed in terms of free-stream conditions instead of the more desirable stagnation chamber conditions because difficulty was experienced in obtaining a simple form of the equation. Free-stream conditions, however, can be accurately and easily converted to stagnation chamber conditions using figure A1 and equation (A15).

A. Modified Newtonian Pressure Coefficient

For a ratio of specific heats equal to 1.1 the charts on figure 2-4 can be approximated by the following equation

$$\frac{C_p}{\sin^2 \delta} = \left\{ 1.05 + \left[1.1025 + \frac{4}{M_\infty^2 \sin^2 \delta} \right]^{1/2} \right\} - 1.278 \frac{M_\infty^2 \sin^2 \delta}{M_\infty^{2.6}} \quad (A1)$$

B. Reference Heat Transfer Coefficient

1. Laminar

The reference laminar heat-transfer coefficient h_o can be approximated for wind-tunnel and flight conditions by the following equations.

(a) Wind Tunnel

$$h_o = \frac{0.004}{R^{0.5}} \left(\frac{P_\infty}{P_{ATM}} \right)^{0.5} M_\infty^{1.18} T_\infty^{0.12} \quad (A2)$$

(b) Flight

$$\begin{aligned}
 h_0 &= \frac{0.24}{R^{0.5}} \left(\frac{P_\infty}{P_{ATM}} \right)^{0.5} \left(\frac{V_\infty}{10^4} \right)^{1.16} \left(\frac{T_\infty}{100} \right)^{-0.5} \\
 &= \frac{0.1055}{R^{0.5}} \left(\frac{\rho_\infty}{\rho_{ATM}} \right)^{0.5} \left(\frac{V_\infty}{10^4} \right)^{1.16}
 \end{aligned} \tag{A3}$$

2. Turbulent

The reference turbulent heat-transfer coefficient, h_{RT} , can be approximated for wind-tunnel and flight conditions by the following equations.

(a) Wind Tunnel

$$h_{RT} = \frac{0.0435}{R^{0.2}} \left(\frac{P_\infty}{P_{ATM}} \right)^{0.8} M_\infty^{1.46} T_\infty^{-0.114} \tag{A4}$$

(b) Flight

$$\begin{aligned}
 h_{RT} &= \frac{1.67}{R^{0.2}} \left(\frac{P_\infty}{P_{ATM}} \right)^{0.78} \left(\frac{V_\infty}{10^4} \right)^{1.54} \left(\frac{T_\infty}{100} \right)^{-0.82} \\
 &= \frac{0.437}{R^{0.2}} \left(\frac{\rho_\infty}{\rho_{ATM}} \right)^{0.78} \left(\frac{V_\infty}{10^4} \right)^{1.54}
 \end{aligned} \tag{A5}$$

Equations (A4) and (A5) are applicable only for flow conditions where turbulence is expected, and where the cylinder radius is near 1 foot. If the radius is much different from 1 foot the $(1/R^{0.2})$ term creates large errors. An alternate method has been developed that uses the above equations as a base and increases the accuracy to within $\pm 0.5\%$. This method follows:

1. Calculate h_{RT} with $R = 1$ foot using equation A4 or A5.
2. Calculate a reference Reynolds number, R_R , using the method described in C. below.
3. Correct h_{RT} to the desired radius by using figure 6-6 of Section VI.

C. Reference Reynolds Number (R_R)

The reference Reynolds number, R_R , is approximated for wind tunnel and flight conditions by the following equations:

(a) Wind Tunnel

$$R_R = 2.65 \times 10^8 \left(\frac{P_\infty}{P_{ATM}} \right)^{0.937} M_\infty^{-0.679} T_\infty^{-0.679} R \quad (A6)$$

(b) Flight

$$\underline{V_\infty < 13,000 \text{ FPS}}$$

$$R_R = 1.55 \times 10^8 \left(\frac{P_\infty}{P_{ATM}} \right) \left(\frac{V_\infty}{10^4} \right)^{1.436} \left(\frac{T_\infty}{100} \right)^{-1.12} R \quad (A7)$$

$$\underline{V_\infty \geq 13,000 \text{ FPS}}$$

$$R_R = 1.288 \times 10^8 \left(\frac{P_\infty}{P_{ATM}} \right)^{1.02} \left(\frac{V_\infty}{10^4} \right)^{1.232} \left(\frac{P_\infty}{P_{ATM}} \right)^{-0.040} \left(\frac{T_\infty}{100} \right)^{-1.0} R \quad (A8)$$

D. Reference Reynolds Number at Location of Maximum Turbulent Heating ($R_{r_{MAX}}$)

The significance of the local reference Reynolds number at the location corresponding to maximum turbulent heating on a hemisphere and unswept cylinder is that it is unique and can be defined in terms of free stream velocity and altitude. The approximate equations for $R_{r_{MAX}}$ for both flight and wind tunnel

are accurate to $\pm 15\%$. At first this appears as a poor approximation, but $R_{r_{MAX}}$ is only required to determine the heat transfer ratio $\frac{h_{MAX}}{h_{SP}}$ and the

location of maximum turbulent heating, θ_{MAX} . The ratio $\frac{h_{MAX}}{h_{SP}}$ is not sensitive

to $R_{r_{MAX}}$. For example, in the range where turbulent flow can be expected, a 10% change in $R_{r_{MAX}}$ will result in a $\frac{1}{2}\%$ change in the ratio $\frac{h_{MAX}}{h_{SP}}$. The

location of maximum turbulent heating, θ_{MAX} , is for practical design purposes independent of $R_{r_{MAX}}$.

1. Hemisphere

Approximate equations for the local reference Reynolds number, $R_{r_{MAX}}$ for a hemisphere have an accuracy of $\pm 15\%$. These equations are:

(a) Wind Tunnel

$$R_{r_{MAX}} = 1.42 \times 10^8 \frac{(P_{\infty}/P_{ATM})}{T_{\infty}^{0.679}} M_{\infty}^{0.287} \quad (A9)$$

(b) Flight

$$\begin{aligned} & \underline{V_{\infty} < 13,000 \text{ FPS}} \\ R_{r_{MAX}} &= 0.91 \times 10^7 \left(\frac{P_{\infty}}{P_{ATM}} \right) \left(\frac{V_{\infty}}{10^4} \right)^{0.786} \left(\frac{T_{\infty}}{100} \right)^{-0.795} \quad (A10) \end{aligned}$$

$$\begin{aligned} & \underline{V_{\infty} \geq 13,000 \text{ FPS}} \\ R_{r_{MAX}} &= 1.03 \times 10^7 \left(\frac{P_{\infty}}{P_{ATM}} \right)^{1.02} \left(\frac{V_{\infty}}{10^4} \right)^{1.232} (P_{\infty}/P_{ATM})^{-0.048} \left(\frac{T_{\infty}}{100} \right)^{-1.0} \quad (A11) \end{aligned}$$

2. Unswept Infinite Cylinder

The approximate equations for the local reference Reynolds number, R_{rMAX} , for an unswept cylinder have an accuracy of $\pm 15\%$. These equations are:

(1) Wind Tunnel

$$R_{rMAX} = 2.3 \times 10^8 \frac{(P_\infty/P_{ATM})^{0.97} M_\infty^{0.278}}{T_\infty^{0.659}} R \quad (A12)$$

(2) Flight

$$\underline{V_\infty < 13,000 \text{ FPS}}$$

$$R_{rMAX} = 1.78 \times 10^7 (P_\infty/P_{ATM}) \left(\frac{V_\infty}{10^4} \right)^{1.196(P_\infty/P_{ATM})^{-0.048}} \left(\frac{T_\infty}{100} \right)^{-0.97} R^{0.97} \quad (A13)$$

$$\underline{V_\infty \geq 13,000 \text{ FPS}}$$

$$R_{rMAX} = 1.59 \times 10^7 (P_\infty/P_{ATM})^{0.97} \left(\frac{V_\infty}{10^4} \right)^{0.762} \left(\frac{T_\infty}{100} \right)^{0.771} R^{0.97} \quad (A14)$$

3. Conversion of Free-Stream Conditions to Stagnation Chamber Conditions

The free stream conditions P_∞ and T_∞ are generally difficult to measure in a wind tunnel whereas stagnation chamber conditions can be obtained with relative ease. The free stream temperature, T_∞ , can be related to stagnation point enthalpy through the energy equation and becomes

$$T_\infty = \frac{H_\infty}{c_p} = \frac{H_S}{c_p} \left(\frac{1}{1 + \frac{\gamma-1}{2} M_\infty^2} \right) \quad (A15)$$

where

$$c_p = 0.24 \text{ BTU/lb}_m^{\circ}\text{R}$$

Equation (A15) applies if the wind tunnel free stream flow has reached chemical equilibrium. The stagnation point pressure can be related to the free-stream pressure by figure A1.

Environmental limitations of approximate expressions for wind tunnel and flight conditions are shown in table A1.

TABLE A1
ENVIRONMENTAL LIMITATIONS OF APPROXIMATE EXPRESSIONS

PARAMETER	WIND TUNNEL	FLIGHT
MACH NUMBER	$5 < M_\infty < 22$	—
VELOCITY —FPS	—	$5,000 < V_\infty < 25,000$
AMBIENT TEMPERATURE —°R	$60 < T_\infty < 120$	$350 < T_\infty < 500$
AMBIENT PRESSURE —ATM	$10^{-5} < \frac{P}{P_{ATM}} < 10^{-1}$	$10^{-5} < \frac{P}{P_{ATM}} < 10^{-1}$

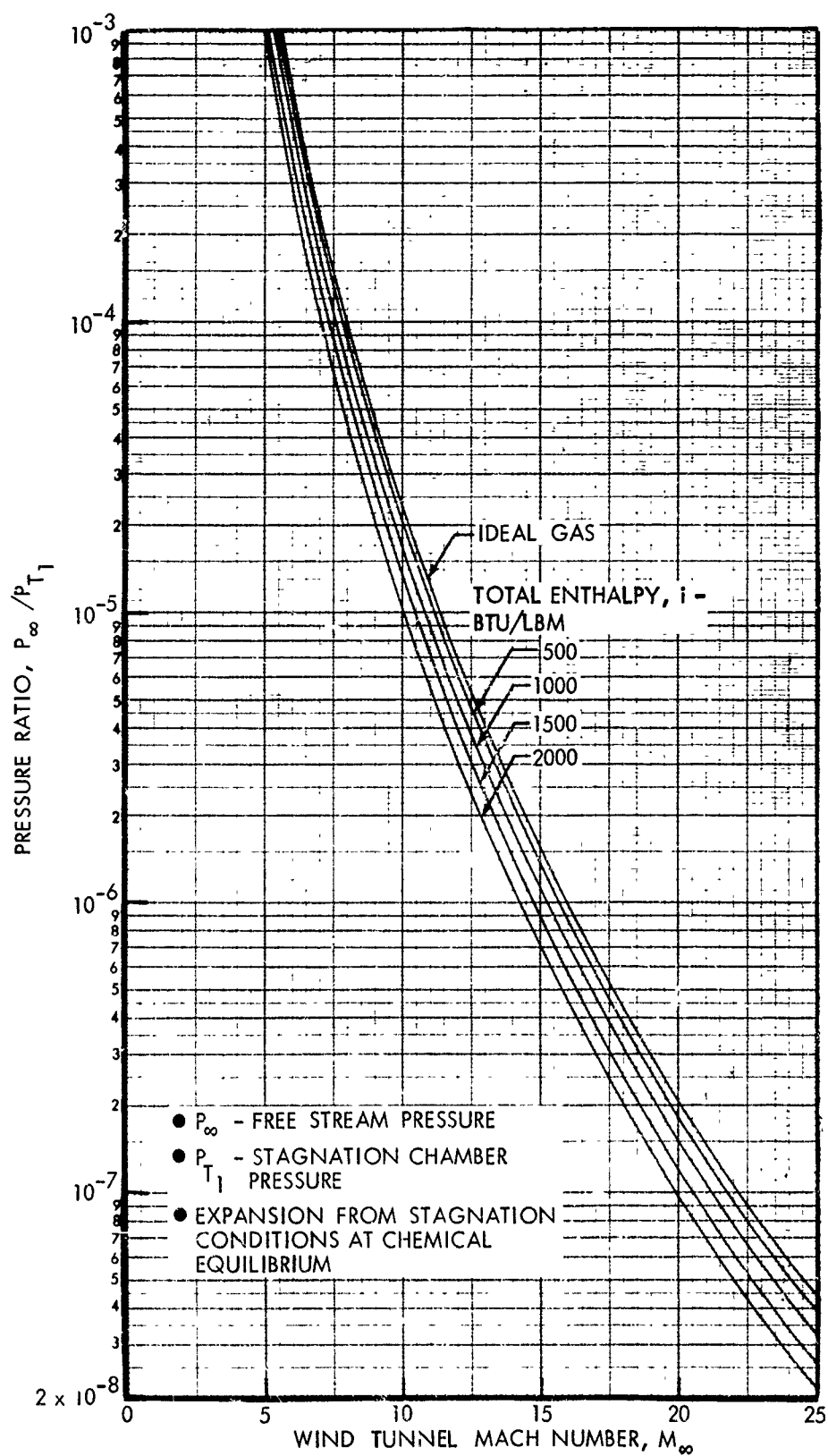


Figure A1: FREE STREAM PRESSURE IN HIGH ENTHALPY WIND TUNNELS

APPENDIX B*

LAMINAR AND TURBULENT $\rho_r \mu_r$ HEAT TRANSFER METHOD

The $\rho_r \mu_r$ method used for theoretical predictions throughout this report was developed by Richard A. Hanks in the course of the X-20 program. The method is based on the integral form of the boundary layer momentum equation. This equation is transformed into an equivalent incompressible form that is then solved to yield a generalized equation that includes the usual boundary layer thickness and form factors as undetermined functions. For laminar flow these functions were evaluated by equating the generalized equation to exact numerical solutions of the differential equations for self-similar boundary layers. Two apparently universal boundary layer functions were evaluated that allow a general heat transfer equation to be written that agrees with essentially all of the exact similarity solutions to within about 3 percent, including the effects of fluid property variations, finite streamwise and crossflow pressure gradients, and streamline divergence. The two functions are:

1. a reference value of the density-viscosity product $\rho_r \mu_r$ that depends only on the density-viscosity products evaluated at the wall, edge, and stagnation enthalpies, and
2. a boundary layer profile parameter, Γ , that depends only on the density evaluated at a linear combination of the wall, edge, and stagnation enthalpies.

No analytic derivations for these functions have been found, and all results in this report were calculated with the aid of curves given in this appendix. Recently, however, simple expressions have been found that agree closely with the plotted curves.

The extension to turbulent flows was guided by the laminar results, physical considerations, and comparisons with experimental results. The functions $\rho_r \mu_r$ and Γ are retained in the turbulent flow method, and are equal to the laminar values. However, the expressions used to calculate the heating are of course somewhat different, and so the effects of $\rho_r \mu_r$ and Γ on the heating rate are also somewhat different. The general form of the basic momentum integral equation allows turbulent flow heat transfer data from different sources to be compared on a consistent and systematic basis. During the X-20 program extensive comparisons to experimental data were made in which no data were consciously ignored. The method described here reflects those comparisons. Although the derivation given is restricted to the vicinity of a plane of symmetry, the resulting expressions have been applied to infinite cylinder distributions with good results.

The following discussion describes the method as it is now programmed for digital computers and as it was used in the preparation of the present report. Some modifications of the method have been made under NASA contract

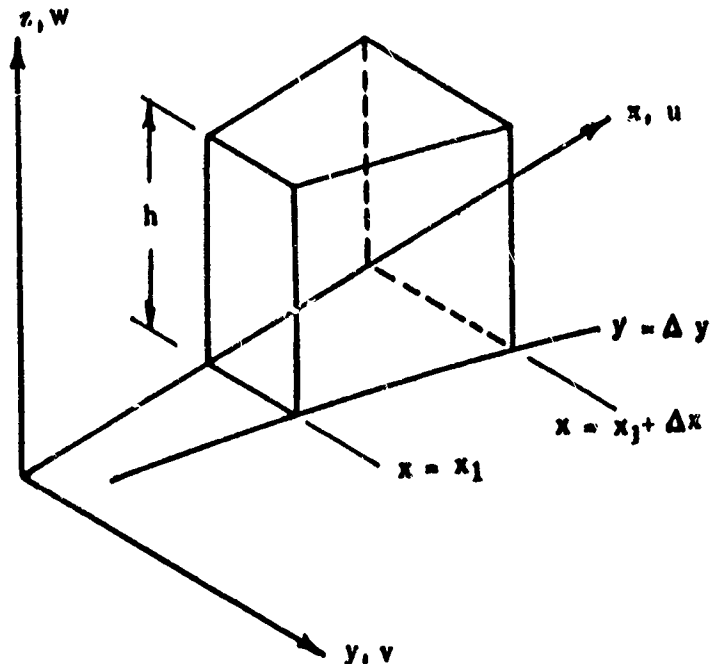
*This appendix is based on Appendix B of reference 16.

NAS8-11321 which are not included in the present calculations. These modifications are primarily for flow conditions other than those of the data discussed in this report, and do not lead to appreciable numerical differences here. Further information regarding the later modifications may be obtained from reference 29. The following description of the derivation and application of the method is in six parts:

1. Derivation of a general form of the boundary layer momentum integral equation.
2. Transformation of the integral equation to an equivalent incompressible form.
3. Correlation of exact laminar solutions.
4. Evaluation of turbulent boundary layer parameters.
5. Combined laminar and turbulent method.
6. Summary of method.

Derivation of the Momentum Integral Equation

A derivation of the boundary layer momentum integral equation in a general curvilinear coordinate system will now be given. The derivation is restricted to the vicinity of a plane of symmetry as well as by the usual boundary layer assumptions. A control volume is defined as shown in the sketch below:



The length elements in the x and z directions are unity. However, the length element for y is determined by the function $g = g(x)$, which is considered arbitrary (subject to the restriction that dg/dx remains finite). Later it will be seen that in some cases the most convenient choice of g is determined by the shape of the body under consideration. The height of the control volume, h , is constant and must be larger than the boundary layer thickness but is otherwise arbitrary. The surface $y = 0$ coincides with the straight streamline; hence $v = 0$ when $y = 0$. However, v is not necessarily zero nor even constant on any other surface of constant y .

Mass conservation.— The mass entering the control volume through the surface $x = x_1$ is given by:

$$\Delta y \left[g \int_0^h \rho u \, dz \right]_{x_1}$$

The mass leaving at $x = x_1 + \Delta x$ is given by a similar expression. Expanding in a Taylor series, and retaining only the first order term yields:

$$\begin{aligned} & \Delta y \left[g \int_0^h \rho u \, dz \right]_{x_1 + \Delta x} \\ &= \Delta y \left[g \int_0^h \rho u \, dz \right]_{x_1} + \Delta y \Delta x \frac{\partial}{\partial x} \left[g \int_0^h \rho u \, dz \right] \end{aligned} \quad (B1)$$

so that the mass remaining within the control volume is:

$$\Delta y \Delta x \frac{\partial}{\partial x} \left[g \int_0^h \rho u \, dz \right] \quad (B2)$$

Applying this technique over all six surfaces of the control volume, and requiring steady flow, yields:

$$\Delta x \Delta y \frac{\partial}{\partial x} \left[g \int_0^h \rho u \, dz \right] + \Delta x \Delta y \frac{\partial}{\partial y} \left[\int_0^h \rho v \, dz \right] + g \Delta x \Delta y [\rho w]_{z=0}^{z=h} = 0 \quad (B3)$$

Since $w(0) = 0$ there results in the limit as Δx and Δy approach zero:

$$\frac{\partial}{\partial x} \left[\int_0^h \rho u \, dz \right] + \frac{1}{g} \frac{\partial g}{\partial x} \left[\int_0^h \rho u \, dz \right] + \frac{1}{g} \frac{\partial}{\partial y} \left[\int_0^h \rho v \, dz \right] + \rho_\theta w_\theta = 0 \quad (B4)$$

x-momentum. - In a similar manner the following expression for x-momentum is obtained:

$$\begin{aligned} & \frac{\partial}{\partial x} \left[g \int_0^h \rho u^2 dz \right] + \frac{\partial}{\partial y} \left[\int_0^h \rho u v dz \right] + g \left[\rho u w \right]_{z=0}^{z=h} \\ & = g \left[\tau \right]_{z=0}^{z=h} - h \frac{\partial}{\partial x} [g p] + h p \frac{\partial E}{\partial x} \end{aligned} \quad (B5)$$

Combining equation (B5) with the previous result for mass conservation, and noting that $\tau(h) = 0$:

$$\begin{aligned} & \frac{\partial}{\partial x} \left[g \int_0^h \rho u^2 dz \right] - u_e \frac{\partial}{\partial x} \left[g \int_0^h \rho u dz \right] + \frac{\partial}{\partial y} \left[\int_0^h \rho v (u - u_e) dz \right] \\ & = -g \tau_w - h g \frac{\partial p}{\partial x} \end{aligned} \quad (B6)$$

Introducing the usual boundary layer thickness parameters:

$$\text{momentum thickness} \quad \theta = \int_0^h \frac{\rho}{\rho_e} \left[\frac{u}{u_e} - \left(\frac{u}{u_e} \right)^2 \right] dz \quad (B7)$$

$$\text{displacement thickness} \quad \delta^* = \int_0^h \left(1 - \frac{\rho u}{\rho_e u_e} \right) dz$$

$$\text{crossflow momentum thickness ratio} \quad \frac{E}{\theta} = \bar{E} = \frac{1}{\theta} \int_0^h \frac{\rho v}{\rho_e v_e} \left(1 - \frac{u}{u_e} \right) dz$$

leads to the following expression for Δx and Δy approaching zero:

$$\frac{\tau_w}{\rho_e u_e^2} = \frac{\partial \theta}{\partial x} + \theta \left[\frac{1}{u_e} \frac{\partial u_e}{\partial x} \left(2 + \frac{\delta^*}{\theta} \right) + \frac{1}{\rho_e} \frac{\partial \rho_e}{\partial x} + \frac{1}{g} \left(\frac{\partial g}{\partial x} + \frac{E}{\theta} \frac{1}{u_e} \frac{\partial v_e}{\partial y} \right) \right] \quad (B8)$$

Definition of $g(x)$. - Since the definition of g is still arbitrary, it seems desirable to make a definition that will simplify equation (B8) if possible. It might appear that if g were selected such that $v_e = 0$ (i.e., streamline coordinates) the last term would be made zero also. Such is not necessarily the case however, since v_e is a divisor in the definition of E . It will be seen that in the limit for small y , the product

$$\frac{\partial v_e}{\partial y} E$$

becomes

$$\frac{1}{y} \int_0^h \frac{\rho v}{\rho_e} \left(1 - \frac{u}{u_e} \right) dz$$

An additional condition, $\partial v / \partial y = 0$ does cause this term to go to zero. An examination of the complete boundary layer differential equation shows that $\partial v / \partial y = 0$ occurs only if

$$\partial p / \partial y = 0$$

and

$$\partial^2 p / \partial y^2 = 0$$

These conditions are met only if the body is: 1) two-dimensional, or 2) axisymmetric and at zero angle of attack. In both cases the surfaces $y = \text{constant}$ follow streamlines if $g \propto r$, the local body radius. In the case of an axisymmetric body at angle of attack the streamlines will not follow surfaces of constant y however. The additional divergence is denoted by f , defined by

$$\frac{1}{f} \frac{\partial f}{\partial x} = \frac{1}{u_e g} \frac{\partial v_e}{\partial y} \quad (\text{B9})$$

where v is measured with respect to the y, x coordinate system. In terms of r and f , equation (B8) becomes

$$\frac{\tau_w}{\rho_e u_e^2} = \frac{\partial \theta}{\partial x} + \theta \left[\frac{1}{u_e} \frac{\partial u_e}{\partial x} \left(2 + \frac{\theta^*}{\theta} \right) + \frac{1}{\rho_e} \frac{\partial \rho_e}{\partial x} + \frac{1}{r} \frac{\partial r}{\partial x} + \frac{E}{\theta} \left(\frac{1}{f} \frac{\partial f}{\partial x} \right) \right] \quad (\text{B10})$$

Physically, the term r may also be thought of as streamline divergence due to body shape while the term f represents streamline divergence due to transverse pressure gradients. The quantities r and f are related by

$$rf \approx \Delta \quad (\text{B9a})$$

where Δ is the total distance between any two streamlines. In the absence of transverse pressure gradients the final term in equation (B10) will be zero.

Transformation of the Momentum Integral Equation

In order to obtain a more useful form of the momentum equation (B10) a modified Stewartson transformation suggested by Mager (ref. 30) is adopted in which:

$$\begin{aligned} X &= \int_0^x F \frac{\rho_r \mu_r}{\rho_o \mu_o} dx \\ Y &= y \\ Z &= F \int_0^z \frac{\rho}{\rho_o} dz \\ U &= u/F \\ V &= v/F \end{aligned} \quad (\text{B11})$$

where X , Y , Z , U and V are the transformed coordinates and velocities. The stagnation values of density and viscosity, ρ_o and μ_o , are required to be constant, and F is an unspecified function of x only. With these definitions, the momentum thickness, skin friction at the wall, and heat transfer rate in the transformed coordinate system are respectively:

$$\begin{aligned} \Theta &= \int_0^\infty \left(\frac{U}{U_e} - \left(\frac{U}{U_e} \right)^2 \right) dZ = F \frac{\rho_e}{\rho_o} \theta \\ \bar{\tau}_w &= \frac{\tau_w}{F} \left(\frac{\rho_o \mu_o}{\rho_r \mu_r} \right) \\ \bar{q}_w &= \frac{q_w}{F^2} \left(\frac{\rho_o \mu_o}{\rho_r \mu_r} \right) \end{aligned} \quad (\text{B11a})$$

The transformed momentum integral equation becomes

$$\begin{aligned} \frac{\bar{\tau}_w}{\rho_e U_e^2} &= F \frac{d}{dX} \left(\frac{1}{F} \frac{\rho_o}{\rho_e} \Theta \right) + \frac{\rho_o}{\rho_e} \Theta \left[\frac{A}{U_e F} \frac{\partial}{\partial X} (U_e F) + \frac{1}{\rho_o} \frac{\partial \rho_o}{\partial X} \right. \\ &\quad \left. + \frac{1}{r} \frac{dr}{d\lambda} + \bar{E} \frac{1}{f} \frac{df}{dX} \right] \end{aligned} \quad (\text{B12})$$

in which $A = 2 + \frac{\delta^*}{\theta}$ (A and \bar{E} are unchanged by the transformation).

Solution of the transformed integral equation. - It is assumed that the local friction coefficient in the transformed plane is given by

$$\frac{\bar{\tau}_w}{\rho_o U_o^2} = \frac{C_m}{\left(\frac{\rho_o U_o \theta}{\mu_o} \right)^{1/m}} \quad (B13)$$

Equation (B13) is substituted into equation (B12) yielding an equation of the form:

$$\frac{d\theta}{dX} + P(X) \theta = \theta^{-\frac{1}{m}} Q(X) \quad (B13a)$$

which becomes a linear first order equation with the change of variable:

$$\varphi = \theta^{\frac{m+1}{m}} \quad (B13b)$$

The solution obtained is:

$$\frac{\bar{\tau}_w}{\rho_o U_o^2} = \frac{C_m \left(F^{A-1} U_o^{A-1} r f \bar{E} \mu_o \right)^{1/m}}{\left\{ \int_0^X C_m \left(\frac{m+1}{m} \right) \rho_o \mu_o^{\frac{1}{m}} U_o^{\frac{A(m+1)-1}{m}} F^{(A-1)\frac{m+1}{m}} \left(r f \bar{E} \right)^{\frac{m+1}{m}} dX \right\}^{\frac{1}{m+1}}} \quad (B14)$$

In the untransformed physical plane, (B14) is:

$$\frac{\tau_w}{u_o} = \frac{C_m \mu_o^{\frac{1-m}{m}} \rho_r \mu_r u_o^{\frac{A+m-1}{m}} (r f \bar{E})^{1/m}}{\left\{ \int_0^x C_m \left(\frac{m+1}{m} \right) \mu_o^{\frac{1-m}{m}} \rho_r \mu_r u_o^{\frac{A(m+1)-1}{m}} (r f \bar{E})^{\frac{m+1}{m}} dx \right\}^{\frac{1}{m+1}}} \quad (B15)$$

Neither ρ_o nor F appear in this equation, and their definitions are therefore immaterial.

Remembering that C_m , m , and μ_o are assumed to be independent of x , and defining

$$C_x = C_m \frac{m}{m+1} \left(\frac{m}{m+1} \right)^{\frac{1}{m+1}} \quad (B16)$$

$$G = \rho_r \mu_r u_e r^{\frac{m+1}{m}}$$

(B15) can then be reduced to:

$$\frac{\tau_w}{u_e} = \frac{C_x \mu_o^{\frac{1-m}{1+m}} [\rho_r \mu_r u_e]^{\frac{m}{m+1}}}{\left[\frac{1}{G \left(f \bar{E} u_e^{A-1} \right)^{\frac{m+1}{m}}} \int_0^x G \left(f \bar{E} u_e^{A-1} \right)^{\frac{m+1}{m}} dx \right]^{\frac{1}{m+1}}} \quad (B17)$$

Noting that the quantity within the brackets in the denominator on the right hand side has the units of length, we can define

$$S_{eq} = \left[\frac{1}{G \left(f \bar{E} u_e^{A-1} \right)^{\frac{m+1}{m}}} \int_0^{x_1} G \left(f \bar{E} u_e^{A-1} \right)^{\frac{m+1}{m}} dx \right]_1^{\frac{m+1}{m}} \quad (B18)$$

where the subscript 1 indicates evaluation at the current point of interest x_1 . All effects due to flow three-dimensionality, streamwise and transverse pressure gradients, and upstream history are now included in S_{eq} , if $\rho_r \mu_r$ is assumed to be independent of these phenomena (the validity of this assumption will be demonstrated subsequently). Thus S_{eq} can be considered to be "the equivalent flat plate distance" for skin friction at the point of interest x_1 .

With (B18), (B17) can be rewritten:

$$\frac{\tau_w}{u_e} = \frac{C_x \mu_o}{S_{eq}} \left[\frac{\rho_r \mu_r u_e S_{eq}}{\mu_o^2} \right]^{\frac{m}{m+1}} \quad (B19)$$

which is identical in form to the corresponding expression for low speed flat plate flow,

$$\frac{\tau_w}{u_e} = c \frac{\mu}{x} Re, e^{\frac{m}{m+1}} \quad (B20)$$

One approach to the solution of a boundary layer integral equation, such as developed in the preceding analysis, involves the assumption and integration of boundary layer profiles to obtain the required boundary layer thickness parameters (see, for instance, Beckwith and Gallagher (ref. 31)). In that approach it is necessary to derive the energy equation corresponding to (B15). An alternative method is used here, wherein a general form of Reynolds analogy is assumed

$$H = \frac{q}{i_{aw} - i_w} = \mathcal{J} \frac{\tau_w}{u_e} \quad (B21)$$

It is of course well known that the Reynolds analogy factor \mathcal{J} has the value unity for constant property, unity Prandtl number, flat plate flow. It will be subsequently demonstrated that, in the presence of more realistic gas properties, \mathcal{J} is for laminar flat plate flows still a function only of the Prandtl number and (in dissociated flow) the Lewis number. For convenience denoting these flat plate flow functional relationships by F_{Pr} and \mathcal{J} respectively, (B21) is rewritten

$$H = \frac{\mathcal{J}}{F_{Pr}} \frac{\tau_w}{S u_e} \quad (B22)$$

where the factor S incorporates all effects of flow three-dimensionality, streamwise and transverse pressure gradients, and upstream history on Reynolds analogy.

Combining (B17), (B18), and (B22),

$$H = \frac{\mathcal{J}}{F_{Pr}} \frac{C_x}{S} \frac{\mu_o^{\frac{1-m}{1+m}} \left(\rho_r \mu_r u_o \right)^{\frac{m}{m+1}}}{\left(S_{eq} \right)^{\frac{1}{m+1}}} \quad (B23)$$

Since S_{eq} includes all effects of flow history and pressure gradient on skin friction, and S performs a similar function on Reynolds analogy, the definition of an equivalent distance for heat transfer suggests itself. Accordingly, we define

$$x_{eq} = S^{m+1} S_{eq}$$

$$x_{eq} = S^{m+1} \int_0^{x_1} \frac{G \left(\bar{f} \bar{E} u_\theta (A-1) \right)^{\frac{m+1}{m}}}{\left[G \left(\bar{f} \bar{E} u_\theta (A-1) \right)^{\frac{m+1}{m}} \right]_{x_1}} dx \quad (B24)$$

leading to a general expression for heat transfer of the form

$$H = \frac{C_x}{F_{Pr}} \frac{\mu_o}{x_{eq}} \left[\frac{\rho_r \mu_r u_\theta x_{eq}}{\mu_o^2} \right]^{m/(m+1)} \quad (B25)$$

Means of evaluating the various parameters appearing in (B25) are presented in the following sections.

Evaluation of Laminar Boundary Layer Parameters

Exact solutions of the similarity form of the laminar boundary layer equations were used to evaluate the parameters appearing in equation (B25). This was done in an orderly manner, beginning with two-dimensional constant-property constant-pressure flow, and progressing to the most complex conditions for which exact solutions are available. The evaluations determined from the simpler cases were retained or amplified in analyzing the more complex cases. Thus, the constant C for laminar flow is always taken to be 0.33206, the value given by Howarth in reference 32 for incompressible flat plate flow. The effects of pressure gradients, wall cooling, etc., are accounted for in other terms of equation (B25).

In some cases alternative definitions were possible. For example, the authors of references 35 and 38 incorporated (in effect) pressure gradients into the term $\rho_r \mu_r$ appearing in equation (B10), while in the present formulation such effects appear in the equivalent distance, X_{eq} . The latter definition is to be preferred as the former cannot be made consistent with the results of reference 33, which presents solutions for various pressure gradients, but with $\rho \mu$ held constant. The definitions used here were adopted only after an examination of several possible alternatives. The criteria for selection were consistency between the results of the various special cases, consistency with physical considerations, accuracy, simplicity, and freedom from interdependencies.

General considerations. - As a matter of physical consistency, it is required that if the fluid properties ρ and μ are constant through the boundary layer, the reference values of the fluid properties be equal to those constant values. This principle is extended to constant products as well, i.e., it is required that when in a given numerical calculation, e.g., references 33 and 34, the product of density and viscosity is held constant at some base value (usually the wall) the reference density viscosity product $\rho_r \mu_r$ must also be equal to that base value. The functions F_{Pr} and \mathcal{L} are equal to 1.0 when σ and Le are equal to 1.0, and $\mathcal{L} \approx 1.0$ for ideal gases. Also, in flat plate flow the equivalent distance is equal to the physical distance from the leading edge.

Two-Dimensional Flat Plate Flow

The special case of two-dimensional flat plate flow is examined first since the effect of fluid property variations within the boundary layer can be examined without the additional complexity of streamwise variations. For the case of constant fluid properties the solutions of Howarth show that $m = 1$ and $C_x = .332$, so that equation (B25) becomes

$$H = .332 \frac{\mathcal{L}}{F_{Pr}} \left[\frac{\rho_r \mu_r u_e}{x_{eq}} \right]^{1/2} \quad (B26)$$

$$= .332 \frac{\mathcal{L}}{F_{Pr}} \left[\frac{\rho_e \mu_e u_e}{x} \right]^{1/2} \quad (B27)$$

where (B27) follows from the principles stated under "General Considerations". For this special case the only undetermined quantity is the Reynolds analogy factors \mathcal{L} and F_{Pr} . Note that the reference stagnation viscosity, μ_0 , no longer appears.

Reynolds analogy factors.— The Prandtl number effect on Reynolds analogy in flat plate flow, usually given as $F_{Pr} = \sigma^{2/3}$ for constant σ is slightly better represented by $\sigma^{.645}$ as may be seen in figure (B1). Following the practice of reference 35, for example, the Prandtl number effect is correlated in terms of σ , the partial Prandtl number for translation, rotation, and vibration.

For variable Prandtl number there is an uncertainty as to which value should be used in correlating its effect. All solutions in the literature for which the Prandtl number is variable also involve variable $\rho\mu$, so that $\rho\mu$ is not necessarily equal to $\rho_e\mu_e$. For such cases it was found that the Prandtl number should be evaluated at the enthalpy and pressure corresponding to $\rho_r\mu_r$. This value of the Prandtl number is hereafter denoted as σ_r . The adequacy of this evaluation is demonstrated by the agreement of the three sets of calculations presented in figure (B1), which also serves to establish the lack of dependency of F_{Pr} on anything other than σ_r .

With the Prandtl number effect correlated in terms of the partial Prandtl number the effect of energy transport by diffusion must be treated separately. This effect was first calculated by the authors of reference 35, wherein the expression

$$\mathcal{L} = \frac{\dot{q}_{Le \neq 1}}{\dot{q}_{Le = 1}} = 1 + (Le^{.62} - 1) \frac{i_{D,S}}{i_S} \quad (B28)$$

was found to agree well with exact solutions for $Le = 1.4$, in stagnation point flow. In high Mach number flows, however, equation (B28) may predict a significant diffusion effect under conditions for which no dissociation actually exists, since the temperatures within the boundary layer are always well below the stagnation value. To avoid this inconsistency, equation (B28)

was modified to operate on the local static enthalpy, rather than the stagnation value. The modified expression,

$$\mathcal{L} = 1 + (Le \cdot 0.52 - 1) \frac{1_{D,e}}{1_e} \quad (B29)$$

of course reduces to (B28) for stagnation point flow. Equation (B29) was used for all calculations in the present report, although later publications, reference 37, for example, indicate that equation (B29) overestimates the heating rate by 5 to 10% in some cases.

Reference density-viscosity product. - The reference density-viscosity product was first evaluated for zero Mach number with various degrees of wall cooling using the solutions of references 36, 38, and 39, and some unpublished solutions by Halvorson and Cassmeyer of The Boeing Company, as shown in figure B2.

For edge Mach numbers greater than zero it was found that the reference density-viscosity product $\rho_r \mu_r$ can be represented as a function only of $\rho_e \mu_e$, $\rho_w \mu_w$ and $\rho_s \mu_s$, where the latter is the density-viscosity product evaluated at stagnation enthalpy but the local pressure. Using the solutions of references 36 and 38 an effective edge value of $\rho \mu$ was determined that allows the use of figure B2 for Mach numbers other than zero. The effective $\rho \mu$ product $(\rho_e \mu_e)^{eff}$ was found to be a function of $\rho_s \mu_s$, and $\rho_e \mu_e$, only. The curve that defines this relation is given in figure B3 (a). All of the solutions discussed so far are well represented by the faired curve of figure B2 when plotted against $\rho_e \mu_e^{eff}$ as may be seen in figure B3 (b).

Subsequent investigations described below have shown that $\rho_r \mu_r$ is independent of pressure gradients. The values of $\rho_r \mu_r$ obtained from figures B2 and B3 were used for all calculations appearing in this report.*

Pressure Gradient Effects - Similar Flows

Referring to equation (B25), and recalling the earlier comment that C_x , m , F_{pr} and \mathcal{L} are by definition taken as the flat plate values it is seen that all pressure gradient effects are reflected in $\rho_r \mu_r$ and x_{eq} . These effects can be evaluated for similar flows from the solution published (for example) in references 33 and 38, which consider streamwise pressure gradients, and references 34 and 37 which consider cross-flow pressure gradients.

*Recently some simple expressions have been found which approximate curves of figures B2 and B4 closely. The expressions are given in the final section of this appendix.

Beginning with the simplest possible case, two-dimensional flow of an ideal gas with Prandtl number of one, and the viscosity proportional to temperature, the equivalent distance effects can be isolated. Since $\rho\mu$ is always equal to $\rho_e\mu_e$, $\rho_r\mu_r$ is also equal to $\rho_e\mu_e$. (Note that $\rho\mu$ is not necessarily constant through the flow field, but varies with the local boundary layer edge pressure.) With these values incorporated, the equivalent distance expression (B24), is reduced to

$$x_{eq} = S^2 \frac{\int_0^{x_1} (P u_e) u_e^{2(A-1)} dx}{\left[(P u_e) u_e^{2(A-1)} \right]_{x_1}} \quad (B30)$$

In equation (B30) the term $(P u_e)$ reflects the effects of upstream variations in $\rho_e\mu_e u_e$, while the terms S^2 and $u_e^{2(A-1)}$ account for local pressure gradient effects on the boundary layer profiles.

Equation (B30) can be evaluated if S and A are known, and although laborious, they could be determined from the numerical solutions. Fortunately, specific evaluation of these parameters has proven to be unnecessary, since a convenient simple correlation has been found for the combined effect of S and u_e^{A-1} , which may be written as

$$S^2 \int_0^{x_1} \frac{(P u_e) (u_e^{2(A-1)}) dx}{\left[(P u_e) u_e^{2(A-1)} \right]_{x_1}} = \frac{1}{1 + \Gamma \sqrt{\beta}} \int_0^{x_1} \frac{P u_e dx}{(P u_e)_{x_1}} \quad (B31)$$

where β is the dimensionless pressure gradient parameter similar to that defined by the authors of reference 33.* The profile parameter Γ is a single valued function of a mean boundary layer density, ρ_m , calculated by

$$\frac{\rho_m}{\rho_e} = \frac{2 T_e}{(T_w + T_e)} \quad (B32)$$

Subsequent investigations of exact solutions for nonunity Prandtl number and nonlinear viscosity laws have shown that expressions of the form of (B31) are valid for these more complex conditions as well, either for two-dimensional flows with streamwise pressure gradients, or for yawed cylinder flow. The expressions finally developed are:

*The definition of β is given in equation (B41).

$$(\rho_r \mu_r)_{\beta} = (\rho_r \mu_r)_{\beta=0} \quad (B33)$$

and a generalization of (B31)

$$x_{eq, L} = \frac{1}{J_L} \int_0^{x_1} \frac{G f^2 \bar{E}_L}{\left[G f^2 \bar{E}_L \right]_{x_1}} dx \quad (B34)$$

where J_L is given by

$$J_L = \left[1 + \Gamma_s \sqrt{\beta_s} \right] \sigma_r \alpha \sqrt{\beta_s} \quad (B35)$$

and

$$\bar{E}_L = \left[1 + \Gamma_c \sqrt{\beta_c} \right] \sigma_r \alpha \sqrt{\beta_c} \quad (B36)$$

where the subscripts "s" and "c" are introduced to distinguish between streamwise and crossflow pressure gradients; it should be noted that J_L is concerned only with streamwise pressure gradient effects and \bar{E}_L only with crossflow effects; also note that $J_L = 1.0$ for $\beta_s = 0$ and $\bar{E}_L = 1.0$ for $\beta_c = 0$.

The function Γ is given for either streamwise or crossflow pressure gradients by the curve of figure B4 as a single-valued function of a parameter Σ defined by:

$$\Sigma_s = \frac{\rho_s}{\rho_{m,s}} = \frac{(Z T)_{m,s}}{(Z T)_s} \quad (B37)$$

for streamwise pressure gradients, and as

$$\Sigma_o = \frac{\rho_{e,SL}}{\rho_{m,o}} = \frac{(Z T)_{m,o}}{(Z T)_{e,SL}} \quad (B38)$$

for crossflow pressure gradients. The subscript "m" denotes evaluation at a mean boundary layer enthalpy, defined by:

$$i_{m,s} = \frac{1}{2} (i_s + i_w) \quad (B39)$$

and

$$i_{m,o} = \frac{1}{2} (i_{e,SL} + i_w) + .206 (i_s - i_{e,SL}) \sigma_r \sqrt{\frac{\rho_s \mu_s}{\rho_o \mu_e}} \quad (B40)$$

The second equality in equations (B37) and (B38) follows from the condition of constant pressure across the boundary layer (all evaluations are made at the local pressure). Again, (B37) through (B40) are the generalizations of equation (B31) and (B32).

While figure B4 and equations (B34-40) were developed solely on the basis of providing the best fit to the available data within the framework of the form of equation (B31) the obvious similarity of (B39-40) to the various reference enthalpies appearing in the literature provides some analytical justification for these correlations.

The streamwise pressure gradient parameter β_s is herein defined as:

$$\beta_s = 2 \frac{i_s}{i_o} J_L \left(\frac{x_{eq,L}}{x} \right) \frac{d(\ln u_e)}{d(\ln x)} \quad (B41)$$

With a minor modification to the definition of $x_{eq,L}$ (to be discussed in the next section), it is easily shown that this definition of β_o is identical to the corresponding parameter of reference 37. In the present report β_c is evaluated only for yawed cylinder flow, in which case $\beta_c = 1.0$, also consistent with the results of reference 37. Except as otherwise noted in the text, a value of unity was used for all leading edge theory calculations, while a value of zero (corresponding to $\bar{E} = 1.0$) was assumed for lower surface theory calculations.

The exponent α in equations (B35) and (B36) is given by

$$\alpha = .090 \left(\frac{\rho_s \mu_s}{\rho_w \mu_w} \right) \quad (B42)$$

which is also based on fits to the solutions of references 33, 34, 35, and 37. The accuracy obtained through the use of equations (B33) through (B42) is illustrated in figure B5, wherein solutions from references 33 and 37 are presented in terms of \bar{r} and Σ . As may be seen by comparing the spread of the individual numerical solutions with the indicated error band, the present method provides excellent agreement with all solutions.

Application to Nonsimilar Flow

The equations presented in this section have all been developed from similarity solutions to the boundary layer equations, and so are strictly applicable only in those situations for which similarity applies. However, based on discussions given in references 37 and 38, it is to be expected that the same correlations could provide good estimates for nonsimilar flow conditions as well, provided their streamwise variations are taken into account. This has been done by incorporating the factor J_L appearing in equation (B35) into the integrand. The expression for equivalent distance then becomes:*

$$x_{eq,L} = \frac{1}{J_L^2} \int_0^{x_1} \frac{G f \frac{2 \bar{E}_L}{(G f \frac{2 \bar{E}_L}{J_L})_{x_1}} J_L dx}{(G f \frac{2 \bar{E}_L}{J_L})_{x_1}} \quad (B43)$$

It is easily seen that for similar flows, wherein J_L is constant, (B43) reduces to (B34). Evaluated for two-dimensional flows ($f \approx 1.0$) the use of (B43) in (B41) results in a definition of β_s identical to that of reference 37, while the use of (B34) in (B41) provides a value of β_s that corresponds to the "local similarity" approach of reference 38, wherein the upstream history of profile effects are neglected (that is, the boundary layer profiles are assumed to adjust instantaneously to the local pressure gradient).

Equation (B43) assumes the crossflow parameter \bar{E}_L to be independent of streamwise pressure gradient effects; however, the presence of the β_s crossflow terms in the resulting definition of β_s provide a coupling between the transverse and streamwise pressure gradient effects, as might be expected. The overall effect predicted is in qualitative agreement with the results of reference 40; unfortunately, the difficulty of relating the correlating parameters of that reference to the present system has so far prevented quantitative comparisons.

Finally, for the general case of curved streamlines (i.e., away from a line of symmetry), it is assumed that the foregoing analysis and correlations are valid if the distance parameter x is taken to be measured along the streamline. As previously noted, the definition of β_0 for the general case is obscure, and all calculations herein other than leading edge values, have been made on the basis of $\beta_0 = 0$ ($\bar{E}_L = 1$), which corresponds to the "zero crossflow" method of reference 41 as far as three-dimensional effects are concerned. All present calculations do retain the effect of streamwise pressure gradients, however.

*Note that by these definitions β_s and J_L are interrelated, so that an iterative method is required for their evaluation, as also stated in reference 37.

Turbulent Flow

There are no exact calculations of turbulent boundary layer flow, so that a development of the type just given is not possible. However, equation (B25) still serves to identify the important parameters, and provides a basis for consistently comparing experimental results. In particular, the transformation introduced with equations (B10) and (B11) allows an empirical incompressible skin friction law to be used in place of the (nonexistent) exact flow solutions. As stated in the section "Transformation of the momentum integral equation," the transformation used is based on the work of Mager, reference 30. A discussion of the reasoning behind the transformation itself is given in his paper. The present method departs from the suggestions of Mager, however, in the evaluation of the various boundary layer parameters. Mr. Hanks was guided in the evaluations by the values of the corresponding laminar parameters, an approach which was suggested by the very successful results of the first such attempt, wherein the laminar values of $\rho_r \mu_r$ were used without modification for turbulent flow. The resulting predictions were in excellent agreement with recently obtained free flight data, some of which (notably, that from the X-15 program) were not in agreement with any of the well known methods.

Mr. Hanks was also guided by the requirements of a design project, and so was constrained to make conservative approximations where approximations were required. Thus, the effects of streamwise and transverse pressure gradients on the turbulent boundary layer profiles were included in the calculations, even though it was known that the effects were small and could only be crudely estimated. The available evidence indicated that such effects would increase heat transfer, so that neglecting them would be unconservative.

Incompressible flow friction law. - In order to determine C_x and α a formula for skin friction in incompressible turbulent flow is required. After a survey of proposed incompressible friction formulas a minor modification of the Schultz-Grunow (ref. 42) equation was selected:

$$C_f = \frac{.370}{[\log_{10} (Re + 3000)]^{2.584}} \quad (B44)$$

The modification that was made is the addition of the constant (3000) to the Reynolds number that appears in the denominator. This modification was made because Mr. Hanks felt that the high values of C_f predicted by the unmodified equation at Reynolds number below 10^4 were not realistic in view of the well supported prediction of stability theory that the incompressible laminar boundary layer is stable at Reynolds less than about 60,000.

The modified and unmodified expressions are shown in figure B6, together with some other proposed methods. As shown, there is little difference between the various methods, except that the Blasius equation falls low at high values of Reynolds number. Equation (B44) was originally selected because of its slight conservatism, although any other expression could have been used.

The form of equation (B44) does not lead itself to calculations in the framework of equation (B23) due to the variation of m with Reynolds number. However, comparisons have been made that show that $m=4$ is an adequate approximation for evaluating geometric effects. For example, if m is evaluated at particular values of Reynolds number using equation (B44) the following comparisons are obtained:

Re_e	$m = \frac{1}{1 + \frac{d(\ln C_f)}{d(\ln Re_e)}}$	$\frac{h_{\text{cone}}}{h_{\text{flat plate}}}$	$\frac{h_{\text{cylinder}}}{h_{\text{cylinder}, m=4}}$
10^5	3.45	1.20	.99
4.2×10^5	4.0	1.17	1.00
10^6	4.34	1.16	1.00
10^6	6.12	1.11	1.01

Thus the effect of variations in m is seen to be small. Accordingly, $m=4.0$ has been selected for the calculation of geometric effects (e.g., $h_{\text{cone}}/h_{\text{flat plate}}$) used herein. However, for actual calculations of C_f equation (B44) was used as there can be considerable error in $m = \text{constant}$ approximations for absolute values of C_f . An example of such a friction law is the Blasius method, for which $m = 4$. As shown in figure B6 the Blasius equation falls well below the other methods at high Reynolds numbers.

Density-Viscosity product; Reynolds Analogy Factor.—As already noted the reference density-viscosity product for turbulent flow is taken to be the laminar value. This basic identity was suggested by the fact that $\rho_r \mu_r$ appears only in connection with the laminar shear terms of the turbulent boundary layer equations.* It is also assumed the effects of Prandtl number and Lewis number on turbulent flat plate heat transfer are also identical to the laminar values. The use of the laminar flow Prandtl number effect is common practice. The use of the laminar flow Lewis number effect is thought to be a conservative upper limit.

*See, for example, equation 13 in reference 30.

Reference stagnation viscosity.— Since the reference stagnation viscosity μ_0 does not appear in the laminar equations, no information regarding its evaluation can be obtained by examining the laminar solutions. The reference stagnation viscosity is assumed by Mager (ref. 30) to be the viscosity evaluated at stagnation conditions. For real gases with the viscosity dependent on the pressure it seems more realistic to consider the local flow composition rather than the composition corresponding to stagnation conditions. Accordingly μ_0 is calculated with the Sutherland law and μ_r using the value of specific heat corresponding to $\rho_r \mu_r$. The result is:

$$\mu_0 = \mu_r \left(\frac{i_s}{i_r} \right)^{3/2} \left[\frac{T_r + 200}{T_r \left(\frac{i_s}{i_r} \right) + 200} \right] \quad (B45)$$

Pressure gradient effects.— As in the laminar case, pressure gradient effects appear primarily in the equivalent distance, which (for $n = 4$) is given by:

$$x_{eq, T} = s^5 \int_0^{x_1} \frac{G_T f^{5/4} \bar{E}_T u_e^{5/4 (A-1)} dx}{\left[G_T f^{5/4} \bar{E}_T u_e^{5/4 (A-1)} \right]_{x_1}} \quad (B46)$$

It is assumed that there exists an analog to the laminar correlation (equation (B43)) of the form:

$$x_{eq, T} = \frac{1}{J_T^2} \int_0^{x_1} \frac{G_T f^{5/4} \bar{E}_T J_T dx}{\left[G_T f^{5/4} \bar{E}_T \right]_{x_1}} \quad (B47)$$

It is to be expected that:

$$(J_T - 1)^{1/5} \ll (J_L - 1)^{1/2}$$

which expresses the well known fact that pressure gradient effects on turbulent heat transfer are much smaller than those in laminar flow. After an examination of available experimental data the value

$$\frac{J_T - 1}{J_L - 1} = .48 \quad (B48)$$

was selected. By analogy to equation (B35) it is assumed that

$$J_T = \left[1 + .48 \Gamma_S \sqrt{\beta_S} \right] \sigma_r^{\alpha \sqrt{\beta_S}} \quad (B49)$$

where Γ_S and β_S are the previously described laminar values. The small exponent α is assumed equal to the laminar value (eq. (B42)) although its ultimate effect on the predicted heating rate is only about 0.3% for $\beta_S = 1.0$.

Similarly, the behavior of \bar{E} in turbulent flow can be described only qualitatively, and most published analyses neglect its effect. However, its effect is to increase heating rates, and was therefore included in the present method. As in the streamwise pressure gradient case, the values actually used were based on modifications of the corresponding laminar correlations. Unlike the streamwise parameter J_L , however, \bar{E}_L is strongly influenced by Mach number, as evidenced in equations (B38) and (B40), so that a dual modification is indicated,

Considering first the case for zero Mach number flow, it is seen from the definitions of (B7) that the upper limit on \bar{E} is δ^+/θ unless the transverse velocity component v within the boundary layer exceeds the external value. Laminar solutions (ref. 34) show that these velocity overshoots do not occur for cold wall zero Mach number flow, hence a correction factor of the following form is suggested:

$$\frac{\bar{E}_{T, 0} - 1}{\bar{E}_{L, 0} - 1} = \frac{\left[\frac{\delta^+}{\theta} + C \right]_T}{\left[\frac{\delta^+}{\theta} + C \right]_L} \quad (B50)$$

The precise value of the constant C in this expression cannot be calculated, of course. For the previously mentioned upper limit case, C of course is equal to -1 ; however, in the interests of conservatism, a value of $C = +1$ was selected to represent an upper limit. Consistent with equations (B48) and (B49), then:

$$\frac{\bar{E}_{T,0} - 1}{\bar{E}_{L,0} - 1} = 0.77 \quad (B51)$$

In equations (B51) $\bar{E}_{L,0}$ is just \bar{E}_L evaluated for Mach number equal to zero. For Mach number zero equation (B40) reduces to

$$i_{m,c,0} = \frac{1}{2} (i_{e, SL} + i_w)$$

since

$$(i_s - i_{e, SL}) = 0$$

at zero Mach number.

The effect of Mach number on \bar{E}_T was determined from observation of empirical trends in turbulent yawed cylinder stagnation line heat transfer data, as

$$\frac{\bar{E}_T}{E_{T,0}} = \left(\frac{\bar{E}_L}{\bar{E}_{L,0}} \right)^{m_T} \quad (B52)$$

An equivalent form that is more convenient for computer applications has been used for all calculations in this report:

$$\frac{x_{eq, T}}{x_{eq, T, 0}} = \left[\frac{x_{eq, L}}{x_{eq, L, 0}} \right]^{m_T}$$

where, in general

$$\begin{aligned} x_{eq, T, 0} &= \frac{1}{J_T} \int_0^{x_1} \frac{G_T J_T r^{5/4} \bar{E}_{T,0} dx}{\left[G_T J_T r^{5/4} \bar{E}_{T,0} \right]_{x_1}} \\ x_{eq, L, 0} &= \frac{1}{J_L} \int_0^{x_1} \frac{G_L J_L r^2 \bar{E}_{L,0} dx}{\left[G_L J_L r^2 \bar{E}_{L,0} \right]_{x_1}} \\ x_{eq, L} &= \frac{1}{J_L} \int_0^{x_1} \frac{G_L J_L r^2 \bar{E}_L dx}{\left[G_L J_L r^2 \bar{E}_L \right]_{x_1}} \end{aligned} \quad (B53)$$

It is easily demonstrated that for infinite yawed cylinder stagnation line flow, (B53) is exactly equivalent to (B52). For other types of flow (B52) and (B53) are not exactly equivalent. However, since (B52) is based on yawed cylinder data, (B52) and (B53) are equally valid assumptions, and (B53) has been found to be more convenient. In any case, the final effect on the predicted heating rate is small.

Combined Laminar - Turbulent Method

A comparison of the equivalent distance expressions for laminar and turbulent boundary layers shows that in general the two values are not equal, so that the Reynolds number based on the equivalent distance will depend on the boundary layer state. This inconsistency can be avoided by employing the following definition of a reference Reynolds number.

$$R_r = \left[\frac{\rho_r \mu_r u_o x_{eq,L,0}}{F_x^2 \mu_o^2} \frac{x_{eq,L,0}}{x_{eq,L}} \right] \quad (B54)$$

where

$$F_x = \left[\frac{x_{eq,T,0}}{x_{eq,L,0}} \right]^{\frac{1}{m_T-1}} \quad m_T = 4 \quad (B55)$$

When terms R_r and F_x are used in equation (B25) there results

$$H = \frac{q}{i_{aw} - i_w} = \frac{\lambda}{2 F_{Pr}} \frac{F_x \mu_o}{x_{eq,L,0}} R_r C_{f,r} \quad (B56)$$

where $C_{f,r}$ is the friction coefficient evaluated for the reference Reynolds number. The formulas used in the present report are:

$$C_{f,r,L} = \frac{.664}{R_r^{1/2}} \quad (B57)$$

and

$$C_{f,r,T} = \frac{.370}{[\log_{10} (R_r + 3000)]^{2.584}} \quad (B58)$$

Note that in equation (B56) only $C_{f,r}$ depends on the boundary layer state. As a result, a simple relationship between laminar and turbulent flow can be obtained that is dependent upon the reference Reynolds number only.

This relationship, obtained by combining equations (B56), (B57) and (B58), follows

$$\frac{H_L}{H_T} = \frac{.185 (R_r)^{0.5}}{.332 \left[\log_{10} (R_r + 3000) \right]^{2.584}} \quad (B59)$$

It is easily shown that the laminar form of equation (B56) reduces identically to any of the special cases previously given. For example, considering only the various equivalent distance terms, and employing the general power law form for $C_{f,r}$ corresponding to equation (B25), there results

$$H \sim F_x^{-\frac{m-1}{m+1}} x_{eq,L,0}^{-\frac{1}{m+1}} \left(\frac{x_{eq,L}}{x_{eq,L,0}} \right)^{-\frac{m}{m+1}} \quad (B60)$$

For laminar flow, $m = 1$, and all terms except $(x_{eq,L})^{-1/2}$ disappear as desired. For turbulent flow, on the other hand, equation (B60) together with the definitions of F_x given in equation (B55), becomes:

$$H_T \sim \left[x_{eq,T,0} \left(\frac{x_{eq,L}}{x_{eq,L,0}} \right) \left(\frac{x_{eq,T,0}}{x_{eq,L,0}} \right)^{\frac{m-4}{3}} \right]^{-\frac{1}{m+1}} \quad (B60a)$$

The term in the brackets differs from the previous definition of $x_{eq,T}$ given in (B53) only by the factor

$$\left(\frac{x_{eq,T,0}}{x_{eq,L,0}} \right)^{\frac{m-4}{3}}$$

arising from the use of a nominal value of $m_T = 4$ in the definition of F_x . For all cases of practical interest, this term will have a negligible effect on heat transfer - on the order of one percent or less.

Use of a skin friction law of the form of (B58) in the heat transfer equation (B56) has the effect of automatically introducing the local value of m in (B60a), so that the proper compressibility effect on \bar{E}_T is obtained.

Summary of Method and Sample Calculations

This section summarizes the calculation procedure for the method. Table B1 lists specific values of the various parameters for several special cases. Since the calculation depends on the functions $\rho_e \mu_{eff}$, Γ and $\rho_r \mu_r$ which exist only as the faired curves of figures B2, B3, and B4 numerical values are given in Tables B2, B3 and B4 from which the reader can construct the necessary plots. Also given in Tables B2, B3 and B4 are simple curve fit expressions that are shown to agree closely with the values from the faired curves. The curve-fit expressions were not discovered until after the bulk of the analysis was complete, however, and were not used for any of the comparisons presented in this report.

It is assumed in the following discussion that the following quantities are known:

$$\begin{aligned} P_e, u_e, l_g, l_e, t_w \\ T_{S'}, T_e, T_w, \mu_e, \mu_w, \mu_{S'} = f(l_g, P_e) \\ \rho_e, \rho_w, \rho_{S'} = f(l_g, P_e) \end{aligned}$$

The basic equations are independent of units, so that any consistent set of units desired can be used.

The basic equations to be solved for each case in general form are

$$H = \frac{\mathcal{L}}{\sigma_r^{.645}} \left(\frac{\mu_o F_x}{x_{eq, L, 0}} \right) \frac{R_r C_{f, r}}{2} \quad (B61)$$

where

$$C_{f, r, L} = .004 / \sqrt{R_r} \quad (B62)$$

$$C_{f,r,T} = \frac{.370}{\left[\log_{10} (R_r + 3000) \right]^{2.584}} \quad (B63)$$

$$R_r = \frac{\rho_r \mu_r u_e x_{eq,L,0}}{F_x^2 \mu_o^2} \frac{x_{eq,L,0}}{x_{eq,L}} \quad (B64)$$

$$F_x = \left(\frac{x_{eq,T,0}}{x_{eq,L,0}} \right)^{1/3} \quad (B65)$$

$$x_{eq,L} = \int_0^{x_1} \frac{G_L f^{2\bar{E}_L} J_L dx}{\left[G_L f^{2\bar{E}_L} J_L^2 \right]_{x_1}} \quad (B66)$$

$$x_{eq,L,0} = \int_0^{x_1} \frac{G_L f^{2\bar{E}_{L,0}} J_L dx}{\left[G_L f^{2\bar{E}_{L,0}} J_L^2 \right]_{x_1}} \quad (B67)$$

$$x_{eq,T,0} = \int_0^{x_1} \frac{G_T f^{\frac{5}{4}\bar{E}_{T,0}} J_T dx}{\left[G_T f^{\frac{5}{4}\bar{E}_{T,0}} J_T^2 \right]_{x_1}} \quad (B68)$$

$$G_L = \rho_r \mu_r u_e r^2 \quad (B69)$$

$$G_T = \rho_r \mu_r u_e r^{5/4} \quad (B70)$$

$$J_L = \left[1 + \Gamma_s \sqrt{\beta_s} \right] \sigma_r \alpha \sqrt{\beta_s} \quad (B71)$$

$$J_T = \left[1 + .48 \Gamma_s \sqrt{\beta_s} \right] \sigma_r \alpha \sqrt{\beta_s} \quad (B72)$$

$$\bar{E}_L = \left[1 + \Gamma_c \sqrt{\beta_c} \right] \sigma_r \alpha \sqrt{\beta_c} \quad (B73)$$

$$\bar{E}_{L,0} = \left[1 + \Gamma_0 \sqrt{\beta_c} \right] \sigma_r \alpha \sqrt{\beta_0} \quad (B74)$$

$$\bar{E}_{T,0} = \left[1 + .77 \Gamma_0 \sqrt{\beta_c} \right] \sigma_r \alpha \sqrt{\beta_0} \quad (B75)$$

$$\alpha = .090 \sqrt{\frac{\rho_s \mu_s}{\rho_w \mu_w}} \quad (B76)$$

If only laminar flow is required (e.g., stagnation point)

$$H = .332 \frac{\sqrt{x}}{\sigma_r} \left[\frac{\rho_r \mu_r u_e}{x_{eq,L}} \right]^{1/2} \quad (B77)$$

The general procedure for a given case is as follows:

a. Examine x_{eq} equations to reduce them to minimum form consistent with the given problem. For example, the flat plate values of $\rho_e \mu_e$ and P_e are all independent of x and $J = 1$, so that $x_{eq} = x$ in all cases.

b. Find $\rho_r \mu_r$ using figures B2 and B3 or Tables B2 and B3. Recently the following expressions have been found for $(\rho_e \mu_e)_{eff}$ and $\rho_r \mu_r$:

$$(\rho_e \mu_e)_{eff} = \rho_{g'} \mu_{g'} \left[1.85 - .85 \frac{\rho_{g'} \mu_{g'}}{\rho_e \mu_e} \right] \quad (B78)$$

$$\rho_r \mu_r = (\rho_e \mu_e)_{eff} \left[1.6 - .6 \frac{(\rho_e \mu_e)_{eff}}{(\rho_w \mu_w)} \right] \quad (B79)$$

As may be seen from the values tabulated in Tables B2 and B3, eq. (B78) and (B79) agree with the curves of Figures B2 and B3 to within about 3%, corresponding to a 2 to 3 percent error in the predicted heating rate, and so are considered adequate for most purposes.

c. Find

1. $(Z T)_r$ from $\rho_r \mu_r, P_e$
2. i_r from $(Z T)_r, P_e$
3. σ_r from $(Z T)_r$
4. μ_o from $i_g, i_r, (Z T)_r$ and equation (B45)

(Note that μ_0 is required only for turbulent flow calculations.) Any gas properties may be used in these calculations. In the present report the gas properties of references 2 and 26 were used.

- d. Determine the streamline divergence parameters r and f . For arbitrary bodies at angle of attack these parameters are often not known, although their product Δ may be estimated from the pressure distribution or oil flow patterns. The values of r and f for several special cases are given in Table B1.

- e. Find β_B if required. Note that for the general case, exact evaluation of β_B requires an iterative solution, since

$$\beta_B = 2 \frac{i_S}{i_0} \left[J_L \frac{x_{eq,L}}{x} \right] \frac{d(\ln u_0)}{d(\ln x)} \quad (B80)$$

and the term in brackets is in itself a function of β_B . In practice however, a finite difference integration along the streamline is performed for the bracket parameter

$$\left[J_L \frac{x_{eq,L}}{x} \right] = \frac{1}{\left[G_L f^{2\bar{E}_L} J_L x \right]_{x_1}} \int_0^{x_1} G_L f^{2\bar{E}_L} J_L dx \quad (B81)$$

and the local value of β_B at $x = n\Delta x$ can be evaluated with sufficient accuracy (if the step size is small) by

$$\left[\beta_B \right]_{x=n\Delta x} = 2 \left[\frac{i_S}{i_0} \frac{d(\ln u_0)}{d(\ln x)} \right]_{x=n\Delta x} \left[J_L \frac{x_{eq,L}}{x} \right]_{x=(n-1)\Delta x} \quad (B82)$$

f. Find Σ_g , Σ_c , and Σ_0 using equations (B37, B38, B39, and B40). As discussed in connection with equation (B50), the subscript 0 denotes evaluation for zero Mach number.

g. Find Γ from Σ using figure B4 or Table B4. Recently, the following expression was found:

$$\Gamma = [.96 \Sigma^{.55} - .5] \quad (B83)$$

The error in heating resulting from the use of eq. (B83) rather than figure B4 is less than 1% for $\beta < 10$.

h. Evaluate J , E , x_{eq} and F_x , and R_x from the definitions given earlier in this section.

i. Find $i_{D,e}$, $i_{D,e}/i_e$ and \mathcal{L} from i_e , P_e

j. The heat transfer coefficient H can now be calculated from equations (B61) through (B63). Specific values of the various boundary layer parameters are given in Table B1.

Case (β_s)	$\frac{\rho_r \mu_r}{(\rho_r \mu_r)_{x_1}}$	$\frac{u_e}{(u_e)_{x_1}}$	$\frac{r}{(r)_{x_1}}$	$\frac{f}{(f)_{x_1}}$	$\frac{J}{(J)_{x_1}}$	(x_{eq}, L) at x_1	$(x_{eq}, L, 0)$ at x_1	$(x_{eq}, T, 0)$ at x_1
1. Flat Plate (0)	1	1	1	1	1	x_1	x_1	x_1
2. Stag Line of Un-yawed Cyl (1)	1	x/x_1	1	1	1	$\frac{x_1}{2J_L}$	$\frac{x_1}{2J_L}$	$\triangle 1$
3. Hemispherical Stag Pt (1/2)	1	x/x_1	x/x_1	1	1	$\frac{x_1}{4J_L}$	$\frac{x_1}{4J_L}$	$\triangle 1$
4. Stag Line of Inf Yawed Cyl (0)	1	1	1	e^{-KZ}	1	$\frac{1}{2K \bar{E}_L}$	$\frac{1}{2K \bar{E}_L, 0}$	$\frac{4}{5K \bar{E}_T, 0}$
5. Unyawed Cone (0)	1	1	x/x_1	1	1	$x_1/3$	$x_1/3$	$\frac{4x_1}{9}$

$\triangle 1$ Not applicable — laminar flow only.

$\triangle 2$ $K = \frac{1}{u_e} \left(\frac{dV_n}{dS_{LE}} \right)_{SL}$
 $\beta_c = 1.0$

TABLE B1
 STREAMLINE DIVERGENCE PARAMETERS
 FOR SEVERAL SPECIAL CASES

TABLE B2

TABULATION OF VALUES OF $\rho_r \mu_r$

$\frac{(\rho_e \mu_e)_{eff}}{\rho_w \mu_w}$	$\frac{\rho_r \mu_r}{\rho_w \mu_w}$	
	From figure (B2)	From equation (B79)
.15	.226	.226
.20	.290	.296
.25	.354	.362
.30	.414	.426
.35	.485	.486
.40	.532	.544
.5	.641	.650
.6	.739	.744
.7	.818	.826
.8	.892	.896
.9	.950	.954
1.0	1.000	
1.1	1.04	equation (B79)
1.2	1.08	not valid for
1.3	1.12	hot wall cases
1.4	1.15	
1.5	1.18	
1.6	1.21	
1.7	1.25	
1.8	1.26	

TABLE B3

TABULATION OF VALUES OF $(\rho_e \mu_e)_{eff}$

$\frac{\rho_s \mu_s}{\rho_e \mu_e}$	$\frac{(\rho_e \mu_e)_{eff}}{\rho_e \mu_e}$	
	From figure B3(a)	From equation (B78)
.2	.335	.336
.3	.478	.478
.4	.610	.604
.5	.715	.713
.6	.791	.804
.7	.850	.879
.8	.905	.936
.9	.955	.976
1.0	1.000	1.000

TABLE B4

TABULATION OF VALUES OF Γ

Σ	Γ	
	From figure B4	From equation (B83)
.5	.164	.155
.6	.232	.224
.8	.360	.349
1.0	.475	.460
1.5	.710	.700
2.0	.925	.905
3.0	1.27	1.26
4.0	1.56	1.56
5.0	1.83	1.82
6.0	2.07	2.07
7.0	2.30	2.30
8.0	2.50	2.51
9.0	2.70	2.72
10.0	2.87	2.90

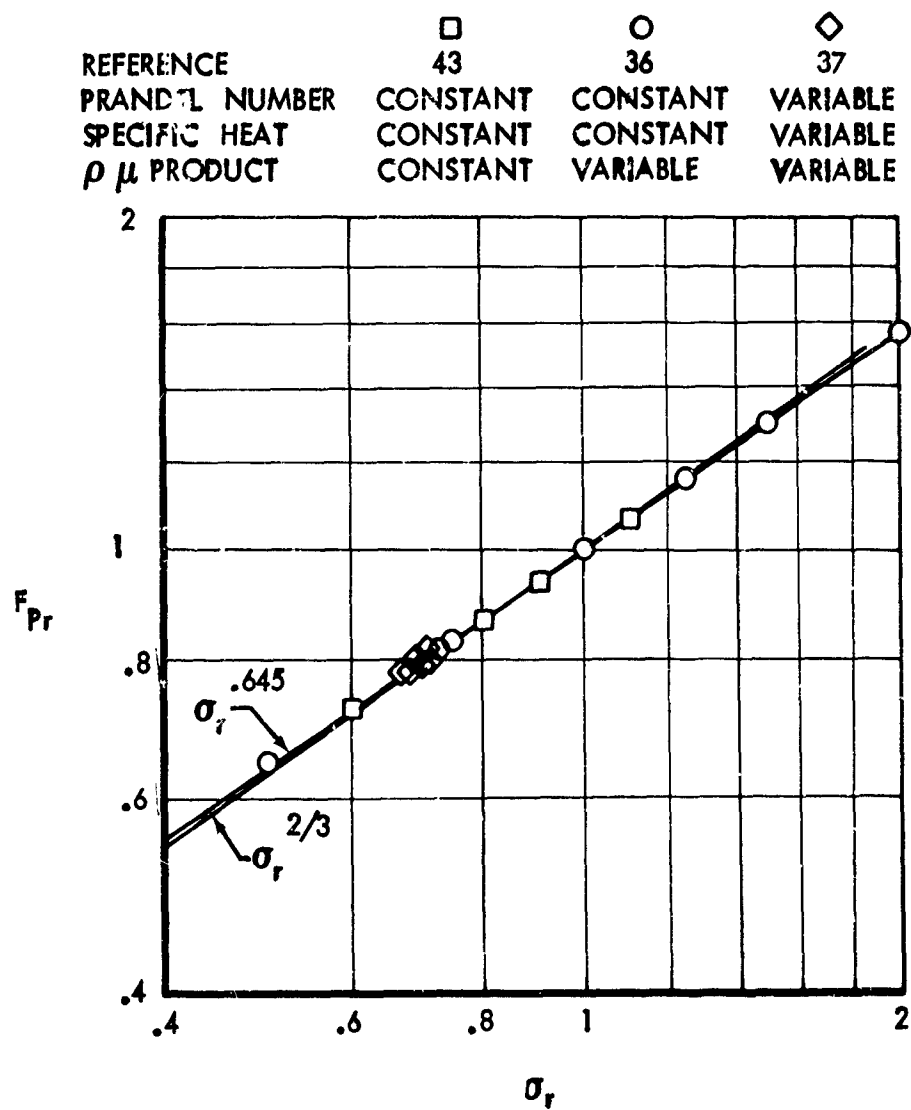


Figure B1: EFFECT OF PRANDTL NUMBER ON REYNOLDS ANALOGY FACTOR

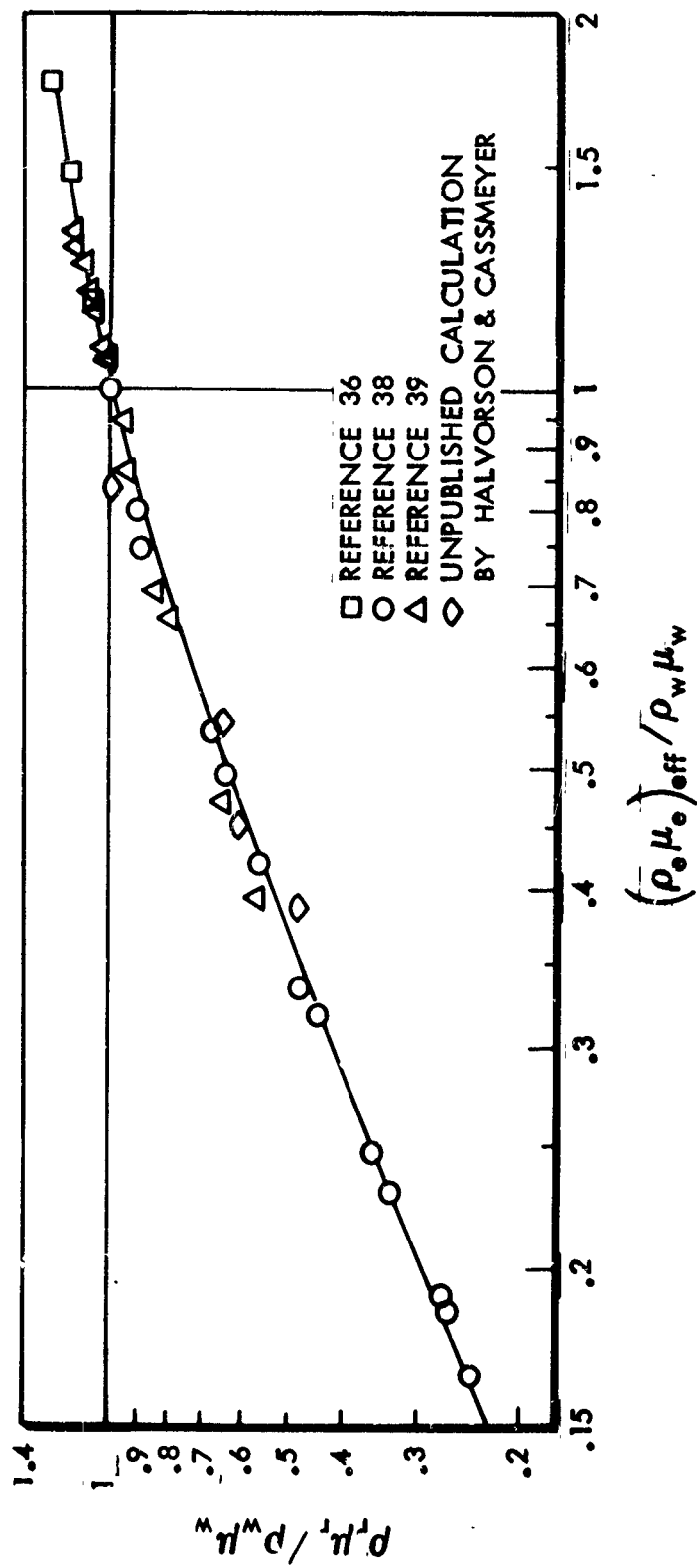
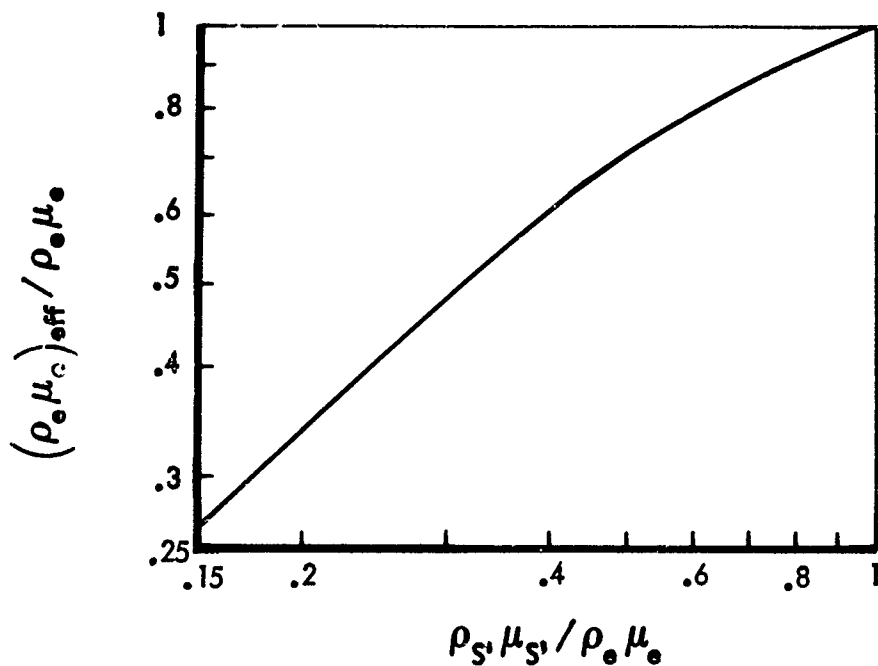
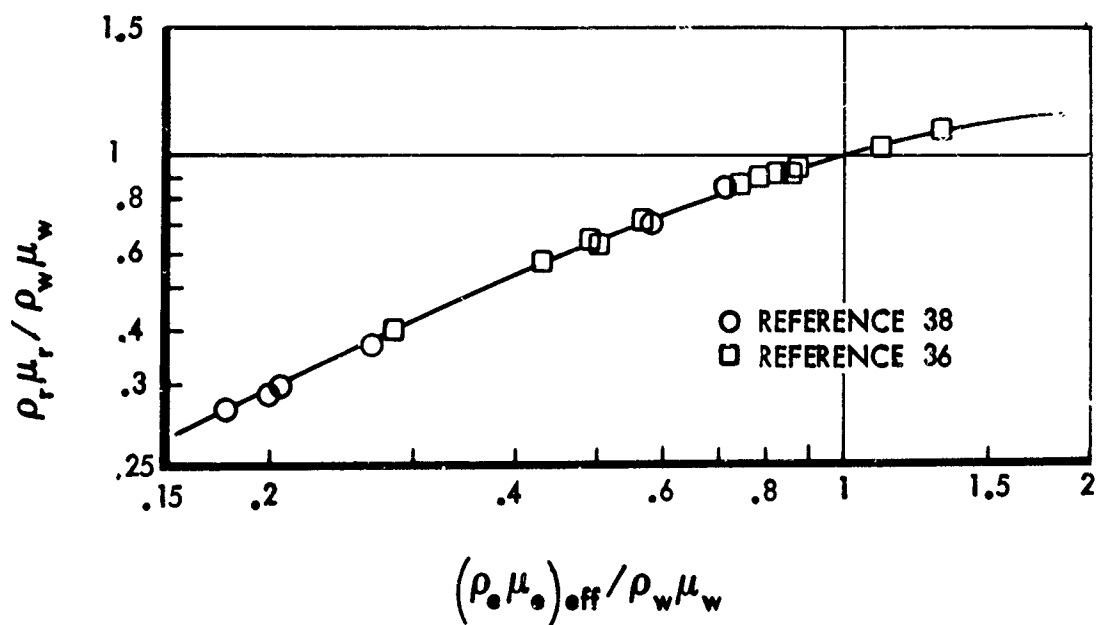


Figure B2: CORRELATION OF REFERENCE DENSITY-VISCOSITY PRODUCT (M = 0)



(a) EFFECTIVE DENSITY-VISCOSITY PRODUCT AS A FUNCTION OF BOUNDARY LAYER EDGE AND STAGNATION ENTHALPY CONDITIONS.



(b) REFERENCE DENSITY-VISCOSITY PRODUCT AS A FUNCTION OF EFFECTIVE EDGE VALUES AND WALL CONDITIONS. $M > 0$.

Figure B3: DENSITY-VISCOSITY PRODUCT CORRELATIONS

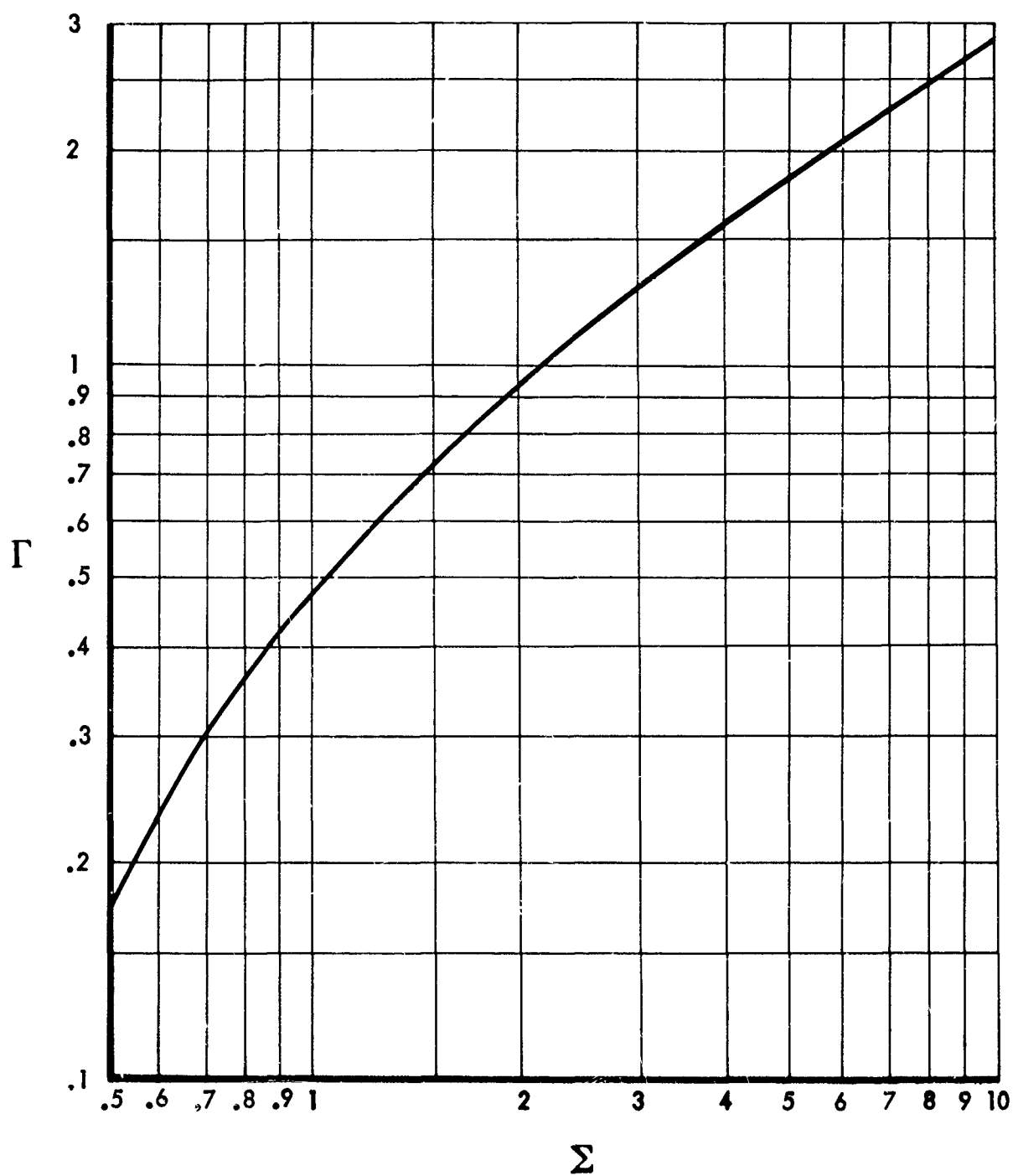


Figure B4: PRESSURE GRADIENT EFFECT CORRELATION PARAMETERS

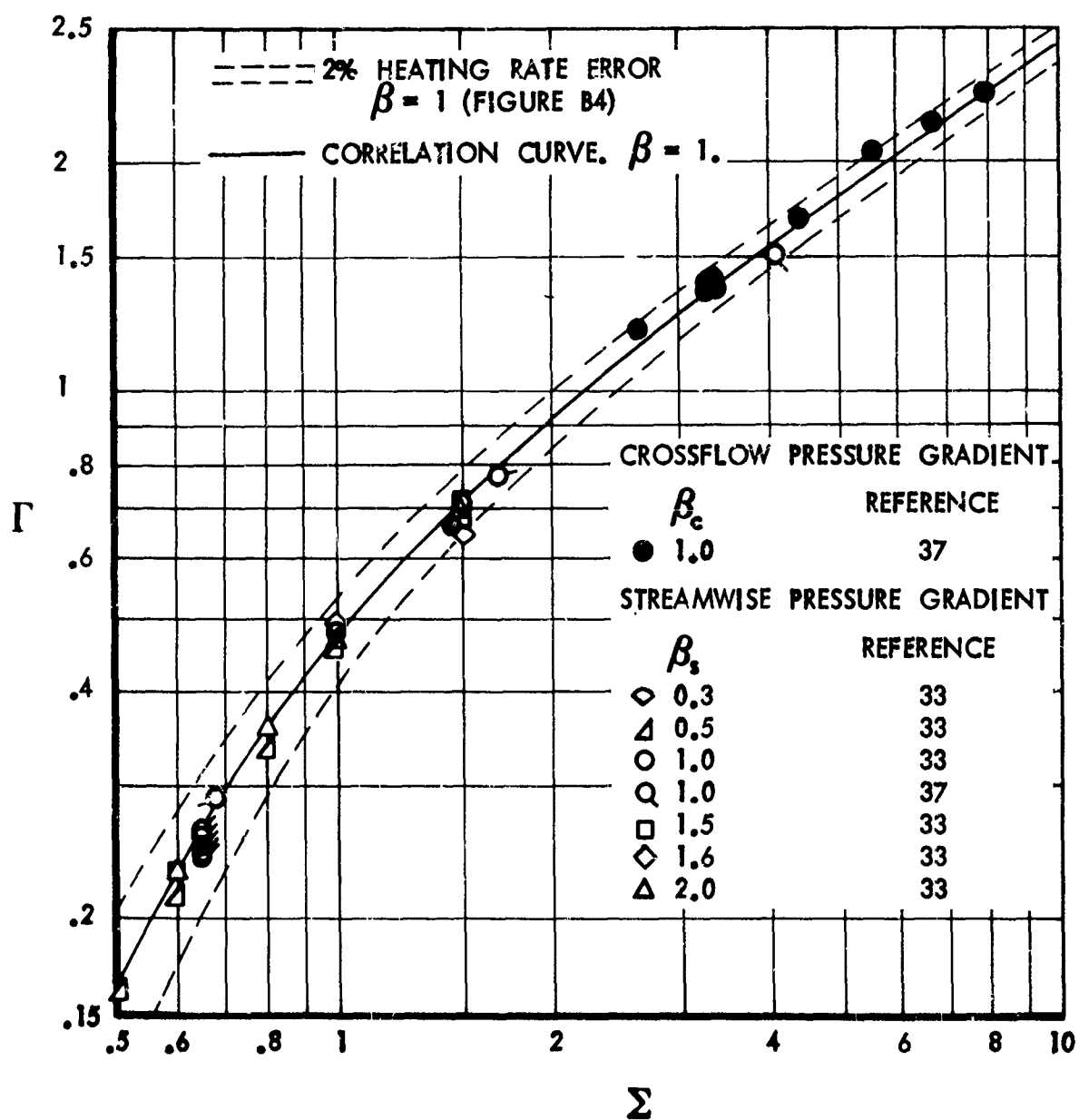


Figure B5: PRESSURE GRADIENT EFFECT CORRELATION
COMPARED WITH EXACT SOLUTIONS

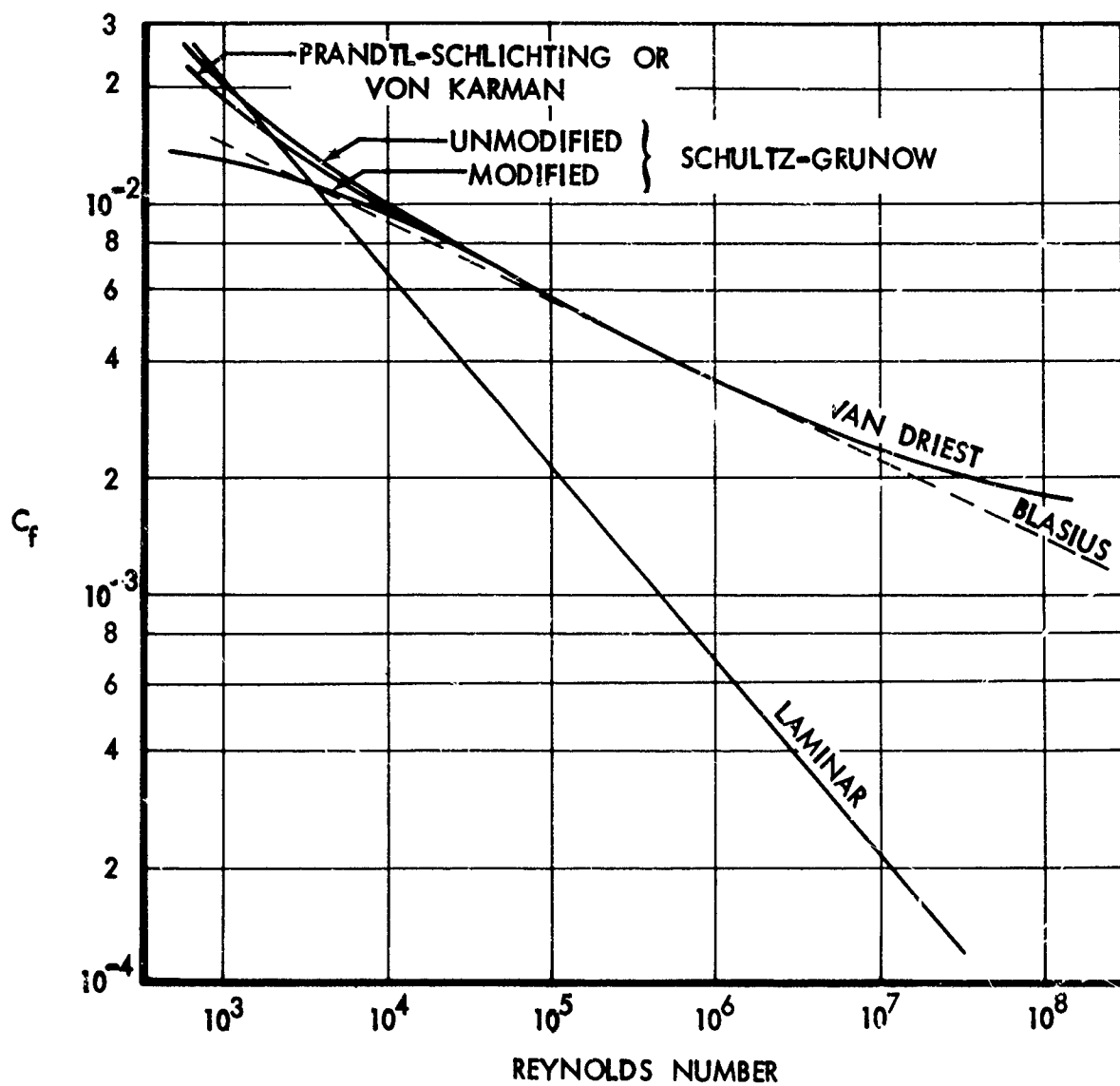


Figure B6: COMPARISON OF INCOMPRESSIBLE
TURBULENT SKIN-FRICTION FORMULAS

APPENDIX C*

NONSIMILAR BOUNDARY LAYER PROGRAM**

The purpose of the Nonsimilar Boundary Layer Program is to integrate the laminar boundary layer partial differential equations using finite difference methods, but without the use of similarity assumptions.

Nearly all published exact laminar boundary layer solutions have been obtained using the concept of similarity. These solutions, which must be obtained numerically, require that the viscous flow partial differential equations be transformed to a set of ordinary, non-linear differential equations. In the transformed system the flow properties are expressed as functions of a single similarity variable, and are therefore independent of chordwise location. Unfortunately, the necessary transformation requires certain flow conditions which are rarely realized on realistic configurations. The Boeing Nonsimilar Program was developed to avoid such limitations.

The Nonsimilar Program can calculate either stagnation or non-stagnation boundary layers with arbitrary pressure gradients, with or without mass injection. Three-dimensional flow effects are calculated using the zero cross-flow approximation, $f/f_1 = 1$, which implies no rotation of the velocity vectors within the boundary layer. The program is also limited to attached flow.

The program described herein treats air in chemical equilibrium. The program can be applied to ideal gas and other fluids by changing the tabulated gas transport property tables.

The program is capable of initiating its own boundary layer solutions, given only external flow properties, for either the stagnation point or sharp tip cones and plates.

Basic Equations. - The equations solved by this computer program are the standard boundary layer equations of state, continuity, x-momentum and energy. These equations are presented in a form used by the program for evaluation at several vertical positions in the boundary layer at each value of x considered.

* This Appendix is based on Appendix C of Reference 18.

** This computer program was developed by A. L. Nagel and R. T. Savage during the X-20 development program.

EQUATION OF STATE

$$\rho = \frac{P}{R (zT)} \quad (C1)$$

CONTINUITY

$$v = \frac{1}{\left[\frac{\partial u}{\partial y} - \frac{2u}{\Delta y} \right]} \left\{ u^2 \left[\frac{1}{r} \frac{dr}{dx} + \frac{1}{P} \frac{\partial P}{\partial x} \right] + \frac{1}{\rho} \left[\frac{\partial}{\partial y} \left(\mu \frac{\partial u}{\partial y} \right) - \frac{\partial P}{\partial x} \right] \right. \\ \left. - \frac{u}{\rho zT} \frac{\partial (zT)}{\partial \left(H - \frac{u^2}{2} \right)} \left[\left[\frac{\partial}{\partial y} \left(\frac{\mu}{P_r} \frac{\partial H}{\partial y} \right) - u \frac{\partial}{\partial y} \left(\mu \frac{\partial u}{\partial y} \right) + u \frac{\partial P}{\partial x} \right] \right. \right. \\ \left. \left. + \frac{\partial}{\partial y} \left[\left(1 - \frac{1}{P_r} \right) \mu u \frac{\partial u}{\partial y} \right] \right] \right] - u \left[\frac{2 v_{i-1}}{\Delta y} + \left(\frac{\partial y}{\partial y} \right)_{i-1} \right] \right\} \quad (C2)$$

where subscript i-1 refers to $y = y - \Delta y$

x-MOMENTUM

$$\frac{\partial u}{\partial x} = \frac{1}{\rho u} \left[\frac{\partial}{\partial y} \left(\mu \frac{\partial u}{\partial y} \right) - \frac{\partial P}{\partial x} \right] - \frac{y}{u} \frac{\partial u}{\partial y} \quad (C3)$$

ENERGY

$$\frac{\partial H}{\partial x} = \frac{1}{\rho u} \left[\left[\frac{\partial}{\partial y} \left(\frac{\mu}{P_r} \frac{\partial H}{\partial y} \right) + \frac{\partial}{\partial y} \left[\left(1 - \frac{1}{P_r} \right) \mu u \frac{\partial u}{\partial y} \right] \right] \right] - \frac{y}{u} \frac{\partial H}{\partial y} \quad (C4)$$

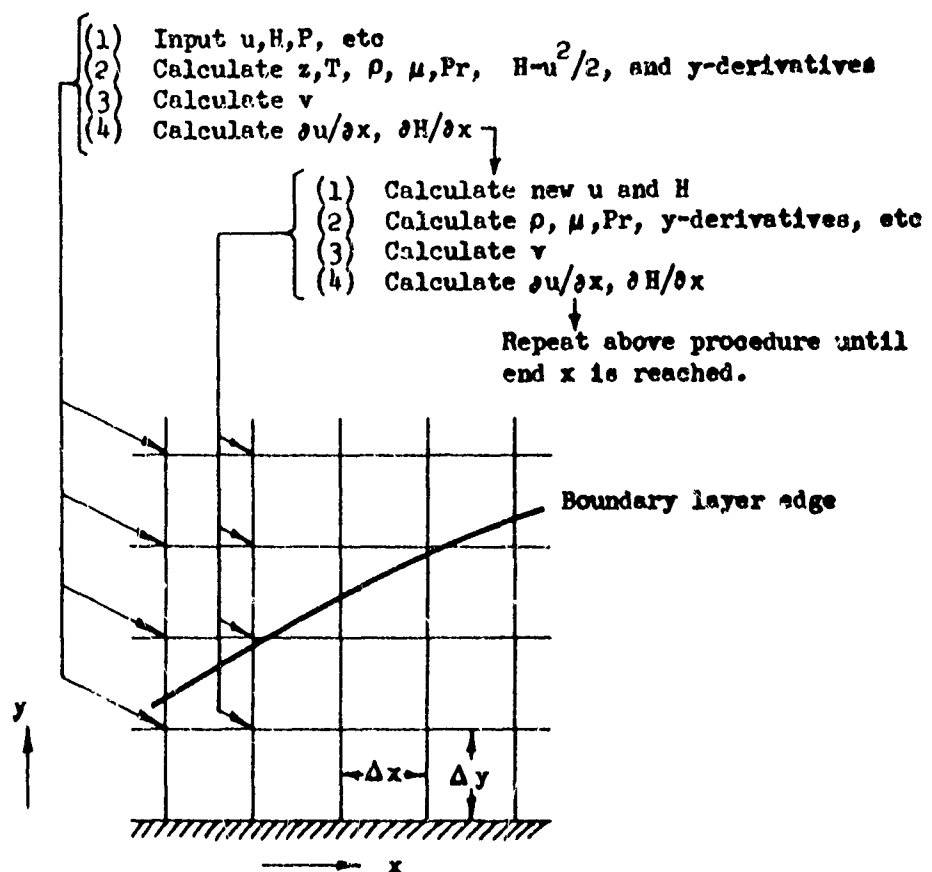
Equation (C2) is obtained from the continuity equation by introducing equation (C3) and (C4) to eliminate $\partial u/\partial x$ and $\partial H/\partial x$. No atomic diffusion terms are required in equation (C4) because this mode of energy transport has been included in the Prandtl number.

Forward integration. - Since v is expressed as a function of input data, v can be determined explicitly at each point in the boundary layer at the initial or start position. With v defined, the initial u and H profiles, $\partial u/\partial x$ and $\partial H/\partial x$ can be determined. With $\partial u/\partial x$ and $\partial H/\partial x$ determined, the profiles at the next station can be obtained by forward integration using the following equations

$$u_{x+\Delta x} = u_x + \left. \frac{\partial u}{\partial x} \right|_x \Delta x \quad (C5)$$

$$H_{x+\Delta x} = H_x + \left. \frac{\partial H}{\partial x} \right|_x \Delta x \quad (C6)$$

This scheme of calculation is presented in the sketch below:



At each point in the boundary layer, the classical similarity parameter is calculated using the following relationship.

$$\eta = \frac{\rho_e u_e r}{\left[\int_0^x \rho_e u_e \mu_e r^2 dx \right]} \int_0^\delta \frac{\rho}{\rho_e} dy \quad (C7)$$

Also calculated at each station (x) are the boundary layer displacement thickness, δ^* , heating rate, \dot{q}_w , and shear at the wall, τ_w .

$$\delta^* = \int_0^\delta \left[1 - \frac{\rho u}{\rho_e u_e} \right] dy \quad (C8)$$

$$\dot{q}_w = - \frac{1}{778} \int_0^\delta \left[\rho u \frac{\partial H}{\partial x} + \rho v \frac{\partial H}{\partial y} \right] dy \quad (C9)$$

$$\tau_w = \tau_e - \int_0^\delta \left[\rho u \frac{\partial u}{\partial x} + \rho v \frac{\partial u}{\partial y} + \frac{\partial P}{\partial x} \right] dy \quad (C10)$$

The heating rate and shear at the wall are calculated using the energy and momentum integral equations rather than the definitions because of the greater accuracy obtainable with the integrals. The use of the definition of \dot{q}_w and τ_w requires very small Δy increments to obtain accurate values of the gradients at the wall.

For problems without vorticity, $\tau_e = 0$. For cases with vorticity, $(\partial u / \partial y)_e$ is input as a function of x.

Stagnation Region Calculation

Stagnation point profiles are obtained by modifying the procedure just discussed. Input profiles are corrected by integrating the u and H profiles, but x (not equal to zero) is not increased during the integration. The profiles are assumed correct when

$$\left| \left(\frac{\partial u}{\partial x} \right)_i - \frac{u_i}{x} \right| < .1 u_e \quad \text{for all } i \quad (C11)$$

where u_e is the velocity at the edge of the input velocity profile (i.e. the input velocity farthest from the wall.) This convergence criterion is obtained with the velocity similarity stated below.

$$\frac{\partial u}{\partial x} \Big|_e = \frac{u_e}{u} \frac{\partial u}{\partial x} \quad (C12)$$

Experience has indicated that an enthalpy profile convergence criterion is not necessary.

For the stagnation region, equations (C5) and (C6) are changed to

$$H_i = H_l + \frac{\partial H}{\partial x} \Big|_l \Delta S \quad (C13)$$

$$u_i = \left[u_l + \frac{\partial u}{\partial x} \Big|_l \Delta S \right] \frac{x_0}{x_0 + \Delta S} \quad (C14)$$

where x_0 = initial x location

ΔS = a fictitious length

Once the convergence criteria have been satisfied, the calculations can be stepped forward around the body as discussed in the previous section.

Gas Properties.- As stated previously the program treats air in chemical equilibrium and can be applied to air as an ideal gas and to other fluids by changing the tabulated gas transport property tables.

The transport properties for equilibrium air were based on the nine-species model (N_2 , O_2 , NO , N , O , N^+ , O^+ , and e^-) of reference 2 and computed using the collision integral method of reference 44. The transport properties are built into the program as tabular functions of enthalpy and pressure.

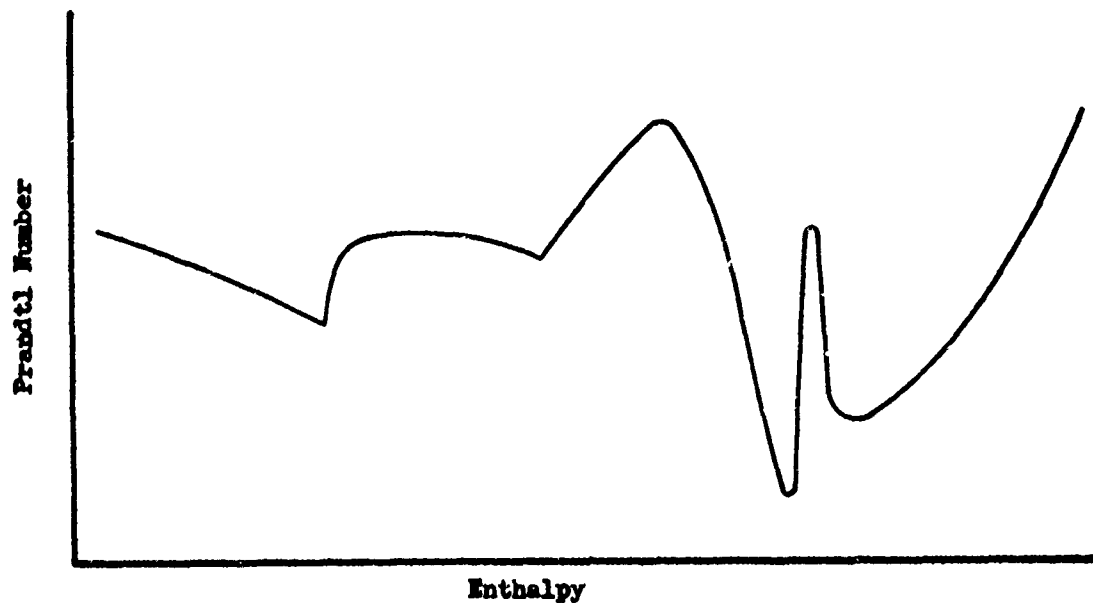
$$T = f\left(P, H - \frac{u^2}{2}\right) \quad (C15)$$

$$z = f\left(P, H - \frac{u^2}{2}\right) \quad (C16)$$

$$\mu = f\left(P, H - \frac{u^2}{2}\right) \quad (C17)$$

$$\int Pr d\left(H - \frac{u^2}{2}\right) = f\left(P, H - \frac{u^2}{2}\right) \quad (C18)$$

The integral of the Prandtl number is used to eliminate errors introduced into the finite difference calculations by the oscillations in the Prandtl number. The oscillations cause



a large Prandtl number gradient to exist between adjacent nodes at which calculations are made.

The Prandtl number is obtained over two nodes by

$$Pr_i = \frac{\int \left[Pr d \left(H - \frac{u^2}{2} \right) \right]_{i+1} - \int \left[Pr d \left(H - \frac{u^2}{2} \right) \right]_{i-1}}{\left(H - \frac{u^2}{2} \right)_{i+1} - \left(H - \frac{u^2}{2} \right)_{i-1}} \quad (C19)$$

where i refers to evaluation at

$i + 1$ refers to evaluation at $y + \Delta y$

$i - 1$ refers to evaluation at $y - \Delta y$

APPENDIX D

FORMULATION OF $h\delta^*$

The boundary layer displacement thickness heating parameter, defined by

$$h\delta^* = h \int_0^{\infty} \left(1 - \frac{\rho u}{\rho_e u_e}\right) dy, \quad (D1)$$

is required for evaluating the effects of shallow surface waves on aerodynamic heating. This appendix describes the methods that were used to compute the values shown on Figure 6-45. Only laminar flow has been considered.

Methods for estimating the laminar displacement thickness were developed by Hanks and Savage, Reference 29, by correlating the boundary layer solutions first presented by Cohen, Reference 37. The closed form equation for δ^* that is presented in Reference 29 is rewritten here and forms the basis for the development of the equations used to define the product, $h\delta^*$. For zero pressure gradient

$$\delta^* = \frac{\left(2 \int_0^x [\rho_w \mu_w u_e r^2] dx\right)^{\frac{1}{2}}}{\rho_e u_e r} \Delta^* \quad (D2)$$

where

$$\Delta^* = \left[-0.905 + 2 (\bar{TZ})_{\text{ref}} + \left(\frac{0.13}{(\bar{TZ})_{\text{ref}}} \right) \right]$$

$$(\bar{TZ})_{\text{ref}} = 0.73 \frac{(TZ)_w}{(TZ)_e} + \frac{(TZ)_s}{(TZ)_e}$$

Results shown on Figure 6-45 were calculated for a sharp flat plate. For this geometry

$$r = 1$$

$$\rho_w \mu_w u_e = \text{const}$$

APPENDIX E

SAMPLE SOLUTIONS

To illustrate the use of the charts in Sections VI and VII, example problems were prepared. In most instances, examples have been chosen that clearly explain the procedure required to reduce the curves to correct numerical results. The applicable text section number precedes each example.

A. Section VI - Reference Condition

Radius Correction - Turbulent Reference Heat Transfer Coefficient

Example: Determine the turbulent stagnation line heat transfer coefficient, $h_{SL,T}$, for a 60° swept cylinder having a leading edge radius of $R = 0.1$ ft. The flight condition is $VEL = 10,000$ fps and $ALT = 100,000$ ft.

	Quantity	Source	Value
①	h_{RT}	Figure 6-4	1.6×10^{-2} Btu/ft ² -sec-°R
②	R_R	Figure 6-7	360,000
③	C_{RT}	Figure 6-6	1.64
④	$h_{SL,T}$	① x ③	2.62×10^{-2} Btu/ft ² -sec-°R

B. Section VI - Basic Shapes

1. Sharp Flat Plate and Sharp Cone

The computational procedure required to obtain heating rates for a sharp flat plate or a sharp unyawed cone is similar. The procedure is illustrated using a sharp flat plate.

a) Laminar Flow

Example: Determine the laminar heat transfer rate to a sharp flat plate at an angle of attack of 20° , at a distance $x = 5$ ft, for $T_w = 1500$ °R and $T_{AW}/T_T = 0.87$. The flight condition is $VEL = 20,700$ fps and $ALT = 200,000$ ft.

	Quantity	Source	Value
①	$h_{FP,L}/h_o$	Figure 6-23	0.275 (Altitude effects neglected for figure 6-23)
②	h_o	Figure 6-2	3.56×10^{-3} Btu/ft ² -sec-°R

③	$h_{FP,L}$	① x ②	$9.77 \times 10^{-4} \text{ Btu/ft}^2\text{-sec-}^\circ\text{R}$
④	C_x	Figure 6-25	0.445
⑤	$h_x = 5 \text{ ft}$	③ x ④	$4.35 \times 10^{-4} \text{ Btu/ft}^2\text{-sec-}^\circ\text{R}$
⑥	C_T	Figure 6-24	1.0
⑦	$h_x = 5 \text{ ft}$	⑤ x ⑥	$4.35 \times 10^{-4} \text{ Btu/ft}^2\text{-sec-}^\circ\text{R}$
⑧	T_{AW}	Figure 6-1	$31,500^\circ\text{R}$
⑨	\dot{q}	$h(T_{AW} - T_W)$ $= \textcircled{7} \textcircled{8} - 1500)$	$13.05 \text{ Btu/ft}^2\text{-sec}$

b) Turbulent Flow

To obtain turbulent heating rates to a sharp flat plate or a sharp un-yawed cone, use the turbulent reference and design charts. The procedure is identical to that shown above.

2. Hemisphere

a) Laminar Flow

Example. Determine the laminar heat transfer rate to a 1-foot radius hemisphere at the angular location $\theta = 60^\circ$. The flight condition is VEL = 20,700 fps and ALT = 200,000 ft. Assume $T_W = 2000^\circ\text{R}$ and $T_{AW}/T_T = 0.95$.

Quantity	Source	Value
① h_θ/h_o	Figure 6-9	0.395 (Altitude effects neglected for figure 6-9)
② h_o	Figure 6-2	$3.56 \times 10^{-3} \text{ Btu/ft}^2\text{-sec-}^\circ\text{R}$
③ $h_{\theta = 60^\circ}$	① x ②	$1.41 \times 10^{-3} \text{ Btu/ft}^2\text{-sec-}^\circ\text{R}$
④ T_{AW}/T_T	Assume	0.95
⑤ T_{AW}	Figure 6-1	$34,500^\circ\text{R}$
⑥ \dot{q}	$h(T_{AW} - T_W)$ $= \textcircled{3} (\textcircled{5} - 2000)$	

Wall temperature corrections can be made using figure 6-3.

b) Turbulent Flow

Example: Determine the turbulent heat transfer rate to a hemisphere using the conditions given in the example for laminar flow.

	Quantity	Source	Value
①	$R_{r_{MAX}}$	Figure 6-10	1420
②	θ_{MAX}	Figure 6-11	36.25°
③	$\Delta\theta$	$60^\circ - \theta_{MAX}$	$+23.75^\circ$
④	h/h_{MAX}	Figure 6-12	0.715
⑤	h_{MAX}/h_{SP}	Figure 6-13	0.66
⑥	h_o	Figure 6-2	$3.56 \times 10^{-3} \text{ Btu/ft}^2\text{-sec-}^\circ\text{R}$
⑦	h	④ x ⑤ x ⑥	$1.53 \times 10^{-3} \text{ Btu/ft}^2\text{-sec-}^\circ\text{R}$
⑧	T_{AW}/T_T	Assume	0.95
⑨	T_{AW}	Figure 6-1	$35,000^\circ\text{R}$
⑩	\dot{q}	$h(T_{AW} - T_W)$ $= \text{⑦} (\text{⑨} - 2000)$	$50.5 \text{ Btu/ft}^2\text{-sec}$

When the radius of the hemisphere is different from $R = 1 \text{ ft}$, the value of $R_{r_{MAX}}$ must be corrected using equation (6.10) before using figures 6-11 and 6-13.

3. Swept Infinite Cylinder

a) Laminar Flow

Example: Find the laminar heat-transfer rate to a 40° swept cylinder, 1 foot in radius at an angular location, $\theta = 60^\circ$. The flight condition is $VEL = 20,700 \text{ fps}$ and $ALT = 200,000 \text{ ft}$. Assume $T_W = 1000^\circ\text{R}$ and $T_{AW}/T_T = 0.94$.

	Quantity	Source	Value
①	h_θ / h_o	Figure 6-17	0.222
②	h_o	Figure 6-2	$3.56 \times 10^{-3} \text{ Btu/ft}^2\text{-sec-}^\circ\text{R}$
③	$h_{\theta = 60^\circ}$	① x ②	$0.79 \times 10^{-3} \text{ Btu/ft}^2\text{-sec-}^\circ\text{R}$

④	$M_{\infty N}$	$M_{\infty} \times \cos 40^\circ$	17
⑤	C_L	Figure 6-3	1.05
⑥	$h_{\theta = 60^\circ}$ $T_W = 1000^\circ R$	③ x ⑤	$0.83 \times 10^{-3} \text{ Btu/ft}^2\text{-sec-}^\circ R$
⑦	T_{AW}/T_T	Assume	0.94
⑧	T_{AW}	Figure 6-1	$34,000^\circ R$
⑨	\dot{q}	$h(T_{AW} - T_W)$ $= \text{⑥} (\text{⑧} - 1000)$	$27.4 \text{ Btu/ft}^2\text{-sec}$

b) Turbulent Flow

The procedure for determining turbulent heating rates to swept cylinders is similar to that shown above for laminar flow.

4. Unswept Infinite Cylinder

a) Turbulent Flow

Example: Determine the turbulent heat transfer coefficient to a 1 foot radius unswept cylinder at an angular location, $\theta = 60^\circ$. The flight condition is VEL = 18,7000 fps and ALT = 180,000 ft. Assume $T_W = 2000^\circ R$.

	Quantity	Source	Value
①	$R_{r_{MAX}}$	Figure 6-20	5,500
②	θ_{MAX}	Figure 6-21	33.6°
③	$\Delta\theta$	$60^\circ - \theta_{MAX}$	$+26.4^\circ$
④	h_{MAX}/h_{SP}	Figure 6-13	0.7
⑤	h_o	Figure 6-2	$4.55 \times 10^{-3} \text{ Btu/ft}^2\text{-sec-}^\circ R$
⑥	h_{SP}	$h_{SP} = h_o(R = 1 \text{ ft})$	$4.55 \times 10^{-3} \text{ Btu/ft}^2\text{-sec-}^\circ R$
⑦	$h_{\theta = 60^\circ}/h_{MAX}$	Figure 6-22	$0.66 \text{ Btu/ft}^2\text{-sec-}^\circ R$
⑧	$h_{\theta = 60^\circ}$	④ x ⑥ x ⑦	$2.10 \times 10^{-3} \text{ Btu/ft}^2\text{-sec-}^\circ R$

NOTE:

When the radius is different from $R = 1 \text{ ft}$, $R_{r_{MAX}}$ must be corrected using

equation (6.10) before using figures 6-13 and 6-21.

4. Sharp Delta Wing

a) Laminar Flow

Example: Determine the laminar heat transfer coefficient to a 75° swept sharp delta wing at $x = 5$ ft. on the centerline, and at $x = 5$ ft. off the centerline on the rayline $\epsilon/\epsilon_{MAX} = 0.5$. The wing is at an angle of attack of 20° at the flight condition $VEL = 20,700$ fps and $ALT = 240,000$ ft.

	Quantity	Source	Value
①	$h_{SD,L}/h_o$	Figure 6-30	0.325
②	h_o	Figure 6-2	1.62×10^{-3} Btu/ft ² -sec-°R
③	$h_{SD,L}$	① x ②	5.26×10^{-4} Btu/ft ² -sec-°R
④	C_X	Figure 6-25	0.445
⑤	$h_{x=5 \text{ ft}}$	③ x ④	2.34×10^{-4} Btu/ft ² -sec-°R
⑥	$(h/h_{\Lambda=70^\circ})_{x=5 \text{ ft}}$	Figure 6-31	1.065
⑦	$h_{x=5 \text{ ft}}$ $\Lambda = 75^\circ$	⑤ x ⑥	2.50×10^{-4} Btu/ft ² -sec-°R
⑧	$h_\epsilon/h_\epsilon = 0^\circ$	Figure 6-32	1.01
⑨	$h_{x=5 \text{ ft}}$	⑦ x ⑧	2.52×10^{-4} Btu/ft ² -sec-°R

The wall temperature correction is obtained from figure 6-24.

To determine turbulent heat transfer coefficients to a sharp delta wing requires the use of turbulent reference and design charts. The procedure is identical to that required to obtain laminar heat transfer coefficients.

C. Section VI - Combinations of Basic Shapes

1. Unyawed Blunt Cone

a) Laminar Flow

Example: Calculate the laminar heat transfer rate to a blunted cone having a hemispherical nose of $R = 0.5$ ft and a semi-vertex angle of 30° at $S/R = 4$. The flight condition is $VEL = 20,700$ fps, and $ALT = 200,000$ ft. Assume $T_W = 2000$ °R and $T_{AW}/T_T = 0.95$.

Quantity	Source	Value
① $(h_{BC,L}/h_{SP})_{S/R=4}$	Figure 6-27	0.198
② h_o	Figure 6-2	$3.56 \times 10^{-3} \text{ Btu/ft}^2\text{-sec-}^\circ\text{R}$
③ $(h_{BC,L})_{S/R=4}$	$h_{SP} = h_o \sqrt{\frac{R_o}{R_{SP}}}$	$5.04 \times 10^{-3} \text{ Btu/ft}^2\text{-sec-}^\circ\text{R}$
④ $h_{S/R}$	① x ③	$.995 \times 10^{-3} \text{ Btu/ft}^2\text{-sec-}^\circ\text{R}$
⑤ T_{AW}/T_T	Assume	0.95
⑥ T_{AW}	Figure 6-1	$34,500^\circ\text{R}$
⑦ \dot{q}	$h(T_{AW} - T_w)$ $= ④ (⑥ - 2000)$	$32.3 \text{ Btu/ft}^2\text{-sec}$

b) Turbulent Flow

Example: Determine the turbulent heat transfer rate to an unyawed blunt con: using the conditions shown in the example above.

Quantity	Source	Value
① $(R_{r_{MAX}})_{R=1 \text{ ft}}$	Figure 6-10	1420
② $(R_{r_{MAX}})_{R=0.5 \text{ ft}}$	$\frac{0.5}{1.0}$ ①	710
③ $(R_r/R_{r_{MAX}})_{S/R=4}$	Figure 6-28	8.5
④ R_r	② x ③	6035
⑤ h_T/h_L	Figure 6-29	1.23
⑥ h_L	From Step ④ in laminar heating example	$0.995 \times 10^{-3} \text{ Btu/ft}^2\text{-sec-}^\circ\text{R}$
⑦ h_T	⑤ x ⑥	$1.193 \times 10^{-3} \text{ Btu/ft}^2\text{-sec-}^\circ\text{R}$
⑧ T_{AW}/T_T	Assume	0.95
⑨ T_{AW}	Figure 6-1	$34,500^\circ\text{R}$
⑩ \dot{q}	$h(T_{AW} - T_w)$ $= ⑦ (⑨ - 2000)$	$38.8 \text{ Btu/ft}^2\text{-sec}$

2. Blunt Delta Wing

a) Laminar Flow

Example: Determine the laminar heat transfer coefficient to a 70° swept blunt delta wing at the centerline location $S/R = 17$. Also determine the leading edge stagnation line value, and its amount of shift due to lower surface effects, as well as the heating on the lower surface at $N/R = 4$. The flight condition is $VEL = 20,700$ fps and $ALT = 200,000$ ft at an angle of attack of 30° . The nose and leading edge radii are 1 ft.

	Quantity	Source	Value
①	$(h_{BD,L}/h_{SP})_{S/R=17}$	Figure 6-34	0.101
②	h_o	Figure 6-2	3.56×10^{-3} Btu/ft ² -sec-°R
③	h_{SP}	$h_{SP,(R=1 \text{ ft})} = h_o$	3.56×10^{-3} Btu/ft ² -sec-°R
④	$h_{BD,L}$	① x ③	3.59×10^{-4} Btu/ft ² -sec-°R
⑤	θ_{SL}	Figure 6-38	65°
⑥	Λ_{EFF}	Figure 6-39	54.5°
⑦	$(h_{SL}/h_o) \Lambda_{EFF}$	Figure 6-16	0.362
⑧	h_{SL}, Λ_{EFF}	② x ⑦	1.29×10^{-3} Btu/ft ² -sec-°R
⑨	$(h_{BD,L}/h_{SP})_{N/R=4}$	Figure 6-36	0.126
⑩	$(h_{BD,L})_{N/R=4}$	③ x ⑨	4.49×10^{-4} Btu/ft ² -sec-°R

b) Turbulent Flow

Example: Solve for the turbulent heat transfer coefficients on a blunt delta wing using the conditions given in the example for laminar flow except let the flight condition change to $VEL = 18,700$ fps and $ALT = 180,000$ ft.

	Quantity	Source	Value
①	$(h_{BD,L}/h_{SP})_{S/R = 17}$	Figure 6-34	0.101
②	h_o	Figure 6-2	4.55×10^{-3} Btu/ft ² -sec-°R
③	h_{SP}	$h_{SP}(R=1 \text{ ft}) = h_o$	4.55×10^{-3} Btu/ft ² -sec-°R
④	$h_{BD,L}$	① x ③	4.59×10^{-4} Btu/ft ² -sec-°R

⑤	$R_{r_{MAX}}$	Figure 6-10	2450
⑥	$(R_r/R_{r_{MAX}}) S/R = 17$	Figure 6-40	37
⑦	$(R_r)_{S/R = 17}$	⑤ x ⑥	91,000
⑧	(h_T/h_L)	Figure 6-29	2.6
⑨	h_T	④ x ⑧	$1.19 \times 10^{-3} \text{ Btu/ft}^2\text{-sec-}^\circ\text{R}$
⑩	θ_{SL}	Figure 6-38	65°
⑪	Λ_{EFF}	Figure 6-39	54.5°
⑫	$(h/h_{RT}) \Lambda_{EFF}$	Figure 6-18	1.22
⑬	h_{RT}	Figure 6-4	$2.82 \times 10^{-3} \text{ Btu/ft}^2\text{-sec-}^\circ\text{R}$
⑭	$h \Lambda_{EFF}$	⑫ x ⑬	$3.44 \times 10^{-3} \text{ Btu/ft}^2\text{-sec-}^\circ\text{R}$

NOTE:

When the nose radius is different from $R = 1 \text{ ft}$, the value of $R_{r_{MAX}}$ must be corrected by equation (6.10) before proceeding with step ⑦.

At the present, no method for evaluating turbulent heating between the centerline and the leading edge is available. Estimates must be made by fairing a curve through the end points.

3. Flap Surfaces

a) Laminar Flow

The increase in laminar heat transfer across a flap can be directly obtained using figure 6-41.

b) Turbulent Flow

Example: Determine the increase in turbulent heating across a 10° positively deflected flap where the initial surface is at an angle of attack of 20° for the flight condition $VEL = 18,700 \text{ fps}$ and $ALT = 180,000 \text{ ft}$.

	Quantity	Source	Value
①	$(h_F/h_{HL})_L$	Figure 6-41	3.3
②	$(h_F/h_{HL})_T / (h_F/h_{HL})_L$	Figure 6-42	0.925

$$\textcircled{3} \quad (h_F/h_{HL})_T \quad \textcircled{1} \times \textcircled{2} \quad 3.05$$

D. Section VI - Surface Condition Effects

Surface Roughness

Example: Determine the increase in laminar surface heating on a flat plate at an angle of attack $\alpha = 20^\circ$, for the flight condition $VEL = 20,700$ fps and $ALT = 240,000$ ft. Assume the wave height parameter $W/R = 25$ and $R = 0.1$ ft.

Quantity	Source	Value
$\textcircled{1} \quad h_o \delta^*$	Figure 6-45	$1.26 \times 10^{-5} \text{ Btu/ft-sec-}^\circ\text{R}$
$\textcircled{2} \quad h/h_o$	Figure 6-23	0.275
$\textcircled{3} \quad h_o$	Figure 6-2	$1.62 \times 10^{-3} \text{ Btu/ft}^2\text{-sec-}^\circ\text{R}$
$\textcircled{4} \quad \delta^*$	$\textcircled{1} / (\textcircled{2} \times \textcircled{3})$	0.0283 ft
$\textcircled{5} \quad R/\delta^*$	$0.1 / \textcircled{4}$	3.53
$\textcircled{6} \quad h_{MAX}/h$	Figure 6-43	>1.7

E. Section VI - Application To Complex Configurations

Control Surface Gaps

a) Laminar Flow

Example: Determine the maximum heat-transfer coefficient on the lower surface fin and control-surface gap for the flight condition $VEL = 20,700$ fps and $ALT = 240,000$ ft. The vehicle is at an angle of attack, $\alpha = 20^\circ$. The surfaces creating the gap have a circular cross-section of radius = 1 ft and are far enough apart to prevent choking.

Quantity	Source	Value
$\textcircled{1} \quad h_{G,L}/h_o$	Figure 6-47	0.0332
$\textcircled{2} \quad h_o$	Figure 6-2	$1.62 \times 10^{-3} \text{ Btu/ft}^2\text{-sec-}^\circ\text{R}$
$\textcircled{3} \quad h_{G,L}$	$\textcircled{1} \times \textcircled{2}$	$0.538 \times 10^{-4} \text{ Btu/ft}^2\text{-sec-}^\circ\text{R}$

b) Turbulent Flow

The solution for turbulent heat-transfer coefficients in a control surface gap requires the use of turbulent reference and design charts. The procedure is identical to that for laminar flow.

F. Section VII - Use of Ground-Test Data in Design

Two methods are used to extrapolate wind-tunnel data to flight conditions. The first method involves the use of compressibility parameter charts and extrapolation factor charts. Flat plates, sharp cones, infinite swept cylinders, sharp delta wings, and control surface gaps fall under this method of extrapolation. The procedure in computing the results is the same in all cases and therefore only one example is provided that is applicable to all of the geometries mentioned above. This procedure is illustrated in the examples under the subheading, "General Method." The second method is illustrated in the examples under the subheading "Method for Deflected Flaps." The extrapolation from wind tunnel to flight for laminar flow on a hemisphere is a special case ($\Delta = 1$) and can be obtained directly from figure 7-25.

1. General Method

a) Laminar Flow

Example: Laminar data is available from a wind tunnel on a flat plate at an angle of attack, $\alpha = 20^\circ$, at $x = 0.4$ ft. When normalized to the stagnation point heat-transfer coefficient for a 1 ft radius sphere the ratio is 0.38. The total enthalpy of the tunnel is 2×10^7 ft²/sec² and the test section Mach number is 12. Determine the heating rate ratio for the laminar design flight condition, VEL = 20,700 fps and ALT = 240,000 ft.

	Quantity	Source	Value
①	$(h_{FP,L}/h_o)_{WT} \quad x = 1 \text{ ft}$	$0.38 \times \frac{.4}{1}$	0.24
②	i_{FLT}	$i_{FLT} \sim V^2/2$	2×10^8
③	i_{WT}/i_{FLT}	$(2 \times 10^7)/(2 \times 10^8)$	0.1
④	$\frac{(h_{FP,L}/h_o)_{WT}}{(h_{FP,L}/h_o)_{FLT}} \cdot \frac{1}{\Delta_{FP,L}}$	Figure 7-19	0.854
⑤	$\Delta_{FP,L}$	Figure 7-11	1.079
⑥	$(h_{FP,L}/h_o)_{FLT}$	① / (④ x ⑤)	0.261
⑦	$(h_x/h_o)_{FLT}$	⑥ $\sqrt{\frac{x = 1 \text{ ft}}{x = .4 \text{ ft}}}$	0.413

b) Turbulent Flow

To determine turbulent heating rate ratios use the turbulent reference, design, and extrapolation charts. The procedure is identical to that for laminar flow.

2. Method for Deflected Flaps

a) Laminar Flow

Example: Laminar heating data from a $M_\infty = 10$ wind tunnel show a 100% increase in heating for a 10° positively deflected flap whose initial surface is deflected 20° , i.e., angle of attack, $\alpha = 20^\circ$. Compute the expected change in heating for the same geometry at the laminar reference condition, $VEL = 20,700$ fps and $ALT = 240,000$ ft. If data show a 20% decrease in heating in the wind tunnel for a 10° negatively deflected flap, compute the expected change for the flight condition stated above.

Quantity	Source	Value
<u>For $\delta = +10^\circ$, $\alpha = 20^\circ$</u>		
① $\frac{(h_F/h_{HL})_{FLT}}{(h_F/h_{HL})_{WT}}$	Figure 7-30	1.29
② $(h_F/h_{HL})_{WT}$	Given	2.0
③ $(h_F/h_{HL})_{FLT}$	① x ②	2.58
<u>For $\delta = -10^\circ$, $\alpha = 20^\circ$</u>		
④ $\frac{(h_F/h_{HL})_{FLT}}{(h_F/h_{HL})_{WT}}$	Figure 7-30	0.82
⑤ $(h_F/h_{HL})_{WT}$	Given	0.8
⑥ $(h_F/h_{HL})_{FLT}$	④ x ⑤	0.656

b) Turbulent Flow

For turbulent flow the procedure is the same as shown above except an additional step is required to convert to expected turbulent values. This is done by using figure 6-42 in conjunction with the calculated laminar value.

REFERENCES

1. Arave, R. J.: Approximate Thermodynamic, Transport and Electrical Properties Of High Temperature Air. Boeing Document D2-11781, January 1963.
2. Moeckel, W. E.: Oblique-Shock Relations At Hypersonic Speeds For Air In Chemical Equilibrium. NACA TN 3895, January 1957.
3. Hayes, W. D.; and Probstein, R. F.: Hypersonic Flow Theory. Academic Press, 1959.
4. Liepmann, H. W.; and Roshko, A.: Elements of Gasdynamics. John Wiley & Sons, Inc., 1957.
5. Truitt, R. W.: Hypersonic Aerodynamics. The Ronald Press. 1959.
6. Van Dyke, M. D.: The Supersonic Blunt Body Problem - Review and Extensions. J. Aero/Space Sci., Vol. 25, 1958.
7. Belotserkovskii, O. M.: Flow Past a Circular Cylinder with a Detached Shock. Dokl. Akad. Nauk SSSR 113, 1957. Translated by Friedman.
8. Ferri, A.; Zakkay, V.; and Ting Lu: Blunt-Body Heat Transfer at Hypersonic Speed and Low Reynolds Numbers. J. Aero/Space Sci., Vol. 28, 1961.
9. Probstein, R. F.; and Kemp, H. N.: Viscous Aerodynamic Characteristics in Hypersonic Rarefied Gas Flow. J. Aero/Space Sci., Vol. 27, 1960.
10. Hoshizaki, H.; Neice, S.; and Chen, K. K.: Stagnation Point Heat Transfer Rates at Low Reynolds Numbers. IAS Paper No. 60-68, Institute of the Aerospace Sciences, June 1960.
11. Van Dyke, M. D.: Second-Order Compressible Boundary-Layer Theory With Application to Blunt Bodies In Hypersonic Flow. AFOSR-TN-61-1270, July 1961.
12. Eastman, D. W.: 2-D or Axially Symmetric Real Gas Flows by the Method of Characteristics. Part I - Formulation of the Equations. Boeing Document D2-10597, 1961. Part II - Flow Fields Around Bodies, Boeing Document D2-10598, August 1963.
13. Kennet, Haim: The Inviscid Hypersonic Flow on the Windward Side of a Pointed Lifting Delta Wing. IAS Paper No. 63-55, Institute of the Aerospace Sciences, January 21, 1963.
14. Lin, S. C.: Cylindrical Shock Waves Produced by Instantaneous Energy Release. J. Applied Physics, January 1954.

15. Tendeland; Nielsen; and Fohrman: The Flow Field Over Blunted Flat Plates and Its Effect on Turbulent Boundary Layer Growth and Heat Transfer at a Mach Number of 4.7. NASA TN D-689, November 1960.
16. Nagel, A. L.; Fitzsimmons, H. D.; and Doyle, L. B.: Analysis of Hypersonic Pressure and Heat Transfer Tests on Delta Wings with Laminar and Turbulent Boundary Layers. To be published by NASA, Langley.
17. Giles, H. L.; and Thomas, J. W.: Analysis of Hypersonic Pressure and Heat Transfer Tests on a Flat Plate with a Flap and a Delta Wing with a Body, Elevons, Fins, and Rudders. To be published by NASA, Langley.
18. Jaeck, C. L.: Analysis of Pressure and Heat Transfer Tests on Surface Roughness Elements with Laminar and Turbulent Boundary Layers. To be published by NASA, Langley.
19. Chapman, D. L.: A Theoretical Analysis of Heat Transfer in Regions of Separated Flow. NACA TN 3792, October 1956.
20. Larson, H. K.: Heat Transfer in Separated Flows. IAS Report No. 59-37, January 1959.
21. Holloway, P. F.; Sterrett, J. R.; and Creekmore, H. S.: An Investigation of Heat Transfer within Regions of Separated Flow at a Mach Number of 6.0. NASA TN D-3074, November 1965.
22. Chung, P. M.; and Viegas, J. R.: Heat Transfer at the Reattachment Zone of a Laminar Boundary Layer. NASA TN D-1072, September 1961.
23. Lees, L.: Laminar heat Transfer over Blunt Nosed Bodies at Hypersonic Speeds. Jet Propulsion, Vol. 26, 1956, pp. 259-269 and 274.
24. Eckert, Ernst R. G.: Survey on Heat Transfer at High Speeds. WADC Tech. Rep. No. 54-70, Wright Air Development Center, Wright Patterson Air Force Base, Ohio, 1954.
25. Baxter, D. C.; and Flugge-Lotz, I.: The Solution of Compressible Laminar Boundary Layer Problems by a Finite Difference Method. Part II-Further Discussion of Method and Computation of Examples. No. 118, Stanford University, October 1957.
26. Hansen, C. F.: Approximations for the Thermodynamic and Transport Properties of High Temperature Air. NACA TN 4150, March 1958.
27. Shapiro, A. H.: The Dynamics and Thermodynamics of Compressible Fluid Flow, Vol. II. The Ronald Press, 1954.

28. Nagel, A. L.; and Thomas, A. C.: Analysis of the Correlation of Wind Tunnel and Ground Test Data to Flight Test Results. AIAA Paper No. 65-208, AIAA/NASA Flight Testing Conference, Huntsville, Ala., Feb. 15-17, 1965.
29. Hanks, R. A.; and Savage, R. T.: Thermal Design Methods for Recoverable Launch Vehicles with Consideration of Arbitrary Wall Temperatures and Surface Conditions. Boeing Document D2-90770-1, August 1965.
30. Mager, A.: Transformation of the Compressible Turbulent Boundary Layer. Journal of Aeronautical Sciences, Vol. 25, No. 5, May 1958, pp. 305-311.
31. Beckwith, I. E.; and Gallagher, J. J.: Local Heat Transfer and Recovery Temperatures on a Yawed Cylinder at a Mach Number of 4.15 and High Reynolds Numbers. NASA Memo 2-27-59L, April 1959.
32. Howarth, L.: Velocity and Temperature Distribution for a Flow Along a Flat Plate. Proc. Roy. Soc., London 1959.
33. Cohen, C. B.; and Reshotko, E: Similar Solutions for Compressible Laminar Boundary Layer with Heat Transfer and Pressure Gradient. NACA TN 3325, February 1955.
34. Reshotko, E; and Beckwith, I. E.: Compressible Laminar Boundary Layer Over a Yawed Infinite Cylinder with Heat Transfer. NACA TN 3986, June 1957.
35. Fay, J. A.; and Riddell, F. R.: Theory of Stagnation Point Heat Transfer in Dissociated Air. Research Report No. 1, AVCO Research Laboratory, April 1957.
36. Van Driest, E. R.: Investigation of Laminar Boundary Layer in Compressible Flow Using the Crocco Method. NACA TN 2597, January 1952.
37. Cohen, N. B.: Boundary Layer Similar Solutions and Correlation Equations for Laminar Heat Transfer Distribution in Equilibrium Air at Velocities up to 41,000 Feet Per Second. NASA TR R-118, 1961.
38. Kemp, N. H.; Rose, P. H.; and Detra, R. W.: Laminar Heat Transfer Around Blunt Bodies in Dissociated Air. AVCO Research Laboratory, Research Report 15, May 1958.
39. Young, G. B. W.; and Janssen, E.: The Compressible Boundary Layer. Journal of Aeronautical Sciences, Vol. 19, No. 4, April 1952, p. 1229.
40. Trella, M.; and Libby, P. A.: Similar Solutions for the Hypersonic Laminar Boundary Layer Near Plane of Symmetry. AIAA Journal, Vol. 3, No. 1, January 1965.
41. Vaglio-Laurin, R.: Laminar Heat Transfer on Three-Dimensional Blunt Nosed Bodies in Hypersonic Flow. ARS Journal, Vol. 29, No. 2, February 1959.

42. Schultz-Grunow, F.: New Frictional Resistance Law for Smooth Plates. NACA Memorandum No. 986, August 1940.
43. Schlichting, Herman: Boundary Layer Theory. Fourth Edition, McGraw-Hill Book Co., New York, 1960.
44. Hirschfelder, J. O.; Curtiss, C. F.; and Bird, R. B.: Molecular Theory of Gases and Liquids. John Wiley and Sons, 1954.

UNCLASSIFIED

Security Classification

DOCUMENT CONTROL DATA - R&D		
(Security classification of title, body of abstract and indexing annotation must be entered when the overall report is classified)		
1 ORIGINATING ACTIVITY (Corporate author)		2a REPORT SECURITY CLASSIFICATION
The Boeing Company Seattle, Washington		Unclassified
		2b GROUP
3 REPORT TITLE		
Advanced Re-entry Systems Heat Transfer Handbook for Hypersonic Flight (U)		
4 DESCRIPTIVE NOTES (type of report and inclusive dates)		
Final Report		
5 AUTHOR(S) (Last name, first name, initial)		
Thomas, Alfred C. Perlbachs, Andrew Nagel, A. L.		
6 REPORT DATE	7a TOTAL NO. OF PAGES	7b NO. OF REFS
June, 1966	213 + xix	44
8a CONTRACT OR GRANT NO.	9a ORIGINATOR'S REPORT NUMBER(S)	
AF33(657)-7132	AFDRL-TR-65-195	
b PROJECT NO.		
c	9b OTHER REPORT NO(S) (Any other numbers that may be assigned this report)	
d	D2-84029-1	
10 AVAILABILITY/LIMITATION NOTICES		
This document is subject to special export controls and each transmittal to foreign governments or foreign nationals may be made only with prior approval of the Air Force Flight Dynamics Laboratory (FDMG), Wright-Patterson AFB, Ohio		
11 SUPPLEMENTARY NOTES	12 SPONSORING MILITARY ACTIVITY	
	Air Force Flight Dynamics Laboratory Air Force Systems Command Wright-Patterson AFB	
13 ABSTRACT		
<p>An advanced re-entry systems heat transfer handbook for hypersonic flight has been developed using aerothermodynamic prediction methods developed during the X-20A (Dyna Soar) Program. It contains 1) design procedures for computing aerodynamic heating rates to re-entry vehicle configurational elements, 2) discussion on differences between aerodynamic heat transfer and pressure distribution observed in present day wind tunnels and those which would occur in actual free flight, 3) wind tunnel to flight extrapolation factors, 4) simplified expressions for estimating stagnation point and swept cylinder turbulent stagnation line heating rates, and 5) graphs for rapid calculation of heating rates and extrapolation to flight factors. The information presented is applicable to complex maneuverable vehicles as well as ballistic bodies. (U)</p>		

DD FORM 1 JAN 64 1473
U3 4802 1030 REV. 4/65
PART 1 OF 2

UNCLASSIFIED

Security Classification

UNCLASSIFIED

Security Classification

14 KEY WORDS	LINK A		LINK B		LINK C	
	ROLE	WT	ROLE	WT	ROLE	WT
Aerodynamic Heating Basic Heat Transfer Methods Boundary Layer Configuration Design Extrapolation Factors Handbook for Heat Transfer						

INSTRUCTIONS

1. **ORIGINATING ACTIVITY:** Enter the name and address of the contractor, subcontractor, grantee, Department of Defense activity or other organization (corporate author) issuing the report.

2a. **REPORT SECURITY CLASSIFICATION:** Enter the overall security classification of the report. Indicate whether "Restricted Data" is included. Marking is to be in accordance with appropriate security regulations.

2b. **GROUP:** Automatic downgrading is specified in DoD Directive 5200.10 and Armed Forces Industrial Manual. Enter the group number. Also, when applicable, show that optional markings have been used for Group 3 and Group 4 as authorized.

3. **REPORT TITLE:** Enter the complete report title in all capital letters. Titles in all cases should be unclassified. If a meaningful title cannot be selected without classification, show title classification in all capitals in parenthesis immediately following the title.

4. **DESCRIPTIVE NOTES:** If appropriate, enter the type of report, e.g., interim, progress, summary, annual, or final. Give the inclusive dates when a specific reporting period is covered.

5. **AUTHOR(S):** Enter the name(s) of author(s) as shown on or in the report. Enter last name, first name, middle initial. If military, show rank and branch of service. The name of the principal author is an absolute minimum requirement.

6. **REPORT DATE:** Enter the date of the report as day, month, year, or month, year. If more than one date appears on the report, use date of publication.

7. **TOTAL NUMBER OF PAGES:** The total page count should follow normal pagination procedures, i.e., enter the number of pages containing information.

7b. **NUMBER OF REFERENCES:** Enter the total number of references cited in the report.

8a. **CONTRACT OR GRANT NUMBER:** If appropriate, enter the applicable number of the contract or grant under which the report was written.

8b, 8c, & 8d. **PROJECT NUMBER:** Enter the appropriate military department identification, such as project number, subproject number, system numbers, task number, etc.

9a. **ORIGINATOR'S REPORT NUMBER(S):** Enter the official report number by which the document will be identified and controlled by the originating activity. This number must be unique to this report.

9b. **OTHER REPORT NUMBER(S):** If the report has been assigned any other report numbers (either by the originator or by the sponsor), also enter this number(s).

10. **AVAILABILITY/LIMITATION NOTICES:** Enter any limitations on further dissemination of the report, other than those imposed by security classification, using standard statements such as:

(1) "Qualified requesters may obtain copies of this report from DDC."

(2) "Foreign announcement and dissemination of this report by DDC is not authorized."

(3) "U.S. Government agencies may obtain copies of this report directly from DDC. Other qualified DDC users shall request through _____."

(4) "U.S. military agencies may obtain copies of this report directly from DDC. Other qualified users shall request through _____."

(5) "All distribution of this report is controlled. Qualified DDC users shall request through _____."

If the report has been furnished to the Office of Technical Services, Department of Commerce, for sale to the public, indicate this fact and enter the price, if known.

11. **SUPPLEMENTARY NOTES:** Use for additional explanatory notes.

12. **SPONSORING MILITARY ACTIVITY:** Enter the name of the departmental project office or laboratory sponsoring (paying for) the research and development. Include address.

13. **ABSTRACT:** Enter an abstract giving a brief and factual summary of the document indicative of the report, even though it may also appear elsewhere in the body of the technical report. If additional space is required, a continuation sheet shall be attached.

It is highly desirable that the abstract of classified reports be unclassified. Each paragraph of the abstract shall end with an indication of the military security classification of the information in the paragraph, represented as (TS), (S), (C), or (U).

There is no limitation on the length of the abstract. However, the suggested length is from 150 to 225 words.

14. **KEY WORDS:** Key words are technically meaningful terms or short phrases that characterize a report and may be used as index entries for cataloging the report. Key words must be selected so that no security classification is required. Identifiers, such as equipment model designation, trade name, military project code name, geographic location, may be used as key words but will be followed by an indication of technical context. The assignment of links, roles, and weights is optional.

UNCLASSIFIED

Security Classification